UNIVERSITAT DE BARCELONA

Models and Computational Methods Applied to Industrial Gas Separation Processes and Enhanced Oil Recovery

Gerard Alonso Benito

Memòria presentada per

Gerard Alonso Benito

Per a optar al grau de Doctor per la Universitat de Barcelona

Programa de doctorat en Química Teòrica i Modelització Computacional

Models and Computational Methods Applied to Industrial Gas Separation Processes and Enhanced Oil Recovery

Dirigida per:

Prof. Ramón Sayós Ortega
(Universitat de Barcelona)

Dr. Pablo Gamallo Belmonte
(Universitat de Barcelona)

Tutor:

Dr. Pablo Gamallo Belmonte
(Universitat de Barcelona)

UNIVERSITAT DE BARCELONA

Barcelona, 2019

UNIVERSITAT DE BARCELONA

FACULTAT DE QUÍMICA

DEPARTAMENT DE CIÈNCIA DE MATERIALS I QUÍMICA FÍSICA

INSTITUT DE QUÍMICA TEÒRICA I COMPUTACIONAL

Models and Computational Methods Applied to Industrial Gas Separation Processes and Enhanced Oil Recovery

Gerard Alonso Benito

2019

UNIVERSITAT DE BARCELONA

Institut de Química Teòrica i Computacional

“Don’t listen to the person who has the answers;
listen to the person who has the questions”

Albert Einstein

The work presented in this doctoral thesis has been developed in the Materials Science and Physical Chemistry Department and the Institute of Theoretical and Computational Chemistry (IQTC) of the University of Barcelona (UB).

This project has been financially supported, in part, by the Spanish *Ministerio de Economia y Competitividad* (Projects CTQ2014-53987-R and CTQ2015-64618-R), by the *Generalitat de Catalunya* (Grants 2014SGR1582 and 2017SGR003) and a private technology transfer project with the oil company REPSOL. All the results presented in this doctoral thesis related with the latter project were presented to REPSOL, who gave explicit consent for publication as it is. Finally, Gerard Alonso Benito is grateful for the pre-doctoral grant from the University of Barcelona (APIF/2016-2018) and his pre-doctoral mobility APIF/2018 grant.

The computational resources employed to develop the work compiled in this doctoral thesis were provided mainly by the IQTC.

Acknowledgements

La compilació de tota la tesis que ve a continuació no hauria estat possible sense totes les persones que han estat al meu costat ajudant-me, ensenyant-me o simplement donant-me suport en els moments més difícils. Respecte a la gent que m'ha ajudat i ensenyat al llarg dels anys que porto a la Universitat de Barcelona, es podria contar pràcticament a tota la Secció de Química Física, però faré un petit incís a aquells que m'han estat més propers: l'Antonio Aguilar, en Pablo Gamallo i en Ramón Sayós. Per mi sou com els meus tres pares científics que m'heu acompanyat al llarg del TFG, TFM i tesis doctoral. Gràcies a vosaltres he aprés humilitat, autocrítica i perdre la por de saber dir "No ho sé", que m'ha ajudat innumerables vegades al llarg de la tesis.

També fa poc vaig fer una estada molt enriquidora a Concepción (Xile) on vaig conèixer a la gent del grup de l'Andrés Mejía, amb la Marce, el Mati, el Gustavo, el Carlos, el Félix y (encara que no sigui formalment del grup) el Harry. Tots em van acceptar al grup amb els braços oberts i em van fer sentir com a casa tot i que estava a l'altra punta del món. Especials agraïments a l'Andrés que més que com a supervisor em va acollir com a un amic.

Des del començament de la carrera fins a acabar el doctorat m'he creuat amb molta mes gent que mereix un petit espai en aquesta pàgina. Aquí contemplo tant al grup d'estudi del grau (l'Anna, el Mik, l'Ernest i el Ferranet) el grup d'estudi del màster (el Toninoh, l'Arturo, la Russy i el Miquel) i tota la gent amb qui he compartit despatx alguna vegada (el Carles, el Pablo Lozano, el Biel, el Joan i el Ángel). Sense tots ells el camí que he recorregut hauria sigut infinitament més avorrit i pobre. Em reservo un espai especial pels dos companys amb qui he passat més temps durant la tesis i que es deuen haver trobat a faltar en el apartat anterior i que m'han aportat alguna cosa important a la meva vida. Hèctor, gràcies a tu he començat a fer moltes més activitats, m'he tornat bastant més sociable i he aprés a focalitzar molt millor els meus esforços al fer recerca. I Manel, gracies a la teva bondat i enorme criteri he crescut interiorment com a persona i crec tenir més sentit comú i ser força menys manipulable.

Fora de la meva vida laboral també hi ha hagut gent important a qui agraeixo per permetre'm desconnectar una mica de tot (Ricard, Josep, Mon i en especial al Aleix).

També els meus pares han estat molt importants per mi des de que era petit, per criar-me amb tot al amor i atenció que em van poder donar amb el poc temps que tenien. També per la seva paciència, el seu suport moral i per pressionar-me a donar més de mi mateix, els dos formen part d'aquests agraïments. Gràcies mama i papa.

Finalment, agrair a la Sara per aguantar-me durant la tesis i tots els anys que portem convivint. Sé que no t'agradarà sortir aquí perquè et semblarà innecessari i potser vergonyós així que aquest paràgraf el guardo per nosaltres. Aquí només deixaré escrit un breu "t'estimo".

Table of Contents

Glossary

AA	All-Atom
AAD	Average Absolute Deviation
ADF	Amsterdam Density Functional
Al-Kao	Aluminum Termination of Kaolinite
CA	Contact Angle
cEOR	Chemical Enhanced Oil Recovery
CG	Coarse-Grained
CM	Center of Mass
CMC	Critical Micelle Concentration
COSMO-RS	COnductor-like Screening MOdel for Realistic Solvents
D2	Grimme D2 Empirical Dispersion Correction
d6r	Double-six Ring
DAY	Dealuminated Faujasite
DFT	Density Functional Theory
DSL	Dual Site Langmuir
EoS	Equation of State
EOR	Enhanced Oil Recovery
FAU	Faujasite
FF	Force Field
GCMC	Grand Canonical Monte Carlo
HS	Hard Spheres
IFT	Interfacial Tension
IL	Ionic Liquid
IZA	International Zeolite Association
LAMMPS	Large-scale Atomic/Molecular Massively Parallel Simulator
LJ	Lennard-Jones
LLE	Liquid Liquid Equilibrium
MC	Monte Carlo

MD	Molecular Dynamics
MOF	Metal Organic Framework
NaX	Faujasite with 1.18 Si/Al ratio
NH	Nosé-Hoover
NPT	Isobaric-Isothermal Ensemble
NVE	Microcanonical Ensemble
NVT	Canonical Ensemble
PBCs	Periodic Boundary Conditions
PES	Potential Energy Surface
PSA	Pressure Swing Adsorption
RDF	Radial Distribution Function
SAFT	Statistical Association Fluid Theory
SARA	Saturate, Aromatic, Resin and Asphaltene
Si-Kao	Silicon Termination of Kaolinite
Sod	Sodalite Cage
ST	Surface Tension
TSA	Temperature Swing Adsorption
UA	United-Atom
vdW	van der Waals
VASP	Vienna Ab-initio Simulation Package
VLE	Vapor Liquid Equilibrium
VSA	Vacuum Swing Adsorption
VTSA	Vacuum/Temperature Swing Adsorption
WC	Working Capacity
ZPE	Zero-Point Energy
μVT	Grand Canonical Ensemble

CHAPTER 1

Introduction and Motivation

In my humble opinion, and I remark that it is only my opinion, “Science” is a discipline that can be carried out in two possible ways. The first one consists in improving current existing technologies in different areas, such as to maximizing efficiency in production plants, reducing wastes and energetic costs, developing drugs to treat diseases or in general, anything that potentially improves the quality of life of the society. I understand this way of doing research as “Engineering” because it focuses on obtaining a profitable final result, which can be directly applied by industries or individuals affecting the way people lives. Usually, what I call “Engineering” is known as “Applied Science” but, to avoid possible confusions, I personally prefer to use a different term instead of adding adjectives to an existing word to modify its meaning. The second way of doing research is what I call simply “Science” and consist in trying to understand the world that surrounds us. It aims at answering questions to strange phenomena that are not yet understood, even if the answer will not necessarily benefit the society in the short term. However, all the understanding and discoveries made in the process of finding that answers are (and indeed were in the past) the basis of new technologies that nowadays we cannot even imagine. This kind of research is commonly known as “Fundamental Science” and, although its importance is more subtle than “Engineering”, the social development is not possible without it.

Every thesis ever written has a motivation focused on “Science”, “Engineering” or both, the present one is not an exception. The main motivation of this doctoral thesis is to study two processes of industrial interest: (i) the gas separation problem in post-combustion power plants, which can permit reducing the emissions of greenhouse gases and other pollutants to the atmosphere; and (ii) the enhanced recovery of oil in petroleum reservoirs, a field that intends to reduce the extraction costs of the main energy source of the world. However, many different methods and models were employed to tackle these challenges, in part driven by the thirst of answering questions and learning imposed to me by the discipline I call “Science”.

Disregarding the results obtained in this period of time, the development of a doctoral thesis has as an additional outcome the training of the future doctor. After these years of doing research I realized that my way of thinking has changed radically. Broadly speaking I have become more

rational, logic, organized and capable of splitting overwhelming challenges into small problems that can be assessed more easily. Moreover, I have become more confident and more critic with myself, which helped me to discover my weaknesses and strengths. These new skills are currently helping me (as well as they help all other researchers) to improve as a scientist and as a human being.

1.1 Outline of the Doctoral Thesis

The two main topics treated in this doctoral thesis (*i.e.,* the gas capture and the enhanced oil recovery) have one point in common: the use of computational methods to derive the different properties of interest once the system has reached the phase equilibrium. For this reason, this chapter contains a short introduction on how modeling and computational calculations are playing an important role in industry. Then, in Chapter 2, a general overview of all the methods used throughout this doctoral thesis and the theory behind them is compiled.

The different methods described allow treating systems with different sizes and simulate different time scales. The order in which the methods are explained in Chapter 2 is related to the system size and simulation time they can handle; thus, it goes from methods that can be applied to small systems and short time scales, and it ends with thermodynamic fluid theories, which can be understood as macroscopic systems at equilibrium. In other words, Chapter 2 starts with Density Functional Theory (DFT) in Section 2.1, which is used to obtain energetic interactions with the accuracy of quantum mechanics. The section is divided in the basis of DFT, the exchange and correlation functionals, periodic vs. non-periodic calculations and calculation of thermodynamic properties in Sections 2.1.1 to 2.1.4, respectively. Then, Section 2.2, explains how to obtain macroscopic properties from molecular simulations. The section is divided into a brief comparison among atomistic, united atom and coarse-grained force fields (Section 2.2.1) and the basics of Molecular Dynamics (MD), Monte Carlo methods (MC) and techniques to increase their efficiency (from Section 2.2.2 to Section 2.2.4, respectively). Finally, two last models based on thermodynamic fluid theories are defined in Section 2.3. The Section 2.3.1 explains the basis of equations of state based on Statistical Association Fluid Theory (SAFT), and concludes at Section 2.3.2 with a short overview of COnductor-like Screening MOdel for Realistic Solvents (COSMO-RS).

The first topic of this doctoral thesis (*i.e.,* the gas separation) is treated in Chapter 3. Three different kinds of materials to capture CO_2 are studied aiming at separating carbon dioxide from a post-combustion gas mixture to store it for further utilization. First, different zeolites from the

Faujasite family are studied with a combination of DFT and MC methods to assess the separation of CO_2 from a flue gas formed by a ternary mixture of CO_2, N_2 and O_2 (Section 3.2). Then, a DFT study of CO_2, N_2 and SO_2 adsorption onto Mg-MOF-74 coupled to a Langmuir isotherm model is presented in Section 3.3. Finally, absorption of CO_2 and SO_2 onto three different phosphonium-based Ionic Liquids (ILs) is addressed using SAFT and COSMO-RS models.

The second topic (*i.e.,* the enhanced oil recovery) is extended through Chapter 4 and Chapter 5. Specifically, Section 4.2 describes a set of compounds proposed to model the different fractions of oil, according to the Saturate/Aromatic/Resin/Asphaltene (SARA) model. Then, two different properties related to wettability (*i.e.,* the oil/water interfacial tension and the oil/water/rock contact angle) are analyzed under different environmental conditions and model oil mixtures in Section 4.3 and Section 4.4. On the other hand, in Chapter 5 the effect of surfactants is considered along with the evaluation of the so-called salt/surfactant synergistic effect to reduce the interfacial tension. The final part of this doctoral thesis contains Chapter 6, with a summary of the main conclusions compiled altogether, and Chapter 7, listing the publications achieved during the working period.

1.2 Brief History of Computational Science

Before the rise of computers, theoreticians applied the theories developed to predict properties of model systems (*i.e.,* ideal gas law, harmonic oscillator, etc.). Despite these theories provided exact solutions for ideal models, they only gave approximate results for real systems. This paradigm changed after the Second World War with the apparition of computers, that were used for the first time to cope with the hard mathematical requirements of developing nuclear weapons in the Manhattan Project. Fortunately, in the early 1950s computers became available for nonmilitary use, which was the beginning of the computer simulation discipline.[1,2]

Computer science allowed the researching community to employ theories with no analytical solutions to predict properties of real systems. Two of the fields related to this doctoral thesis were enormously benefitted from computation: (i) theoretical chemistry and (ii) the theory of dense fluids. The former was able to predict the electronic structure and exact energy of the simplest existing two-particle system (*i.e.,* the hydrogen atom) using the basis of quantum mechanics (*i.e.,* the Schrödinger equation).[3] However, an exact solution of the Schrödinger equation for more complex systems does not exists, but it could be solved numerically after 1930 with the works pioneered by Hartree,[4] Slater [5] and Fock,[6] who developed the Self-Consistent Field (SCF) method. On the other hand, very few analytical theories were available in the field of dense fluids. The

numerical models available treated liquids as a set of macroscopic droplets, but the calculation of the solution was too tedious to perform it by hand. One of the first molecular simulations were performed by Metropolis *et al.,* in 1953,[7] where a set of Lennard-Jones particles were evolved stochastically through the currently known "Metropolis Monte Carlo" algorithm. From that moment, molecular simulations were performed to describe properties of liquids through Monte Carlo and Molecular Dynamics techniques as described in the works of Alder *et al.,*[8] who studied the assembly of hard spheres, Gibson *et al.,*[9] who simulated radiation damage on crystalline Cu, or Rahman,[10] who performed the first molecular dynamics simulations of a real argon fluid.

These computational methods provided a deeper understanding of the experiments that were carried out in the last years; thus, the electronic structure of complex species and the molecular interaction between different particles were information that could be derived from these calculations. Molecular simulations coupled to statistical mechanics also provided a route to predict properties of matter at any set of pressure and temperature conditions. Despite there might be situations where these properties are easier to obtain from experimental measurements (*e.g.,* the melting point of water), the capability of simulations to work equally under any condition allows to easily predict these properties when experimental measurements are extremely expensive, or simply impossible. On the other hand, these simulations also allow to predict properties of materials that have not yet been synthesized.

The applicability of computer science was encompassed by a substantial increase of computer power as predicted by the Moore's Law curve. Thanks to this increase, more complex systems could be treated in reasonable amounts of time, allowing companies to incorporate simulations in the research and development divisions. Some of the more important applications of applied computer science include: (i) the field of biocatalysis, which is key in the pharmaceutical industry;[11,12] (ii) the biomedical field, that is closely related to biocatalysis for drug development,[13] along with the studies on organic membranes;[14] (iii) the field of materials that is based on understanding and developing new structures for several applications like energy (*e.g.,* for batteries [15] or solar cells [16]), enhanced electronic devices (*e.g.,* based on graphene [17] or other magnetic materials [18]) or gas capture and separation (*e.g.,* microporous materials for CO_2 capture) [19]; (iv) the field of green chemistry, that tries to improve the available technologies to capture different pollutants or remove them from wastewater; (v) the fields of catalysis and photocatalysis, both homogeneus [20] and heterogeneous,[21] which are of great interest to improve the efficiency of chemical production plants;[22] and (vi) the field of phase equilibrium based on describing the thermodynamic equilibria of multiple phases in contact at different conditions of pressure and temperature, which is the basis of phase diagrams and of many modeling processes in industry.[23,24] Many of these topics currently employ quantum chemistry calculations to understand interactions

at a molecular level or to obtain electronic-based processes. However, for large systems, molecular simulations are commonly employed, such as in the fields of phase equilibria, gas capture or biomedical fields. The use of computational methods has increased enough to even develop multiscale methods that permit the application of expensive quantum chemistry calculations in large systems such as in proteins for biocatalysis,[25] becoming an important part of research at the present time.

1.3 References

1 M. P. Allen and D. J. Tildesley, *Computer Simulation of Liquids*, Oxford University Press, New York, 2017.

2 D. Frenkel and B. Smit, *Understanding Molecular Simulation. From Algorithms to Applications*, Academic Press, London, 2002.

3 E. Schrödinger, Quantisierung als Eigenwertproblem, *Ann. Phys.*, 1926, **384**, 361–376.

4 D. R. Hartree, The Wave Mechanics of an Atom with a Non-Coulomb Central Field. Part I. Theory and Methods, *Math. Proc. Camb. Philos. Soc.*, 1928, **24**, 89–110.

5 J. C. Slater, Note on Hartree's Method, *Phys. Rev.*, 1930, **35**, 210–211.

6 V. Fock, Näherungsmethode zur Lösung des Quantenmechanischen Mehrkörperproblems, *Z. Für Phys.*, 1930, **61**, 126–148.

7 N. Metropolis, A. W. Rosenbluth, M. N. Rosenbluth, A. H. Teller and E. Teller, Equation of State Calculations by Fast Computing Machines, *J. Chem. Phys.*, 1953, **21**, 1087–1092.

8 B. J. Alder and T. E. Wainwright, *Molecular Dynamics by Electronic Computers*, Wiley, New York, 1958.

9 J. B. Gibson, A. N. Goland, M. Milgram and G. H. Vineyard, Dynamics of Radiation Damage, *Phys. Rev.*, 1960, **120**, 1229–1253.

10 A. Rahman, Correlations in the Motion of Atoms in Liquid Argon, *Phys. Rev.*, 1964, **136**, A405–A411.

11 A. Z. Khan, M. Bilal, T. Rasheed and H. M. N. Iqbal, Advancements in Biocatalysis: From Computational to Metabolic Engineering, *Chin. J. Catal.*, 2018, **39**, 1861–1868.

12 J.-M. Choi, S.-S. Han and H.-S. Kim, Industrial Applications of Enzyme Biocatalysis: Current Status and Future Aspects, *Biotechnol. Adv.*, 2015, **33**, 1443–1454.

13 G. Sliwoski, S. Kothiwale, J. Meiler and E. W. Lowe, Computational Methods in Drug

Discovery, *Pharmacol. Rev.*, 2014, **66**, 334–395.

14 H. Martinez-Seara and T. Róg, *Biomolecular Simulations: Methods and Protocols*, Humana Press, New Jersey, 2013.

15 A. Urban, D.-H. Seo and G. Ceder, Computational Understanding of Li-Ion Batteries, *Npj Comput. Mater.*, 2016, **2**, 16002:1–13.

16 S. Y. Reddy and V. K. Kuppa, Molecular Dynamics Simulations of Organic Photovoltaic Materials: Investigating the Formation of π-Stacked Thiophene Clusters in Oligothiophene/Fullerene Blends, *Synth. Met.*, 2012, **162**, 2117–2124.

17 J. Chauhan, A. Rinzler and J. Guo, A Computational Study of Graphene Silicon Contact, *J. Appl. Phys.*, 2012, **112**, 104502:1–7.

18 J. Cirera and E. Ruiz, *Molecular Magnetic Materials*, John Wiley & Sons, Ltd, Barcelona, 2016.

19 J. Yu, L. Xie, J. Li, Y. Ma, J. M. Seminario and P. B. Balbuena, CO_2 Capture and Separations Using MOFs: Computational and Experimental Studies, *Chem. Rev.*, 2017, **117**, 9674–9754.

20 P. W. N. M. van Leeuwen and J. C. Chadwick, *Homogeneous Catalysts: Activity - Stability - Deactivation*, Wiley-VHC, Weinheim, 2011.

21 R. Schlögl, Heterogeneous Catalysis, *Angew. Chem. Int. Ed.*, 2015, **54**, 3465–3520.

22 A. Asthagiri and M. J. Janik, *Computational Catalysis*, The Royal Society of Chemistry, Cambridge, 2014.

23 M. Ramdin, S. H. Jamali, T. M. Becker and T. J. H. Vlugt, Gibbs Ensemble Monte Carlo Simulations of Multicomponent Natural Gas Mixtures, *Mol. Simul.*, 2018, **44**, 377–383.

24 N. Denham, M. C. Holmes and A. V. Zvelindovsky, The Phases in a Non-Ionic Surfactant ($C_{12}E_6$)−Water Ternary System: A Coarse-Grained Computer Simulation, *J. Phys. Chem. B*, 2011, **115**, 1385–1393.

25 A. Warshel and M. Levitt, Theoretical Studies of Enzymic Reactions: Dielectric, Electrostatic and Steric Stabilization of the Carbonium Ion in the Reaction of Lysozyme, *J. Mol. Biol.*, 1976, **103**, 227–249.

CHAPTER 2

Theoretical Background

The aim of this chapter is to give a general overview of the different methods used in this doctoral thesis. The techniques employed in this work range from quantum-based methods (*i.e.,* DFT), which are suitable to treat systems with only a few atoms, going through different molecular simulations, that are able to deal with the evolution of thousands of interacting molecules, to thermodynamic equilibrium theories (*e.g.,* SAFT), which intend to reproduce thermophysical properties of pure fluids and their mixtures at equilibrium.

Quantum-based methods explicitly represent all the electrons and orbitals of the system, which make them suitable to reproduce properties that depend on the electronic distribution. These calculations are known as *ab initio* because they solve the Schrödinger equation without needing previous information to be carried out. This fact makes them completely predictive at a high computational cost. The main limitation of quantum-based methods is that they can treat relatively small systems and dynamics at very short time scales. An important part of this doctoral thesis is based on achieving dynamical equilibrium for complex systems, which is hardly attainable by this method, so only static *ab initio* calculations were performed to obtain useful information that can be included in other models to predict phase equilibria.

Contrarily, the representation of the system can be simplified by disregarding the electrons and modeling molecules as atoms bonded to each other by a set of springs. Intermolecular electrostatic interactions are then substituted by classical point charges located onto the atoms laying under a Coulomb potential. These assumptions increase several orders of magnitude the calculation speed, but they require a good fitting of some parameters to accurately reproduce molecular properties (*e.g.,* the bond spring constants or the atomic charges). The fitting can be done to mimic the *ab initio* potential energy surface or a reliable set of experimental data, and if done accurately, it can be used to study the evolution of extended systems via molecular simulations. Within these techniques two different approaches to achieve equilibrium can be highlighted: (i) the dynamic approach, that evolves the system in time integrating the Newton's equations of motion until equilibrium conditions are met, or (ii) the Monte Carlo approach, which samples the configurational space to ignore time and directly achieve the equilibrium state.

Finally, thermodynamic fluid theories are tools capable of predicting thermophysical and phase equilibria properties of pure fluids and their mixtures but losing much molecular information obtainable by *ab initio* or molecular simulation techniques. The assumptions and simplifications made in these models usually require previous fittings to extensive experimental data at different conditions of pressure and temperature. However, they give thermodynamic information that can be used to predict the behavior of a system directly at equilibrium by solely solving iteratively a set of equations.

The combination of methods that work at different scales of time and length enriches this doctoral thesis because it intends to combine DFT calculations to understand the basic interactions between molecules and surfaces, to later connect it to larger scale methods that can predict macroscopic effects. This strategy was followed specifically in Chapter 3 with gas separation processes. On the other hand, collective properties such as pressure, density, molecular self-assembly or interfacial tension required to simulate a large set of molecules. Those kinds of systems are treated solely with molecular simulations as described in Chapter 4 and Chapter 5.

2.1 Density Functional Theory

The basis of any non-relativistic *ab initio* method is to solve the Schrödinger equation (eq. 2.1),[1] which uses the Hamiltonian operator ($\widehat{H}$) to obtain the energy of a system (E) from the so-called wavefunction (Ψ).[2,3] The wavefunction completely determines the state of the system and depends on the coordinates of all nuclei ($\mathcal{R} = (\vec{R}_1, \vec{R}_2, \dots, \vec{R}_{N_n}, W_1, W_2, \dots, W_{N_n})$) and electrons ($\mathcal{r} = (\vec{r}_1, \vec{r}_2, \dots, \vec{r}_{N_e}, w_1, w_2, \dots, w_{N_e})$). Notice that the variables $\mathcal{R}$ and $\mathcal{r}$ contain the three spatial coordinates (*i.e.,* $\vec{R}_i$ and $\vec{r}_i$) and the spin coordinates (*i.e.,* W_i and w_i) of the N_n nuclei and N_e electrons of the system. On the other hand, the Hamiltonian is defined as the sum of kinetic ($\widehat{K}$) and potential ($\widehat{U}$) energy operators as it can be seen in eq. 2.2.

$$\widehat{H}\Psi(\mathcal{R}, \mathcal{r}) = \mathrm{E}\Psi(\mathcal{R}, \mathcal{r}) \qquad 2.1$$

$$\widehat{H} = \widehat{K}_n + \widehat{K}_e + \widehat{U}_{nn} + \widehat{U}_{ne} + \widehat{U}_{ee} \qquad 2.2$$

where $\widehat{K}_n$ and $\widehat{K}_e$ are the kinetic energy of nuclei and electrons, respectively, $\widehat{U}_{nn}$ and $\widehat{U}_{ee}$ refer to the potential energy due to the repulsion of the nuclei and electrons, respectively, and $\widehat{U}_{ne}$ is the

nuclei-electron interaction potential. *Ab initio* calculations are usually carried out under the Born-Oppenheimer approximation,[4] which assumes that the velocity of nuclei is much slower than that of the electrons. This implies that electrons adapt almost instantly to any nuclear motion and allows the factorization of the wavefunction onto its electronic and nuclear counterparts (*i.e.*, $\Psi(\mathcal{R},\mathcal{r}) = \Psi_{e,\mathcal{R}}(\mathcal{r})\Psi_n(\mathcal{R})$). After the factorization, the electronic wavefunction depends explicitly on the coordinates of all electrons ($\mathcal{r}$) and parametrically on the nuclear coordinates ($\mathcal{R}$), whereas the nuclear wavefunction depends only on the coordinates of all nuclei ($\mathcal{R}$) moving under the mean-field potential generated by the electrons. Then, an electronic Hamiltonian ($\widehat{H}_{e,\mathcal{R}}$) can be defined grouping all the terms that depend on the electrons: the kinetic energy of electrons ($\widehat{K}_e$), the interaction potential between nuclei and electrons ($\widehat{U}_{ne}$) and the coulombic repulsion between electrons ($\widehat{U}_{ee}$). The resolution of this electronic Schrödinger equation gives the electronic energy ($E_{e,\mathcal{R}}$) of the system, which also depends parametrically on the position of the nuclei (eq. 2.3).

$$\widehat{H}_{e,\mathcal{R}}\Psi_{e,\mathcal{R}}(\mathcal{r}) = \left(\widehat{K}_e + \widehat{U}_{ne} + \widehat{U}_{ee}\right)\Psi_{e,\mathcal{R}}(\mathcal{r}) = E_{e,\mathcal{R}}\Psi_{e,\mathcal{R}}(\mathcal{r}) \qquad 2.3$$

The Hamiltonian that gives the total energy of the system, also renamed as nuclear Hamiltonian ($\widehat{H}_n$), is written in terms of the electronic Hamiltonian ($\widehat{H}_{e,\mathcal{R}}$), whose value ($E_{e,\mathcal{R}}$) and has been solved in eq. 2.3, the potential energy repulsion ($\widehat{U}_{nn}$), which is a constant for a given nuclear configuration ($U_{nn}(\mathcal{R})$), and the kinetic energy of nuclei ($\widehat{K}_n$). In general, static electronic structure calculations within the Born-Oppenheimer approximation neglect the $\widehat{K}_n$ term and combine the constant nuclear-nuclear potential repulsion with the electronic energy to yield the effective potential energy of a system with fixed nuclei ($U(\mathcal{R}) = E_{e,\mathcal{R}} + U_{nn}(\mathcal{R})$). This implies that the main focus of electronic structure calculations is the solution of the electronic Schrödinger equation (eq. 2.3). However, after solving the electronic problem, the motion of the nuclei can be included by applying the nuclear Hamiltonian ($\widehat{H}_n = \widehat{K}_n + U(\mathcal{R})$) to the nuclear wavefunction as seen in eq. 2.4.

$$\widehat{H}_n\Psi_n(\mathcal{R}) = \left(\widehat{K}_n + U(\mathcal{R})\right)\Psi_n(\mathcal{R}) = E_{tot}\Psi_n(\mathcal{R}) \qquad 2.4$$

2.1.1 The Basis of DFT

As stated previously, the basis of *ab initio* methods is to solve the electronic Schrödinger equation using $4N_e$-dimensional wavefunctions (*i.e.,* 3 spatial and 1 spin coordinates per electron). The basis of DFT is also to obtain the electronic energy of the system ($E_{e,\mathcal{R}}$) but using the electron density ($\rho(\vec{r})$) instead of the wavefunction. In fact, the dimensionality of the problem is radically reduced when using $\rho(\vec{r})$ instead of $\Psi_{e,\mathcal{R}}(\boldsymbol{r})$, because the electron density depends only on three spatial coordinates ($\vec{r}$) regardless on the number of electrons of the system, as opposed to the rapid scaling of the wavefunction. However, it is not practical a priori, because the electron density of N_e indistinguishable electrons must be obtained from the wavefunction (eq. 2.5).

$$\rho(\vec{r}_1) = N_e \int_{w_1} \int_{\vec{r}_2} \int_{w_2} \dots \int_{\vec{r}_{N_e}} \int_{w_{N_e}} \left|\Psi_{e,\mathcal{R}}(\boldsymbol{r})\right|^2 dw_1 d\vec{r}_2 dw_2 \dots d\vec{r}_{N_e} dw_{N_e} \qquad 2.5$$

Notice, that as all electrons are indistinguishable in practice $\rho(\vec{r}_1)$ of eq. 2.5 can be written simply as $\rho(\vec{r})$. The use of the DFT formulation started with the two theorems of Hohenberg and Kohn (HK) [5]:

1st theorem: "*Any observable of a stationary non-degenerate ground state can be calculated, exactly in theory, from the electron density of the ground state. In other words, any observable can be written as a functional of the electron density of the ground state".*

2nd theorem: *"The electron density of a non-degenerate ground state can be calculated, exactly in theory, determining the density that minimizes the energy of the ground state".*

The 1st theorem specifies that the energy of the system can be calculated from the electron density as it can be seen in eq. 2.6, where the external potential ($U_{ext}[\rho]$) contains the one electron potential term, while the HK functional ($F_{HK}[\rho]$) that contains the kinetic energy ($K_e[\rho]$) and the two-electron potential ($U_{ee}[\rho]$) terms. On the other hand, the 2nd theorem determines that the electron density of the ground state can be obtained using the variational principle.

$$E[\rho] = F_{HK}[\rho] + \int \rho(\vec{r})\, U_{ext}[\rho]\, d\vec{r} \qquad 2.6$$

Moreover, the terms grouped inside the HK functional are not well-determined, specially the kinetic energy of a system of N interacting electrons. A huge change in DFT came after Kohn and Sham,[6] who proposed to solve eq. 2.6 of a reference system, where electrons do not interact, but that move under an external potential that resembles the electron density of the real system. In this ideal system, the known kinetic term of the non-interacting reference system ($K_s[\rho]$), is separated from the rest of the unknown kinetic energy ($K_e[\rho] - K_s[\rho]$). Similarly, the known coulomb potential term ($U_C[\rho]$) is separated from the rest of the unknown two-electron repulsion term ($U_{ee}[\rho] - U_C[\rho]$). The two unknown terms are grouped into the so-called exchange and correlation functional ($E_{xc}[\rho]$), as shown in eq. 2.7, which must be approximated or parameterized.

$$E_e[\rho] = K_s[\rho] + U_C[\rho] + E_{xc}[\rho] + \int \rho(\vec{r})\, U_{ext}[\rho]\, d\vec{r} \qquad 2.7$$

2.1.2 The Exchange and Correlation Functionals

Different approximations can be made for the exchange and correlation functional. The simplest one is the so called Local Density Approximation (LDA),[7] which assumes that the density can be treated as a homogenous electron gas and locally, $E_{xc}[\rho]$ depends only on the electron density. This approximation has a well-defined analytic expression, but it is usually too simple to reproduce properties of real systems. For this reason, more complex expressions were developed including the gradient of the density (*i.e.,* the Generalized Gradient Approximation or GGA, where $E_{xc}[\rho, \nabla\rho]$) or even the Laplacian of the density (*i.e.,* the Meta-Generalized Gradient Approximation or meta-GGA, where $E_{xc}[\rho, \nabla\rho, \nabla^2\rho]$). Unfortunately, these expressions did not have a well-defined analytic expression and were fitted to experimental results. Within the GGA family, the most popular functionals are the Perdew and Wang functional (PW91),[8] the Perdew-Burke-Ernzerhof functional (PBE) [9] and its subsequent modifications to increase its usability (*i.e.,* PBEsol [10] for solids or RPBE [11]) in reproducing the gas adsorption energies on metal surfaces. On the other hand, meta-GGA formulations derived into functionals such as TPSS [12] or M06,[13] which have increased accuracy in exchange of a larger parameterization and a higher computational cost.

A different approach widely used to describe chemical bonding of molecules are the so-called hybrid functionals. They mix some non-local Fock exchange (*i.e.,* from the original wavefunction formulation) into the DFT exchange and correlation functional. The two more popular hybrid functionals are PBE0,[14,15] which treats the exchange as 25 % Fock / 75 % PBE, and B3LYP,[16,17] which uses a 20 % Fock / 80 % LDA exchange.

Another challenge of DFT calculations is the inclusion of dispersion corrections (E_D) to the total energy.[18] These are produced by long-ranged electron correlation effects and are key to reproduce phenomena that are not based on wavefunction overlapping. A common approach is to add an additional corrective term to the final DFT energy to account for the dispersion interactions. This term is calculated from an empirical equation fitted to experimental data. The most commonly used corrections are the well-known D2 and D3 Grimme corrections,[19–21] for their simplicity and reliability. However, in the last years, non-empiric dispersion corrections are being included in some exchange and correlation functionals. The idea behind these methods is to compute the E_D using only the electron density as input, expressing the dispersion energy as a functional of the density ($E_D[\rho]$). Some of the most widely used functionals in this area is the vdW-DF family, initially developed by Langreth *et al.*[22]

2.1.3 Periodic *vs.* Non-Periodic DFT calculations

The wavefunction allows computing any property or observable of the system, either using a wavefunction formalism or a DFT formalism (*i.e.,* as seen, the electron density is calculated from the wavefunction). The electronic wavefunction of a non-periodic system can be approximated with a polyelectronic function that accounts for the antisymmetry of the wavefunction with respect the permutation of two indistinguishable electrons. To simplify the notation, this polyelectronic function is expressed as a Slater determinant (eq. 2.8) and defines a single configuration of N_e electrons in N_e spinorbitals ($\psi_1 \dots \psi_{N_e}$). Each spinorbital is a function of the spatial and spin coordinates of an electron, so they are constructed through the factorization of the spatial orbital ($\varphi_i(\vec{r})$) and the spin function ($\chi_i(w)$) as shown in eq. 2.9, and finally, each spatial orbital is approximated as a linear combination of basis functions (Φ_j) as seen in eq. 2.10.

$$\Psi_{e,\mathcal{R}}(r) = \frac{1}{\sqrt{N_e!}} \begin{vmatrix} \psi_1(\vec{r}_1, w_1) & \cdots & \psi_1(\vec{r}_{N_e}, w_{N_e}) \\ \vdots & \ddots & \vdots \\ \psi_{N_e}(\vec{r}_1, w_1) & \cdots & \psi_{N_e}(\vec{r}_{N_e}, w_{N_e}) \end{vmatrix} \quad 2.8$$

$$\psi_i(\vec{r}, w) = \varphi_i(\vec{r})\chi_i(w) \quad 2.9$$

$$\varphi_i(\vec{r}) = \sum_j a_{ij}\Phi_j(\vec{r}) \quad 2.10$$

The a_{ij} coefficients of the linear combination of basis functions in eq. 2.10 define the shape of the orbital, and they have to be optimized iteratively to obtain the *"best"* set of orbitals of the system. The *"best"* orbitals are the ones that allow building a wavefunction that resemble an electron density that minimizes the electronic energy of the system, according to the variational principle.[3]

The basis of choice to build orbitals of non-periodic isolated molecules in the gas phase are the linear combination of gaussian functions (eq. 2.11) centered at each nucleus, where b_j is a parameter that determines the width of the gaussian. Otherwise, if virtually infinite systems, such as bulk phases or solid surfaces need to be addressed, it is usually preferable to employ periodic basis functions such as plane waves (eq. 2.12). Each of these functions depends on the crystal wave vector ($\vec{k}_j$) and they have a spatial symmetry that makes them more suitable to reproduce extended periodic systems. However, a very large number of plane waves are needed to reproduce the core electrons due to their natural extended shape. For this reason, a set of parameterized functions called pseudopotentials are commonly used to include the effect of the core electrons and reduce the size of the basis set.[23]

$$\Phi_j(\vec{r}) = e^{-b_j\vec{r}^2} \qquad 2.11$$

$$\Phi_j(\vec{r}) = e^{i\vec{k}_j\vec{r}} \qquad 2.12$$

2.1.4 Calculation of Thermodynamic Properties from *Ab initio* Calculations

The resolution of the electronic Schrödinger equation gives the effective energy of a system with fixed nuclei in a given set of atomic coordinates. Obviously, the gradient of the energy (*i.e.,* obtained from its first derivatives) can be used to obtain the atomic coordinates that minimize the energy, finding the minimum of the potential energy surface (PES), also known as equilibrium geometry. In this minimum the hessian matrix of the energy (*i.e.,* obtained from its second derivatives) is used to obtain the frequencies of the 3N normal modes of the system, where N is the number of atoms. The combination of this information with statistical thermodynamics can ultimately be used to obtain many interesting thermodynamic properties, such as the internal energy, the enthalpy, the entropy or the Gibbs free energy at different temperatures.

According to statistical thermodynamics,[24] the partition function (Q) of a system with N indistinguishable molecules can be used to obtain the thermodynamic functions of the ensemble,

and can be usually factorized onto translational (q_{trans}), rotational (q_{rot}) and vibrational (q_{vib}), electronic (q_e) and nuclear (q_n) partition functions as seen in eq. 2.13. The expressions of each partition function are compiled from eq. 2.14 to eq. 2.19, respectively.

$$Q = \frac{(q_{trans} q_{rot} q_{vib} q_e q_n)^N}{N!} \qquad 2.13$$

$$q_{trans} = \left(\frac{2\pi m k_B T}{h^2}\right)^{3/2} V \qquad 2.14$$

$$q_{rot} = \frac{1}{\sigma_r}\left(\frac{8\pi I k_B T}{h^2}\right) \qquad \textit{(For linear molecules)} \qquad 2.15$$

$$q_{rot} = \frac{\sqrt{\pi}}{\sigma_r}\sqrt{\left(\frac{8\pi I_A k_B T}{h^2}\right)\left(\frac{8\pi I_B k_B T}{h^2}\right)\left(\frac{8\pi I_C k_B T}{h^2}\right)} \qquad \textit{(For non-linear molecules)} \qquad 2.16$$

$$q_{vib} = \prod_i \frac{e^{-h\nu_i/2k_B T}}{1 - e^{-h\nu_i/k_B T}} \qquad 2.17$$

$$q_e = g_{e,0} + \sum_i g_{e,i}\, e^{-\Delta E_{e,i}/k_B T} \qquad 2.18$$

$$q_n = g_{n,0} + \sum_i g_{n,i}\, e^{-\Delta E_{n,i}/k_B T} \qquad 2.19$$

In general, all the partition functions depend on the temperature (T). Specifically, the translational partition function (eq. 2.14) also depends on the mass of the molecule (m) and the available volume it has for moving (V). The terms k_B and h are the Boltzmann and the Plank constants, respectively. On the other hand, the rotational partition function for linear molecules (eq. 2.15) depends on the symmetry number (σ_r) and the moment of inertia (I). Alternatively, the three principal moments of inertia (*i.e.,* I_A, I_B, I_C) have to be calculated for non-linear molecules to obtain the total rotational partition function (eq. 2.16). Then, the vibrational partition function in eq. 2.17, which uses the bottom of the potential energy curve as zero of energy, is the product of i contributions, being i each vibrational normal mode with a frequency ν_i. Finally, the electronic and nuclear partition functions (eq. 2.18 and eq. 2.19) depend on the degeneracy of the electronic and nuclear ground states ($g_{e,0}$ and $g_{n,0}$), the degeneracy of all of their excited states ($g_{e,i}$ and $g_{n,i}$) and the energy difference between the ground and the i^{th} excited state ($\Delta E_{e,i}$ and $\Delta E_{n,i}$). However,

in many molecules the excited energy levels are much higher in energy than $k_B T$, which implies that q_e and q_n become approximately $g_{e,0}$ and $g_{n,0}$, respectively.

From the partition functions different thermodynamic magnitudes can be obtained, such as the internal energy of a molecular gas or its entropy, both at temperature T. Both magnitudes depend on the number of particles of the system (*i.e.,* the partition function depends on N), but they have all been referred to molar values, which make $N = N_A$ and $N_A k_B = R$. Specifically, the internal energy of the gas (eq. 2.20) is calculated by adding a thermal correction on the effective energy obtained from an electronic structure calculation ($U(\mathcal{R})$), which can be approximated as the internal energy of a gas at 0 K ($U(\mathcal{R}) \approx U(0K)$). Otherwise, the entropy is directly calculated from the partition functions (eq. 2.21). With respect the other thermodynamic quantities: the enthalpy of the system can be calculated simply adding the PV term to the internal energy of the system (eq. 2.22), which can be assumed to be RT for ideal gases, and the Gibbs free energy can be calculated by subtracting the term TS from the enthalpy (eq. 2.23).

$$U(T) = U(0\ K) + RT^2 \left(\frac{\partial \ln(q_{trans} q_{rot} q_{vib} q_e q_n)}{\partial T} \right)_{N,V} \quad 2.20$$

$$S(T) = R \left[\ln \left(\frac{q_{trans} q_{rot} q_{vib} q_{elec}\ e}{N_A} \right) + T \left(\frac{\partial \ln(q_{trans} q_{rot} q_{vib} q_{elec})}{\partial T} \right)_{N,V} \right] \quad 2.21$$

$$H(T) = U(T) + P\ V \quad 2.22$$

$$G(T) = H(T) - T\ S(T) \quad 2.23$$

Although the equations from eq. 2.20 to eq. 2.23 allow to apparently calculate absolute thermodynamic magnitudes, most of them are meaningless on its own. The relevant magnitudes of interest are their difference between two states. Some examples are: the difference in Gibbs free energy between reactants and products of a gas phase chemical reaction, which determines if a reaction can occur spontaneously, or the difference in enthalpy between a molecule in gas phase or adsorbed, which allows to obtain the heat of adsorption.

The method for calculating thermodynamic functions is valid for the former example (*i.e.,* the reactants and products of a gas phase chemical reaction) because both reactants and products can translate, rotate and vibrate. This means that the total partition function can usually be approximated as a product of $q_{trans} q_{rot} q_{vib} q_e q_n$, as explained. However, when a molecule is adsorbed onto a surface, it cannot translate nor rotate from its equilibrium geometry (*i.e.,* its

rotational and translational modes become frustrated). For adsorbed molecules, these modes can be treated as vibrations, so the total partition function of an adsorbed species becomes $q_{vib}q_e q_n$. This assumption is known as the harmonic approximation and can be applied to chemisorptions and relatively strong physisorptions. Finally, the PV term cannot be converted to RT when solids are involved, the state function of the solid should be used instead to find the value of PV. Alternatively, the calculation of the PV term in solid state can be avoided in many situations, because thermodynamic functions are calculated as differences between initial and final states. This fact means that if the solid is present in both the initial and final states the PV_{final} and $PV_{initial}$ will cancel each other. With these considerations the thermodynamic functions of adsorbed species can also be obtained solely from electronic structure calculations combined with statistical thermodynamics.

2.2 Molecular Simulations

Molecular simulations intend to connect the microscopic world of molecular interactions with the macroscopic world of collective properties (*e.g.,* pressure, density or free energy) This connection is made through ensemble averages or time averages as described by classical statistical mechanics.[24,25] According to statistical mechanics, any property ($\mathcal{A}$) of a macroscopic system with M particles is a function of the microscopic state of the system, which in turn is defined by a set of microscopic variables. For example, the pressure (P) of the system depends on the position and momenta of all M particles, so P will be a function of 6M variables. These microscopic variables can also be regarded as a single point in a multidimensional space called "the phase space" ($\mathcal{Q}$), where the instantaneous value of P is a function of $\mathcal{Q}$ (*i.e.,* $P(\mathcal{Q})$). Unfortunately, the simulation of a M particle system is generally impossible because M is in the order of 10^{23} particles. For this reason, the target of molecular simulations is to sample the whole phase space through simulation of smaller N particle systems.

The sampling can be equivalently carried out in two different manners depending on how different configurations in the phase space are generated. The first one is preparing a swarm of different configurations (*i.e.,* an ensemble). Then, any property ($\mathcal{A}$) can be calculated from an average of the instantaneous values of $\mathcal{A}(\mathcal{Q})$ in all the ensemble, weighted by the probability of a system to be in each generated state (*i.e.,* an ensemble average). The probability of a system to be found in a determined state ($\mathcal{P}_i$) is related to the total energy of this state (E_i) through the Boltzmann factor ($e^{-\beta E_i}$, with $\beta = 1/k_B T$), where the denominator of eq. 2.24 is the sum of all

possible states that the system can be in (*i.e.,* the partition function). This sampling is similar to the one employed in Monte Carlo simulations. Alternatively, the phase space can be sampled through time evolution of a single N particle system, considering that the evolution is designed to visit the same microscopic states as the ensemble average. Macroscopic properties are then obtained through averages of all visited states during the evolution. If the evolution of a system accomplishes visiting the whole available phase space, then the time average ($\langle \mathcal{A} \rangle_{time}$) becomes equal to the ensemble average ($\langle \mathcal{A} \rangle_{ensemble}$) and to the macroscopic observable ($\mathcal{A}$). This is known as the "ergodic hypothesis" and can be expressed mathematically through eq. 2.25 or graphically in Figure 2.1.

$$\mathcal{P}_i = \frac{e^{-\beta E_i}}{\sum_i e^{-\beta E_i}} \qquad 2.24$$

$$\mathcal{A} = \langle \mathcal{A} \rangle_{ensemble} = \sum_{i=1}^{N_{sys}} \mathcal{P}_i \, \mathcal{A}(Q_i) = \langle \mathcal{A} \rangle_{time} = \frac{1}{t_f} \sum_{t=1}^{t_f} \mathcal{A}\big(Q(t)\big) \qquad 2.25$$

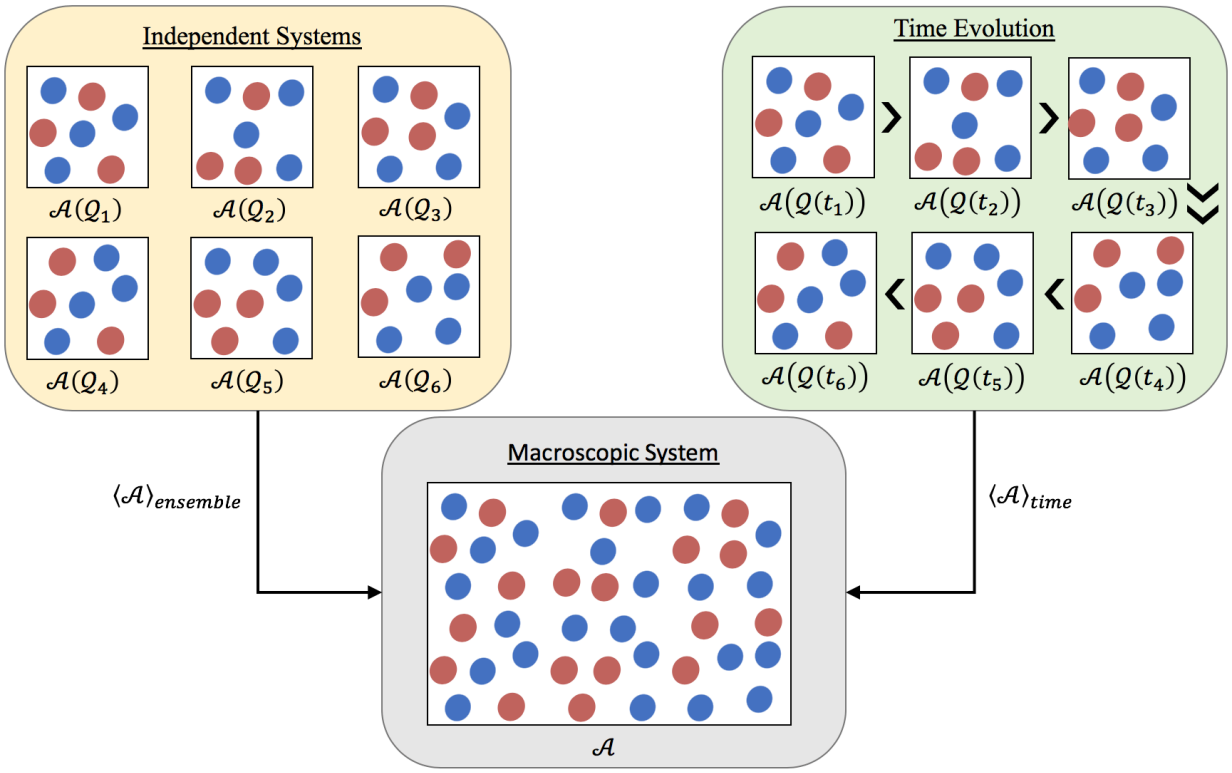

Figure 2.1. Graphical representation of eq. 2.25, where the property $\mathcal{A}$ is obtained from the ensemble average of independent systems ($\langle \mathcal{A} \rangle_{ensemble}$) and from the time average of a single time evolved system ($\langle \mathcal{A} \rangle_{time}$).

In eq. 2.25 the subscript i runs over the different independent systems used to calculate $\langle \mathcal{A} \rangle_{ensemble}$ from $i = 1, \dots, N_{sys}$, and the variable t recalls the different states of a single simulation visited through time evolution, in the range $t = 1, \dots, t_f$, that are used to calculate the value of $\langle \mathcal{A} \rangle_{time}$. Regardless of the method employed, it is recommended to obtain ideally an infinite number of configurations that sample the phase space. In practice, the number of states to average will be the maximum that the available computational resources permit.

Notice that in both evolution schemes it is necessary to compute the energy of the system. In the case of performing ensemble averages is necessary to compute the energy to obtain the Boltzmann factor and the partition function for each state, whereas in the case of the time evolution scheme it is necessary to compute the energy to ensure that the evolution of the system samples states according to a Boltzmann distribution. In principle, the energy of the system can be obtained through any of the electronic structure calculations described in Section 2.1. However, molecular simulations require to calculate the energy of a large number of configurations to compute properly a macroscopic property. This task becomes rapidly unfeasible with such an expensive method. For this reason, the quantum representation of the system (*i.e.,* nuclei surrounded by electron orbitals) is usually simplified to a set of classical point particles, all carrying a partial charge and bonded to each other through a set of springs (*i.e.,* forming molecules). The Hamiltonian of the system does not need to treat the electrons anymore and is then reduced to a sum of intermolecular and intramolecular contributions to the total energy. These simplified contributions must be parameterized to be able to reproduce either experimental properties or quantum chemical structural/energetic data. The set of equations and parameters used in the Hamiltonian is commonly called a force field (FF).

2.2.1 Atomistic, United Atom and Coarse-Grained Force Fields

As denoted in the previous section, the calculation of the energy is key to predict any property of the system. Although it can be done by *ab initio* methods (*e.g.,* in *ab initio* molecular dynamics), it is usually too expensive to effectively sample the phase space. For this reason, different simplifications on the molecular representation can be made depending on the property to be computed. The first step in the simplification scheme is to treat all atoms as charged spheres connected by springs to simulate bonds. This representation is known as atomistic molecular simulation or All-Atom (AA) approach. In this representation, the total energy is calculated as a sum of the intermolecular and intramolecular interactions of all atoms in the system (eq. 2.26). Intramolecular interactions are commonly split onto three categories depending on their

connectivity: (i) bonds (*i.e.,* also known as 1-2 interactions), (ii) angles (*i.e.,* or 1-3 interactions) or (iii) torsions (*i.e.,* 1-4 interactions). In turn, torsions can be either described through dihedral torsions (*i.e.,* four atoms connected consecutively, as the carbons of a butane molecule) or through an improper torsion (*i.e.,* the out-of-plane angle of a structure of a central atom with three atoms connected to it, as the ammonia molecule). Intermolecular interactions can be described by any kind of function that reproduces the common long-range attractive and short-range repulsive behavior. This is commonly accomplished by a combination of a vdW and Coulomb functions to account for the dispersive and electrostatic interactions between different atoms. If needed, additional terms can be included in the intermolecular term to reproduce other physical phenomena, such as polarization or many-body intermolecular interactions (*i.e.,* represented in eq. 2.26 with "...").

$$U(\mathcal{R}) = \sum_{bonds} U_{bnd} + \sum_{angles} U_{ang} + \sum_{torsions} U_{trs} + \sum_{pairs} (U_{wdW} + U_C + \cdots) \qquad 2.26$$

The terms of eq. 2.26 used in this doctoral thesis are described in the equations from eq. 2.27 to eq. 2.31. U_{bnd} and U_{ang} have been treated with quadratic functions, whose energy is minimum at the equilibrium angle ($\theta_{e_{ijk}}$) or distance ($r_{e_{ij}}$). Torsions usually have multiple minima, which have been reproduced with a periodic Fourier expansion according to eq. 2.29. The vdW interactions of any pair of atoms have been calculated via a LJ potential ($U_{vdW} = U_{LJ}$),[26,27] as seen in eq. 2.30. Finally, the Coulomb potential (U_C) is used to calculate the electrostatic interactions of each pair of atoms (eq. 2.31). Although the mostly used functions for modeling molecular fluids is the combination of Lennard-Jones (LJ) + Coulomb functions, other equations like the Buckingham potential [28] or the Embedded Atom Model (EAM) [29] are commonly seen in the literature to reproduce ionic or metal systems, respectively. Finally, intermolecular interactions are calculated for each pair of atoms whose motion is not already described by any of the intramolecular terms. This includes atoms in different molecules or atoms in the same molecule separated by more than three bonds.

$$\sum_{bonds} U_{bnd} = \sum_{i} \sum_{j>i} \frac{1}{2} K_b \left(r_{ij} - r_{e_{ij}}\right)^2 \qquad 2.27$$

$$\sum_{angles} U_{ang} = \sum_{i} \sum_{j>i} \sum_{k>j} \frac{1}{2} K_a \left(\theta_{ijk} - \theta_{e_{ijk}}\right)^2 \quad 2.28$$

$$\sum_{torsions} U_{trs} = \sum_{i} \sum_{j>i} \sum_{k>j} \sum_{l>k} \frac{1}{2} K_{d1}\left[1 + \cos(\phi_{ijkl})\right] + \frac{1}{2} K_{d2}\left[1 - \cos(2\phi_{ijkl})\right] + \frac{1}{2} K_{d3}\left[1 + \cos(3\phi_{ijkl})\right] \quad 2.29$$

$$\sum_{pairs} U_{LJ} = \sum_{i} \sum_{j>i} 4\varepsilon_{ij} \left[\left(\frac{\sigma_{ij}}{r_{ij}}\right)^{12} - \left(\frac{\sigma_{ij}}{r_{ij}}\right)^{6}\right] \quad 2.30$$

$$\sum_{pairs} U_{C} = \sum_{i} \sum_{j>i} \frac{1}{4\pi\varepsilon_0} \frac{q_i q_j}{r_{ij}} \quad 2.31$$

where the K_b, K_a, K_{d1}, K_{d2} and K_{d3} are the bond, angle and the three dihedral force constants respectively, which are usually parameterized fitting some *ab initio* structural data. The parameter ε_{ij} of the LJ potential represents the depth of the attractive potential well due to dispersion interactions, which is related to the interaction energy of the ij pair. On the other hand, the term σ_{ij} refers to the distance under which the potential becomes repulsive, which is related to the molecular diameter of species i and j. Both parameters are usually obtained by fitting a large set of experimental properties, although they can also be fitted to *ab initio* pair interaction energy data. Finally, Coulomb interactions depend on the partial charges of the ij pair separated by a distance r_{ij}. This parameter can be fitted to experimental data along with the LJ potential or to quantum mechanical calculations of electronic distributions and occupancies.

The atomistic molecular representation allows to reproduce systems with thousands of molecules and to sample millions of configurations of the phase space (*i.e.,* either through ensemble averages or time averages). With this technique, one is able to describe collective properties of many fluids including effects such as hydrogen bonding or dipole-dipole interactions. However, there are many atoms in molecules that have very weak interactions with other molecules (*e.g.,* the hydrogen atoms of organic CH_x chains). A more efficient representation applicable in those cases is the so-called United-Atom (UA) approach, who groups the light weak-interacting hydrogen atoms with their central heavy carbon atom. Using this representation, the number of interacting pairs of an organic fluid is significantly reduced, increasing the computational efficiency (*e.g.,* the hexane molecule has 6 carbon atoms and 14 hydrogen atoms in an AA

representation, whereas it only has 6 CH_x groups when modeled as UA). All energy contributions can be calculated through the equations from eq. 2.26 to eq. 2.31, equivalently to the AA representation.

If very large systems need to be treated, even a coarser representation can be done grouping some UA particles into large spherical beads. This molecular modeling is known as Coarse-Grained (CG) and is specifically successful in non-polar molecules or in species where collective properties depend on very localized functional groups. However, many research laboratories are extending the functionality of CG models by obtaining parameters for many different fluids.[30–32] The number of beads needed to model a molecule can vary depending on the size of the bead. Usually, beads pack from 3 to 4 CH_x groups together, known as 3-to-1 or 4-to-1 coarse-graining levels, respectively. Lower coarse-graining levels are allowed but are less computationally efficient and higher coarse-graining levels usually lose too much molecular information to be consistent with experimental data. Additionally, functional groups (*e.g.,* amines, alcohols, carboxylic acids or ketones, among others) are also modeled by a single bead. Within this representation, the UA groups are so packed that the sum of partial charges within a group is usually zero, and the Coulombic interactions can be neglected. The problem is that the LJ function alone is rarely capable of reproducing the properties of real fluids, even after fitting to experimental data. For this reason, more flexibility has to be added into the pair potential function, to better fit the intermolecular interactions. Some examples of CG representations are the Martini FF,[30] which uses a LJ potential and a shifted Coulomb potential to calculate the energy of the system, or the Shinoda, Devane and Klein (SDK) FF,[31] which does not consider the Coulomb interactions and it changes the 12-6 scheme of the LJ potential to either a 12-4 or 9-6 potential to increase the flexibility of the potential function. A similar approach is followed with the Mie potential (*i.e.,* also known as Generalized Lennard-Jones potential),[33] where the exponents can be optimized to compensate the lack of the Coulomb potential term (eq. 2.32).

$$\sum_{pairs} U_{Mie} = \sum_{i} \sum_{j>i} \left(\frac{\lambda_{r_{ij}}}{\lambda_{r_{ij}} - \lambda_{a_{ij}}} \right) \left(\frac{\lambda_{r_{ij}}}{\lambda_{a_{ij}}} \right)^{\left(\frac{\lambda_{a_{ij}}}{\lambda_{r_{ij}} - \lambda_{a_{ij}}} \right)} \varepsilon_{ij} \left[\left(\frac{\sigma_{ij}}{r_{ij}} \right)^{\lambda_{r_{ij}}} - \left(\frac{\sigma_{ij}}{r_{ij}} \right)^{\lambda_{a_{ij}}} \right] \quad 2.32$$

Notice that the term before the ε_{ij} recovers the value of 4 when using the standard LJ exponents (*i.e.,* $\lambda_{r_{ij}} = 12$ and $\lambda_{a_{ij}} = 6$). Regarding intramolecular interactions, simple quadratic bond springs (eq. 2.27) are used to keep beads together and quadratic angles (eq. 2.28) are used if one needs to prevent overfolding of molecules. Higher order intramolecular interactions such as

torsions are generally neglected within this molecular model. A summary of the four representations explained in this section is compiled in Figure 2.2.

Intermolecular pair potentials require all values of ε_{ij} and σ_{ij} to be defined, which is a relatively large number of parameters if many different types of atoms are present in the simulation. To reduce the dimensionality and transferability of parameters, some mixing rules can be used to approximate adequate values of the pair-wise parameters (ij) from the atom-wise values (ii and jj). The most commonly used mixing rules are the so-called Lorentz-Berthelot,[34] that approximate the pair-wise ε_{ij} and σ_{ij} as a geometric and arithmetic mean of the ii and jj values, respectively (eq. 2.33 and eq. 2.34), without using any additional parameters. However, in situations where the average mixing is not capable of reproducing the properties of a fluid mixture, the crossed (ij) terms must be fitted. This is commonly done adding an additional dimensionless parameter ($\hbar_{ij}$) on the mixing rules of ε_{ij}. Two examples are: the eq. 2.35, which is an extension of the Lorentz-Berthelot mixing rules that includes the adjustable parameter for extra flexibility; or the mixing rule proposed by Lafitte *et al.,*[35] where the difference in atomic radii (σ) is also taken into account to obtain the value of ε_{ij} (eq. 2.36). Finally, in the case of the Mie potential, the repulsive (λ_r) and attractive (λ_a) exponents also have to be defined. However, since λ_r and λ_a are intimately related (*i.e.,* as shown by Mejía *et al.,*[36]), the latter is fixed to 6 and only λ_r is adjusted to tune the shape

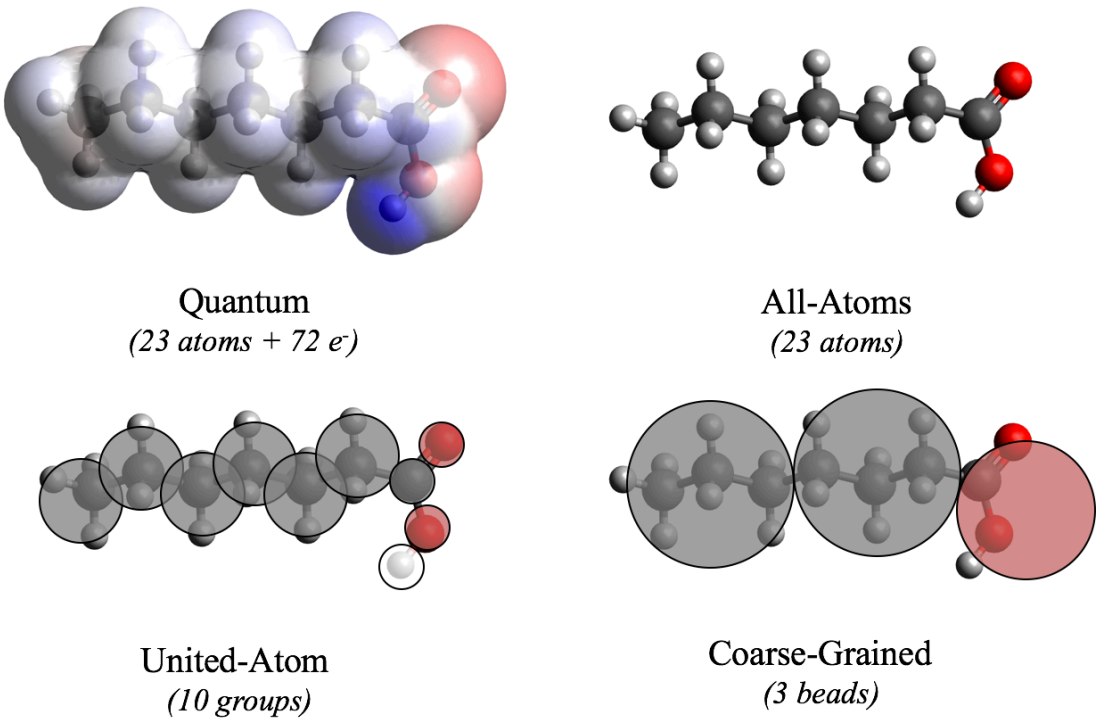

Figure 2.2. Some of the possible models usable in molecular simulations: from the finest possible quantum representation to the simplest Coarse-Grained structure.

of the potential energy curve. The mixing rules for the repulsive exponent are similar to the geometric mixing rule as it can be seen in eq. 2.37.

$$\varepsilon_{ij} = \sqrt{\varepsilon_{ii}\varepsilon_{jj}} \tag{2.33}$$

$$\sigma_{ij} = \frac{\sigma_{ii} + \sigma_{jj}}{2} \tag{2.34}$$

$$\varepsilon_{ij} = \not{k}_{ij}\sqrt{\varepsilon_{ii}\varepsilon_{jj}} \tag{2.35}$$

$$\varepsilon_{ij} = \not{k}_{ij}\left(\frac{\sqrt{\sigma_{ii}^3\sigma_{jj}^3}}{\sigma_{ij}^3}\right)\sqrt{\varepsilon_{ii}\varepsilon_{jj}} \tag{2.36}$$

$$\lambda_{ij} - 3 = \sqrt{(\lambda_{ii} - 3)(\lambda_{jj} - 3)} \tag{2.37}$$

Up to now, it is clear that to predict any macroscopic property in molecular simulations one needs to sample effectively the phase space. To do so, different configurations generated through a random ensemble or a time evolution have to be averaged. In the following subsections, the two different approaches to sample the phase space will be discussed: the molecular dynamics and the Monte Carlo simulations.

2.2.2 Molecular Dynamics

Molecular Dynamics (MD) samples the phase space by generating several configurations via time evolution of a relatively small N particle system through integration of the Newton's equations of motion.[37] Generally, the evolution of the position of a particle $\vec{r}_i(t)$ can be calculated from the Taylor expansion around a time t (eq. 2.38). In this expansion, the first time derivative of the particle position has been substituted by its velocity ($\dot{\vec{r}}_i = \vec{v}_i$) and the second the derivative by its acceleration ($\ddot{\vec{r}}_i = \vec{a}_i$), but explicitly written in terms of the force ($\vec{a}_i = \vec{F}_i/m_i$). Finally, the force is calculated from the gradient of the energy (*i.e.,* $\vec{F}_i = -\vec{\nabla}U_i$). However, the truncation of this expansion at low order derivatives (*e.g.,* order two) induces a numerical error in long time evolutions that makes the simulation non-time reversible, so it would not resemble a real system

dynamics. For this reason, the election of an adequate algorithm to integrate the equations of motion is a key point in MD simulations.

$$\vec{r}_i(t+\Delta t) = \vec{r}_i(t) + \vec{v}_i(t)\Delta t + \frac{1}{2!}\frac{\vec{F}_i(t)}{m_i}\Delta t^2 + \frac{1}{3!}\dddot{\vec{r}}\,\Delta t^3 + \cdots, \quad 2.38$$

A successful integrator should be if possible: (i) fast and require little memory, (ii) it should permit a long timestep (Δt), (iii) it should reproduce a classical trajectory as closely as possible, (iv) it should be time reversible, conserve energy, and (v) it should be simple and easy to program. Although no integrator meets all the previous conditions, one of the mostly used algorithms in MD is the so-called Verlet algorithm.[38] This integrator is fast and simple, it is time reversible, it has a reasonable conservation of energy and a very low energy drift in long simulations, which makes it a good algorithm to integrate equations of motion. Verlet algorithm evolves the system without using the velocities of the particles. To do so, the Taylor expansions of $\vec{r}_i(t+\Delta t)$ in eq. 2.38 and $\vec{r}_i(t-\Delta t)$ in eq. 2.39 are summed to give an expression that only depends on the positions and forces of all particles (eq. 2.40). The new position contains an error of the order Δt^4 after truncation of the Taylor expansion, represented by $O(\Delta t^4)$ in eq. 2.40. Finally, even though the velocities are not needed to evolve the position of the particles in time, they are usually calculated when needed using eq. 2.41.

$$\vec{r}_i(t-\Delta t) = \vec{r}_i(t) - \vec{v}_i(t) + \frac{1}{2!}\frac{\vec{F}_i(t)}{m_i}\Delta t^2 - \frac{1}{3!}\dddot{\vec{r}}\,\Delta t^3 + \cdots, \quad 2.39$$

$$\vec{r}_i(t+\Delta t) \approx 2\vec{r}_i(t) - \vec{r}_i(t-\Delta t) + \frac{\vec{F}_i(t)}{m_i}\Delta t^2 + O(\Delta t^4) \quad 2.40$$

$$\vec{v}_i(t) = \frac{\vec{r}_i(t+\Delta t) - \vec{r}_i(t+\Delta t)}{2\Delta \mathrm{t}} + O(\Delta t^2) \quad 2.41$$

As stated at the beginning of this section, collective properties in molecular simulations can be calculated from the positions and velocities of the atoms. For example, according to the equipartition theorem, the temperature of a system (T) is related to its kinetic energy (K) as in eq. 2.42. At the same time, the kinetic energy is calculated from the velocity of the particles composing the system (also eq. 2.42). This implies that the temperature in MD can be obtained from the velocity of all particles. Another property that can be obtained through MD is the pressure of the

system (P). The pressure is expressed as a sum of an ideal term that depends on the velocities (*i.e.,* a kinetic term), plus a correction that depends on the positions and the forces (*i.e.,* the virial term). Notice that the kinetic term in eq. 2.43 is called ideal because it can be substituted by eq. 2.42 to become Nk_BT, as in the ideal gas equation.

$$K = \frac{1}{2}\sum_i mv_i^2 = \frac{3}{2}Nk_BT \qquad 2.42$$

$$P = \frac{1}{3V}\left[\sum_i m_i v_i^2 + \sum_i \sum_{j>i} \vec{F}_{ij} \cdot \vec{r}_{ij}\right] \qquad 2.43$$

MD simulations are performed aiming at reproducing a determined ensemble. Generally, MD will evolve in time an isolated system resembling the microcanonical ensemble, that is at constant number of particles, volume and energy (*i.e.,* NVE ensemble). However, the experiments where the magnitudes of interest are measured, are usually set up at constant pressure or temperature. For this reason, one can couple a virtual thermostat to the simulation, that will insert or subtract energy in the form of heat, to drag the system to thermal equilibrium at the desired temperature. Then, the temperature of this closed system is constant instead of the total energy, and the canonical ensemble is reproduced (*i.e.,* NVT ensemble). Temperature is related to the velocity of the particles, as seen in eq. 2.42, so thermostats work adding or subtracting energy from the kinetic term. The simplest thermostats only rescale the velocities of the particles by a certain factor to change the temperature of the system, and despite they might be efficient to drag the system to the equilibrium temperature, they do not reproduce the thermal fluctuations of the canonical ensemble. On the other hand, the Nosé-Hoover (NH) [39–41] thermostat proves the NVT ensemble, making it the thermostat of choice in many MD simulations in the canonical ensemble. The idea behind the NH thermostat is to add an additional degree of freedom to the system with an associated "fictitious mass" (Q) coupled to the equations of motion. This "fictitious mass" has units of energy·(time)^2 and its value is related to the coupling strength between the bath and the system. Within the NH formalism, the time evolution of the velocity includes an additional $\zeta_T v_i/Q$ term, representing the coupling of the thermostat (eq. 2.44). The ζ_T value in that equation is known as friction coefficient and evolves in time according to the difference between the kinetic energy of the system ($\sum_i m_i v_i(t)^2$) and the desired kinetic energy (Lk_BT_0), as described in eq. 2.45. In the latter equation, T_0 refers to the target equilibrium temperature and L are the number of degrees of freedom of the system. It is important to mention that the "fictitious mass" of the thermostat is an

adjustable parameter and it should be set to a value that proves the thermal fluctuations of the canonical ensemble.[42]

$$\dot{\vec{v}}_i = \frac{\vec{F}_i}{m_i} - \frac{\zeta_T}{Q}\vec{v}_i \tag{2.44}$$

$$\dot{\zeta}_T = \sum_{i=1}^{N} m_i v_i(t)^2 - Lk_B T_0 \tag{2.45}$$

Similarly, if one wants to control the pressure in a simulation, a barostat can be added to change the volume of the system modifying the equations of motion accordingly. When both a barostat and a thermostat are both applied, the pressure and temperature of the system equilibrate to a constant value, resembling the isothermal-isobaric ensemble (*i.e.,* NPT ensemble). There is an extension of the NH formalism applied to barostats based on coupling an extra degree of freedom representing a piston with an associated "fictitious weight" (W) coupled to the equations of motion.[39,43–45] this "fictitious weight" also has units of energy·(time)^2 and its value is related to the coupling strength between the piston and the system. Additionally, the barostat and the thermostat are coupled among each other to adequately reproduce the ensemble, so the equations of motion modified by the coupled NH barostat and thermostat become:

$$\dot{\vec{v}}_i = \frac{\vec{F}_i}{m_i} - \frac{\zeta_T}{Q}\vec{v}_i - \left(1 + \frac{1}{N}\right)\frac{\zeta_P}{W}\vec{v}_i \tag{2.46}$$

$$\dot{\vec{r}}_i = \vec{v}_i - \frac{\zeta_P}{W}\vec{r}_i \tag{2.47}$$

$$\dot{\zeta}_T = \sum_{i=1}^{N} m_i v_i^2 - Lk_B T_0 + \frac{\zeta_P^2}{W} \tag{2.48}$$

$$\dot{\zeta}_P = 3V(P - P_0) + \frac{1}{N}\sum_{i=1}^{N} m_i v_i^2 - \frac{\zeta_T}{Q}\zeta_P \tag{2.49}$$

where both the velocity and the position include the barostat coupling (ζ_P/W) as an additional term. As previously stated, the thermostat is coupled to the barostat through the term ζ_P^2/W. At the same time, the barostat, which depends on the volume of the system (V), the pressure (P) and the

target pressure (P_0), is coupled to the thermostat through the term ζ_T/Q. Equivalently to the thermostat coupling, W is also an adjustable parameter that must be defined to prove the fluctuations of the isothermal-isobaric ensemble. It is worth mentioning that the pressure in NPT simulations is not calculated through eq. 2.43, because it needs to include the variation of the potential energy with the volume ($\partial U/\partial V$) as an additional term due to the barostat as in eq. 2.50. Finally, the barostat is acting like a piston, so it changes the volume of the system as described by eq. 2.51.

$$P = \frac{1}{3V}\left[\sum_i m_i v_i^2 + \sum_i \sum_{j>i} \vec{F}_{ij} \cdot \vec{r}_{ij}\right] - \left(\frac{\partial U}{\partial V}\right)_{NT} \quad 2.50$$

$$\dot{V} = 3V\frac{\zeta_P}{W} \quad 2.51$$

Now that all of the necessary ingredients of a MD simulation are defined, the process to perform it can be revised. First, create a simulation box with a determined volume and fill it with a set of molecules, either placed in a symmetrical lattice or following a uniform random distribution. At this point, the equations to calculate the energy of the system have to be defined along with the parameters for each pair, bond, angle or torsion potential. If the system was created randomly it is probable that some particles overlap to each other, so a relaxation step (*i.e.,* an energy minimization) will be mandatory prior to the simulation. Then, velocity is given to each paricle according to a Boltzmann distribution, a time step is defined, and an integrator is chosen (*e.g.,* the velocity Verlet algorithm with 1 fs timestep). This set of steps are known as "Initialization" stage.

The second phase of a MD simulation consists on letting the system reach the equilibrium state through time evolution (*i.e.,* where all observables do not change in time). To that end, the energy and the forces of the system are calculated at each timestep to update the positions and velocities of the system according to the Verlet algorithm. This time evolution can be performed either conserving the total energy (*i.e.,* reproducing an NVE microcanonical ensemble), adding a thermostat to keep the temperature constant (*i.e.,* reproducing an NVT canonical ensemble), or adding both a barostat and a thermostat to control pressure and temperature (*i.e.,* reproducing an NPT isothermic-isobaric ensemble). It is worth mentioning that other ensembles can be reproduced with MD (*e.g.,* the NPH isoenthalpic-isobaric ensemble), but they will not be covered in this

doctoral thesis. This phase is called “Equilibration” stage and its time length will depend on the system to simulate.

When all observables are converged, macroscopic properties can be calculated through time averages during the following stage of the time evolution. This phase is known as “Production” stage and it should be as long as possible to sample the whole phase space. Some magnitudes exhibit strong oscillations of their instantaneous values in molecular simulations, so it is strongly recommended to perform averages at different time blocks to monitor when the equilibration stage ends, and the production stage starts.

2.2.3 Monte Carlo Simulations

Monte Carlo (MC) simulations are based on generating a very large random set of configurations. Then, to obtain any observable, one has to perform ensemble averages of the instantaneous property value multiplied by the probability of the system to be in that configuration, according to a Boltzmann distribution (eq. 2.25). However, this practice is inappropriate because many configurations with high energy would be created. These configurations would have very low weight in the ensemble average due to their low probability, so computational time would be wasted accounting for them. For this reason, Metropolis *et al.,*[46] proposed a method to generate random configurations with a probability that directly follows an adequate Boltzmann distribution for the desired ensemble. With this constraint, averaging all configurations would yield the correct ensemble average, because the probability to be in a determined state is accounted when creating each configuration.

The Metropolis algorithm is based on building a single N particle system in a determined configuration. Then, a new state is proposed where the system “evolves” in the phase space changing the position of the particles a random small distance and in a random direction (*i.e.,* also known as trial move). If the energy of this new proposed configuration is reduced, the process is accepted. On the other hand, if the energy of the new state is increased it can be randomly accepted or rejected according to the probability given by the Boltzmann factor. The probability of acceptance depends on the partition function, which in turn depends on the ensemble to simulate. A summary of the acceptance probabilities in the different ensembles are compiled in Table 2.1.

The Metropolis algorithm allows the system to “evolve” in the phase space until it reaches the equilibrium by accepting all moves that reduce the energy and also generates a distribution of configurations according to the Boltzmann distribution when the system is at equilibrium. Notice that although MC methods generate a set of random configurations, the term “evolve” has been

Table 2.1. Metropolis acceptance probabilities on different ensembles along with the possible random trial moves allowed (*i.e.,* with $\beta = 1/k_B T$ and $\Lambda = h/\sqrt{2\pi m k_B T}$).

Ensemble	Trial Move	Acceptance Probability ($\mathcal{P}_{n\to n+1}$)
Microcanonical (NVE)	Trans / Rot	If: $(\Delta U_{n\to n+1} \leq 0) \to \mathcal{P} = 1$ // Else: $\to \mathcal{P} = 0$
Canonical (NVT)	Trans / Rot	$\min\left[1, e^{-\beta(U_{n+1}-U_n)}\right]$
Isobaric-Isothermal (NPT)	Trans / Rot	$\min\left[1, e^{-\beta(U_{n+1}-U_n)}\right]$
	Volume Change	$\min\left[1, e^{-\beta(U_{n+1}-U_n)+P(V_{n+1}-V_n)-Nk_BTln\left(\frac{V_{n+1}}{V_n}\right)}\right]$
Grand Canonical (μVT)	Trans / Rot	$\min\left[1, e^{-\beta(U_{n+1}-U_n)}\right]$
	Particle Insertion	$\min\left[1, \frac{V}{\Lambda^3(N+1)} e^{-\beta(\mu-U(N+1)+U(N))}\right]$
	Particle Removal	$\min\left[1, \frac{\Lambda^3 N}{V} e^{-\beta(\mu+U(N-1)-U(N))}\right]$

used in quotes because this random walk follows a process similar to a MD simulation (*i.e.,* a single N particle system is evolved to reach equilibrium, followed by the calculation of properties through an unweighted average of all configurations generated in the production phase).

Temperature and pressure can also be controlled in MC simulations, but thermostats or barostats are not used like in MD. The temperature control in a MC NVT simulation is imposed in the probability of accepting or rejecting a MC move, which generates configurations of an adequate canonical ensemble at a determined temperature. Also, velocities are not defined in the random walk, so the temperature cannot be calculated through eq. 2.42. Otherwise, the pressure of the system still can be calculated through eq. 2.43 using the target temperature to calculate the ideal term. In a MC NPT simulation, the pressure is controlled treating the volume of the system as a coordinate that can be randomly changed in a trial move (*i.e.,* equivalently to a particle move). This MC move can be accepted or rejected according to the Metropolis algorithm.

The method of generating an ensemble of configurations in MC simulations allows to extend its application towards the evaluation of open systems such as in the Grand Canonical ensemble (*i.e.,* μVT ensemble). This ensemble is similar to the NVT ensemble, where the volume and temperature of the system is kept constant, but it can exchange particles with an ideal gas reservoir at a determined chemical potential during the evolution. The number of particles of the system will change through insertions or eliminations until the chemical potential of the system equals that of the ideal reservoir; then, the system achieves phase equilibrium and the random walk resembles an

open μVT ensemble. The generation of configurations within this ensemble is hard to implement in MD, but it is straightforward in MC simulations after defining an adequate set of acceptance probabilities for the insertion or elimination of particles.

A summary of all MC simulations in the ensembles defined in this section are compiled in Figure 2.3, along with their interactions with an ideal implicit reservoir. In the NVE ensemble the system cannot interact with its surroundings because it represents an isolated system, in the NVT ensemble the system can exchange energy in the form of heat with the reservoir, in the NPT ensemble it can also change its volume doing work against the pressure of the surroundings, and finally, in the μVT ensemble it can exchange energy in the form of heat and matter with the reservoir.

Equivalently to MD, now that all the necessary ingredients of a MC simulation have been defined, the process to perform it can be revised. First, create a simulation box with a determined volume and fill it with a set of molecules, either placed in a symmetrical lattice or following a uniform random distribution. At this point, the equations to calculate the energy of the system have

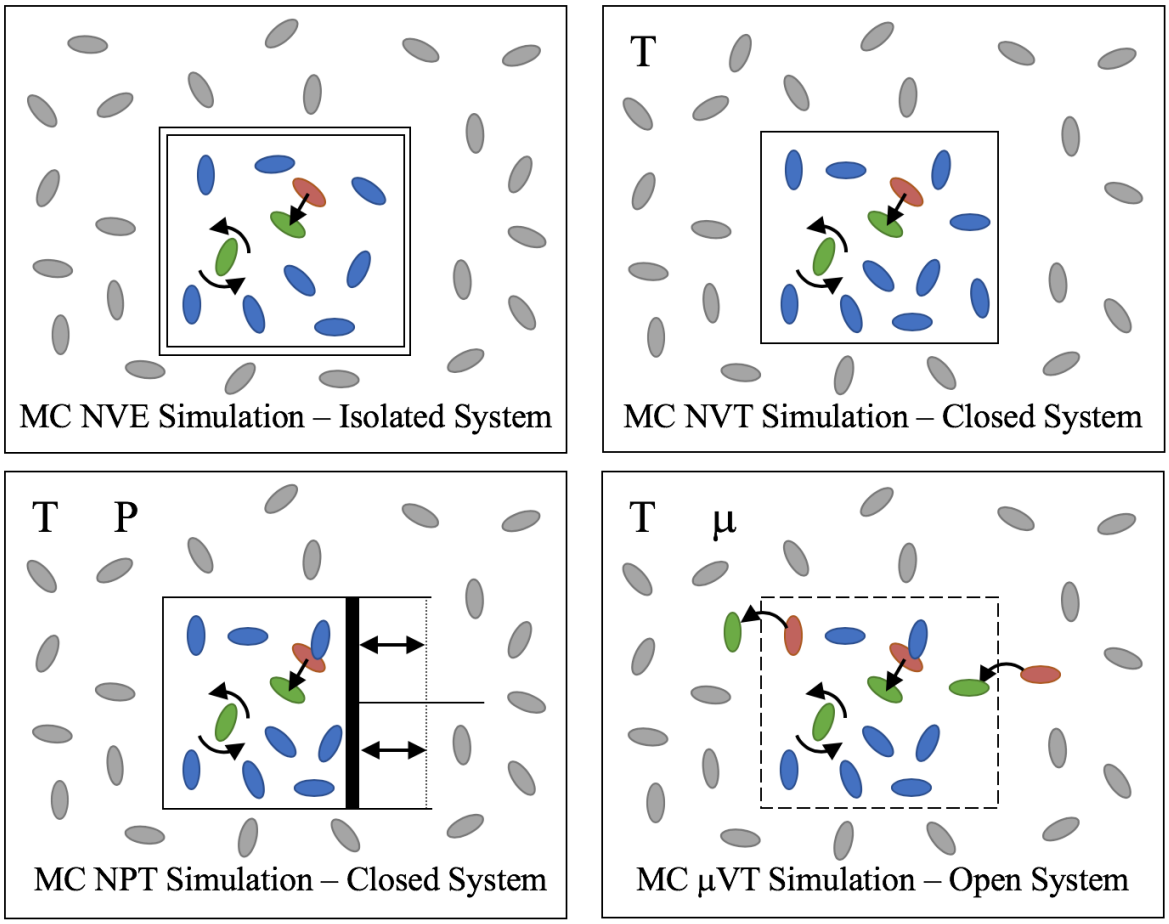

Figure 2.3. Scheme showing the different possible moves in MC simulations depending on the ensemble chosen along with their implicit reservoirs.

to be defined along with the parameters for each pair, bond, angle or torsion potential. In principle a relaxation step is not necessary (although recommendable) in MC because forces are not used in the random walk. If the energy of the system is reduced the trial move will be accepted and the system will relax by itself. The working ensemble must be chosen at this point to determine the different available moves in the random walk. The working conditions also have to be defined (*i.e.,* temperature, pressure and/or chemical potential) to calculate the acceptance probabilities of the desired ensemble. All these steps encompass the "Initialization" stage.

The second phase of a MC simulation is the "Equilibration" stage and it consists on letting the system reach the equilibrium state (*i.e.,* where all observables do not change in time) through phase space evolution. To that end, a single MC move is randomly selected at each MC step from the list of available moves. The probability of each move being selected is defined by the user, along with the maximum system volume, particle translational distance or particle rotational angle that can change in a single MC move. If the maximum values for the MC moves are chosen very small, the trial moves will have a high probability of acceptance, but the system will evolve very slowly. Otherwise, if the maximum values are large, the system will evolve rapidly but the probability of acceptance will be low. Neither end allows efficient sampling of the phase space, so it is recommendable to select adequate values of these MC parameters, which depend on the simulated system, to optimize the sampling of the random walk.

Finally, when all observables are converged, macroscopic properties can be calculated through ensemble averages during the following stage of the phase space evolution. This phase is known as "Production" stage and it should be as long as possible to sample the whole phase space. Recall that some magnitudes exhibit strong oscillations of their instantaneous values in molecular simulations, so it is strongly recommended to perform averages at different time blocks to monitor when the equilibration stage ends, and the production stage starts.

2.2.4 Additional Aspects to Accelerate Molecular Simulations

Generally, either MD or MC simulations are employed to predict collective properties of matter. To calculate any property from a molecular simulation it is required that the system samples a large phase space. This can be accomplished in two ways by the application of the ensemble definition and the ergodic hypothesis: (i) through the simulation of an infinitely large system during a short evolution, or (ii) by an infinitely long evolution of a small system.

The best solution comes by evolving the largest possible system during the longest possible time, according to the available computational power. This makes molecular simulations very

costly, even when the calculation of the energy is accelerated with simplified molecular representations. However, there are a set of techniques commonly applied to MD and MC simulations that allow reducing this computational cost. These are: (i) the application of periodic boundary conditions (PBC), (ii) the truncation of pair wise interactions, (iii) the use of tail corrections or Ewald sums and (iv) the construction of neighbor lists.

First, the application of PBCs is based on using the symmetry of the system to reduce the computational cost. It was already discussed in the DFT section that solids exhibit spatial symmetry, so they can be modeled in a small cell and use their periodicity to account for their long-range distribution. Bulk fluids behave similarly due to their long-range structural homogeneity, so one can virtually replicate the system in all directions of the space to mimic a system surrounded by an infinite bulk. All particles can interact with the virtual images, which permits the calculation of long-range pair potentials (Figure 2.4). When PBCs are applied, a molecule that crosses the boundaries of the box reappears at the opposite side, effectively removing the need of a wall that confines the system. With this technique macroscopic bulk properties can be simulated with relatively small systems because all molecules behave as in bulk phase. It is important to mention that the usage of PBCs can lead to spurious results when the system exhibits phenomena with a larger wavelength than the size of the box. For example, if a micelle with 50 Å of diameter has to be formed in a simulation, the box must be larger than 50 Å. However, if a cell

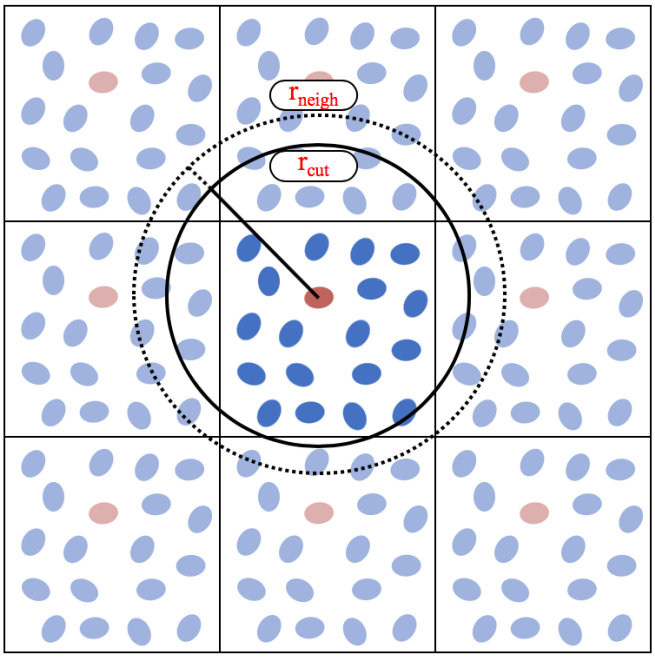

Figure 2.4. Representation of a system surrounded by virtual images of itself (*i.e.,* PBCs). The pair interaction cutoff distance along with the neighbor cutoff distance is also displayed in the figure.

with length 30 Å is built, the molecules will form some other spurious macrostructure (*e.g.,* a bilayer) due to finite size effects.

With PBCs the calculation of pair interactions becomes an infinite sum that considers all atoms in all periodic images. This makes the numerical calculation unpractical, so pair interactions are usually truncated at a certain cutoff radius (r_{cut}) to limit the number of interactions to calculate. LJ interactions decay very rapidly at a rate of r^{-6}, making this potential almost to vanish at 10 Å, as it can be seen in Figure 2.5. On the other hand, the Coulomb interactions decay at a much slower rate (*i.e.,* r^{-1}). Although this approximation is good enough for LJ, the truncation of the Coulomb potential neglects a significantly large portion of the interaction energy. So, an additional term must be added to account for the missing long-range tail of the energy. Also, as the pressure depends on the sum of the pair forces, the truncation of the energy also affects the pressure of the system. These issues gave rise to the development of long-range tail correction techniques for both the LJ and the Coulomb potentials.

As beforementioned, the truncation of the LJ potential is a reasonably good approximation even at $r_{cut} = 10$ Å. However, the cost of adding an analytic tail correction is almost negligible and justifies the accounting of the small missing energy. Analytic tail corrections (eq. 2.52) can be applied to any rapidly converging function such as the LJ potential (*i.e.,* decays faster than r^{-3}).[47] This equation depends on the pair potential chosen ($U_{pair}(r)$) and the number density of the simulated fluid (ρ). However, if this equation is applied to a Coulomb potential the integral diverges, which forces to develop more sophisticated methods to account for these long-range interactions.

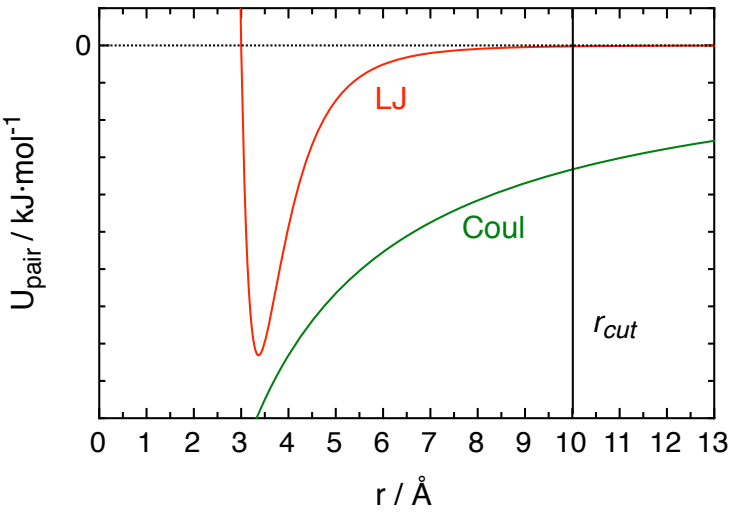

Figure 2.5. Shape of the LJ (red) and the attractive Coulomb (green) potentials as a function of the intermolecular distance. A hypothetical cutoff radius (r_{cut}) have been set at 10 Å to denote the loss of long-range interactions in the truncation of the Coulombic potential.

$$U_{tail} = 2\pi N\rho \int_{r_{cut}}^{\infty} r^2 U_{pair}(r) dr \qquad 2.52$$

One of the first methods developed to account for the Coulomb energy (U_C) with long-range interactions is known as the Ewald sum.[48] This method transforms the poorly-converging sum of interacting point charges by a sum of two rapidly converging terms plus a correction (eq. 2.53). To do so, each particle with charge q_i is assumed to be surrounded by a gaussian charge distribution with charge $-q_i$. This assumption generates a set of screened charges that are a rapidly converging direct sum (eq. 2.54). Then, one must subtract the screening charges from the direct sum to resemble the system of point charges. This is accounted in the second term of the Ewald method (eq. 2.55), which can be represented as a rapidly converging Fourier series. Finally, this implementation includes a spurious interaction between each point particle i with its own gaussian screening charge, that must be subtracted (eq. 2.56),

$$U_C = U_{Screen+Point} - U_{Screen} - U_{Self} \qquad 2.53$$

$$U_{Screen+Point} = \sum_i \sum_{j>i} q_i q_j \frac{ercf(\sqrt{\alpha}\, r_{ij})}{r_{ij}} \qquad \textit{(Direct sum)} \qquad 2.54$$

$$U_{Screen} = -\frac{1}{2V} \sum_{k\neq 0} \frac{4\pi}{k^2} \left|\rho(\vec{k})\right|^2 e^{-k^2/4\alpha} \qquad \textit{(Fourier series)} \qquad 2.55$$

$$U_{Self} = \sqrt{\frac{\alpha}{\pi}} \sum_i q_i^2 \qquad \textit{(Self-correction)} \qquad 2.56$$

where, α is the width of the gaussian screening charges and $\vec{k}$ is a vector in the Fourier space. The Ewald sum accounts for the long-range Coulomb energy scaling as $\mathcal{O}(N^{2/3})$, which is prohibitively expensive for large systems. To overcome this limitation, alternative algorithms similar to Ewald, but with better scaling and comparable results, were developed. The mostly used long-range Coulombic solver in this doctoral thesis is the so-called particle-particle/particle-mesh summation.[49] This method is based on discretizing the screening charges in a grid and split the potential similarly to the Ewald sum. Then, the most expensive part of the calculation becomes the Fast Fourier Transform (FFT), which scales as $\mathcal{O}\big(Nlog(N)\big)$. The final technique used here to optimize molecular simulations is the construction of neighbor lists. When performing an energy

calculation of a system using a truncated potential, all pairs that are at a distance greater that r_{cut} will not contribute to the total energy. If the system to simulate is relatively large, an important part of the time during the energy calculation is wasted in determining if a pair of atoms is close enough to calculate its energy contribution or not. To that end, at the beginning of a simulation, a set of lists are built, containing all neighbors that are at a "reasonably close" distance to each atom. Building these neighbor lists is expensive because one needs to make a double loop over all N atoms in the simulation. Once the neighbor list is built, the system can be evolved without updating it during a relatively long time (*e.g.,* 10-100 timesteps). Pair interactions are only calculated between atoms present in the corresponding neighbor lists instead of the full N particle loop, which radically increases the probability of a pair to be at $r < r_{cut}$. The atoms belonging to a neighbor list must be selected and updated carefully to prevent effects such as an approaching atom becoming at a distance $r < r_{cut}$ without considering its interaction. This is usually accounted defining a second cutoff radius (r_{neigh}), which must be larger than r_{cut}. Then, the neighbor lists are built considering all atoms within this second radius (see Figure 2.4). Using this technique, rapidly approaching atoms will enter the outer radius (*i.e.,* where interactions are neglected) and will be included in the neighbor lists before entering the inner (r_{cut}) cutoff radius (*i.e.,* where interactions are calculated).

2.3 Thermodynamic Fluid Theories

Within this section, two different theories based on statistical thermodynamics and phase equilibria will be covered to obtain macroscopic properties of a system. First, molecular-based equations of state will be explained along with a short introduction throughout the evolution of these theories from the ideal gas law. Then, the main ideas behind the COSMO-RS model will be explained, which is an almost completely predictive tool to calculate solubilities on liquids based on *ab initio* calculations.

An Equation of State (EoS) is a mathematical relationship that links the thermodynamic variables of a system. The simplest EoS is the ideal gas law, that represents a gas formed by a set of non-interacting particles. This equation is unable to capture the attractive and repulsive molecular interactions of a gas, so high density fluids (*i.e.,* gases at high pressures or liquids) deviate significantly from the behavior predicted by this EoS. The ideal gas law can be written equivalently either relating P, V and T, as it is commonly known (eq. 2.57), or through the Helmholtz free energy of the ideal gas (*i.e.,* A_{ideal} in eq. 2.58).[24] The former equation is written in

terms of the number of gas mols (n) and R, which is the ideal gas constant, whereas the latter is expressed through the number of molecules (N), the Boltzmann constant (k_B) and the De Broglie wavelength ($\Lambda = h/\sqrt{2\pi m k_B T}$).

$$PV = nRT \tag{2.57}$$

$$A_{ideal} = Nk_BT\left[\ln\left(\frac{N\Lambda^3}{V}\right) - 1\right] \tag{2.58}$$

A significant improvement to the ideal gas law was the development of the first cubic vdW EoS,[50] which was not only the first expression to predict a vapor/liquid equilibria, but also settled the basis for fluid theories and the development of more sophisticated EoS. This relationship assumes that gases behave like hard spheres of diameter (σ_{HS}) under an attractive long-range potential of magnitude (a). Unlike the ideal gas law, the hard spheres (HS) model prevents overlapping of particles, which means that fluids have a determined excluded volume. Specifically, two particles cannot be closer to each other than their diameter, so the excluded volume of two colliding particles is assumed to be the half of a sphere with radius σ_{HS} (i.e., $b = 2/3\pi\sigma_{HS}^3$). Finally, anaglogous to the ideal gas law, the vdW EoS can be written in terms of n, R, P, V and T (eq. 2.59) or in terms of A_{VdW}, N, k_B, Λ, V and T (eq. 2.60), where the attractive, repulsive an ideal contributions are clearly separated.

$$P = \frac{nRT}{V - nb} - \frac{an^2}{V^2} \tag{2.59}$$

$$A_{vdW} = Nk_BT\left\{\left[\ln\left(\frac{N\Lambda^3}{V}\right) - 1\right] - \left[\ln\left(\frac{V - Nb}{V}\right)\right] - \left[\frac{N^2}{Nk_BTV}a\right]\right\} = A_{ideal} + A_{rep} + A_{att} \tag{2.60}$$

The sum of the ideal and repulsive terms corresponds to the simple model of hard spheres (*i.e.,* $A_{ideal} + A_{rep} = A_{HS}$). This model was successful due to its simplicity but overestimates the repulsion of molecules at high densities due to the HS repulsion, which yielded anomalously high predicted pressures of high-density fluids. That issue could be tackled improving the HS repulsion model, as done by Carnahan and Staring in eq. 2.61 when developing their CSvdW EoS (*i.e.,* where $y = b/4V$).[51] A different improvement to the vdW model is the inclusion of a temperature dependent parameter ($w(T)$) in the attractive term such as in the Peng-Robinson EoS (eq. 2.62).[52]

This term, known as acentric factor is useful for accounting for the non-sphericity of the molecules, improving the modeling of chains such as hydrocarbons. These kinds of modifications drove the generation of cubic EoSs, which are being currently used to predict properties of fluids and their phase equilibria.

$$P = \frac{nRT}{V}\left(\frac{1 + y + y^2 - y^3}{(1-y)^3}\right) - \frac{an^2}{V^2} \qquad 2.61$$

$$P = \frac{nRT}{V - nb} - \frac{an^2\, w(T)}{V^2 + 2nbV - n^2b^2} \qquad 2.62$$

2.3.1 SAFT Equations of State

Although cubic equations of state are very accurate and valuable tools, they represent molecules as spheres moving under an attractive mean field. This representation has several limitations to describe the behavior of more complex fluids, such as chains or molecules with strong directional interactions. Even though these issues are usually overcome by fitting additional parameters that add flexibility to the EoS (*e.g.,* temperature dependent parameters such as the acentric factor in the Peng-Robinson equation), they are not related to an explicit intermolecular potential, which limits the transferability and predictability of these methods. For this reason, a family of molecular-based EoS were developed through the Wertheim's 1st order thermodynamic perturbation theory (TPT1) [53–56] that considers strong directional interactions (*e.g.,* hydrogen bonds) and formation of chains as perturbations of the Helmholtz energy of the system. This family of equations, known as the Statistical Association Fluid Theory (SAFT),[57,58] model molecules as a set of beads connected in the form of chains, that interact via a molecular-based intermolecular potential. This model also includes a term known as "association" to account for strong directional interactions. Notice that the molecular model used in SAFT EoS is almost equivalent to the CG representation used in molecular simulations, so the parameters used within this framework have a direct microscopical connection.

As TPT1 theory is based on energy perturbations, SAFT EoS is generally built in terms of the Helmholtz energy of the system (eq. 2.63), where A_{ideal} contains the ideal gas term specified in eq. 2.58, A_{mono} refers to the reference energy of an independent set of interacting spheres (*i.e.,* similar to $A_{rep} + A_{att}$ in vdW EoS), A_{chains} accounts for the energy perturbation due to having

the independent spheres bonded in chains of length m, and A_{assoc} is the energy perturbation used to include the strong associative interactions. A visual representation of eq. 2.63 can be seen in Figure 2.6.

$$A = A_{ideal} + A_{mono} + A_{chains} + A_{assoc} \quad 2.63$$

The different SAFT-based EoS developed from that framework differ mainly on the reference fluid and the intermolecular potential for dispersion interactions. For example, the reference fluid is usually selected as the set of independent beads described by A_{mono}, but the framework of the perturbed chain PC-SAFT EoS [59] uses as a reference a set of hard chains (*i.e.,* where the term A_{chains} becomes implicit in the reference term). On the other hand, the first SAFT equations used a HS model to account for the attractive and repulsive interactions, which were further developed to accommodate molecular potentials such as LJ (eq. 2.30) or Mie (eq. 2.32). Some examples of these EoSs are the SAFT-LJ,[60] soft-SAFT [61] (*i.e.,* that use a LJ potential), the variable range SAFT-VR,[62,63] (*i.e.,* that started to use a Mie potential after the work of Laffite *et al.*[35,64]) and the SAFT-γ-Mie EoS.[65]

Specifically, the soft-SAFT EoS has been used in this doctoral thesis, whose monomer term (eq. 2.64) is based on a LJ fluid, as initially proposed by Müller *et al.,*[66] and Kraska *et al.,*[60] and later modified by Blas *et al.,*[61] under the name of soft-SAFT. This term comes from an expansion with three parameters (*i.e.,* a_k, b_k and G_k) that are fitted to molecular simulation data of the LJ fluid and also depends on the reference density of a LJ fluid (ρ^{ref}). The density of the fluid depends on the potential, so A_{mono} is also a function of the LJ parameters (*i.e.,* σ and ε) and the length of the monomer chains (m). Alternatively, according to the vdW one-fluid theory,[67] the A_{mono} term

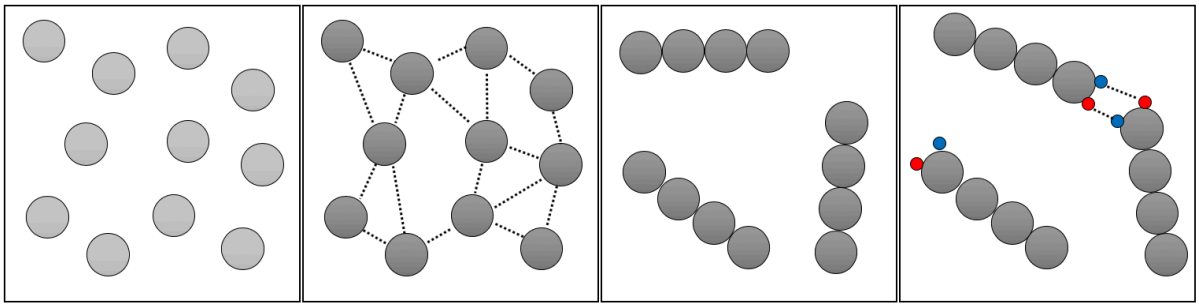

Figure 2.6. Representation of the four energy terms in SAFT-based EoS. The grey beads denote molecular segments, the dotted lines represent intermolecular interactions and the red and blue dots model two different associative sites in the SAFT framework.

for mixtures can be approximated to the Helmholtz free energy of a hypothetically pure LJ pseudo-compound with the same thermodynamic properties as the mixture. This pseudo-compound has parameters m^x, σ^x and ε^x, which can be obtained by a combination of all the explicit m_i, σ_{ij} and ε_{ij} values as shown in eq. 2.65, eq. 2.66 and eq. 2.67, respectively. These combinations depend on the composition of the mixture, as reflected by the molar fractions of each species (*i.e.,* x_i and x_j). Finally, the crossed σ_{ij} and ε_{ij} terms have been obtained using the mixing rules presented in eq. 2.34 and eq. 2.35, respectively.

$$A_{mono} = N k_B T\, \varepsilon^x \left[\sum_{k=1}^{8} \frac{a_k}{k} (\rho^{ref})^k + \sum_{k=1}^{6} b_k G_k \right] \tag{2.64}$$

$$m^x = \sum_{i}^{species} x_i\, m_i \tag{2.65}$$

$$(\sigma^x)^3 = \frac{\sum_i^{species} \sum_j^{species} m_i\, m_j\, x_i\, x_j\, \sigma_{ij}^3}{\sum_i^{species} \sum_j^{species} m_i\, m_j\, x_i\, x_j} \tag{2.66}$$

$$\varepsilon^x = \frac{1}{(\sigma^x)^3} \frac{\sum_i^{species} \sum_j^{species} m_i\, m_j\, x_i\, x_j\, \varepsilon_{ij}\, \sigma_{ij}^3}{\sum_i^{species} \sum_j^{species} m_i\, m_j\, x_i\, x_j} \tag{2.67}$$

The other terms (*i.e.,* A_{ideal}, A_{chains} and A_{assoc}) are formally equivalent in all other versions of SAFT and their extension to fluid mixtures are collected in eq. 2.68, eq. 2.69 and eq. 2.71, respectively. In general, all terms depend on the molar fraction of each component in the mixture (x_i). Then, A_{chains} depends on both the length of each bead chain (m_i) and the radial distribution functions (g_{ii}) obtained from the intermolecular potential. On the other hand, to calculate A_{assoc} one has to define an association scheme for each species, which implies the specification of the total number of association sites (M_i) and the type of each site (α). After this definition, the association term depends mainly on the fraction of molecules not bonded to sites type α ($X_{\alpha,i}$), which can be calculated with eq. 2.71 within the soft-SAFT framework. Notice that this expression includes two additional adjustable parameters related to the strength ($\varepsilon^{HB}_{\alpha\beta,ij}$) and volume ($K^{HB}_{\alpha\beta,ij}$) of the site-site ($\alpha\beta$) associative interactions. To clarify the definition of the association scheme, take a liquid alcohol as an example. The O and H atoms of this fluid can interact via hydrogen bonding. To reproduce this behavior within soft-SAFT, two associative sites are defined (M_i = 2): one representing the oxygen atom (*i.e.,* type 1) and the other to model the hydrogen atom (*i.e.,* type

2). Within this association scheme there is a maximum of three possible associations (*i.e.,* O-O, H-H and O-H). To prevent O-O and H-H associations, the strength for those interactions are set to zero and the O-H parameters are fitted to reproduce the hydrogen bonding behavior. Finally, as eq. 2.71 refers to a fluid mixture, the crossed ij parameters for the strength and volume of association have also to be mixed from the pure ii and jj parameters. The strength of association (eq. 2.72) has been mixed by using the common Lorentz-Berthelot combination rules. However, as the volume of association has units of Å^3 (*i.e.,* instead of Å) the $K^{HB}_{\alpha\beta,ii}$ values are cubic rooted, averaged and cubed back again to obtain the mixed volume of association (eq. 2.73).

$$A_{ideal} = Nk_BT\left[\sum_{i}^{species}\left[x_i \ln\left(\frac{N_i\Lambda_i^3}{V}\right)\right] - 1\right] \quad 2.68$$

$$A_{chains} = Nk_BT\left[\sum_{i}^{species} x_i(1-m_i)\ln(g_{ii})\right] \quad 2.69$$

$$A_{assoc} = Nk_BT\left[\sum_{i}^{species} x_i\left[\sum_{\alpha}^{site\ types}\left(\ln(X_{\alpha,i}) - \frac{1}{2}X_{\alpha.i}\right) + \frac{M_i}{2}\right]\right] \quad 2.70$$

$$\frac{1}{X_{\alpha,i}} = 1 + \frac{N}{V}\left[\sum_{j}^{species} x_j\left[\sum_{\beta}^{site\ types} X_{\beta,j}\, K^{HB}_{\alpha\beta,ij}\left[e^{(\varepsilon^{HB}_{\alpha\beta,ij}/k_BT)} - 1\right]g_{ij}\right]\right] \quad 2.71$$

$$\varepsilon^{HB}_{\alpha\beta,ij} = \sqrt{\varepsilon^{HB}_{\alpha\beta,ii}\cdot\varepsilon^{HB}_{\alpha\beta,jj}} \quad 2.72$$

$$K^{HB}_{\alpha\beta,ij} = \left(\frac{\sqrt[3]{K^{HB}_{\alpha\beta,ii}} + \sqrt[3]{K^{HB}_{\alpha\beta,jj}}}{2}\right)^3 \quad 2.73$$

To conclude, to calculate the properties of fluids with the soft-SAFT EoS one usually has to define between three and five parameters per species, depending on their molecular description. The interaction between different monomers depends on the intermolecular potential, which at the same time depends on the LJ parameters (*i.e.,* σ_{ii} and ε_{ii}). In the soft-SAFT description, these monomers are connected to each other forming chains of a certain length (m_i), that is also defined

beforehand. Additionally, if the fluid exhibits any kind of directional interactions (*e.g.,* hydrogen bonding or dipole/dipole interactions) an associative scheme with two additional parameters must be included, to account for the strength ($\varepsilon^{HB}_{\alpha\beta,ii}$) and the volume ($K^{HB}_{\alpha\beta,ii}$) of association. Finally, the crossed parameters in mixtures are completed with mixing rules.

As a special case, soft-SAFT EoS included an additional term to eq. 2.63 to account for quadrupole-quadrupole interactions (A_{polar}) as described in the work of Stell *et al.*[68] This term depends on the quadrupole moment of the molecule (Q) and the fraction of beads (x_p) in a chain that contains the quadrupole. This term is only used, in the soft-SAFT EoS, to include the quadrupole-quadrupole interactions of some gas molecules, while dipolar interactions are taken into account as directional associative bondings.

Once the Helmholtz energy of the system is obtained, the macroscopic properties can be obtained through the thermodynamic derivatives shown in the equations from eq. 2.74 to eq. 2.78. Finally, equilibrium conditions for phase equilibria can be obtained by solving a set of equations (*i.e.,* one per each phase), where the equality of the pressure, the Gibbs free energy and the chemical potential (*i.e.,* only in the case of mixtures) is imposed.

$$P = -\left(\frac{\partial A}{\partial V}\right)_{NT} \qquad 2.74$$

$$S = -\left(\frac{\partial A}{\partial T}\right)_{NV} \qquad 2.75$$

$$\mu = \left(\frac{\partial A}{\partial N}\right)_{VT} \qquad 2.76$$

$$G = A + PV \qquad 2.77$$

$$H = G + TS \qquad 2.78$$

2.3.2 COSMO-RS

COnductor-like Screening MOdel for Realistic Solvents (COSMO-RS) is a quantum-based method, coupled to equilibrium thermodynamics that is capable of predicting the chemical potential of a liquid phase.[69–71] Once the chemical potential is obtained, one can calculate infinite dilution activity coefficients and phase equilibrium data, such as vapor pressures and solubilities

using classical thermodynamics. In theory, COSMO-RS has some adjustable parameters in its equations, but they were adjusted for general purpose liquids by Klamt *et al.*[71] So, in practice, COSMO-RS only depends on information derived from quantum-based methods and does not need to fit any specific parameter prior to the calculation. The initial step of a COSMO-RS calculation is a DFT geometry optimization using the so-called COSMO solvation model. Implicit solvation models approximate the presence of a solvent by means of a dielectric constant. This simple, yet effective model is widely used in quantum calculations, selecting the adequate dielectric constant value to represent the solvent of interest.

On the other hand, COSMO is a polarizable continuum model where a molecule is fitted in a cavity of an ideal conductor solvent. The surface of the cavity is discretized into a relatively fine grid of points, each one called a "segment", where the electrostatic potential is computed from the electron density (*e.g.,* from a DFT calculation). Then, the screening charge density (*i.e.,* represented by σ, do not confuse with σ_{HS}, the HS diameter, or σ_{ij}, the distance at which the LJ potential becomes repulsive) at the surface of the cavity is obtained when the electrostatic potential at the segments induced by the polarizable continuum and the molecule becomes zero. This convergence criterion comes from the boundary conditions of an ideal conductor and, it is calculated in practice through an iterative process, where the polarizable model affects the electron density, and at the same time the electron density affects the polarizable model. At this point, the screening charges can be used to obtain the chemical potential of the solvent ($\mu_s(\sigma)$) through eq. 2.79, which has been derived from the partition function of an ensemble of pair-wise interacting surface segments.

$$\mu_s(\sigma) = -k_B T \, ln \int p_s(\sigma') e^{-\left(E_{int}(\sigma,\sigma') - \mu_s(\sigma')\right)/k_B T} d\sigma' \qquad 2.79$$

The value of $\mu_s(\sigma)$ depends on the temperature, the distribution of screening charges at the surface of the cavity (*i.e.,* $p_s(\sigma)$, also known as σ-profile and calculated via a DFT calculation), the energy of two interacting segments ($E_{int}(\sigma, \sigma')$) and the chemical potential ($\mu_s(\sigma')$). The latter represents the cost in free energy required to release a segment from other contacts to allow it to interact with a determined segment. Finally, as the chemical potential is at both sides of the equation, it must be solved iteratively until convergence. All aforementioned parameters of COSMO-RS are located in the energy between a pair of interacting segments ($E_{int}(\sigma, \sigma')$), but as they were fitted for general purpose liquids, eq. 2.79 in practice only depends on the σ-profile calculated through DFT.

After the calculation of the σ-profiles and chemical potentials of two different species, the chemical potential of a mixture can be calculated integrating the σ-profile of the solute through eq. 2.80. The term $\mu_{s,comb}^{X}$ is the so-called "combinatorial chemical potential", which describes the solute (X) and solvent (s) size dependence of the chemical potential. Using eq. 2.79 and 2.80, COSMO-RS is capable of providing the chemical potential of an arbitrary solute in an arbitrary liquid solvent as a function of temperature and concentration only using as information the σ-profiles obtained from quantum chemistry calculations.

$$\mu_s^X = \mu_{s,comb}^X + \int p_X(\sigma)\mu_s(\sigma)\, d\sigma \qquad 2.80$$

2.4 References

1 E. Schrödinger, Quantisierung als Eigenwertproblem, *Ann. Phys.*, 1926, **384**, 361–376.

2 J. Andrés and J. Bertran, *Theoretical and Computational Chemistry: Foundations, Methods and Techniques*, Publicacions de la Universitat Jaume I, Castelló de la Plana, 2007.

3 J. C. Panigua and P. Alemany, *Química Quàntica*, Ediciones de la Tempestad, Barcelona, 2003.

4 M. Born and R. Oppenheimer, Zur Quantentheorie der Molekeln, *Ann. Phys.*, 1927, **84**, 457–484.

5 P. Hohenberg and W. Kohn, Inhomogeneous Electron Gas, *Phys. Rev.*, 1964, **136**, B864–B871.

6 W. Kohn and L. J. Sham, Self-Consistent Equations Including Exchange and Correlation Effects, *Phys. Rev.*, 1965, **140**, A1133–A1138.

7 J. P. Perdew and A. Zunger, Self-Interaction Correction to Density-Functional Approximations for Many-Electron Systems, *Phys. Rev. B*, 1981, **23**, 5048–5079.

8 Y. Wang and J. P. Perdew, Spin scaling of the electron-gas correlation energy in the high-density limit, *Phys. Rev. B*, 1991, **43**, 8911–8916.

9 J. P. Perdew, K. Burke and M. Ernzerhof, Generalized Gradient Approximation Made Simple, *Phys. Rev. Lett.*, 1996, **77**, 3865–3868.

10 J. P. Perdew, A. Ruzsinszky, G. I. Csonka, O. A. Vydrov, G. E. Scuseria, L. A. Constantin, X. Zhou and K. Burke, Restoring the Density-Gradient Expansion for Exchange in Solids and Surfaces, *Phys. Rev. Lett.*, 2008, **100**, 136406:1–4.

11 Y. Zhang and W. Yang, Comment on "Generalized Gradient Approximation Made Simple," *Phys.*

Rev. Lett., 1998, **80**, 890–890.

12 J. Tao, J. P. Perdew, V. N. Staroverov and G. E. Scuseria, Climbing the Density Functional Ladder: Nonempirical Meta--Generalized Gradient Approximation Designed for Molecules and Solids, *Phys. Rev. Lett.*, 2003, **91**, 146401:1–4.

13 Y. Zhao, N. E. Schultz and D. G. Truhlar, Exchange-Correlation Functional with Broad Accuracy for Metallic and Nonmetallic Compounds, Kinetics, and Noncovalent Interactions, *J. Chem. Phys.*, 2005, **123**, 161103:1–2.

14 J. P. Perdew, M. Ernzerhof and K. Burke, Rationale for Mixing Exact Exchange with Density Functional Approximations, *J. Chem. Phys.*, 1996, **105**, 9982–9985.

15 C. Adamo and V. Barone, Toward Reliable Density Functional Methods Without Adjustable Parameters: The PBE0 Model, *J. Chem. Phys.*, 1999, **110**, 6158–6170.

16 A. D. Becke, Density-Functional Exchange-Energy Approximation with Correct Asymptotic Behavior, *Phys. Rev. A*, 1988, **38**, 3098–3100.

17 A. D. Becke, Density-Functional Thermochemistry. III. The Role of Exact Exchange, *J. Chem. Phys.*, 1993, **98**, 5648–5652.

18 S. Grimme, A. Hansen, J. G. Brandenburg and C. Bannwarth, Dispersion-Corrected Mean-Field Electronic Structure Methods, *Chem. Rev.*, 2016, **116**, 5105–5154.

19 S. Grimme, Semiempirical GGA-type Density Functional Constructed with a Long-Range Dispersion Correction, *J. Comput. Chem.*, 2006, **27**, 1787–1799.

20 S. Grimme, J. Antony, S. Ehrlich and H. Krieg, A Consistent and Accurate Ab Initio Parametrization of Density Functional Dispersion Correction (DFT-D) for the 94 Elements H-Pu, *J. Chem. Phys.*, 2010, **132**, 154104:1–19.

21 S. Grimme, S. Ehrlich and L. Goerigk, Effect of the Damping Function in Dispersion Corrected Density Functional Theory, *J. Comput. Chem.*, 2011, **32**, 1456–1465.

22 D. C. Langreth, B. I. Lundqvist, S. D. Chakarova-Käck, V. R. Cooper, M. Dion, P. Hyldgaard, A. Kelkkanen, J. Kleis, L. Kong, S. Li, P. G. Moses, E. Murray, A. Puzder, H. Rydberg, E. Schröder and T. Thonhauser, A Density Functional for Sparse Matter, *J. Phys. Condens. Matter*, 2009, **21**, 084203:1–15.

23 P. Schwerdtfeger, The Pseudopotential Approximation in Electronic Structure Theory, *ChemPhysChem*, 2011, **12**, 3143–3155.

24 D. A. McQuarrie, *Statistical Mechanics*, Harper and Row, New York, 1976.

25 M. P. Allen and D. J. Tildesley, *Computer Simulation of Liquids*, Oxford University Press, New York, 2017.

26 J. E. Jones and S. Chapman, On the Determination of Molecular Fields.—I. From the Variation of the Viscosity of a Gas with Temperature, *P. Roy. Soc. Lond. A Mat.*, 1924, **106**, 441–462.

27 J. E. Jones and S. Chapman, On the Determination of Molecular Fields. —II. From the Equation of State of a Gas, *P. Roy. Soc. Lond. A Mat.*, 1924, **106**, 463–477.

28 R. A. Buckingham and J. E. Lennard-Jones, The Classical Equation of State of Gaseous Helium, Neon and Argon, *P. Roy. Soc. Lond. A Mat.*, 1938, **168**, 264–283.

29 M. S. Daw and M. I. Baskes, Embedded-Atom Method: Derivation and Application to Impurities, Surfaces, and Other Defects in Metals, *Phys. Rev. B*, 1984, **29**, 6443–6453.

30 S. J. Marrink, A. H. de Vries and A. E. Mark, Coarse Grained Model for Semiquantitative Lipid Simulations, *J. Phys. Chem. B*, 2004, **108**, 750–760.

31 W. Shinoda, R. DeVane and M. L. Klein, Multi-Property Fitting and Parameterization of a Coarse Grained Model for Aqueous Surfactants, *Mol. Simul.*, 2007, **33**, 27–36.

32 Å. Ervik, A. Mejía and E. A. Müller, Bottled SAFT: A Web App Providing SAFT-γ Mie Force Field Parameters for Thousands of Molecular Fluids, *J. Chem. Inf. Model.*, 2016, **56**, 1609–1614.

33 G. Mie, Zur Kinetischen Theorie der Einatomigen Körper, *Ann. Phys.*, 1903, **316**, 657–697.

34 H. A. Lorentz, Ueber die Anwendung des Satzes vom Virial in der Kinetischen Theorie der Gase, *Ann. Phys.*, 1881, **248**, 127–136.

35 T. Lafitte, A. Apostolakou, C. Avendaño, A. Galindo, C. S. Adjiman, E. A. Müller and G. Jackson, Accurate Statistical Associating Fluid Theory for Chain Molecules Formed from Mie Segments, *J. Chem. Phys.*, 2013, **139**, 154504:1–38.

36 A. Mejía, C. Herdes and E. A. Müller, Force Fields for Coarse-Grained Molecular Simulations from a Corresponding States Correlation, *Ind. Eng. Chem. Res.*, 2014, **53**, 4131–4141.

37 D. Frenkel and B. Smit, *Understanding Molecular Simulation. From Algorithms to Applications*, Academic Press, London, 2002.

38 L. Verlet, Computer "Experiments" on Classical Fluids. I. Thermodynamical Properties of Lennard-Jones Molecules, *Phys. Rev.*, 1967, **159**, 98–103.

39 W. G. Hoover, Canonical Dynamics: Equilibrium Phase-Space Distributions, *Phys. Rev. A*, 1985, **31**, 1695–1697.

40 S. Nosé, A Molecular Dynamics Method for Simulations in the Canonical Ensemble, *Mol. Phys.*, 1984, **52**, 255–268.

41 G. J. Martyna, M. E. Tuckerman, D. J. Tobias and M. L. Klein, Explicit Reversible Integrators for Extended Systems Dynamics, *Mol. Phys.*, 1996, **87**, 1117–1157.

42 H. J. C. Berendsen, J. P. M. Postma, W. F. van Gunsteren, A. DiNola and J. R. Haak, Molecular Dynamics With Coupling to an External Bath, *J. Chem. Phys.*, 1998, **81**, 3684–3690.

43 W. G. Hoover, Constant-Pressure Equations of Motion, *Phys. Rev. A*, 1986, **34**, 2499–2500.

44 G. J. Martyna, D. J. Tobias and M. L. Klein, Constant Pressure Molecular Dynamics Algorithms, *J. Chem. Phys.*, 1994, **101**, 4177–4189.

45 S. Melchionna, G. Ciccotti and B. L. Holian, Hoover NPT Dynamics for Systems Varying in Shape and Size, *Mol. Phys.*, 1993, **78**, 533–544.

46 N. Metropolis, A. W. Rosenbluth, M. N. Rosenbluth, A. H. Teller and E. Teller, Equation of State Calculations by Fast Computing Machines, *J. Chem. Phys.*, 1953, **21**, 1087–1092.

47 H. Sun, COMPASS: An ab Initio Force-Field Optimized for Condensed-Phase Applications Overview with Details on Alkane and Benzene Compounds, *J. Phys. Chem. B*, 1998, **102**, 7338–7364.

48 P. P. Ewald, Die Berechnung Optischer und Elektrostatischer Gitterpotentiale, *Ann. Phys.*, 1921, **369**, 253–287.

49 J. W. Eastwood and R. W. Hockney, Shaping the Force Law in Two-Dimensional Particle-Mesh Models, *J. Comput. Phys.*, 1974, **16**, 342–359.

50 J. D. van der Waals, PhD Thesis, University of Leiden, 1873.

51 N. F. Carnahan and K. E. Starling, Intermolecular Repulsions and the Equation of State for Fluids, *AIChE J.*, 1972, **18**, 1184–1189.

52 D.-Y. Peng and D. B. Robinson, A New Two-Constant Equation of State, *Ind. Eng. Chem. Fundam.*, 1976, **15**, 59–64.

53 M. S. Wertheim, Fluids with highly directional attractive forces. I. Statistical thermodynamics, *J. Stat. Phys.*, 1984, **35**, 19–34.

54 M. S. Wertheim, Fluids with highly directional attractive forces. II. Thermodynamic perturbation theory and integral equations, *J. Stat. Phys.*, 1984, **35**, 35–47.

55 M. S. Wertheim, Fluids with highly directional attractive forces. III. Multiple attraction sites, *J. Stat. Phys.*, 1986, **42**, 459–476.

56 M. S. Wertheim, Fluids with highly directional attractive forces. IV. Equilibrium polymerization, *J. Stat. Phys.*, 1986, **42**, 477–492.

57 W. G. Chapman, K. E. Gubbins, G. Jackson and M. Radosz, SAFT: Equation-of-State Solution Model for Associating Fluids, *Fluid Phase Equilibr.*, 1989, **52**, 31–38.

58 W. G. Chapman, K. E. Gubbins, G. Jackson and M. Radosz, New Reference Equation of State for

Associating Liquids, *Ind. Eng. Chem. Res.*, 1990, **29**, 1709–1721.

59 J. Gross and G. Sadowski, Perturbed-Chain SAFT: An Equation of State Based on a Perturbation Theory for Chain Molecules, *Ind. Eng. Chem. Res.*, 2001, **40**, 1244–1260.

60 T. Kraska and K. E. Gubbins, Phase Equilibria Calculations with a Modified SAFT Equation of State. 1. Pure Alkanes, Alkanols, and Water, *Ind. Eng. Chem. Res.*, 1996, **35**, 4727–4737.

61 F. J. Blas and L. F. Vega, Critical Behavior and Partial Miscibility Phenomena in Binary Mixtures of Hydrocarbons by the Statistical Associating Fluid Theory, *J. Chem. Phys.*, 1998, **109**, 7405–7413.

62 A. Gil-Villegas, A. Galindo, P. J. Whitehead, S. J. Mills, G. Jackson and A. N. Burgess, Statistical associating fluid theory for chain molecules with attractive potentials of variable range, *J. Chem. Phys.*, 1997, **106**, 4168–4186.

63 A. Galindo, L. A. Davies, A. Gil-Villegas and G. Jackson, The thermodynamics of mixtures and the corresponding mixing rules in the SAFT-VR approach for potentials of variable range, *Mol. Phys.*, 1998, **93**, 241–252.

64 T. Lafitte, D. Bessieres, M. M. Piñeiro and J.-L. Daridon, Simultaneous Estimation of Phase Behavior and Second-Derivative Properties using the Statistical Associating Fluid Theory with Variable Range Approach, *J. Chem. Phys.*, 2006, **124**, 024509:1–16.

65 V. Papaioannou, T. Lafitte, C. Avendaño, C. S. Adjiman, G. Jackson, E. A. Müller and A. Galindo, Group contribution methodology based on the statistical associating fluid theory for heteronuclear molecules formed from Mie segments, *J. Chem. Phys.*, 2014, **140**, 054107:1–29.

66 E. A. Müller and K. E. Gubbins, An Equation of State for Water from a Simplified Intermolecular Potential, *Ind. Eng. Chem. Res.*, 1995, **34**, 3662–3673.

67 J. P. Hansen and I. R. McDonald, *Theory of Simple Liquids*, Academic Press, New York, 1990.

68 G. Stell, J. C. Rasaiah and H. Narang, Thermodynamic Perturbation Theory for Simple Polar Fluids. II, *Mol. Phys.*, 1974, **27**, 1393–1414.

69 A. Klamt and G. Schüürmann, COSMO: a New Approach to Dielectric Screening in Solvents with Explicit Expressions for the Screening Energy and its Gradient, *J. Chem. Soc. Perkin Trans. 2*, 1993, **0**, 799–805.

70 A. Klamt, Conductor-like Screening Model for Real Solvents: A New Approach to the Quantitative Calculation of Solvation Phenomena, *J. Phys. Chem.*, 1995, **99**, 2224–2235.

71 A. Klamt, V. Jonas, T. Bürger and J. C. W. Lohrenz, Refinement and Parametrization of COSMO-RS, *J. Phys. Chem. A*, 1998, **102**, 5074–5085.

CHAPTER 3

Gas Capture and Separation for Post-Combustion Processes

Since the industrial revolution in the second half of the XVIII century, there has been a steady increase of CO_2 emissions from anthropogenical sources.[1,2] These emissions were generated, at the time, through the burning of coal to power production and transport vehicles, which pushed the economy of the occidental society. From that moment, the combustion of fossil fuels became a common source of energy and it is even currently used today worldwide, especially in China, United States and Europe.[3] Fortunately, many scientific studies found that CO_2 emissions were causing an important greenhouse effect steadily increasing the average Earth temperature by 1 ºC in the last 100 years.[4,5] Additionally, the growing amount of CO_2 in the air can solve in water, increasing the acidity of oceans and affect its flora and fauna.[6,7] To prevent irreversible environmental effects, governments set up objectives and proposed measures to reduce CO_2 emissions, favoring renewable energy sources.[8] Since 2006, there has been a significant reduction in CO_2 emissions in Europe, for both countries in (EU-28) and out the European Union, and United States up to 2015. Unfortunately, even with this reduction, the total amount of globally emitted CO_2 has increased due to contribution from Asiatic countries, specially China (Figure 3.1).

In the slow-paced adaptation process of industries from fossil fuels to renewable energies, it is required to develop cost-efficient technologies capable of preventing CO_2 release to the atmosphere. The capture of CO_2 is also beneficial because there are several industrial applications where this gas is needed (*e.g.,* it can be used in the synthesis of methanol,[9] methane,[10] bicarbonate[11] or formaldehyde,[12] among others; added to food as an acidity regulator; used in carbonated water and sodas, combined with water to produce fire extinguishers, and in supercritical conditions it becomes a very good solvent for lipophilic compounds, currently applied to remove caffeine from coffee [13] or to extract oil in enhanced oil recovery processes,[14] among others). For all these reasons, there is a large interest in capturing and separating CO_2 either from air (*i.e.,* to reduce atmospheric CO_2 content) or from industrial flue gases (*i.e.,* to prevent increasing CO_2 emissions and reuse it for any of the beforementioned applications).

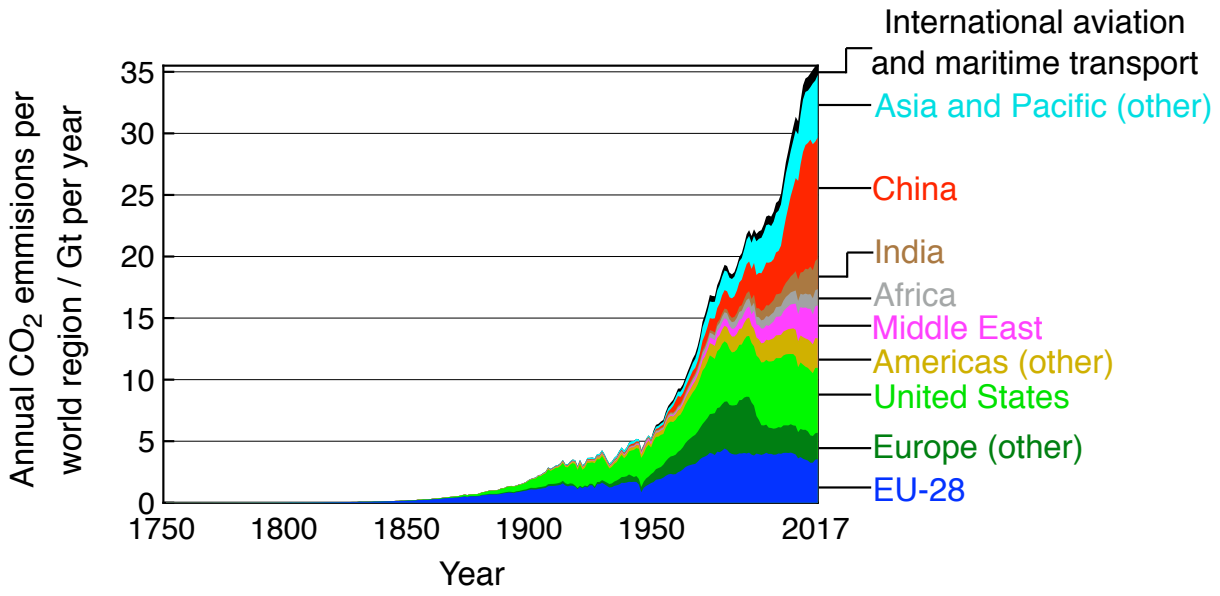

Figure 3.1. Annual CO_2 emissions by world region, from the XVIII century (*i.e.,* before the industrial revolution) to 2017.[3]

3.1 Introduction to Industrial Post-Combustion Gas Separation

A common industrial post-combustion gas separation scheme can be seen in Figure 3.2, where a fuel/air mixture is burnt to produce energy. A perfect combustion from pure hydrocarbons would give CO_2, H_2O and the excess N_2 from air. However, fossil fuels are enormous mixtures of compounds, many of them containing organic nitrogen and sulphur, among others. These compounds may yield in the combustion process sulphur oxides (*i.e.,* SO_x) and nitrogen oxides (*i.e.,* N_xO_y) in addition to CO_2 and H_2O, which are toxic or environmentally unfriendly species.[15,16] Fortunately, some fossil fuels are pre-treated to reduce their sulphur content up to 10 ppm (*e.g.,* gasoline).[17] However, in general the mixture after the combustion contains many gas species that must be separated to obtain pure CO_2 for use and commercialization. In this process, water is removed from the flue gas mixture in a previous drying unit through condensation. Then, a consecutive stage is performed to separate CO_2 and all the contaminant species to store them for further use or elimination. The remaining N_2 and O_2 from the combustion process are harmless species that can be released again to the atmosphere.

There are several technologies that can be used nowadays to capture CO_2, being absorption with aqueous amine solutions the most widely implemented in industry.[18] This technology is dominant because it is a cheap solvent who is proven to effectively absorb CO_2 under ambient conditions. However, the gas must be recovered through solvent evaporation, which also

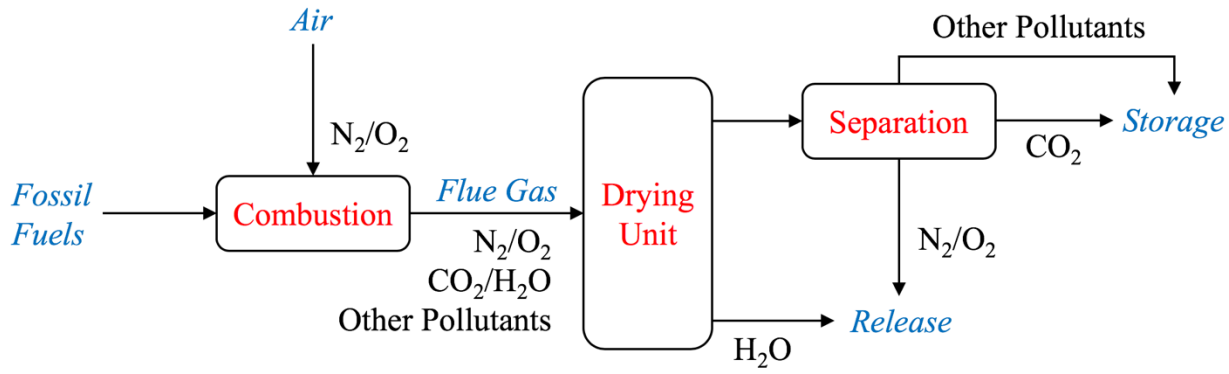

Figure 3.2. Simplified process for CO_2 capture and separation of a post-combustion flue gas. Notice that the separation stage can contain many steps to capture different gas components at each step.

regenerates the absorbent, but it consumes a relatively high amount of energy. A part of the previously generated energy during the combustion is usually taken to regenerate the adsorption/absorption material, which reduces the efficiency of the power plant when regeneration is an expensive step of the process. Additionally, amines are relatively volatile compounds who have an adverse environmental impact and present corrosive issues.[19–21] For these reasons, alternatives to aqueous amines have been studied by the scientific community to capture CO_2 in a more sustainable, efficient and economical way.

Several alternative technologies are available for CO_2 capture, as they are compiled in Figure 3.3. This thesis focuses on studying gas separation by absorption in non-amine solvents and adsorption in microporous materials. Membrane, biological and cryogenical technologies are also worth mentioning because they are also good alternatives for CO_2 capture, but there is a tradeoff between permeability and selectivity,[22] whereas absorption and adsorption technologies do not suffer from this issue.

The capture through adsorption in microporous materials has been studied using two different adsorbent materials: Zeolites and Metal Organic Frameworks (MOFs). The former are aluminosilicates, usually hydrated, with a very large surface area and general molecular formula $[M]_{n/a}^{a+}\,[SiO_2]_m[AlO_2]_n \cdot xH_2O$. Due to their porosity, these materials present different types of pores and channels, and the different molecular arrangements give rise to a huge amount of different Zeolite families.[23] Gas molecules inside Zeolites are restrained in the pores and can be separated either by size (*i.e.,* through molecular sieving) or through selective adsorption upon their structure.[24] These materials excel at gas separation not only due to their good uptake and selectivity but also for their good thermal stability. Specifically, a study of CO_2 capture and separation with Zeolites is described in Section 3.2.

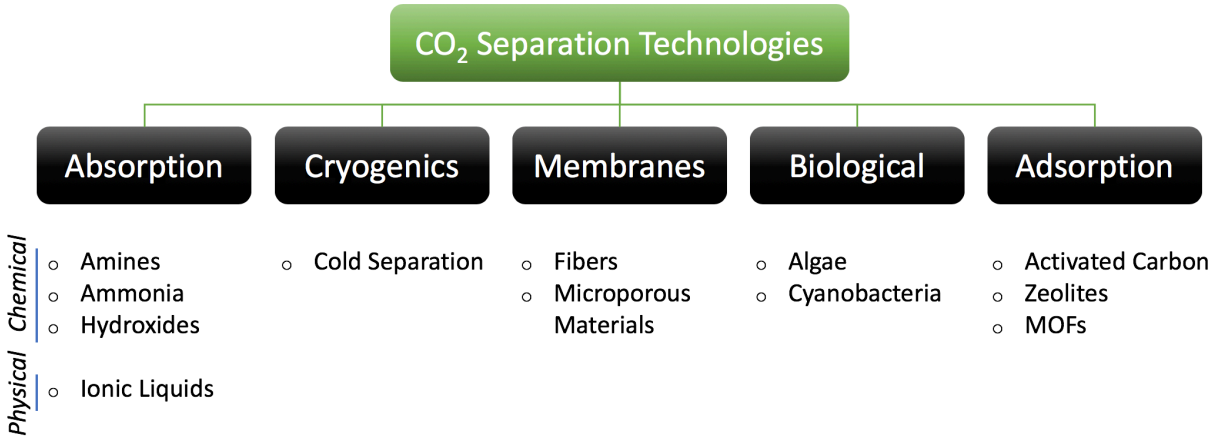

Figure 3.3. Summary of the different carbon capture technologies industrially available.

On the other hand, MOFs are another group of porous materials based on networks of metal cations connected through organic linkers and with a general molecular formula $[M]^{a+}[L]^{n-}_{a/n}$. They share many features with Zeolites but some MOFs, specially the so-called Mg-MOF-74, are better suited for CO_2 separation at a cost of a lower thermal and chemical stability.[25] Both materials exhibit improvements with respect amine absorption because they have a lower regeneration cost, very low environmental impact and they can be tuned during the synthesis to be optimized for specific purposes. However, the adsorption on these materials can be hampered by poisoning with other polar gases, which can interact strongly with the cations and block the adsorption sites. For this reason, it is important to include a preliminary separation step to remove some of these contaminants from flue gas mixtures. In this sense, a study of gas adsorption on the Mg-MOF-74, considering possible SO_2 poisoning, is detailed in Section 3.3.

Regarding capture by absorption, the gas separation using ionic liquids (ILs) as alternative solvents with good affinity for CO_2 has been studied. ILs are organic salts that remain liquid at ambient conditions and have relatively strong interactions with gas molecules due to the charges of both the cation and the anion. They generally have good physicochemical properties for industrial applications such as low vapor pressure, high stability, low corrosivity and non-flammability.[26–28] However, the uptake of ILs is usually low when compared to amines. The advantage of ILs is that they are formed by a cation/anion pair and any member can be exchanged to modify the properties of the fluid and optimize it for a determined application. Specifically, in this thesis, the absorption of CO_2 in three different phosphonium-based ILs is assessed, as it is compiled in Section 3.4.

To separate CO_2 from a flue gas, ideally one has to use a material that can selectively capture this gas under operative conditions. When the material is saturated, a desorption step must be carried out to recover the CO_2, regenerating the material in the process to use it in further separation

cycles. The capture/desorption cycles can be performed through a temperature swing process (*i.e.,* capturing gas at low temperatures and heating to recover the CO_2), a pressure swing process (*i.e.,* capturing gas at high pressures and releasing it at atmospheric conditions) or through a vacuum swing process (*i.e.,* capturing gas at atmospheric pressure and recovering it at lower pressures). Different technologies for CO_2 capturing might require using different conditions or employing a determined swing process to optimize the capture and separation of CO_2.

To optimize the gas separation with a determined technology, one has to take under consideration the selectivity of the material to capture this gas. A high CO_2 selectivity is desirable because it implies that the technology is capturing almost only the desired gas, and it will be almost pure when released in the desorption step. Selectivity ($S_{A/B}$) must be defined against other components (*e.g.,* selectivity of CO_2 with respect N_2) and can be estimated from pure component adsorption/absorption isotherms through the relationship of Henry's coefficients (*i.e.,* H_A and H_B in eq. 3.1). However, this estimation does not include competition between sites and can only be applied at low pressures. Alternatively, molecular simulations can be employed to calculate the selectivity of the material in mixtures (eq. 3.2), finding the ratio of molar fractions of component A with respect B captured by the material (x_A^*/x_B^*) scaled by the ratio of molar fractions of these components in the gas phase (x_A^g/x_B^g).

$$S_{A/B}^{id} = H_A/H_B \tag{3.1}$$

$$S_{A/B} = \left(\frac{x_A^*}{x_B^*}\right) / \left(\frac{x_A^g}{x_B^g}\right) \tag{3.2}$$

Apart from the selectivity it is important to evaluate the total uptake (N_A^*) and the working capacity of the material (WC_A).[29] The former is the total amount of gas that can be captured by the material at a determined pressure and temperature expressed as the quantity captured (*i.e.,* either in moles or mass) per kilogram of adsorbent. The latter is defined as the amount of gas that can be recovered in a capture/recovery cycle (eq. 3.3), and it depends on the swing process used along with the pressure and the temperature conditions employed in the cycle (Figure. 3.4).

$$WC_A = N_A^*(P^{ads}, T^{ads}) - N_A^*(P^{des}, T^{des}) \tag{3.3}$$

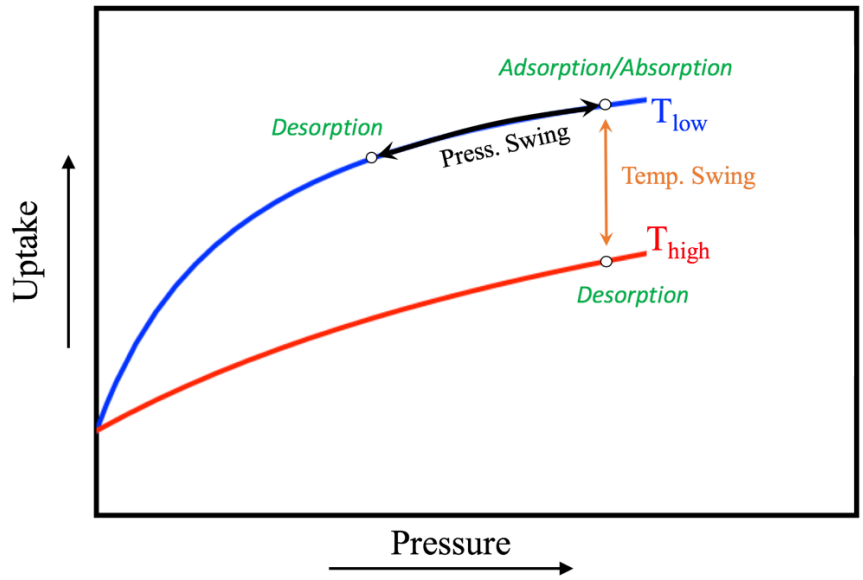

Figure 3.4. Graphical representation of the working capacity in two different swing processes. The blue and red curves represent adsorption/absorption isotherms at low and high temperatures, respectively.

Finally, it is important to evaluate the isosteric heat of adsorption (q_{st}) in microporous materials, which is defined as the heat released when a molecule is adsorbed (*i.e.,* the negative of the differential enthalpy of adsorption $q_{st} = -\Delta H^{ads}$). This magnitude depends on the temperature, the surface coverage and the affinity of the gas molecule towards the surface. The dependence on the surface coverage reveals how the lateral interactions among adsorbed gas molecules affect the adsorption capability of the material or even unveils the presence of different adsorption sites with different affinities and isosteric heats. On the other hand, when the capture is performed with liquid solvents, a comparable magnitude is the differential enthalpy of dissolution (ΔH^{dis}), which gives similar information as ΔH^{ads} but in liquid phase. Both magnitudes can be obtained from the temperature dependence of the adsorption/absorption isotherms, in a relatively small temperature window, using the Clausius-Clapeyron equation (eq. 3.4). In fact, this is the commonly used method by experimentalists to obtain enthalpies of absorption/adsorption, which can be converted to q_{st} if required. Notice that the partial derivative is calculated at constant composition: either at constant coverage for solid adsorbents (θ) or at constant molar fraction for liquid solvents (x). Alternatively, the isosteric heat of adsorption can also be calculated through molecular simulations from the energy/particle fluctuations in the Grand Canonical ensemble (eq. 3.5).

$$\left(\frac{\partial \ln P}{\partial 1/T}\right)_{\theta \text{ or } x} = \frac{\Delta H^{ads}}{R} = \frac{\Delta H^{dis}}{R} \quad 3.4$$

$$q_{st} = -\frac{\langle U^{ads} \times N\rangle - \langle U^{ads}\rangle\langle N\rangle}{\langle N^2\rangle - \langle N\rangle^2} + \langle U^g\rangle + k_B T \quad 3.5$$

where, U^{ads} is the internal energy of a system with N adsorbed molecules, U^g is the internal energy of a single isolated gas molecule and the brackets denote a Grand Canonical ensemble average. Finally, the isosteric heat of adsorption can also be obtained from the derivative of the integral enthalpy of adsorption ($\Delta_{\text{int}}H^{ads}$) with respect the surface coverage at constant temperature (eq. 3.6). As explained in Section 2.1.4 this value can be calculated via DFT coupled to statistical thermodynamics.

$$q_{st} = -\left(\frac{\partial \Delta_{\text{int}} H^{ads}}{\partial \theta}\right)_T \quad 3.6$$

The benefit of modeling the gas adsorption into microporous materials or the gas absorption in liquid solvents is threefold; first, it allows to determine the main interactions and driving forces that favors gas capture at the molecular level. This fact helps to understand the system behavior and develop some "rules of thumb" to predict which materials could be promising just by their molecular structure. Additionally, the modeling also allows to obtain the adsorption/absorption isotherms of any possible material, either synthesized or not, to perform a screening of the best capture technologies and best working conditions. Finally, the cost of performing a simulation in any material at any pressure/temperature condition or gas mixture is relatively low because it only requires the electricity for computers to perform calculations. On the other hand, experiments usually require expensive equipment, materials or reactants and a properly set up lab to work. For this reason, the following chapter compiles different computational methods for studying CO_2 capture and gas separation in different materials: from DFT up to mean field fluid theories such as soft-SAFT EoS.[30]

3.2 CO_2 Separation in Faujasites

Zeolites are a set of microporous aluminosilicate materials formed by $[SiO_2]$ and $[AlO_2]^-$ units connected tetrahedrally, forming large pores.[31] Notice that Al tetrahedrons have a net negative charge that must be compensated with alkali or alkali earth cations (*i.e.,* usually Na^+ or Ca^{2+}) commonly known as extra-framework cations, which affects the properties of Zeolites.[32,33] Additionally, other species with tetrahedral coordination, such as $[GeO_2]$ or $[GaO_2]^-$, can also be found in the framework as substitutions of the beforementioned units, also changing the properties of the Zeolite.[34–36]

Zeolites are minerals first discovered by Cronsted in 1765, who found Stilbite after heating this unknown material and observing it released a large amount of steam.[33,37] The term zeolite, which means "boiling stone", were assigned to this family of minerals after that event. The large pores of Zeolites are naturally formed by the presence of fluids (*e.g.,* generally gases, like steam) within the melted minerals before crystallization. For this reason, Zeolites can be naturally found in areas of high volcanic activity.[38–40] After this discovery, Zeolites started to be synthesized throughout hydrothermal processes, being Levynite the first completely synthetic structure obtained by St. Claire Deville.[41]

Although many Zeolites have very similar molecular formulas, the synthetic process may yield significantly different structures. These structures are classified with a three letter name by the International Zeolite Association (IZA), based on the different building units they contain and how they are connected to form the different pores.[23] Currently, more than 230 different Zeolite frameworks have been assigned by the association,[42] evidencing the high interest of the community in these materials. Zeolites can be used in many different applications depending on their framework and their amount of extra-framework cations nested in the structure (*i.e.,* the number of $[AlO_2]^-$ units or, equivalently, their Si/Al ratio). Cations are very polar sites that can interact strongly with polar gas molecules such as CO_2 or H_2O, which makes Al-rich Zeolites good candidates for gas capture and separation or even heterogeneous catalysis.[43,44] However, their high activity comes at the price of a lower chemical stability and with the risk of becoming easily poisoned.[45] Other Zeolites with low amount of Al (*i.e.,* with a few number of extra-framework cations) have lower polarity, becoming more chemically stable, and turning the surface more selective towards adsorption of non-polar organic molecules. This property makes Al-poor Zeolites good candidates for treating wastewater [46,47] or to be used as inert molecular sieves.[48]

This part of the thesis focuses on modeling the Faujasite (FAU) framework for gas separation, because it was experimentally observed to be a promising material for capturing CO_2.[49–51] The

Faujasite framework is formed by a set of 24-tetrahedron structures known as sodalite cages (sod) connected among each other through double-six-rings (d6r). This structure generates large cavities in different directions with a very large surface area for gas adsorption as it can be seen in Figure 3.5. The extra-framework cations nested in the structure (*i.e.,* shown in Figure 3.6) can be found near the $[AlO_2]^-$ units and in the open cavities or inside the sodalite cages. It is worth noticing that stable structures must accomplish the Lowenstein's rule,[52] which states that there cannot be two $[AlO_2]^-$ tetrahedrons connected to each other. This fact implies that in the structures with maximum Al content, $[AlO_2]^-$ units must be separated by at least one $[SiO_2]$ tetrahedron, forming a network of Al-O-Si-O-Al-O-Si. According to the Löwenstein's rule, the possible Si/Al ratios that can be found in a Zeolitic framework range from Si/Al = ∞ to Si/Al = 1.

3.2.1 DFT Adsorption of CO_2, N_2 and O_2 in Faujasites

The affinity of Faujasite structures for different flue gas components (*i.e.,* CO_2, N_2 and O_2) has been assessed through periodic DFT calculations performed with the Vienna *Ab initio* Simulation Package (VASP) [53,54]. The GGA functional of Perdew, Burke and Ernzerhof (PBE) [55] has been chosen adding the dispersion correction through the empirical D2 method of Grimme.[56,57] The plane wave basis has been expanded up to a cutoff energy of 600 eV and only the Γ-point has been used to represent the reciprocal space due to the large size of the Faujasite primitive unit cell. The primitive unit cell (Figure 3.6) is a rhombohedral box with cell parameter $a = b = c$ =17.30 Å and cell angles $\alpha = \beta = \gamma = 60^{\circ}$. The totally silicated structure contains a total of 48 $[SiO_2]$ units, whereas more aluminated Faujasites have some of the Si atoms substituted by Al/Na^+ pairs.

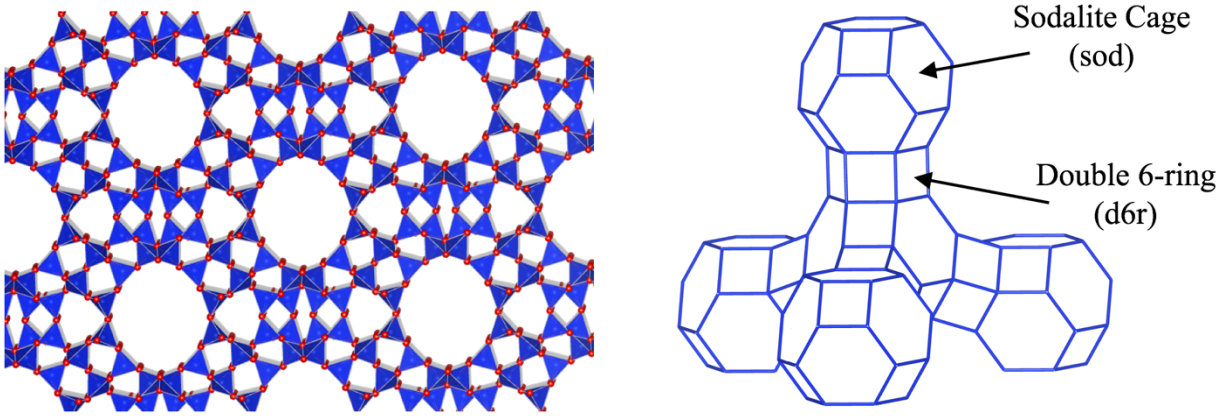

Figure 3.5. Faujasite atomic structure shown in the direction of the pores, along with a simplified representation of the main building units of the FAU framework: the sodalite cages (sod) tetrahedrally connected throughout the hexagonal double 6-rings (d6r).

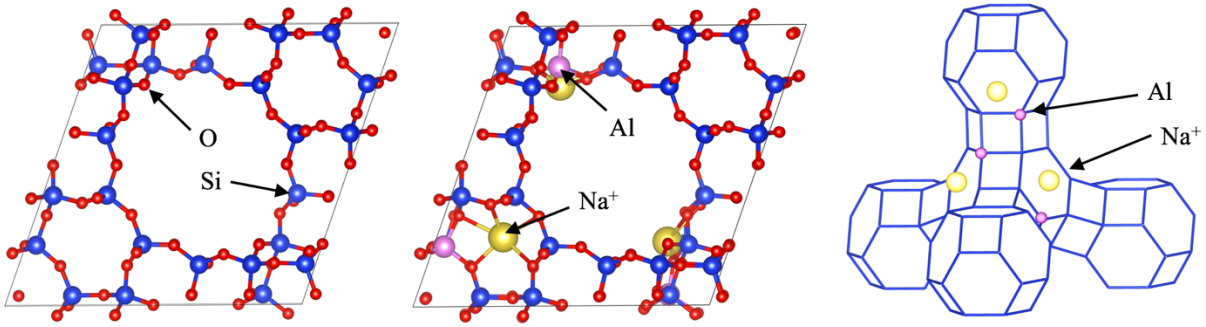

Figure 3.6. Primitive unit cell view of the (100) direction of two Faujasite structures: a completely silicated FAU (left) and a cell with three $[AlO_2]^-/Na^+$ pairs (center). A representation of the Faujasite framework with three $[AlO_2]^-/Na^+$ pairs with Na^+ in the favored positions is also displayed for clarity (right).

Two structures of Faujasite have been modeled with different Si/Al ratio. First, a totally silicated Faujasite with molecular formula $[SiO_2]_n$, which does not have any $[AlO_2]^-$ units and thus, no extra-framework cations (*i.e.,* an infinite Si/Al ratio). Second, a Faujasite with three $[SiO_2]$ units substituted by $[AlO_2]^-$, giving a structure with Si/Al = 15 (*i.e.,* uniformly distributed and accounting for the Löwenstein's rule) accompanied by the corresponding Na^+ as extra-framework cations, initially located near the Al ions. Both structures have been minimized by means of DFT, and the Na^+ cations of the second structure have moved into the centers of the hexagonal rings that connect the large pores with the sodalite cages (Figure 3.6). This distribution is in agreement with previous works that stated that extra-framework cations prefer to be located in these positions up to Si/Al = 5.[58]

Gas adsorption energies (eq. 3.7) have first been studied in the totally silicated structure after minimizing the Faujasite at the PBE level. This magnitude (ΔE_i^{ads}) gives an idea of the strength in which a gas molecule adsorbs onto a solid structure, and it is obtained as the energy difference between a system with a gas molecule adsorbed in the framework ($E_i^{gas/adsorbent}$), the individual isolated gas molecule (E_i^{gas}) and the adsorbent material ($E^{adsorbent}$). In this structure, the three gas molecules can adsorb on the walls of the large pores, which is the region that contains the most easily accessible adsorption sites for gas molecules that flow through the microporous structure. All gas molecules can absorb on both the Si atoms or the O atoms of the Faujasite walls, presenting equivalent adsorption energies for both sites. The calculated energies in this structure, including the zero-point energy are compiled in Table 3.1, and their values are -16.6 $kJ \cdot mol^{-1}$ for CO_2, -9.6 $kJ \cdot mol^{-1}$ for N_2 and -8.3 $kJ \cdot mol^{-1}$ for O_2. An alternative favorable adsorption site is located inside the sodalite cages, which has higher interaction energies, such as -33.9 $kJ \cdot mol^{-1}$ for CO_2, -27.0 $kJ \cdot mol^{-1}$ for N_2 and -21.4 $kJ \cdot mol^{-1}$ for O_2. The sodalite cage sites are connected to the main

Table 3.1. CO_2, N_2 and O_2 adsorption energies on the pore walls, on top of the Na^+ cations and within the sodalite cage, along with the diffusion energy barrier that connects the main pores with the sodalite cages. All energies were calculated using the totally silicated Faujasite, except the adsorption energy on a Na^+ cation, which was obtained from the structure with three Al/Na^+ pairs.

Adsorption energies and diffusion energy barriers	$\Delta E_{CO_2}^{ads}$ / kJ·mol^{-1}	$\Delta E_{N_2}^{ads}$ / kJ·mol^{-1}	$\Delta E_{O_2}^{ads}$ / kJ·mol^{-1}
Pore walls	-16.6	-9.6	-8.3
Sodalite cages	-33.9	-27.0	-21.4
Na^+ cations	-34.7	-11.8	-12.5
Pore-Sodalite Barrier	165.5	226.1	162.5

channels through a hexagonal ring that gas molecules need to cross before accessing the sodalite cage. The diffusion from the main pores to the soldalite cage has also been studied with DFT calculations, finding energy barriers higher than 150 kJ·mol^{-1} for all the studied species. This result suggests that gas molecules will need a significant amount of energy to get into the sodalite cages, effectively preventing adsorption onto the most favorable sites. In general, the totally silicated Faujasite has higher adsorption energies for CO_2 than for the other components of post-combustion flows, but the differences do not seem to be large enough to selectively separate CO_2 from the post-combustion flue gas.

$$\Delta E_i^{ads} = E_i^{molec/adsorbent} - E^{adsorbent} - E_i^{molec} \qquad 3.7$$

On the other hand, the addition of some $[AlO_2]^-$ units and extra-framework cations makes new adsorption sites to appear. The adsorption energies of the three gas molecules on top of the Na^+ cation are enhanced to -34.7 kJ·mol^{-1}, -11.8 kJ·mol^{-1} and -12.5 kJ·mol^{-1}, respectively. Despite all adsorption energies are increased by the addition of Na^+, the surface gains much more affinity for CO_2 than for the other gas molecules, increasing the selectivity of the material towards CO_2 separation. Additionally, the Na^+ cations preferentially occupy the hexagonal rings that connect the sodalite cage with the main pores. In this structure the diffusion of gas molecules inside the sodalite cages is blocked by the presence of Na^+ cations, so gas molecules are unable to enter inside the sodalite cages.

From DFT calculations one can conclude that both N_2 and O_2 have very similar behavior when adsorbing into a Faujasite structure, either with or without extra-framework Na^+ cations. Also, their interaction energies are very similar when adsorbing on both the Faujasite wall and in a Na^+ cation. On the other hand, CO_2 exhibits higher interaction energies than O_2 and N_2 in both sites.

However, the adsorption of CO_2 is highly favored by the presence of extra-framework cations increasing the selectivity of the material to capture this gas.

3.2.2 CO_2 Separation in Faujasites from GCMC Simulations (Pure Compounds)

The DTF study of Faujasites is useful to get information such as the affinity of a surface for a gas or the energy needed to diffuse onto different regions of the microporous structure. However, other macroscopic or collective properties, such as the adsorption isotherms as a function of pressure, are not affordable solely by DFT calculations. For this reason, a second stage of the study involved Grand Canonical Monte Carlo (GCMC) simulations to predict adsorption isotherms of gases within Faujasite structures by means of LAMMPS code.[59] To prevent finite size effects, the simulation cell was increased from the rhombohedral DFT model with 48 tetrahedral units to a conventional squared box with cell parameters $a = b = c$ =24.26 Å, angles $\alpha = \beta = \gamma = 90^{o}$ and 192 tetrahedrons (Figure 3.7). Finally, as the GCMC algorithm can insert molecules in random positions of the simulation cell based only on energy criteria, dummy atoms with a short-range repulsive potential have been inserted in the center of the sodalite cages to prevent them becoming occupied. This technique allows to simulate adequately the inability of gas molecules to diffuse into the sodalite cages.

The effect of Na^+ as an extra-framework cation is evaluated modeling a set of structures with different Si/Al ratio, from the totally silicated up to the maximum possible ratio of Si/Al = 1. These

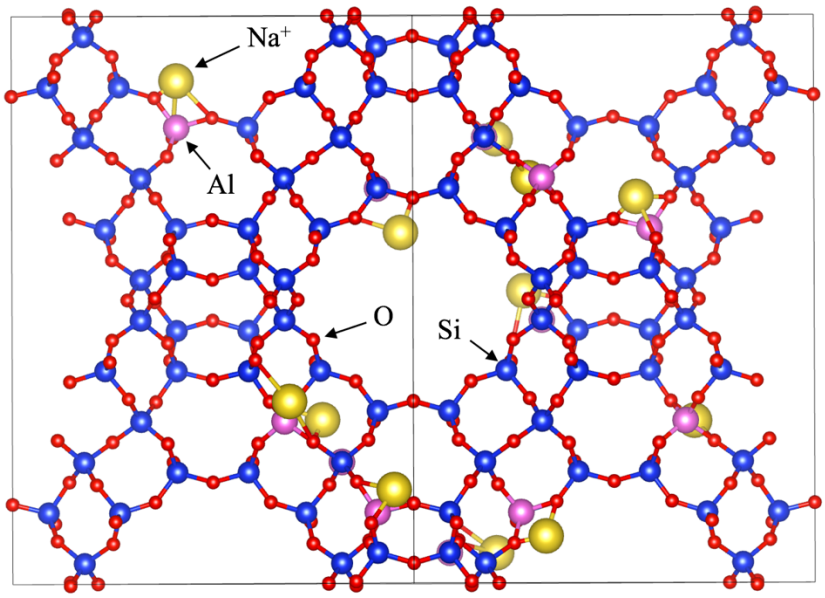

Figure 3.7. Conventional unit cell of Faujasite with some extra-framework Na^+ cations.

structures were built exchanging random Si atoms in the framework per Al with the restriction of the Löwenstein's rule. Na^+ cations were added close to the Al atoms and relaxed through a NVT MC simulation. In this situation, the MC relaxation is preferable to MD because it samples the phase space without following the Newton's equations of motion. This feature allows Na^+ cations to change their position from one minimum to another in relatively low amount of time steps, helping them to abandon local stationary points and find the absolute minimum of the PES.

The previously defined systems are too large to perform molecular simulations with DFT, so atomistic force fields based on a LJ + Coulomb potential are used instead. The Faujasite structure has been modeled using the parameter set of Calero *et al.,*[60,61] which is a transferable force field fitted to reproduce CO_2 adsorption in Zeolites (Table 3.2). In this force field the structure of the Zeolite is considered to be rigid and its intramolecular interactions are neglected. For this reason,

Table 3.2. Force field parameters used in this study to reproduce gas-gas and gas-Faujasite interactions obtained from Calero *et al.*[60–62] The X in N_2 and O_2 parameters corresponds to the dummy atom located in the center of the bond.

Species	Atom	ε/k_B / K	σ / Å	q / e$^-$	Bond length / Å
CO_2	C	29.933	2.745	0.652	1.149 (C-O)
	O	85.671	3.017	-0.326	
N_2	N	38.298	3.306	-0.405	0.55 (N-X)
	X	-	-	0.810	
O_2	O	53.023	3.045	-0.112	0.60 (O-X)
	X	-	-	0.224	
Faujasite	Si	-	-	0.786	
	Al	-	-	0.486	
	O_{Zeo} [Si-O-Si]	-	-	-0.393	
	O_{Zeo} [Si-O-Al]	-	-	-0.414	
	Na^+	-	-	+0.384	

	O_{Zeo} – Y pair interactions		Na^+ – Y pair interactions	
Y	ε/k_B / K	σ / Å	ε/k_B / K	σ / Å
C (CO_2)	37.595	3.511	362.292	3.320
O (CO_2)	78.980	3.237	200.831	2.758
N (N_2)	60.580	3.261	225.568	2.766
O (O_2)	65.189	3.129	241.284	2.060
Na^+	23.000	3.400	-	-

there are no atom-wise parameters for the Si, Al, O and Na^+ species of the Faujasite and only pair-wise parameters and partial charges are given.

The parameters for other gas molecules, such as O_2 and N_2 are taken from other works of Calero *et al.*,[62] who also developed compatible force fields to simulate adsorption of these species in Zeolitic materials. It is worth noticing that the force field accounts for the quadrupole moment of diatomic gas molecules adding a dummy atom (X) in the center of the bond that carries a positive partial charge. The three gas molecules are modeled as rigid bodies that can be translated, rotated or exchanged in the GCMC scheme. Additionally, Na^+ cations are allowed to move during the simulation performing a single MC translation after each MC step on a gas molecule. The simulations were evolved for at least 10^7 MC steps to obtain a large amount of production steps in order to average the gas uptake in the Faujasite for each gas and pressure condition.

To validate the force field, pure CO_2, N_2 and O_2 adsorption isotherms were calculated in two of the most common Faujasite structures, where experimental data were available (Figure 3.8). The first structure is the totally silicated structure (*i.e.,* also known as DAY), where Maurin *et al.*[63] reported experimental adsorption isotherms for CO_2 at 300 K. The second is the so-called NaX (*i.e.,* a Faujasite with Si/Al = 1.18), in which experimental adsorption isotherms from Dunne *et al.*,[64] are available for CO_2 at 306 K. In both structures, the force field is capable to reproduce accurately the uptake of CO_2 at different pressures. Additionally, the force field was able to yield the gas adsorption isotherms for both N_2 and O_2 in good agreement with the experimental data at 313 K.[65]

After the validation of the force fields, pure adsorption isotherms have been calculated at a temperature of 313 K and pressures up to 50 atm (Figure 3.9). These values have been selected to mimic the common pressure and temperature conditions of a separation process in a post-

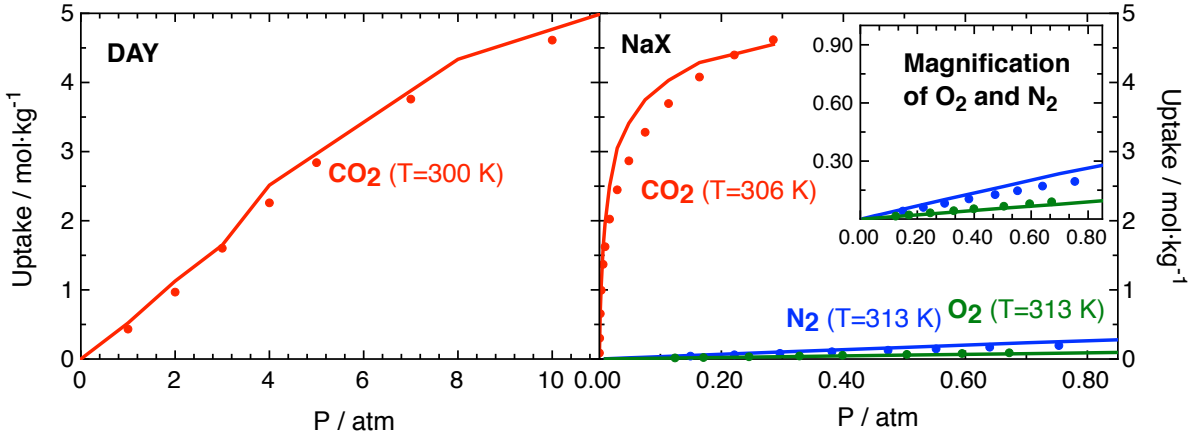

Figure 3.8. Pure gas adsorption isotherm validation in two of the most common Faujasites, the totally silicated structure (DAY) and the structure with Si/Al = 1.18 (NaX). GCMC simulations are shown in lines, while experimental data is depicted in dots.

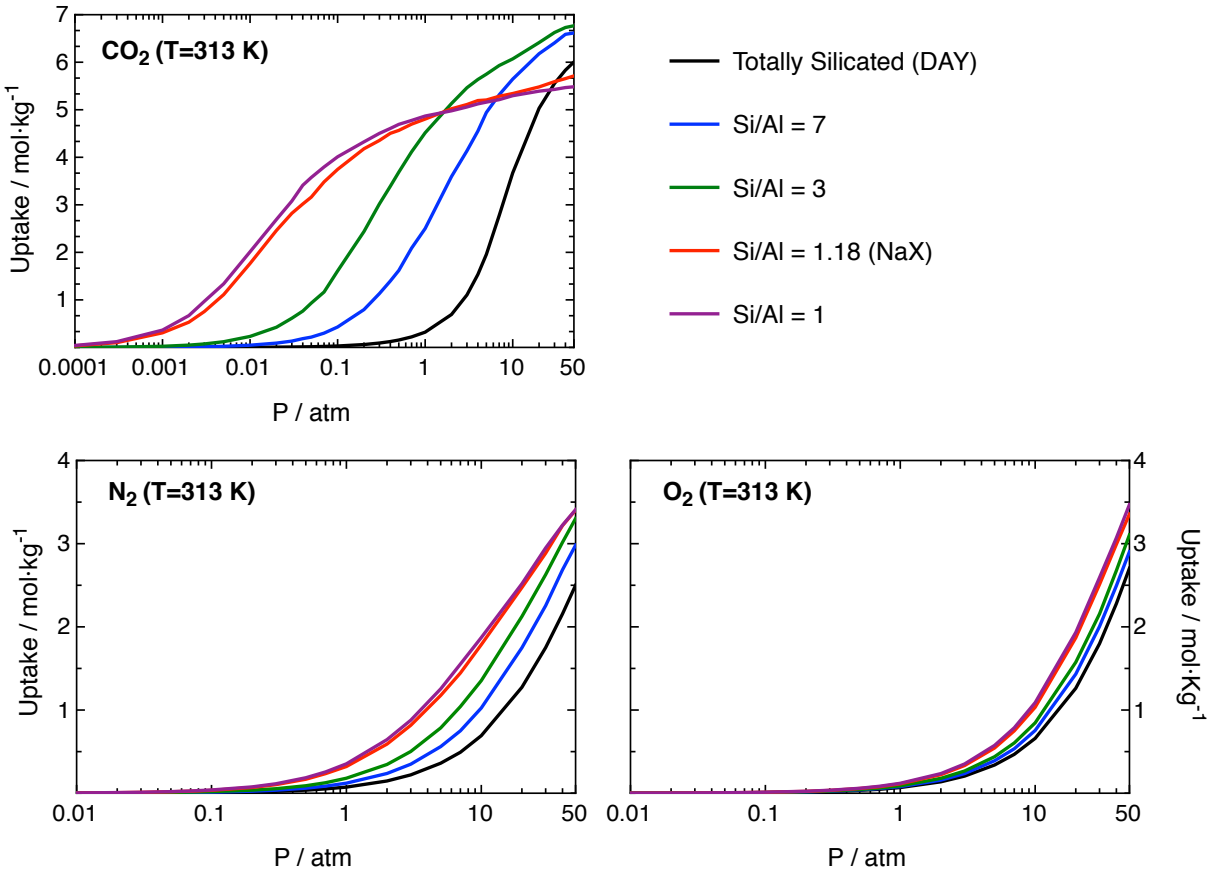

Figure 3.9. Pure CO_2, N_2 and O_2 adsorption isotherms in Faujasite structures with different Si/Al ratio.

combustion flue gas. In the results shown in Figure 3.9 one can see that Faujasites have the highest affinity for CO_2, presenting the larger adsorption uptakes in contrast to N_2 or O_2 for any Si/Al ratio. It can also be seen that both N_2 and O_2 have a relatively similar behavior when adsorbing into Faujasites and none of them exhibits a significantly large adsorption uptake at pressures lower than 10 atm. As previously concluded with DFT calculations, the presence of extra-framework cations enhances the adsorption of all gas molecules, but the effect is more noticeable with CO_2. Otherwise, GCMC simulations also show that Na^+ cations behave as a double-edged sword: on one side, they increase the affinity of the material to capture CO_2, but on the other, they occupy some volume in the framework reducing the total available pore volume. This effect is reflected in the calculated adsorption isotherms, where Faujasites with more extra-framework cations (*i.e.,* low Si/Al ratio) exhibit lower maximum CO_2 uptakes at high pressures.

The zero-coverage isosteric heats of adsorption for CO_2 in all Faujasite structures have been calculated from the energy/particle fluctuations in the grand canonical ensemble (eq. 3.5). This magnitude gives information about the affinity of an adsorbate towards a substrate. From the information compiled in Figure 3.10 one can see that the DFT adsorption energy in the main

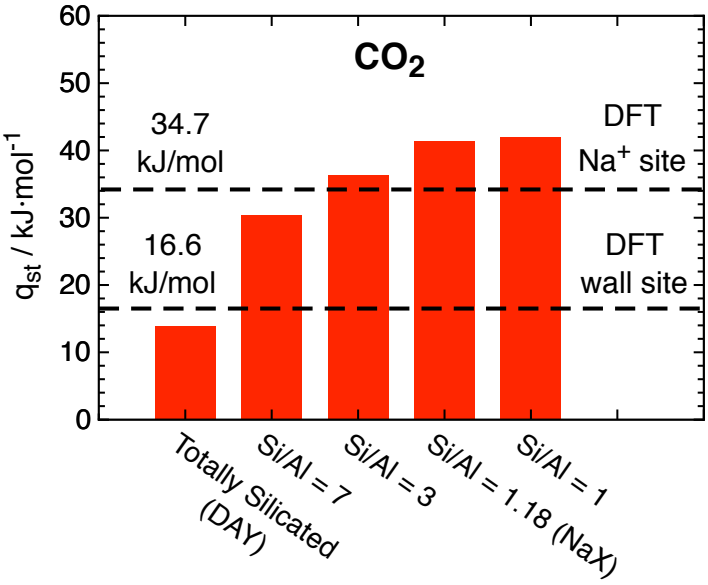

Figure 3.10. Zero-coverage isosteric heats of adsorption for pure CO_2 as a function of the Si/Al ratio at 313 K. DFT interaction energies in the walls of the main channels, obtained from DAY, and the Na^+ sites, calculated from the Si/Al = 15 structure, are included in dashed lines for the sake of comparison.

channel wall is comparable to the zero-coverage q_{st} of DAY. However, as more extra-framework cations are present in the material, the zero-coverage isosteric heat of adsorption increases up to a value comparable to the Na^+ site interaction energy. This result is another proof that Na^+ becomes a new adsorption site for CO_2, where it can adsorb with enhanced affinity.

With the currently analyzed results it seems that a higher amount of Na^+ cations is beneficial for CO_2 capture and separation. However, to economically optimize CO_2 recovery, it is important to select the Si/Al ratio of the Faujasite that can recover the maximum amount of gas per adsorption/desorption cycle at the desired working conditions. This magnitude can be obtained by the working capacity (eq. 3.3). A reasonable set of pressures for an adsorption/desorption cycle in a pressure swing adsorption (PSA) process are: adsorption at 10 atm and desorption at 1 atm. Under these conditions DAY is capable of recovering a total of 3.35 mol of CO_2 per kg and cycle (Table 3.3). On the other hand, the structure with Si/Al = 7 has a higher uptake at both adsorption and desorption conditions, yielding a similar working capacity than the totally silicated Faujasite (*i.e.,* 3.14 mol of CO_2 per kg and cycle). The other structures with increased Al content (*i.e.,* Si/Al = 3, Si/Al = 1.18 and Si/Al = 1) have lower working capacities, and are able to recover only 1.55, 0.54 and 0.43 mol of CO_2 per kg and cycle, respectively. On the other hand, if a vacuum swing adsorption (VSA) process is used to capture and recover CO_2, the adsorption pressure becomes 1 atm, and the desorption is performed at 0.1 atm. Under these particular conditions, DAY becomes very inefficient to recover CO_2, presenting a working capacity of 0.29 mol of CO_2 per kg

Table 3.3. Pure CO_2 equilibrium adsorption uptakes predicted by GCMC in mol of $CO_2 \cdot kg^{-1}$ Faujasite. The working capacities of each structure assuming a PSA or a VSA process at 313 K is also shown in units of mol of $CO_2 \cdot kg^{-1}$ Faujasite recovered per cycle.

Structure	Uptake at 0.1 atm	Uptake at 1 atm	Uptake at 10 atm	PSA WC [10 atm/1 atm]	VSA WC [1 atm/0.1 atm]
DAY	0.03	0.32	3.67	3.35	0.29
Si/Al = 7	0.43	2.50	5.64	3.14	2.07
Si/Al = 3	1.61	4.52	6.07	1.55	2.91
Si/Al = 1.18 (NaX)	3.74	4.80	5.34	0.54	1.06
Si/Al = 1	4.01	4.87	5.30	0.43	0.86

and cycle. Also, high Al content Faujasites (*i.e.,* Si/Al = 1.18 and Si/Al = 1) have very high uptakes at the desorption conditions and are only capable of recovering 1.06 and 0.86 mol of CO_2 per kg and cycle, respectively. However, medium Al content structures are better suited for this process, as it can be seen by the CO_2 recovery accomplished by Si/Al = 7 and Si/Al = 3 (*i.e.,* 2.07 and 2.91 mol of CO_2 per kg and cycle, respectively). To conclude, unless the desorption conditions are carried out under vacuum up to 0.01-0.001 atm, the recovery of CO_2 with high Al content seems to be suboptimal.

3.2.3 CO_2 Separation in Faujasites from GCMC Simulations (Mixtures)

The conclusions achieved up to now are only based on pure adsorption isotherms, zero-coverage heats of adsorption or interaction energies. All of these magnitudes do not take into consideration the competition of different gas molecules towards the Faujasite sites. Fortunately, molecular simulations can help to evaluate the behavior of gas mixtures with the same effort that pure gases. A mixture containing a 15 % CO_2, 80 % N_2 and 5 % O_2 (*i.e.,* in % mol,mol) at 313 K has been employed to simulate the adsorption isotherms of a common post-combustion flue gas mixture. The results can be seen in Figure 3.11, where a comparison between mixture and pure gas isotherms along with the CO_2 selectivities with respect N_2 are displayed for all studied Faujasite structures. The CO_2 uptake in mixtures is significantly lower than in pure isotherms due to the relatively low CO_2 partial pressure in the flue gas compared to N_2. In fact, DAY adsorbs almost the same amount of CO_2 than N_2, which suggests that this structure is not selective enough to effectively separate the CO_2 from the flue gas. Additional extra-framework cations radically increase the selectivity of Faujasites towards CO_2, increasing their uptake and reducing the amount of N_2 adsorbed. The maximum selectivity is achieved for the Si/Al = 1 structure, which is two

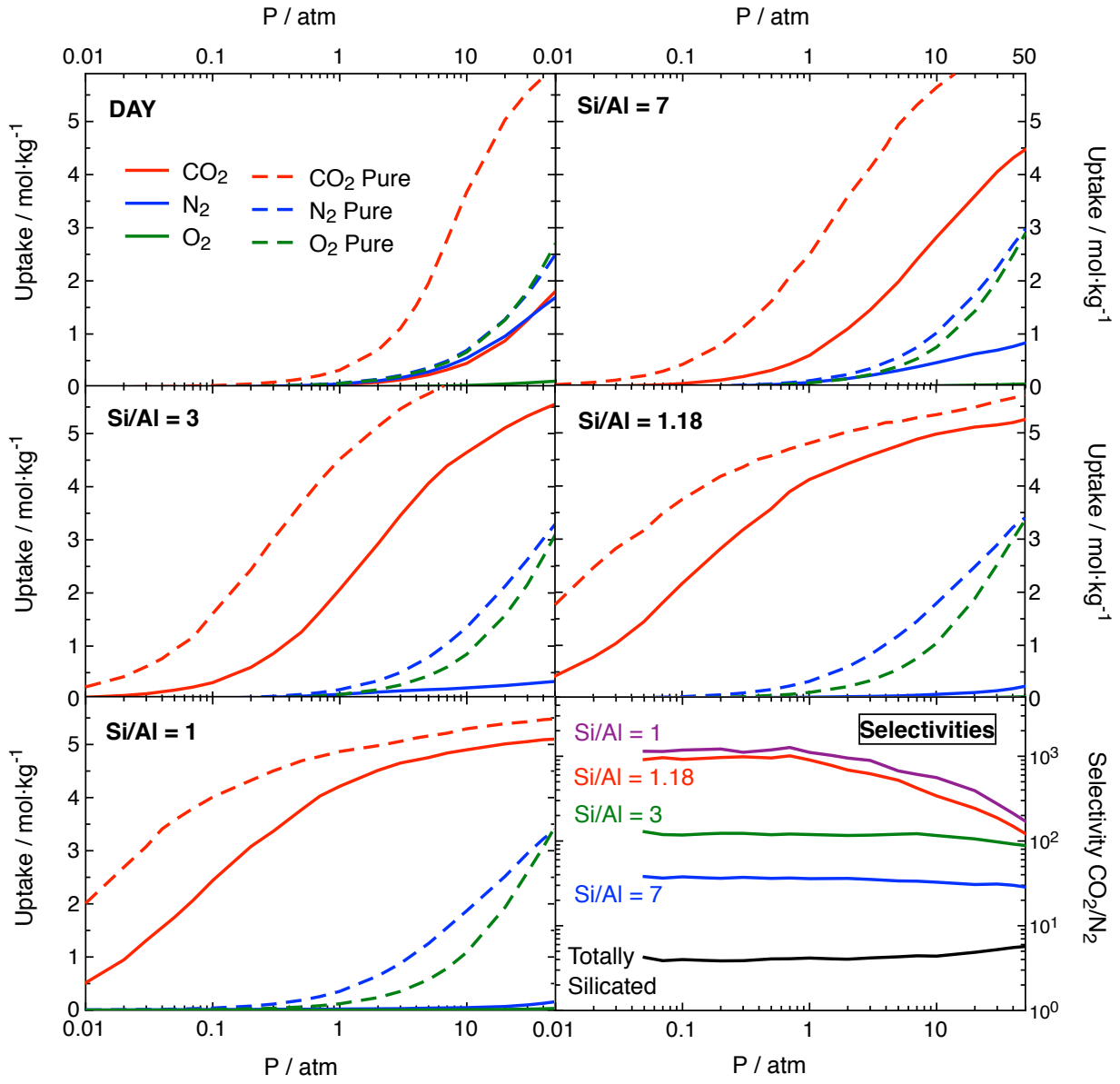

Figure 3.11. Ternary mixture adsorption isotherms at 313 K with 15 % CO_2, 80 % N_2 and 5 % O_2 (solid lines) compared to the pure adsorption isotherms (dashed lines) of each gas on all the studied Faujasite structures. The CO_2 selectivities with respect N_2 in all structures are also displayed as a function of the pressure.

orders of magnitude higher than the totally silicated structure. Notice that in all cases the adsorption of O_2 is negligible due to its low partial pressure and the lack of Faujasite affinity for this gas.

The CO_2 working capacity in a mixture flue gas cannot be directly calculated solely from the mixture adsorption isotherms (eq. 3.3), because at the desorption step the Faujasite is not in equilibrium with a gas with 15 % CO_2, 80 % N_2 and 5 % O_2. If the material is capable of selectively capturing CO_2, a good approximation for the working capacity of mixtures would be to use the pure CO_2 isotherm to obtain the uptake at the desorption step. This practice was already

implemented by other authors.[66–68] However, in some of the studied Faujasites the adsorbed gas is not pure enough to apply the previous approximation. To improve the method of calculating the working capacities, the pure CO_2 adsorption isotherm was used but rescaling the uptake at the desorption step by the CO_2 molar fraction at the adsorbed phase. This method yields the same working capacity as the pure isotherm method for cases where the selectivity of the material is very high, but it serves as an ideal approximation for situations with competing adsorbates.

The CO_2 working capacities in a mixture flue gas (Table 3.4) differ significantly of the previously calculated values for pure CO_2. In fact, in the studied mixtures, the amount of recoverable CO_2 is lesser than 0.8 mol CO_2/kg of Faujasite regardless the swing adsorption process used. According to mixture calculations, the most suitable structures for CO_2 recovery according to their working capacities are the Si/Al = 7 and Si/Al = 3 for PSA and VSA processes, respectively. Although this conclusion is equivalent to pure gas simulations, the study of mixtures also allows to obtain the CO_2 purity of the desorbed gas (*i.e.,* purity at the outlet). The CO_2 purity can be obtained by the relationship between the working capacity and the sum of the working capacities for all the other components. If PSA and VSA are compared (Table 3.4), one can see that the CO_2 purity obtained by the VSA process is significantly higher than with the PSA cycle. Additionally, high Al content favors a large purity at the outlet reaching values up to 64 % and 92 % for the widely used NaX (*i.e.,* Si/Al = 1.18) with PSA and VSA respectively. If both parameters (*i.e.,* the working capacity and the purity at the outlet) are considered, one can see that although NaX is the most suitable structure in terms of purity, the Si/Al = 7 and the Si/Al = 3 Faujasites offer higher working capacities at a cost of a small purity penalty. This fact makes these structures deserve more attention in industrial CO_2 capture and separation processes.

Table 3.4. CO_2 working capacities (*i.e.,* in mol of $CO_2 \cdot kg^{-1}$ Faujasite) and CO_2 purity at the outlet (*i.e.,* in %) for a PSA and a VSA cycles predicted by GCMC simulations at 313 K.

Structure	PSA WC [10 atm/1 atm]	PSA Purity [10 atm/1 atm]	VSA WC [1 atm/0.1 atm]	VSA Purity [1 atm/0.1 atm]
DAY	0.33	33 %	0.035	33 %
Si/Al = 7	0.71	56 %	0.23	69 %
Si/Al = 3	0.36	57 %	0.54	83 %
Si/Al = 1.18 (NaX)	0.22	64 %	0.40	92 %
Si/Al = 1	0.07	56 %	0.22	87 %

3.2.4 Summary and Conclusions

In this section, the adsorption in different Faujasite structures of CO_2, N_2 and O_2 was assessed. Two different computational methods (*i.e.,* DFT and GCMC) were used to determine the adsorption properties of Faujasites at a molecular level. The results obtained from DFT were used to evaluate the affinity of the surface towards all gas molecules as well as characterizing the different adsorption sites. Also, the pore-sodalite diffusion barriers obtained suggest that gas molecules cannot enter the sodalite cages unless very high pressures are used. For this reason, sodalite cages were blocked in the GCMC simulations to limit de gas adsorption to the main pores. GCMC results are in good agreement with DFT, showing lower isosteric heats of adsorption in low Al content structures. In that materials, gas molecules can only adsorb on the pore walls, whereas in high Al content structures, gas molecules can adsorb onto the preferential extra-framework cation sites, also presenting higher q_{st} values

It was seen that the Si/Al ratio has a strong influence in the adsorption properties because the extra-framework cations add additional adsorption sites with high CO_2 preference at a cost of some available adsorption volume within the Faujasite. A lower Si/Al ratio (*i.e.,* more extra-framework cations) increases the selectivity of the framework towards CO_2 capture, also increasing the purity at the outlet. However, it can reduce the total working capacity because it prevents CO_2 desorption in the recovery step. The combination of working capacities and purities modeled in a ternary mixture containing a typical post-combustion composition (*i.e.,* 15 % CO_2, 80 % N_2 and 5 % O_2) suggests that the most efficient studied structures for CO_2 capture could be the Si/Al = 7 for PSA and the Si/Al = 3 for VSA. Both of these structures have a slightly lower purity than the widely used NaX, but the higher CO_2 working capacities compensate this penalty and make them potentially better candidates for industrial CO_2 recovery.

3.3 CO_2 Separation in Mg-MOF-74

Metal-Organic Frameworks (MOFs) are an alternative set of microporous materials with some common features with Zeolites. Generally, MOFs tend to have larger pore volumes and surface area than Zeolites, which is translated into higher adsorption capacities.[69] However, their molecular nature reduces their mechanical and chemical stabilities.[70] On the other hand, MOFs have a highly functionalizable structure, which opens the possibility of tuning these materials for a specific application.[71] In that sense, computational studies on these kinds of systems become remarkably useful in material screening for specific applications.

MOFs are structures of metal cations coordinated to organic linkers, where each linker is interacting with no less than two cations creating a three-dimensional net of L-M-L-M-L (*i.e.,* where L and M correspond to linker and metal cation, respectively). The shape and size of the generated pores highly depends on the coordination number of the metal cation and the nature of the organic linkers.[72,73] In general, stable MOF structures have highly coordinated metal cations, which facilitates the repair of structural defects and prevents decomposition. However, cations with low coordination numbers generate more opened structures, with larger pores and an overall higher activity. Similarly, short and rigid linkers confer to the framework high stability, whereas longer linkers offer higher porosities. Finally, notice that the bond between the metal cations and the linkers is a coordination bond, which means that if other external chemical species with high affinity for the metal were present, they could potentially be exchanged by the linkers. This exchange would produce several defects in the solid structure ultimately collapsing the material. For this reason, very polar molecules such as H_2O are capable of decomposing several MOFs and they should be removed from the flue gas before CO_2 capture.[74] To minimize this effect, it is imperative that the interaction energies between the cations and the linkers are strong enough to prevent linker exchange.[75] To conclude, the selection of an adequate MOF structure for a determined application is constrained to cation-linker pairs with strong coordination bonds and the tradeoff between activity and stability.

The main feature that confers high CO_2 capture capability to MOFs are their metal cations. Due to their natural porous structure metal cations are relatively unprotected and can interact with gas molecules flowing through the structure pores. Analogously to Zeolites, cations can interact strongly with polar species favoring the separation of gases by a coordinative adsorption onto the metal sites.[76–78] In fact, some MOFs have shown higher adsorption uptakes and working capacities for CO_2 than some Zeolites, such as the widely used NaX.[79,80] However, the metal sites in MOFs have also very high affinities for other contaminant species found in post-combustion flue gas mixtures (*e.g.,* SO_2 or NO_x among others). To explore the impact of contaminants onto the CO_2 capture and separation with MOFs, the adsorption properties of CO_2, N_2 and SO_2 have been studied in the well-known Mg-MOF-74. The O_2 molecule has not been considered because it had a similar behavior to N_2, so the % of O_2 is just treated as N_2.

Mg-MOF-74 (*i.e.,* also known as CPO-27-Mg or Mg_2(DOBDC)) is one of the most interesting MOFs for CO_2 capture, having one of the best adsorption performances and with equilibrium uptakes higher than 8.0 $mol \cdot kg^{-1}$ of MOF at 298 K and 1 atm.[81] The structure of Mg-MOF-74 is based on Mg^{2+} cations octahedrically coordinated to 2,5-dioxido-1,4-benzene-dicarboxilate linkers ($DOBDC^{4-}$) forming large one dimensional hexagonal pores (Figure 3.12).[82]

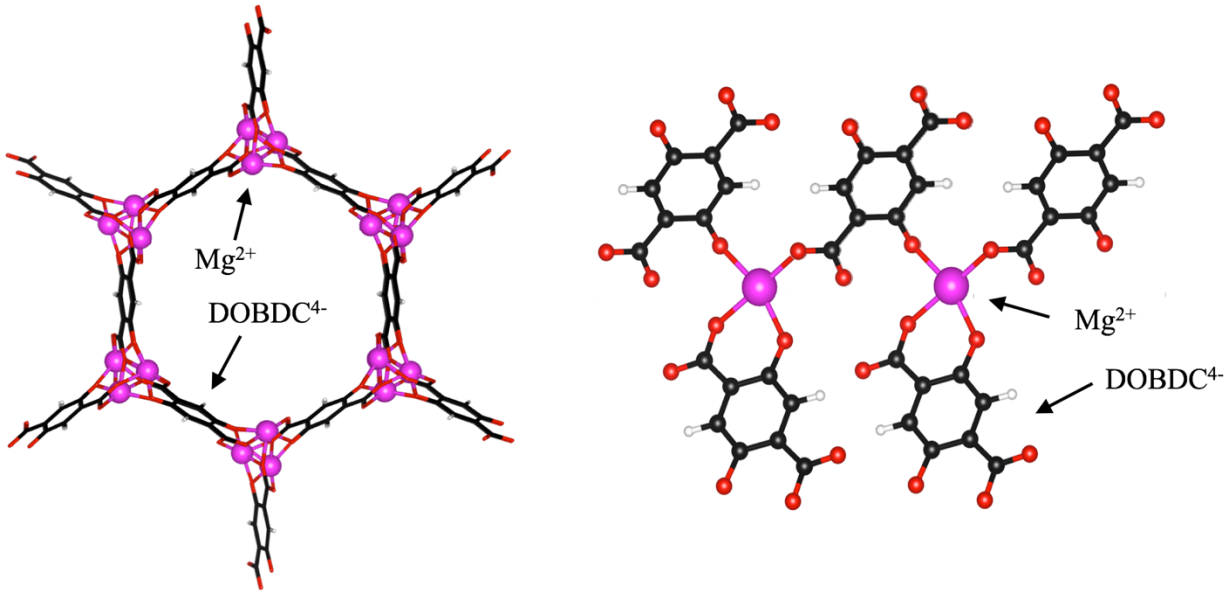

Figure 3.12. Mg-MOF-74 atomic structure shown in the direction of the pores along with a representation of the Mg^{2+} cations coordinated to some of the $DOBDC^{4-}$ linkers.

3.3.1 DFT Adsorption of CO_2, N_2 and SO_2 in Mg-MOF-74

The affinity of Mg-MOF-74 for different flue gas components (*i.e.,* CO_2, N_2 and SO_2) has been assessed through periodic DFT calculations performed with VASP.[53,54] The vdW-DF2 functional [83,84] has been used to evaluate the interaction energies between the three gas molecules and the MOF. This functional already includes the dispersion corrections in their exchange and correlation term, and was proven to be superior than the standard GGA+D2 functionals [55–57] when reproducing adsorption energies of gas molecules in Mg-MOF-74.[85] The plane wave basis has been expanded up to a cutoff energy of 600 eV and only the Γ-point was used to represent the reciprocal space due to the large size of the MOF primitive unit cell. The conventional unit cell used (Figure 3.13) is a rhombohedral box with cell parameters $a = b =$ 26.2 Å, $c =$ 13.8 Å and cell angles $\alpha = \beta = \gamma = 60^{\circ}$. This cell is large enough in all directions to prevent interactions of the adsorbed gas molecules with their periodic images. Finally, the unit cell has a total of 24 Mg^{2+} + 24 $DOBDC^{4-}$ linkers, and each pore contains 12 Mg^{2+} + 12 $DOBDC^{4-}$ linker sites.

Gas adsorption energies (eq. 3.7) in Mg-MOF-74 were obtained by minimizing the MOF structure at the vdW-DF2 level, and then absorbing the gas molecules onto different adsorption sites within the framework. All the framework atoms close to the adsorbed gas molecule (*i.e.,* less than 7 Å to any gas atom) have been relaxed to accurately locate the adsorption minima in the DFT

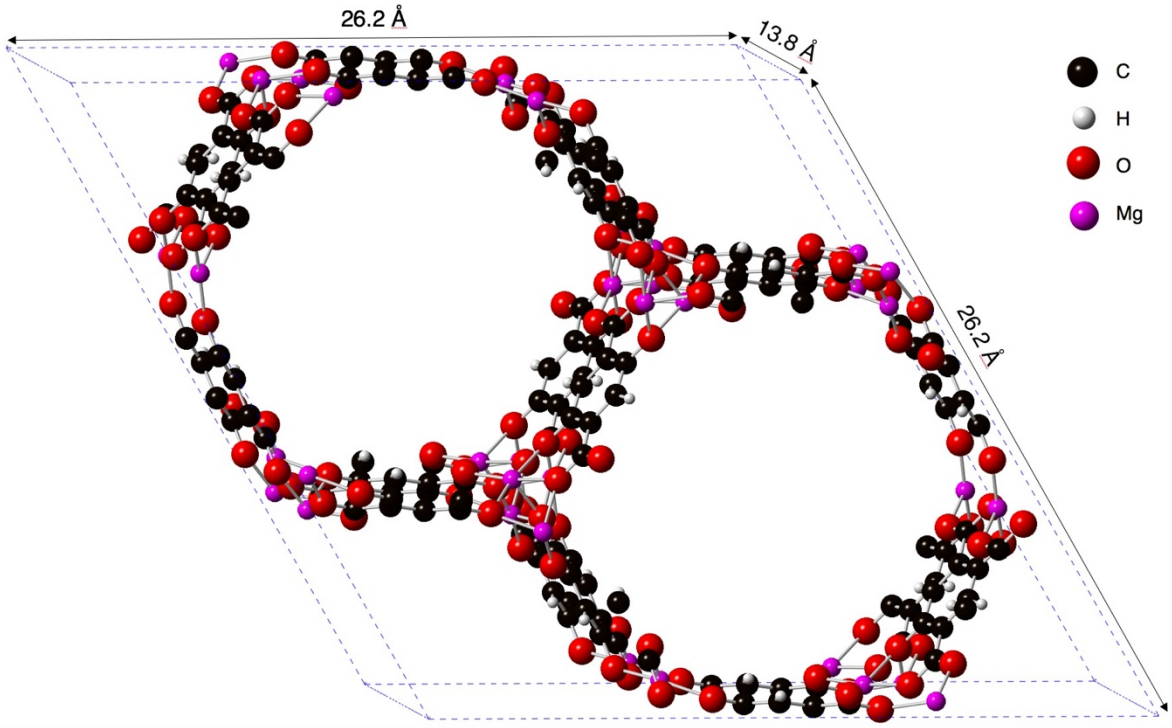

Figure 3.13. Conventional unit cell view from the (100) direction of the Mg-MOF-74 structure used for the DFT study.

energy minimization. All minima have been characterized through vibrational frequency calculations.

Two main adsorption sites have been found in Mg-MOF-74. For the three studied gas molecules, the Mg^{2+} cation is characterized as the main adsorption site, presenting interaction energies including zero-point energy (ZPE) of -46.1, -29.3 and -78.9 kJ·mol^{-1} for CO_2, N_2, and SO_2, respectively. These results are in good agreement with other theoretical data that propose interaction energies in the order of -41.0/-44.9 kJ·mol^{-1} for CO_2,[76–78,86] -28.0/-28.5 kJ· mol^{-1} for N_2 [76,77] and -62.0/-88.0 kJ· mol^{-1} for SO_2.[76,77,87] The interaction energies for all gas molecules in the metal site are larger than the adsorption energies in the extra-framework cations of Faujasite. This fact means that this structure should have higher CO_2 affinity than any Faujasite structure studied in the previous section. Additionally, the interaction energy of CO_2 is significantly higher than the adsorption energy of N_2, which implies that Mg-MOF-74 should also be highly selective towards CO_2 capture in a CO_2/N_2 mixture. These results also show that SO_2 has a much stronger binding to the metal site than CO_2, according to the poisonous nature of this contaminant species.[88]

A secondary adsorption site is located in the halfway between two metal cations. In these sites, gas molecules adsorb interacting with the π rings of the $DOBDC^{4-}$ linkers and can also weakly interact with three different Mg^{2+} cations: two of them are the closest Mg^{2+} main sites and the third is a Mg^{2+} cation slightly shielded by the linkers. However, the closest moiety to the adsorbed gas

molecules are the $DOBDC^{4-}$ units, so this site will be referred as the linker site from now on. All of these adsorption sites are shown in Figure 3.14, where orange gas molecules represent CO_2 adsorbed onto the Mg^{2+} metal sites and blue molecules show CO_2 adsorbed in the linker sites. The linkers interact weaklier with gas molecules, presenting adsorption energies of -29.5 $kJ \cdot mol^{-1}$ for CO_2 and -36.6 $kJ \cdot mol^{-1}$ for SO_2. Surprisingly, no adsorption site was located in this region for N_2 probably due to the weaker interactions between this species and the MOF. The difference between adsorption energies between CO_2 and SO_2 in this site is significantly lower, showing that the poisoning capabilities of SO_2 should be carried out mainly in the metal sites.

According to the symmetry of the system, and confirmed by DFT calculations, there are 12 Mg^{2+} sites and 12 linker sites available per Mg-MOF-74 pore. This fact implies that a maximum of 24 molecules can be adsorbed simultaneously to form a monolayer of gas over the surface. Notice that, when molecules are adsorbed, the interactions with other gas molecules already attached to the framework can affect the adsorption properties due to gas-gas lateral interactions. For this reason, the effect of the coverage at the Mg^{2+} site has been analyzed by means of DFT. The coverage of the linker site has been neglected because the metal has a much stronger gas affinity, so it will become saturated before the secondary linker starts adsorbing molecules. In fact, other theoretical and experimental works revealed that molecules will mainly adsorb on Mg^{2+} sites

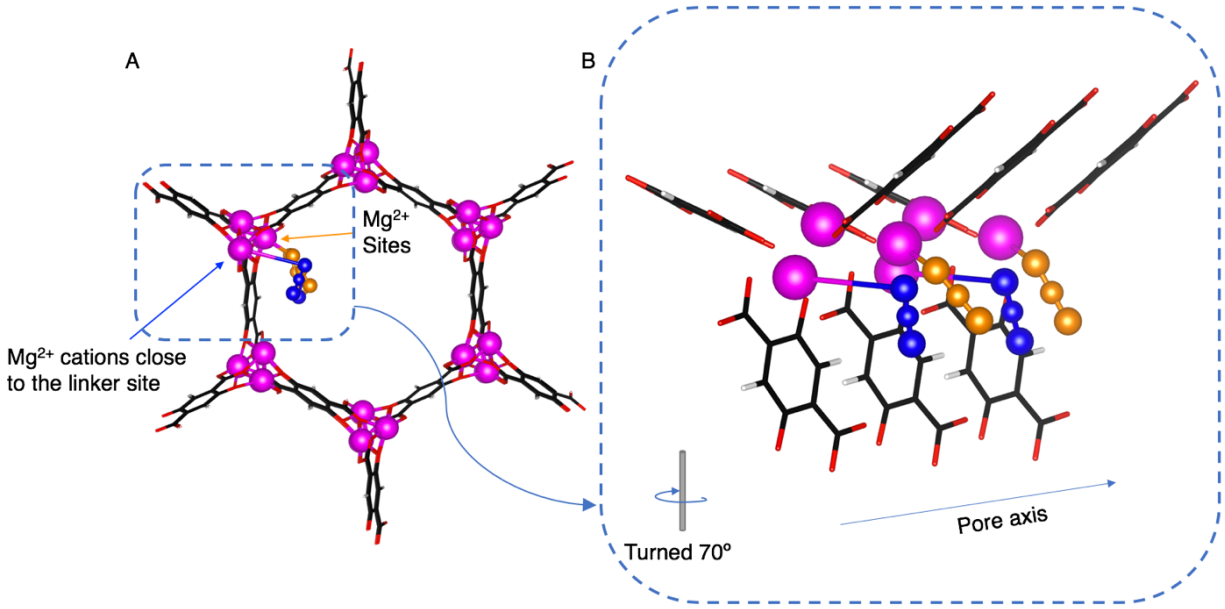

Figure 3.14. Representation of a Mg-MOF-74 pore with two orange CO_2 molecules adsorbed onto the main Mg^{2+} sites and two blue CO_2 molecules adsorbed onto the secondary linker sites. The third weakly interacting Mg^{2+} of the linker site is pointed out in the structure and bonded to the blue CO_2 molecules for clarity. A magnification of a segment of de cell is also displayed to better show the location of the adsorption minima.

until relatively large pressures,[81,89,90] so the Mg-MOF-74 adsorption properties are well described with this approximation.

The adsorption on the Mg^{2+} site at full Mg^{2+} coverage was calculated by adsorbing a gas molecule into a pore that already has 11 molecules adsorbed onto Mg^{2+} sites (eq. 3.8). The calculated adsorption energies, including ZPE, at these conditions are -45.6 kJ·mol^{-1} for CO_2, -30.5 kJ·mol^{-1} for N_2 and -83.8 kJ·mol^{-1} for SO_2. The CO_2/MOF and N_2/MOF interactions are weakly affected by the presence of other gases, but SO_2 adsorption is almost 4 kJ·mol^{-1} more stable due to its lateral interactions. On the other hand, the linker site interaction energies are calculated by adsorbing a gas molecule into a linker site in a framework with 12 gas molecules adsorbed onto the Mg^{2+} site (eq. 3.9). The results obtained are: -34.5 kJ·mol^{-1} for CO_2 and -55.1 kJ·mol^{-1} for SO_2. The interaction of CO_2 with the linker is strengthened by 5 kJ·mol^{-1} with respect to the zero-coverage values but the adsorption of SO_2 in enhanced by almost 20 kJ·mol^{-1}, showing a strong stabilizing effect due to lateral interactions induced by these species. It is noticeable that after full Mg^{2+} coverage the linker site for N_2 becomes a minimum with an interaction energy of -15 kJ·mol^{-1}. All of these results are compiled in Table 3.5. It is worth noticing that the affinity of the linker sites is significantly increased by the gas-gas lateral interactions, whereas the adsorption energies at the Mg^{2+} sites stay relatively unaffected. This difference is explained because the Mg^{2+}/linker site distance is approximately 3.7 Å, which is significantly smaller than the Mg^{2+}/Mg^{2+} site distance (*i.e.,* 7 Å).

$$\Delta E_i^{ads} = E_i^{12\ molec\ in\ Mg^{2+}/adsorbent} - E_i^{11\ molec\ in\ Mg^{2+}/adsorbent} - E_i^{molec} \quad 3.8$$

$$\Delta E_i^{ads} = E_i^{12\ molec\ in\ Mg^{2+};1\ molec\ in\ L/adsorbent} - E_i^{12\ molec\ in\ Mg^{2+}/adsorbent} - E_i^{molec} \quad 3.9$$

In summary, according to the obtained results at zero-coverage, SO_2 should selectively adsorb into the Mg^{2+} sites, preventing CO_2 and N_2 adsorption. In absence of SO_2 the preferential

Table 3.5. Gas/MOF adsorption energies calculated from DFT. The results at full-coverage are shown in parentheses below the data at zero-coverage.

	CO_2		N_2		SO_2	
	Mg^{2+}	Linker	Mg^{2+}	Linker	Mg^{2+}	Linker
ΔE_i^{ads} / kJ·mol^{-1}	-47.9 (-47.0)	-30.4 (-35.1)	-32.2 (-33.4)	N/A (-16.4)	-81.5 (-86.4)	-38.6 (-57.0)
ΔE_i^{ads} / kJ·mol^{-1} (with ZPE)	-46.1 (-45.6)	-29.5 (-34.5)	-29.3 (-30.5)	N/A (-15.0)	-78.9 (-83.8)	-36.6 (-55.1)

adsorption should be for CO_2 because it has a significantly larger adsorption energy than N_2. On the other hand, the linker sites should be disputed between CO_2 and SO_2 with a slight preference for the latter. However, if the gas-gas lateral interactions (*i.e.,* the effect of coverage) are included, the adsorption of SO_2 becomes highly enhanced, overcoming the CO_2 adsorption even at the linker sites. This result implies that all sites on this structure have a very high potential of being poisoned by SO_2.

3.3.2 CO_2 Separation in Mg-MOF-74 from DFT Calculations Enhanced with a Langmuir model (Pure Compounds)

A complete study of Mg-MOF-74 includes the prediction of adsorption isotherms and other derived properties, such as the selectivity and the isosteric heats. As it was stated in the Faujasite section, such magnitudes cannot be obtained solely from DFT calculations. In these cases, GCMC simulations can be applied to obtain the adsorption of different gas mixtures at different conditions of pressure and temperature. However, GCMC simulations on extended systems such as Faujasites or MOFs require a specific force field, fitted ideally to reproduce experimental data. Unfortunately, the experimental information of SO_2 adsorption on Mg-MOF-74 is scarce and cannot be used effectively to develop a force field capable of reproducing SO_2/MOF interactions. For this reason, an alternative approach based on the combination of DFT calculations with a mean field Langmuir model is used to predict adsorption properties. The main advantage of the DFT/Langmuir model is that it can be used to calculate adsorption isotherms from DFT results, which does not need any specific fitting, making it an entirely predictive technique.

The DFT/Langmuir model was recently applied by Sillar *et al.,*[91] to study the adsorption of pure CO_2 in Mg-MOF-74. In their work, a complex procedure to calculate the lateral interactions is employed, based on a combination of periodic DFT and highly accurate cluster models. The work here developed, uses the basis of the model of Sillar *et al.,*[91] but simplifying the calculation of lateral interactions to study the adsorption of pure CO_2, N_2 and SO_2, as well as their mixtures.

The main idea of the DFT/Langmuir model to obtain the adsorption isotherm of a pure gas (i) on Mg-MOF-74 by solving the Langmuir isotherm equation (eq. 3.10). This expression relates the coverage of a gas species (θ_i) over a solid surface as a function of the pressure (P) at constant temperature. Here, the Langmuir equilibrium constant (K_i) is proportional to the strength of the gas/MOF interactions and depends exponentially on the Gibbs free adsorption energy (ΔG_i^{ads}), as it can be seen in eq. 3.11. In summary, the prediction of adsorption isotherms within the DFT/Langmuir scheme is carried out through the following three steps: (i) calculate the Gibbs free

energy of adsorption in a material, (ii) obtain the equilibrium constant through eq. 3.11 for a determined temperature (*i.e.,* where P_0 corresponds to the standard pressure of 1 atm) and finally, (iii) apply eq. 3.10 to calculate the θ_i vs P isotherm.

$$\theta_i = \frac{K_i P}{1 + K_i P} \tag{3.10}$$

$$K_i = \frac{1}{P_0} e^{-\Delta G_i^{ads}/RT} \tag{3.11}$$

However, Langmuir made three assumptions in the derivation of the isotherm that makes eq. 3.10 to fail for non-ideal surfaces.[92] First, it considered that all adsorption sites within a surface are equivalent; second, it neglected the lateral interactions between adsorbed gas molecules; and third, it assumed that each site can only hold a single gas molecule. The first and second assumptions do not apply to Mg-MOF-74 because it has two different adsorption sites,[81] and lateral interactions have a noticeable effect in the adsorption energies, especially on the linker site. On the other hand, the third statement holds for low pressures, where multilayers are still not formed, as suggested by previous experimental and theoretical studies on MOFs.[89,93,94] To improve the capability of the Langmuir isotherm in describing real systems, two modifications have been performed into eq. 3.10. First, two adsorption sites are accounted by using a dual-site Langmuir (DSL) isotherm model (eq. 3.12), where the adsorption at each site is described by a single Langmuir isotherm with its own equilibrium constant.[95] Then, the total coverage can be obtained by the sum of the individual site coverages scaled by the site distribution (*i.e.,* $\chi_S = N_s/N_{tot}$, with S = M or L for the Mg^{2+} and the linker sites, respectively). It was already stated that Mg-MOF-74 has a total of 12 Mg^{2+} and 12 linker sites per pore, so the site distribution is $\chi_M = \chi_L = 0.5$. Finally, the effect of the coverage has been considered by making the Langmuir equilibrium constants to depend on the coverage. In practice, this is done through the calculation of the coverage dependent Gibbs free energies of adsorption at each site (*i.e.,* the $\Delta G_{i,S}^{ads}$ with lateral interactions).[95] The two modifications described are the basis of the DFT/dual-site Langmuir (DFT/DSL) model, and make eq. 3.10 and eq. 3.11 to become eq. 3.12 and eq. 3.13, respectively.

$$\theta_i = \chi_M \frac{K_{i,M}(\theta_i)P}{1 + K_{i,M}(\theta_i)P} + \chi_L \frac{K_{i,L}(\theta_i)P}{1 + K_{i,L}(\theta_i)P} \tag{3.12}$$

$$K_{i,S}(\theta_i) = \frac{1}{P_0} e^{-\Delta G_{i,S}^{ads}(\theta_i)/RT} \quad 3.13$$

The underscore S in eq. 3.13 refers to the site where a gas molecule i is adsorbed (*i.e.,* either S = M or L for Mg^{2+} or linker). Analogously to the previous section, the effect of the linker coverage can be neglected at the pressures considered in this work, as suggested by the results of previous theoretical an experimental works.[81,89,90] Within this approximation, the values of $\Delta G_{i,S}^{ads}(\theta_i)$ in our model depend only on the temperature, the nature of the adsorption site (*i.e.,* Mg^{2+} or linker) and the coverage of Mg^{2+} sites. To evaluate the coverage dependence in $\Delta G_{i,S}^{ads}(\theta_i)$, a mean-field approximation is used,[96,97] which effectively assumes that the Gibbs free energy of adsorption changes linearly with the surface coverage. This approximation is expressed in eq. 3.14, where the value of $\Delta G_{i,S}^{ads}(\theta_i)$ changes linearly from the zero-coverage value (*i.e.,* at $\theta_i \approx 0$) to the full Mg^{2+} coverage value (*i.e.,* at $\theta_{i,M} = 1$). In eq. 3.14, the $\Delta\left(\Delta G_{i,S}^{ads}\right)$ term corresponds to the difference between the adsorption Gibbs free energy at Mg^{2+} full-coverage and zero-coverage. Recall that the calculation of $\Delta G_{i,S}^{ads}$ can be carried out from DFT calculations coupled to statistical thermodynamics as already detailed in Section 2.1.4.

$$\Delta G_{i,S}^{ads}(\theta_i) = \Delta G_{i,S}^{ads}(\theta_i \approx 0) + \theta_{i,M}\, \Delta\left(\Delta G_{i,S}^{ads}\right) \quad 3.14$$

Different thermodynamic magnitudes (*i.e.,* $\Delta U_{i,S}^{ads}$, $\Delta H_{i,S}^{ads}$, $T\Delta S_{i,S}^{ads}$ and $\Delta G_{i,S}^{ads}$), along with the equilibrium Langmuir constants, have been calculated for the three studied gas molecules in the previously characterized DFT adsorption minima at 298 K (Table 3.6). The obtained results show that the adsorption of both CO_2 and SO_2 on the Mg^{2+} sites of Mg-MOF-74 are spontaneous processes, whereas the adsorption of N_2 is not. Also, the adsorption at the linkers has a positive or a very small $\Delta G_{i,S}^{ads}$ for all gases, which become more negative at high coverages due to gas-gas lateral interactions.

The pure gas adsorption isotherms have been predicted with the DFT/DSL model up to a pressure of 1 atm by solving iteratively the equations eq. 3.12, eq. 3.13 and eq. 3.14 for each pressure at 298 K. It is worth noting that DFT/DFL model gives an upper bound of the total gas adsorption on Mg-MOF-74 due to the perfect crystal assumption. In experiments, some Mg^{2+} sites might be poisoned or blocked during the synthesis of Mg-MOF-74, which can result in a lower experimental adsorption uptake with respect to that of the perfect crystal. Additionally, defects on

Table 3.6. Gas/MOF thermodynamic adsorption functions (*i.e,* $\Delta U_{i,S}^{ads}$, $\Delta H_{i,S}^{ads}$, $T\Delta S_{i,S}^{ads}$ and $\Delta G_{i,S}^{ads}$) and Langmuir equilibrium constants ($K_{i,S}$) calculated at 298 K. The results at full-coverage are shown in parentheses below the data at zero-coverage.

	CO_2		N_2		SO_2	
	Mg^{2+}	Linker	Mg^{2+}	Linker	Mg^{2+}	Linker
$\Delta U_{i,S}^{ads}$ / kJ·mol^{-1}	-42.2 (-41.4)	-24.9 (-29.6)	-25.6 (-26.8)	N/A (-10.2)	-75.0 (-80.0)	-31.7 (-50.3)
$\Delta H_{i,S}^{ads}$ / kJ·mol^{-1}	-44.7 (-43.9)	-27.4 (-32.1)	-28.1 (-29.3)	N/A (-12.7)	-77.5 (-82.5)	-34.2 (-52.8)
$T\Delta S_{i,S}^{ads}$ / J·mol^{-1}	-37.4 (-33.2)	-33.7 (-34.3)	-32.2 (-31.2)	N/A (-24.6)	-52.1 (-54.0)	-51.3 (-51.3)
$\Delta G_{i,S}^{ads}$ / kJ·mol^{-1}	-7.3 (-10.7)	6.3 (2.2)	4.1 (1.9)	N/A (11.9)	-25.6 (-28.5)	17.1 (-1.5)
$K_{i,S}$ / atm^{-1}	19.3 (75.6)	0.08 (0.4)	0.2 (0.5)	0.0 (0.008)	30493.5 (97757.8)	0.001 (1.8)

the framework could also affect the site distribution, reducing the adsorption capacity of the MOF as noted by other authors.[91,98,99] Specifically, Wu *et al.,*[100] have proven that different gas adsorption uptakes can be obtained with different MOF synthetic procedures. For this reason, the adsorption isotherms obtained by this method correspond to the "perfect crystal", so they need to be rescaled by a constant factor to account for the possible lack of experimental site availability. The factor was obtained scaling the DFT/DSL CO_2 isotherms to match the experimental uptake value of 8.24 mol·kg^{-1} from Dietzel *et al.,*[101] and Mason *et al.,*[81] which are both in good agreement among each other (data set 1). The majority of the reported experimental isotherms are in good agreement with data set 1, so the obtained scaling factor of 81 % is used in this work for all gases in Mg-MOF-74. Other experimental information relative to CO_2 and N_2 adsorption is available from the works of Wu *et al.,*[100] (data set 2) and Queen *et al.,*[89] (data set 3). The scaling factors on these data sets were also obtained to compare their experimental availabilities with the results of data set 1. From the data of Wu *et al.,*[100] (data set 2) an experimental availability of a 93 % was obtained, whereas the data of Queen *et al.,*[89] (data set 3) exhibits an availability of 86.5 %. To conclude, it seems that experimental results can have variations around a 10 % of the total uptake depending on how the MOF was synthesized.

The predicted "perfect crystal" and "81 % availability" adsorption isotherms at 298 K for CO_2, N_2 and SO_2 are shown from Figure 3.15a to Figure 3.15c comparing them with the experimental data sets 1 and 2. The "perfect crystal" model overestimates the total gas uptake for all gases within the framework, whereas the "81 % availability" isotherms of CO_2 and N_2 are in very good agreement with the experimental data set 1 up to a pressure of 1 atm. This result confirms that ignoring the effect of the linker coverage is a valid approximation for this pressure range. A

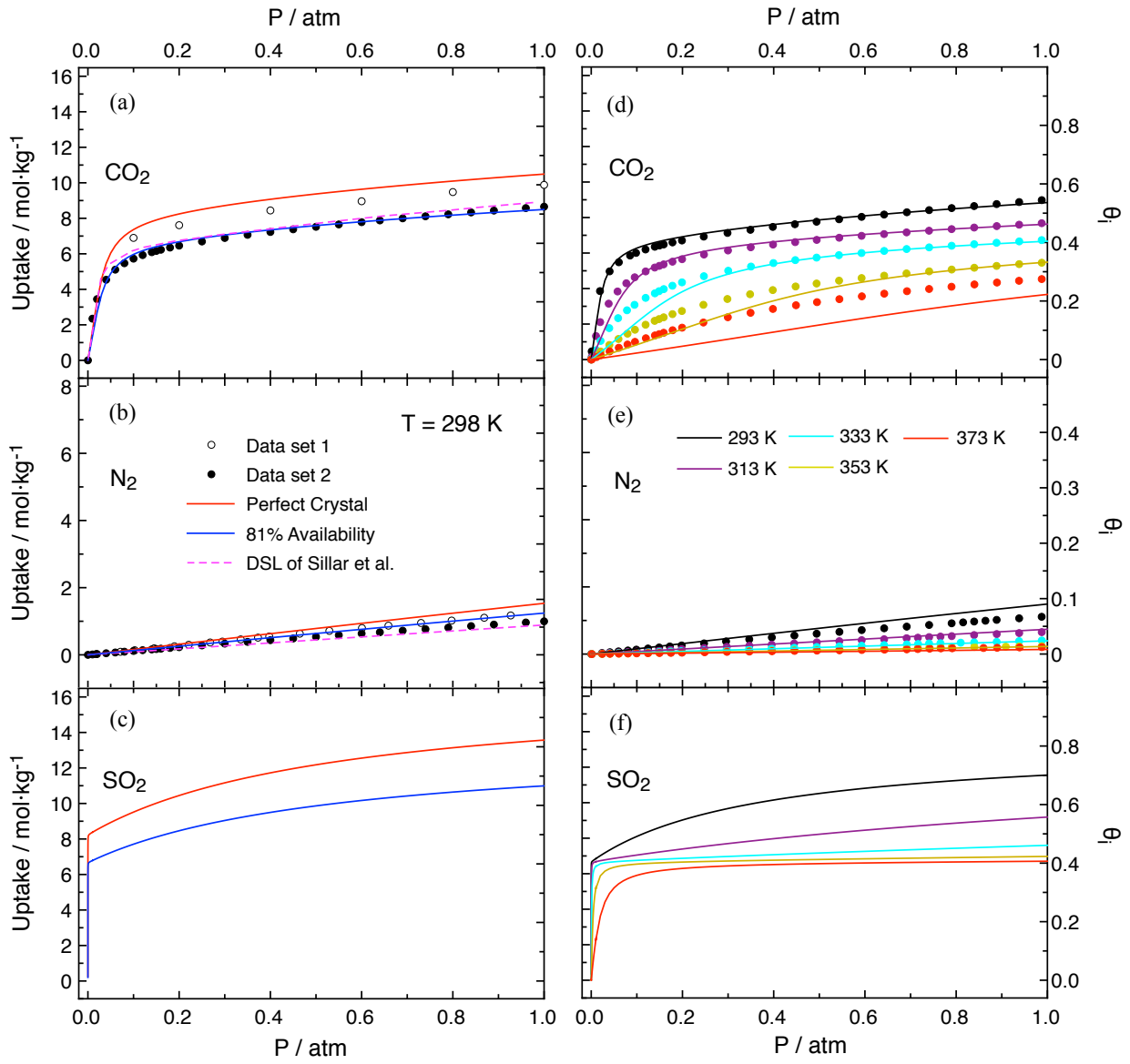

Figure 3.15. Pure CO_2 (a), N_2 (b) and SO_2 (c) DFT/DSL predicted adsorption isotherms on Mg-MOF-74. The red and blue solid lines represent the "perfect crystal" and the "81 % availability" structures, respectively. Experimental results from data set 1 [81,101] (*i.e.,* 81 % availability) and data set 2 [100] (*i.e.,* 93 % availability) are shown, along with DSL of Sillar *et al.,*[91,99] for comparison. The predicted "81 % availability" pure CO_2 (d), N_2 (e) and SO_2 (f) adsorption isotherms at different temperatures form 293 K to 373 K are represented in solid lines, while the experimental data of Mason *et al.,*[81] are shown in dots for comparison.

comparison with the more sophisticated model of Sillar *et al.,*[91,99] is also represented in Figure 3.15a and Figure 3.15b, showing that even though the calculation of the lateral interactions is significantly simplified, the predicted adsorption isotherms are almost equivalent. To our knowledge, there are no reliable experimental information regarding SO_2 adsorption in Mg-MOF-74, so the calculated adsorption isotherms could not be compared with any data set.

From the compiled results one can see that Mg-MOF-74 has a significantly higher affinity for CO_2 (*i.e.,* yielding uptakes higher than 8.0 mol·kg^{-1} at 1 atm) than for N_2 (*i.e.,* which adsorbs less

than 1.0 mol·kg^{-1} at 1 atm). Additionally, in the adsorption isotherm of CO_2 two different regions can be identified: (i) the low-pressure region (*i.e.,* from 0 to 0.2 atm), where the adsorption occurs mainly in the Mg^{2+} sites, and a higher-pressure region (*i.e.,* from 0.2 to 1 atm), where Mg^{2+} sites are almost saturated and the adsorption starts taking place at the linker sites. A similar pattern can be seen in the SO_2 isotherms, with a very steeped region at very low pressures that remarks the capability of Mg^{2+} sites to be poisoned by this species. On the other hand, N_2 did not exhibit an adsorption site in the linker at zero-coverage, so its isotherm does not show a DSL pattern like the other gases.

The "81 % availability" adsorption isotherms at different temperatures have also been calculated with DFT/DSL model (from Figure 3.15d to Figure 3.15f). The CO_2 and N_2 results have been compared with the extensive experimental data from Mason *et al.,*[81] for temperatures ranging from 293 K to 373 K. In general, all the isotherms reduce their uptakes when increasing the temperature in a reasonably good agreement with the experimental reported isotherms. Notice that, at very high temperatures the harmonic approximation used to calculate the partition functions might not be applicable anymore. Without any approximations, gas molecules could have enough thermal energy to overcome the barriers of some frustrated rotational motions, turning them free rotations. In this situation the harmonic approximation could be overestimating the entropy loss upon adsorption and predicting more positive $\Delta G_{i,S}^{ads}$, that is translated into lower equilibrium uptakes. To prevent this overestimation, some authors have considered that the lowest frequency mode should be treated as a 1D free rotation.[91] In the present thesis, only the harmonic approximation has been considered for simplicity, so adsorption isotherms at higher temperatures might be underestimated.

The calculated DFT values of $\Delta G_{i,S}^{ads}$ necessary to build the adsorption isotherms are collected in Table 3.7. The Gibbs free energy of adsorption becomes more positive with the increase of temperature reducing the spontaneity of the process in both the linker and the metal sites. According to the obtained results, the $\Delta G_{i,S}^{ads}$ of CO_2 and N_2 increase between 7 kJ·mol^{-1} and 10 kJ·mol^{-1} when increasing the temperature from 293 K to 373 K, regardless of the adsorption site. On the other hand, SO_2 shows an increase of approximately 15 kJ·mol^{-1} in the same temperature range. This fact implies that more entropy is lost when adsorbing SO_2 than other gas molecules in Mg-MOF-74, so higher temperatures penalize more the $\Delta G_{i,S}^{ads}$ of SO_2 than other gases.

Table 3.7. Gas/MOF Gibbs free energies of adsorption at different temperatures calculated from DFT for both the Mg^{2+} and the linker site. The results at full-coverage are shown in parentheses below the data at zero-coverage.

$\Delta G_{i,S}^{ads}$ / kJ·mol^{-1}	CO_2		N_2		SO_2	
Temperature / K	Mg^{2+}	Linker	Mg^{2+}	Linker	Mg^{2+}	Linker
293	-8.0 (-11.3)	5.8 (1.6)	3.5 (1.4)	N/A (11.5)	-26.5 (-29.5)	16.1 (-2.4)
313	-5.5 (-9.1)	8.0 (3.9)	5.7 (3.5)	N/A (13.1)	-22.7 (-25.5)	19.9 (1.3)
333	-3.0 (-6.9)	10.3 (6.2)	7.8 (5.6)	N/A (14.7)	-19.0 (-21.6)	23.6 (5.0)
353	-0.5 (-4.7)	12.5 (8.5)	10.0 (7.6)	N/A (16.4)	-15.2 (-17.6)	27.3 (8.8)
373	2.0 (-2.5)	14.7 (10.7)	12.1 (9.7)	N/A (18.0)	-11.4 (-13.7)	31.0 (12.5)

To evaluate the capacity of Mg-MOF-74 in recovering CO_2, its pure gas working capacities (WC) have been calculated assuming two different swing adsorption processes (Table 3.8). First, a VSA cycle with adsorption/desorption pressures of [1 atm/0.1 atm] is used, equivalent to the one employed in the study of Faujasites. Second, a TSA process is considered, which maintains the pressure constant to 1 atm throughout the entire cycle, adsorbs at a determined temperature (T) and desorbs at 373 K. A PSA cycle has not been considered in this study because adsorption isotherms were calculated up to 1 atm due to the approximations made in our DFT/DSL model. Regarding the VSA WC, Mg-MOF-74 yields significantly high values specially at intermediate temperatures (*i.e.,* 333-353 K) that outperform Faujasites in this kind of cycle. On the other hand, the efficiency of the TSA process depends on the adsorption temperature, giving WC as high as 5.17 mol CO_2·kg^{-1} MOF when using 293 K/373 K as adsorption/desorption temperatures.

The zero-coverage isosteric heat of adsorption, along with its variation with coverage, have been calculated for each gas through the coverage derivative of the enthalpies of adsorption calculated with DFT data (eq. 3.6). The integral $\Delta_{int}H_i^{ads}(\theta_i)$ has been calculated by summing the contribution of the enthalpies of adsorption of both sites (*i.e.,* $\Delta H_{i,M}^{ads}(\theta_i)$ and $\Delta H_{i,L}^{ads}(\theta_i)$) in Mg-MOF-74, weighed by their respective coverage (eq. 3.15). The enthalpies of adsorption at each site depend on the surface coverage, so a mean-field approximation is also applied to determine the $\Delta_{int}H_i^{ads}(\theta_i)$ value, through an expression equivalent to eq. 3.14 but using enthalpies instead of Gibbs free energies.

Table 3.8. Pure CO_2 equilibrium adsorption uptakes DFT/DSL predicted in mol of $CO_2 \cdot kg^{-1}$ MOF. The working capacities of each structure assuming a VSA or a TSA process are also shown in units of mol of $CO_2 \cdot kg^{-1}$ MOF recovered per cycle. The TSA WC is calculated by changing the adsorption temperature while keeping the desorption temperature constant at 373 K.

Temperature / K	Uptake at 0.1 atm	Uptake at 1 atm	VSA WC [1 atm/0.1 atm]	TSA WC 1 atm [T/373 K]
293	6.28	8.84	2.56	5.17
313	4.59	7.63	3.04	3.96
333	2.10	6.67	4.57	3.00
353	0.84	5.49	4.65	1.82
373	0.37	3.67	3.30	-

$$\Delta_{int} H_i^{ads}(\theta_i) = \theta_{i,M}\, \Delta H_{i,M}^{ads}(\theta_i) + \theta_{i,L}\, \Delta H_{i,L}^{ads}(\theta_i) \qquad 3.15$$

The isosteric heats of adsorption have been calculated as a function of the coverage for the three studied gas molecules at 298 K to compare with the available experimental data sets (Figure 3.16).[89,101] From the q_{st} plots of all gases, three different regions can be identified: first, a low-coverage region ($\theta_i < 0.3$), where the isosteric heat is governed by the adsorption at the Mg^{2+} sites, and its value is almost constant and similar to $\Delta H_{i,M}^{ads}(\theta_i \approx 0)$. There is an exception for the case of SO_2, in which the strong gas-gas lateral interactions strongly affect the adsorption properties, making the value of q_{st} to increase with the coverage. Then, an intermediate coverage region ($0.3 < \theta_i < 0.7$) where Mg^{2+} sites start to become saturated and the adsorption of gases is disputed between both sites. In this region, the isosteric heats of adsorption change smoothly from the value at the low-coverage region to the full-coverage heat of adsorption at the linker (*i.e.,* $\Delta H_{i,L}^{ads}(\theta_i = 1)$). Finally, in the high-coverage region ($\theta_i > 0.7$), the Mg^{2+} sites are completely saturated and the isosteric heat of adsorption is mainly due to the linker sites. In this region the value of q_{st} is constant in our model and equal to $\Delta H_{i,L}^{ads}(\theta_i = 1)$.

The isosteric heats obtained by the DFT/DSL model reproduce the experimental q_{st} values for CO_2 at different coverages reasonably well, including the sigmoidal shape presented by the experimental data of Dietzel *et al.,*[101] and Queen *et al.*[89] The inflection point that determines the saturation of Mg^{2+} sites depends also on the MOF site availability, showing a shift to higher coverages in structures with higher availability. Experimental data of isosteric heats of adsorption for N_2 at high pressure are generally not available due to its low affinity for these kinds of

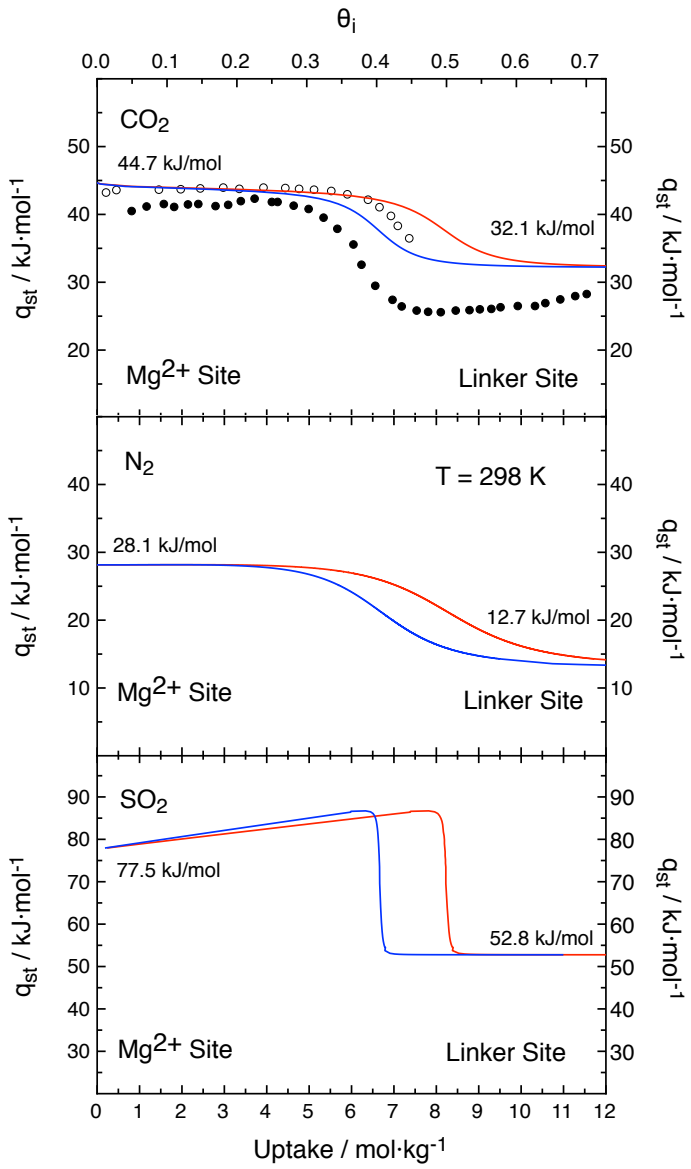

Figure 3.16. CO_2, N_2 and SO_2 DFT/DSL isosteric heat of adsorption (q_{st}) in Mg-MOF-74 as a function of the coverage for the "perfect crystal" (red) and for the "81 % availability" model (blue). The experimental results from the data sets 1 [101] and 3 [89] are shown for comparison in black and white dots, respectively.

adsorbents. For this reason, an experimental zero-coverage q_{st} value has been derived from the adsorption isotherms measured by Mason *et al.*,[81] between 293 K and 313 K using data up to $\theta_i = 0.1$. The derived experimental value is equal to 23.5 kJ·mol^{-1}, which is in relatively good agreement to the value of 28.1 kJ·mol^{-1} calculated via DFT/DSL. Finally, SO_2 has very high isosteric heats, almost doubling the values of CO_2 at any coverage. This fact suggests again that this gas would easily poison the Mg-MOF-74 in a gas mixture containing both CO_2 and SO_2.

The calculated isosteric heats have shown that the Mg-MOF-74 has a great affinity for SO_2 adsorption, followed by CO_2 and N_2. However, it does not give a direct idea of the adsorption rates

between the different species. To that end, the Henry's coefficients can be obtained from the adsorption isotherms to quantify the gas/MOF affinity and derive an estimate for the selectivity of the material to adsorb a determined gas in an ideal mixture (eq. 3.1). The Henry's coefficient (H_i) can be obtained from the slope at the zero-pressure/composition region of the adsorption isotherm, where the Langmuir equation reduces to a linear expression ($\theta_i \approx K_{i,M}(\theta_i)P$). Additionally, the linker term can be neglected because at zero-coverage the adsorption is dominated by Mg^{2+} sites and the slope of the isotherm becomes equal to the Langmuir equilibrium constant for the metal sites without lateral interactions ($H_i = K_{i,M}(\theta_i \approx 0)$).

The resulting Henry's coefficients, and some selectivity values are compiled in Figure 3.17 as a function of temperature. As it was expected, the Henry's coefficients for CO_2 are large enough to selectively adsorb in Mg-MOF-74 if a binary mixture containing CO_2 and N_2 is used. However, they are not large enough to prevent poisoning from SO_2, specially at low temperatures. Specifically, the studied material is selective enough to adsorb 110 times more CO_2 than N_2 at 293 K according to the Henry's coefficients ratio. However, Mg-MOF-74 will adsorb 2061 times more SO_2 than CO_2 at the same conditions. Even though the material becomes less selective when increasing temperature, the Mg-MOF-74 is still adsorbing 76 times more SO_2 than CO_2 at 373 K. This result suggests that the poisoning ability of SO_2 is reduced with temperature, but it is still strong enough to make the separation of CO_2 completely impractical by this material. Additionally, very high temperatures reduce the total uptake and working capacities of the framework making the material less effective in recovering CO_2. However, higher temperatures also reduce the CO_2/N_2 selectivity of Mg-MOF-74, which adsorbs 26 times more CO_2 than N_2 at 373 K. To

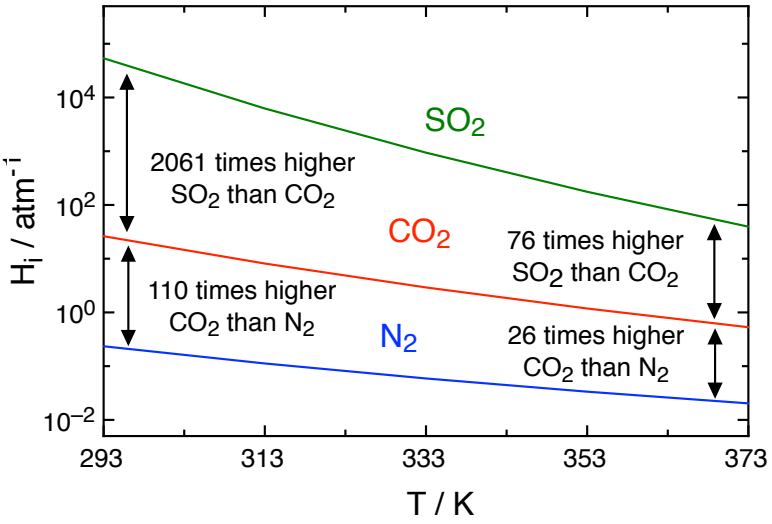

Figure 3.17. CO_2, N_2 and SO_2 Henry's coefficients in Mg-MOF-74 at different temperatures in the range 293-373 K. The selectivity of the material is displayed at 293 K and at 373 K to see the effect of temperature on this property.

conclude, even though a lower selectivity towards SO_2 might slightly prevent poisoning, it is strongly recommended to remove SO_2 from a post-combustion flue gas mixture before employing Mg-MOF-74 as the adsorbent material for CO_2 capture and separation.

3.3.3 CO_2 Separation in Mg-MOF-74 from DFT Calculations Enhanced with a Langmuir model (Mixtures)

Similarly to the study of Faujasites, the conclusions achieved up to now are only based on pure adsorption data, which does not take into consideration the effect of competition among different gas molecules towards the Mg-MOF-74 sites. In this regard, a multicomponent extension of the DFT/DSL model has been applied to model the CO_2 capture phenomena in a flue gas containing CO_2, N_2 and SO_2 (eq. 3.16). The extended eq. 3.16 gives the equilibrium coverage of the i species (θ_i) as a function of its molar faction at the gas phase (x_j^g) and the total gas pressure (P) in the ternary mixture. As eq. 3.16 only gives the θ_i of a single component but depends on the coverage of all species, a set of equations (*i.e.,* one per component) must be solved simultaneously in an iterative process to obtain the equilibrium adsorption of all species within the framework. Although the multicomponent DFT/DSL model implicitly considers the thermodynamic equilibrium competition among different species for each adsorption site, only pure component lateral interactions have been calculated. This means that some lateral interactions are missing in our model and might lead to small deviations in regions where two or more gases have simultaneous non-negligible adsorption. However, the results with the complete set of lateral interactions are not expected to be significantly different from the ones presented here due to the large difference in SO_2/CO_2 affinity of Mg-MOF-74.

$$\theta_i = \chi_M \frac{K_{i,M}(\theta_i) x_i^g P}{1 + \sum_i K_{i,M}(\theta_i) x_i^g P} + \chi_L \frac{K_{i,L}(\theta_i) x_i^g P}{1 + \sum_i K_{i,L}(\theta_i) x_i^g P} \qquad 3.16$$

Different ternary mixtures have been modeled with a 15 % of CO_2 and different amounts of SO_2, from a few tenths ppm up to a 1 % (*i.e.,* in molar percentages). The surplus has been considered to be N_2, which varies from 85 % to 84 % depending on the concentration of SO_2. This inlet composition has been selected aiming at reproducing the typical post-combustion flue gas mixture at 313 K.[102] It has been assumed that the flue gas is dried before the adsorption step, so

the initial mixture does not contain water. Additionally, as O_2 showed to behave similarly to N_2 in previous studies, its % has been added to the N_2 surplus.[93,103]

Adsorption isotherms of three ternary mixtures are compiled in Figure 3.18 to show the behavior of CO_2 adsorption with the explicit presence of SO_2 impurities. In the first concentration (*i.e.,* 0.005 % of SO_2), the contaminant is too diluted to significantly affect CO_2 adsorption in Mg-MOF-74. In the second concentration (*i.e.,* 0.02 % of SO_2), the SO_2 is capable of adsorbing onto several Mg^{2+} sites, strongly competing with CO_2. Finally, in the third concentration (*i.e.,* 0.1 % of SO_2), the SO_2 almost completely poisons the Mg-MOF-74 structure adsorbing only a marginal portion of CO_2. In all the calculated isotherms, the amount of adsorbed N_2 is negligible in front of the other two gases, showing the low selectivity of the material towards this gas. From the three

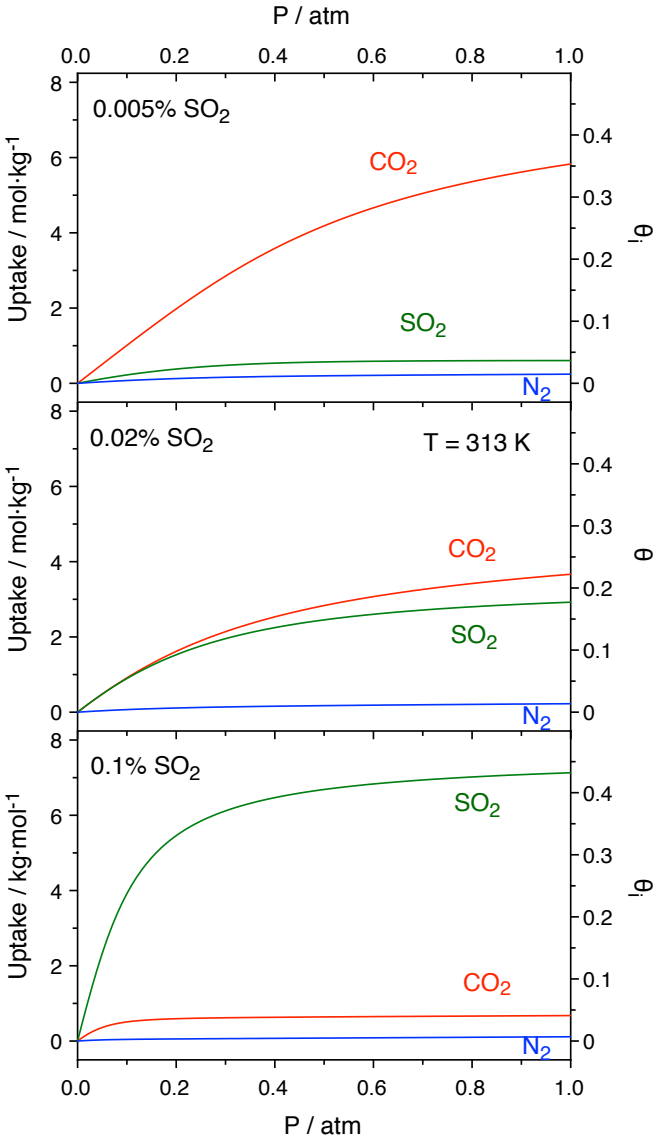

Figure 3.18. DFT/DSL isotherms for the ternary mixture obtained with the "81 % availability" multicomponent dual-site Langmuir model at 313 K. Three different SO_2 molar percentages are considered in gas mixtures, with 15 % of CO_2 and N_2 as the surplus.

previous plots one can conclude that Mg-MOF-74 can selectively adsorb CO_2 at very low SO_2 partial pressure, but it exhibits a turning point at a certain % of SO_2 where the contaminant adsorbs more selectively than CO_2.

Notice that, the turning point changes with the adsorption conditions. In Figure 3.19, the % of CO_2 adsorbed onto Mg-MOF-74 at 1 atm is shown as a function of the % of SO_2 at the inlet and the temperature. As N_2 is practically not adsorbing in the framework, the % complementary to the adsorbed CO_2 is approximately the % of SO_2. According to the obtained results, low temperatures and moderate SO_2 content at the inlet make the structure to adsorb almost only SO_2. For example, at 293 K and at 0.01 % of SO_2, only a 25 % of CO_2 adsorbs in Mg-MOF-74. On the other hand, higher temperatures (*i.e.,* 353 K) allow to adsorb a 75 % of CO_2 at the same % of SO_2. However, very high temperatures also reduce the CO_2/N_2 selectivity of the material, so to absorb a high percentage of CO_2 (*i.e.,* higher than 90 %) it is recommended to work at temperatures lower than 333 K and an inlet SO_2 concentration lower than 0.002 %.

It was seen in the previous section how the working capacities of Faujasites were significantly reduced when modeling mixtures instead of pure CO_2 gas. To evaluate the capacity of Mg-MOF-74 to capture and separate CO_2 from a post-combustion flue gas mixture, the working capacities and purities of the recovered gas are calculated from DFT/DSL isotherms. The same two different swing adsorption processes were considered in consistency to the analysis of pure compounds: (i) a VSA process at 313 K, with adsorption pressure of 1 atm and desorption pressure of 0.1 atm; and (ii) a TSA process at a pressure of 1 atm, with an adsorption/desorption temperature cycle performed at [313 K/373 K]. Additionally, a combined VTSA cycle is also analyzed, where the

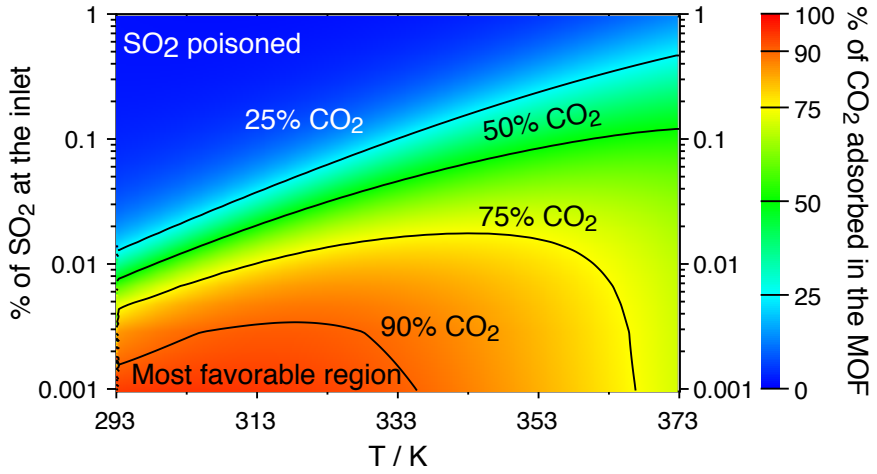

Figure 3.19. Amount of CO_2 captured by Mg-MOF-74 in % at 1 atm as a function of temperature and SO_2 content in the gas mixture, also in %. Red, green and blue regions show conditions of selective CO_2 capture, strong competition between CO_2 and SO_2, and SO_2 poisoning of Mg-MOF-74, respectively.

adsorption is performed at 1 atm and 313 K and the desorption conditions are 0.1 atm and 373 K. The resulting working capacities as a function of the SO_2 composition at the inlet are collected in Figure 3.20.

The working capacity of Mg-MOF-74 in VSA is reduced to a value of 1.0 mol $CO_2 \cdot kg^{-1}$ of MOF at low SO_2 content. This value is higher than the CO_2 working capacity of NaX at equivalent conditions, which makes this material very competitive for CO_2 separation. On the other hand, in the defined TSA cycle, working capacities up to 2.0 mol of $CO_2 \cdot kg^{-1}$ of MOF can be achieved. Finally, the combined VTSA process allows to recover 5.9 mol of $CO_2 \cdot kg^{-1}$ of MOF at each cycle. This amount is slightly lower than the ideal complete desorption (*i.e.,* 6.4 mol of $CO_2 \cdot kg^{-1}$ of MOF), meaning that the VTSA process can recover almost all CO_2 adsorbed in the framework. All of these working capacities are affected by contaminant concentration, being reduced almost to zero at SO_2 inlet concentrations between 0.1 % and 1 %. The calculated working capacities show again that it is imperative to work in a very low SO_2 concentration to prevent negative effects in the adsorption properties. Concentrations higher than 0.01 % of SO_2 induce significant decreases in the effective CO_2 working capacities regardless of the swing adsorption cycle chosen, making the recovery very inefficient.

Apart from the working capacities, the purity of the recovered CO_2 has also been analyzed as a function of the % of SO_2 at the inlet. According to the results compiled in Figure 3.21, VTSA yields the highest CO_2 purity at a very low % of SO_2. This feature, along with the highest working capacity, makes VTSA the most efficient cycle for CO_2 capture and separation. However, between 0.02 % and 0.03 % of SO_2 at the inlet, VTSA starts desorbing part of the captured contaminant,

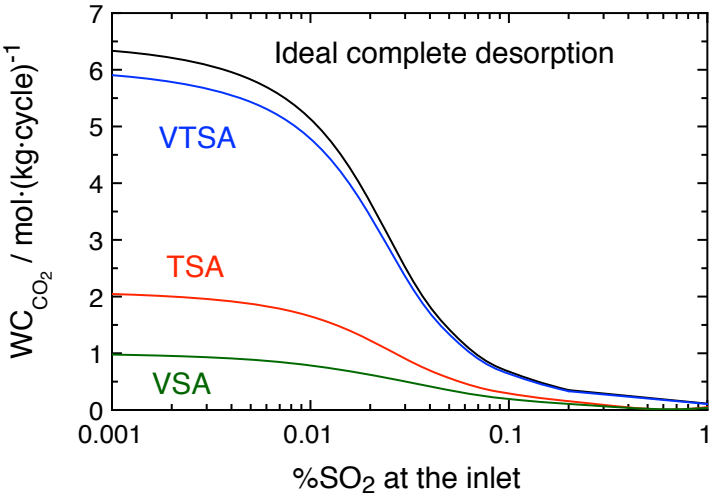

Figure 3.20. CO_2 working capacities as a function of the % of SO_2 at the inlet. The three swing adsorption processes considered are: VSA in green [1 atm/0.1 atm], TSA in red [313 K/373 K] and VTSA in blue [1 atm,313 K/0.1 atm,373 K], all compared to the ideal case of complete desorption in black.

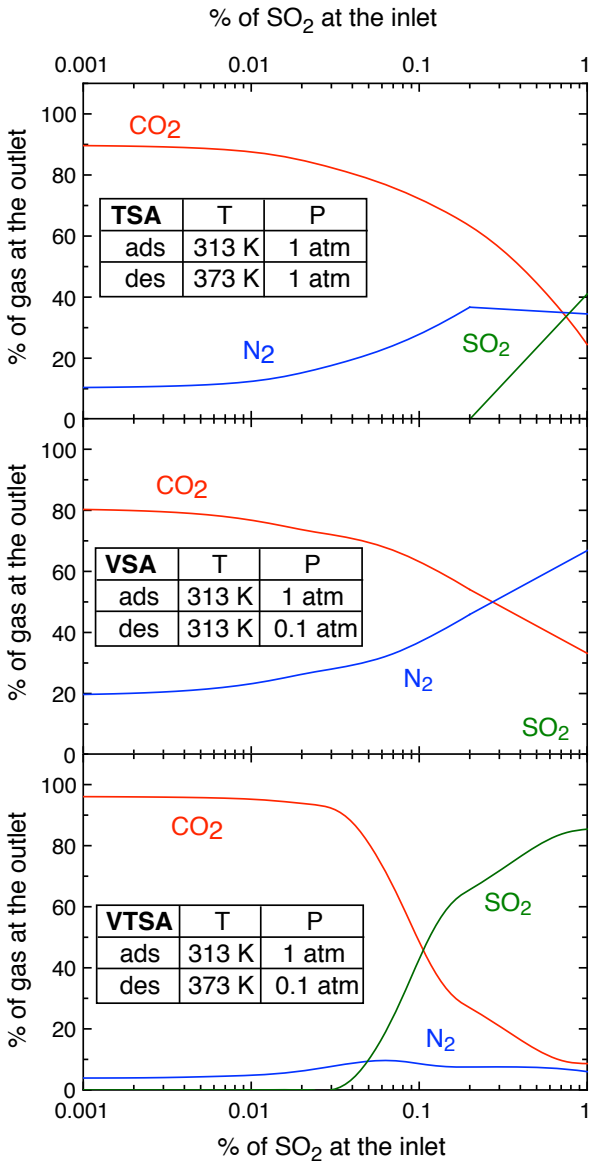

Figure 3.21. CO_2, N_2 and SO_2 composition in the recovered gas mixture (*i.e.,* at the outlet) as a function of the SO_2 content at the inlet. Each plot shows a different swing adsorption cycle and their adsorption/desorption conditions.

rapidly dropping the CO_2 purity at the outlet. TSA is the second most efficient technique for CO_2 recovery, because it exhibits high WC and purity at the outlet (*i.e.,* 90 %) at very low % of SO_2 at the inlet. The purity of CO_2 becomes reduced with SO_2 content, but it only starts desorbing the contaminant at % of SO_2 higher than 0.2 %. Finally, VSA yields the lowest WC and purity (*i.e.,* 80 %) but SO_2 does not desorb at any of the studied conditions. The VSA or TSA processes are not as efficient as VTSA for CO_2 recovery, but as they do not release the contaminant as easily as VTSA they might be usable in inlet mixtures with more than 0.03 % of SO_2.

3.3.4 Summary and Conclusions

In this section, the adsorption of different ternary gas mixtures containing CO_2, N_2 and SO_2, in Mg-MOF-74 was assessed. Due to the low availability of high-quality force fields for SO_2 adsorption in Mg-MOF-74, a mean field theory based on a double-site Langmuir isotherm was used along with DFT calculations to evaluate the impact of pollutants in CO_2 separation. The target of DFT calculations was to characterize the main adsorption sites of the framework, along with their affinities towards the different gas molecules, and calculate different thermodynamic functions of adsorption (*e.g.,* enthalpy, entropy or Gibbs free energy of adsorption). Additionally, the values of $\Delta G_{i,S}^{ads}$ could be used to calculate the Langmuir equilibrium constants for the DFT/DSL model employed in this work. Adsorption isotherms are predicted with the DFT/DSL model in good agreement with the available experimental information, even considering the effect of lateral interactions with a simplified mean field model.

With this study, it was seen that Mg-MOF-74 is a very competitive CO_2 adsorbent material yielding high gas uptakes, working capacities and purities, even outperforming the widely used NaX Faujasite. However, SO_2 has a very strong affinity for the Mg^{2+} metal sites saturating them completely at very low pressures. This effect makes SO_2 to have a very strong influence on the adsorption properties of mixtures. Specifically, at moderate temperatures (*i.e.,* from 313 K to 333 K) it is imperative to reduce the inlet concentration of SO_2 under 0.002 % to selectively adsorb a 90 % of CO_2 into Mg-MOF-74 at 1.0 atm. Higher concentrations poison the structure reducing the total amount of sites available for gas adsorption. This fact reduces the working capacity of the structure significantly, specially at % of SO_2 higher than 0.01 %. Finally, the purity of the recovered CO_2 depends on the swing adsorption process used. In general, VTSA is the most efficient technique to recover CO_2, because it has the higher WC and purities. However, when the inlet concentration of SO_2 is larger than 0.02 % - 0.03 % the recovered gas becomes contaminated by SO_2 and different cycles such as VSA or TSA become more appropriate for CO_2 recovery. Even though alternative cycles can be applied, the results suggest that the % of SO_2 at the inlet should be kept at least below 0.03 % to obtain a high CO_2 purity at the outlet.

3.4 CO_2 Separation in Phosphonium-Based Ionic Liquids

In the previous sections, the CO_2 capture and separation in post-combustion flue gases with microporous materials has been analyzed. However, the currently used separation technology is based on liquid absorbents, which means that many power plants have their facilities built around the usage of liquid solvents for CO_2 capture. For this reason, the implementation of alternative liquid technologies is favored because they can be used in the currently implemented separation units. An interesting set of components for CO_2 separation are Ionic Liquids (ILs), which are salts that remain liquid at a temperature below 100 ºC. ILs exhibit a set of advantages with respect the currently used amines, some of them are: low vapor pressure, high physicochemical stability, low corrosivity and non-flammability.[26–28] These features prevent solvent evaporation issues or chemical degradation of the solvent, making the separation process less cumbersome. Even though the use of ILs is interesting for their stability, they are still not widely implemented because they usually have relatively low absorption capacities and high prices in comparison with amines.[104]

As all salts, ILs are formed by a strongly interacting combination of a cation and an anion. In general, the cation is a large organic charged species whereas the anion is a smaller organic or inorganic moiety.[105] Equivalently to the solid adsorbents, the charged species tend to favor the capture capabilities of the material (*e.g.,* the extra-framework cations in Zeolites or the unprotected metal sites in MOFs). Due to the charged nature of ILs, both the cation and the anion contribute significantly to the gas/IL interactions. Additionally, cations or anions can be exchanged to modify the properties of ILs for specific tasks. Specifically, many recent studies were devoted to find the optimal cation/anion pair for CO_2 capture and separation to substitute the current amine technology.[106–110]

Modeling techniques are required in the study of ILs to perform thorough screening of the most suitable cation/anion pairs for a determined application. In fact, molecular-based EoSs based on thermodynamic fluid theories, such as SAFT,[111,112] and more specifically the soft-SAFT EoS,[30] have been widely used to study the phase equilibria between different gases and ILs. Some of the most studied ILs with this theory are the imidazolium-based ILs (*i.e.,* [$C_n$mim][X]) [113–117] and pyridinium-based ILs (*i.e.,* [$C_n$py][X] or [$C_n$mpy][X]) [118]. Some members of these families showed good CO_2 absorption capacities, especially when ILs contained fluorinated anions.[119] In fact, within these sets of ILs it was seen that changing the cations had a relatively low impact on CO_2 capture, whereas changing the anions had a significant effect. Finally, it was shown experimentally that tetraalkylammonium and tetraalkylphosphonium-based ILs also have good CO_2 absorption capacities.[120–123] In that sense, some works were devoted to study with soft-SAFT EoS the

physicochemical properties of tetraalkylammonium-based ILs blended in deep-eutectic solvents,[124,125] but not tetraalkylphosphonium ILs.

The great success of SAFT-based EoS is due to the coarse-grained models used to define the interactions between different species. These models directly connect the thermodynamic fluid theories with molecular structures and functional groups, which makes all the adjustable parameters to have physical meaning in a molecular representation. This practice allows to successfully predict thermophysical properties of pure ILs and IL/gas mixtures. Additionally, the parameter/structure relation allows to transfer parameters from similar molecules, increasing the predictability of the model. An alternative tool to SAFT-based EoS to predict gas/liquid solubility is the COnductor Screening MOdel for Realistic Solvents (COSMO-RS).[126,127] This method is capable of obtaining the chemical potential (*i.e.,* either of pure species or species in solution) based on quantum chemical calculations combined with statistical thermodynamics. COSMO-RS is in practice a purely predictive method, ideal for solvent screening. In fact, this technique was previously applied to predict many liquid/liquid equilibria (LLE) and vapor/liquid equilibria (VLE) with reasonably good results, especially in the reproduction of Henry's coefficients.[128–130]

In this section, the capability of phosphonium-based ILs for gas adsorption and separation will be evaluated by using both soft-SAFT and COSMO-RS complementarily. Up to date, phosphonium-based ILs have been characterized by several authors using different EoSs, but not with soft-SAFT. Specifically, among the works of Ferreira *et al.,*[131] Tomé *et al.,*[132] Mozaffari *et al.,*[133,134] and Hosseini *et al.,*[135] pure IL properties were characterized using equations such as the Goharshadi-Morsali-Abbaspour EoS, the Sanched-Lacombe EoS, a modified version of the Song-Mason EoS and the Vogel-Fulcher-Tamman correlation. Finally, Banerjee *et al.,*[136] used COSMO-RS to model some tetradecyltrihexylphosphonium-based ILs. On the other hand, the gas absorption on these ILs were assessed in the works of Carvalho *et al.,*[123] Manic *et al.,*[137] Ramdin *et al.,*[138] Camper *et al.,*[121] Scovazzo *et al.,*[139] who determined the CO_2 absorption capacity by using either the Peng-Robinson EoS or the regular solution theory.

In particular, three different ILs (Figure 3.22), formed by the tetradecyltrihexylphosphonium $[P_{6,6,6,14}]^+$ cation and (i) Chlorine $[Cl]^-$, (ii) bis(trifluorosulfonyl)imide $[NTf_2]^-$ and (iii) dicyanamide $[DCA]^-$ anions have been modeled to evaluate their CO_2 absorption capacities and selectivity in front of SO_2 as a pollutant. Since this is the first time these ILs are modelled with soft-SAFT EoS, COSMO-RS has been employed as a support tool to develop accurate and meaningful associative soft-SAFT schemes. To that end, the soft-SAFT parameters have been partially fitted to experimental data, and partially assigned via with DFT calculations. Then, the

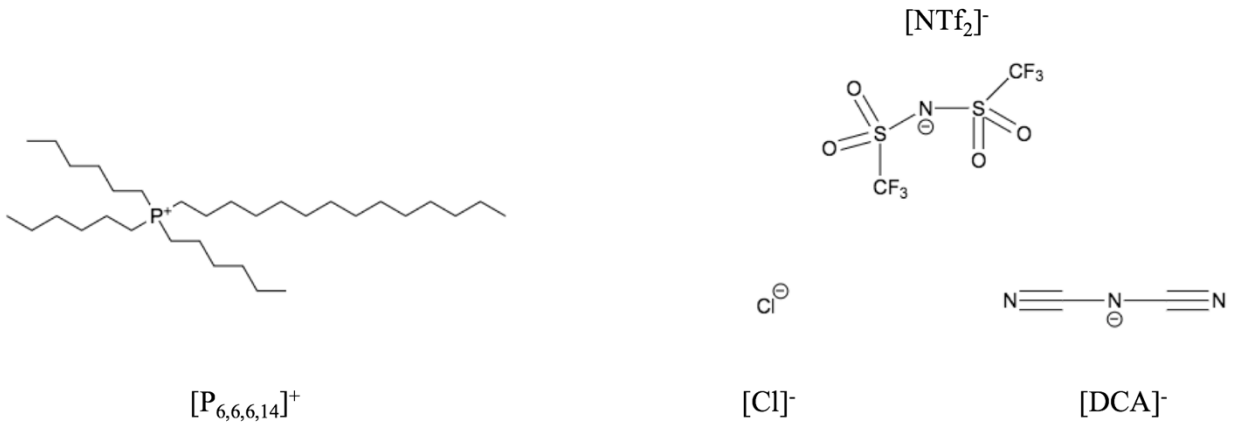

Figure 3.22. Molecular structure of the tetraalkylphosphonium cation and the three anions used in this work.

two aforementioned methods have been simultaneously used to evaluate CO_2 and SO_2 solubilities, as well as the CO_2 vs SO_2 selectivity in the three ILs.

3.4.1 Soft-SAFT EoS Modeling of ILs from DFT Information

When using the soft-SAFT EoS, it is key to select a representative coarse-grained model capable of accurately describing the thermophysical properties of fluids. Both species (*i.e.,* the cation and the anion) are modeled as a single component in the soft-SAFT framework to consider that the electrostatic interactions will always keep both moieties together. The three modeled compounds have a large cation with a long aliphatic chain (C_{14}) and three shorter aliphatic chains (C_6) all connected to a central phosphonium cation. Even though the cation is highly ramified, the three ILs were reproduced with a single non-ramified chain of coarse-grained beads. This approximation was successfully used in previous works where soft-SAFT EoS was employed to model tetraalkylammonium ILs.[125]

Regarding the associative scheme, three different kinds of sites have been defined: (i) positively charged, (ii) negatively charged, and (iii) dual sites (*i.e.,* [+], [−] and [±] respectively). In this definition, [+] sites can only interact with [−] sites but not with other [+] sites. Similarly, [−] sites can only interact with [+] sites. However, dual sites (*i.e.,* [±]) can have simultaneously a positive and negative nature, so they can interact with any other kind of site, including other [±] sites. Dual sites represent regions where cations and anions are very close to each other, allowing any other associative molecule to either interact with the cation or the anion. According to that definition, all ILs have been considered to have a dual site, to represent the region where the cation and the anion bond to each other.[115] Additional associative sites have been added based on the

σ-profiles obtained from ADF/COSMO-RS calculations.[140,141] These profiles allow to identify the molecular regions with high electrostatic potential and their nature (*i.e.,* positively charged or negatively charged), which can be translated into associative sites in the soft-SAFT framework. Recall, from Section 2.3.2 that the values of the σ-profile correspond to the electrostatic potential that perfectly screens the electron density, so they are the opposite values of the electron density.

In Figure 3.23 the calculated σ-profiles for all species are shown. Regarding the cation, a positively charged region of the electron density is localized around the phosphorus atom. Similarly, $[Cl]^-$ also has a single spherical negatively charged region around its only atom. Then, the soft-SAFT model for $[P_{6,6,6,14}][Cl]$ contains only a unique dual site to represent the P-Cl interaction region. On the other hand, $[DCA]^-$ and $[NTf_2]^-$ are symmetrical species with a central negatively charged nitrogen atom connected to two electronegative regions where the charge can delocalize (*i.e.,* the CN groups in $[DCA]^-$ and the SO_2 groups in $[NTf_2]^-$). In both cases, their soft-SAFT models contain a dual site, to account for the cation/anion pair region, and two negatively charged sites to consider the associative interactions with the other two electronegative regions.

The soft-SAFT EoS uses a LJ potential to account for intermolecular interactions. For this reason, each IL requires a fitted value of the segment diameter (σ_{ii}), the dispersion interaction parameter (ε_{ii}) and the length of the chain (m_i). Additionally, associative sites need two additional adjustable parameters to be modeled: the strength ($\varepsilon^{HB}_{\alpha\beta,ii}$) and the volume ($K^{HB}_{\alpha\beta,ii}$) of association, which adds to a total of five adjustable parameters per IL. To reduce the dimensionality of the fitting, the $\varepsilon^{HB}_{\alpha\beta,ii}$ and $K^{HB}_{\alpha\beta,ii}$ of all associative sites in a single IL have been considered equal and non-periodic DFT calculations have been performed to determine reasonable values for the associative sites. To that end, the cation/anion interaction energies (ΔE) and equilibrium

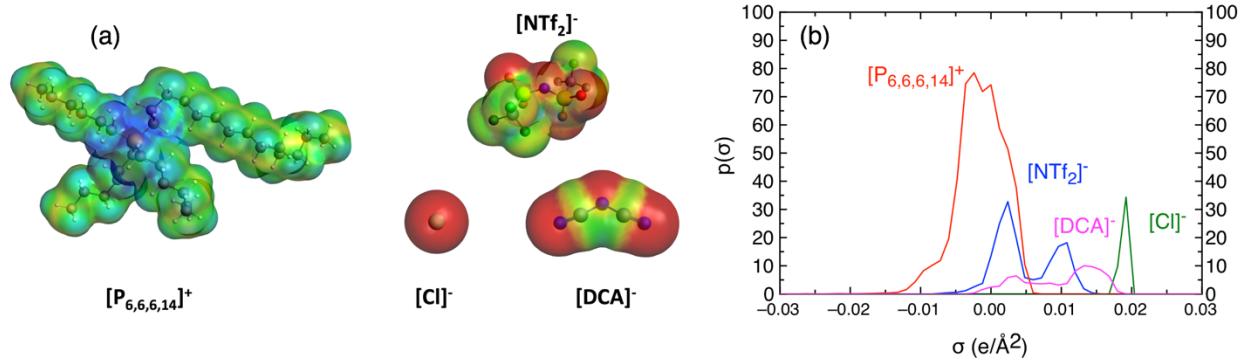

Figure 3.23. (a) Electrostatic potential distribution for the $[P_{6,6,6,14}]^+$ cation, which contains a single positively charged region (blue), and all anions, which show one or more negatively charged regions (red). Green regions represent the non-associative non-polar segments of the molecules. (b) σ-profiles of the four moieties modeled in this work.

distances (r) among six different ILs (*i.e.,* the three studied ILs and three references) have been calculated. The three references are compounds somehow similar to the three phosphonium-based ILs, which are already modeled by soft-SAFT EoS, so their associative parameters are already fitted and validated elsewhere.[124,142] The associative strengths ($\varepsilon^{HB}_{\alpha\beta,ii}$) for the three studied ILs have been obtained rescaling the reference values by the relative cation/anion interaction energies (ΔE) calculated through DFT. Similarly, the volume of association ($K^{HB}_{\alpha\beta,ii}$) has been derived rescaling the values of the references by the relative cation/anion equilibrium distances (r). Finally, the obtained parameters have been rounded to be presented in the most common format of soft-SAFT EoS associative scheme. After obtaining reasonable values for $\varepsilon^{HB}_{\alpha\beta,ii}$ and $K^{HB}_{\alpha\beta,ii}$ the rest of the parameters (*i.e.,* σ_{ii}, ε_{ii} and m_i) have been fitted to reproduce pure IL density data at several pressures and temperatures to readjust the EoS to reproduce the correct intermolecular interactions. The $[N_{6,6,6,14}][Cl]$ IL was used as the reference compound to derive $[P_{6,6,6,14}][Cl]$ parameters.[142] Unfortunately, this is the only tetraalkylammonium compound already modeled with soft-SAFT EoS, so the references for the other compounds were chosen as the 1-n-butyl-3-methylimidazolium ILs with the same anion (*i.e.,* $[C_4mim][NTf_2]$ and $[C_4mim][DCA]$).[124]

All non-periodic DFT calculations have been performed with ADF modeling suite [141] and the B3LYP functional.[143,144] These calculations do not include dispersion corrections for two reasons: (i) the associative strength is a purely coulombic effect, not a dispersive one, and (ii) García *et al.*[145] showed that many DFT functionals were capable of describing the relative cation-anion interaction energies among different ILs without needing to consider dispersion corrections. The aug-cc-pVTZ, which is a relatively large basis set, has been used to minimize the effects of basis set superposition errors. And finally, the phosphonium and ammonium cations have been reduced to a cluster model that contains the central cation and four propyl chains (*i.e.,* $[P_{3,3,3,3}]^+$ and $[N_{3,3,3,3}]^+$, respectively), to reduce the computational cost while keeping the steric hindrance of the environment around the cation-anion interacting region. All atoms in $[C_4mim]^+$ and all anions have been represented explicitly in the DFT calculations.

Figure 3.24 contains the B3LYP/aug-cc-pVTZ equilibrium geometries of the six abovementioned ILs, and Table 3.9 compiles the cation/anion interaction energies and distances. First, the differences between $[P_{3,3,3,3}][Cl]$ and $[N_{3,3,3,3}][Cl]$ are very subtle. In both structures, the $[Cl]^-$ anion coordinates directly with the central heteroatom that carries the positive charge. $[P_{3,3,3,3}][Cl]$ exhibits an interaction energy of -87.0 kcal·mol^{-1} and an equilibrium distance of 3.46 Å. On the other hand, $[N_{3,3,3,3}][Cl]$ has a slightly longer equilibrium distance (*i.e.,* 3.63 Å) and an almost equivalent interaction energy (*i.e.,* -86.4 kcal·mol^{-1}). In this case, the reference associative values of the tetraalkylammonium chloride have been minimally rescaled from

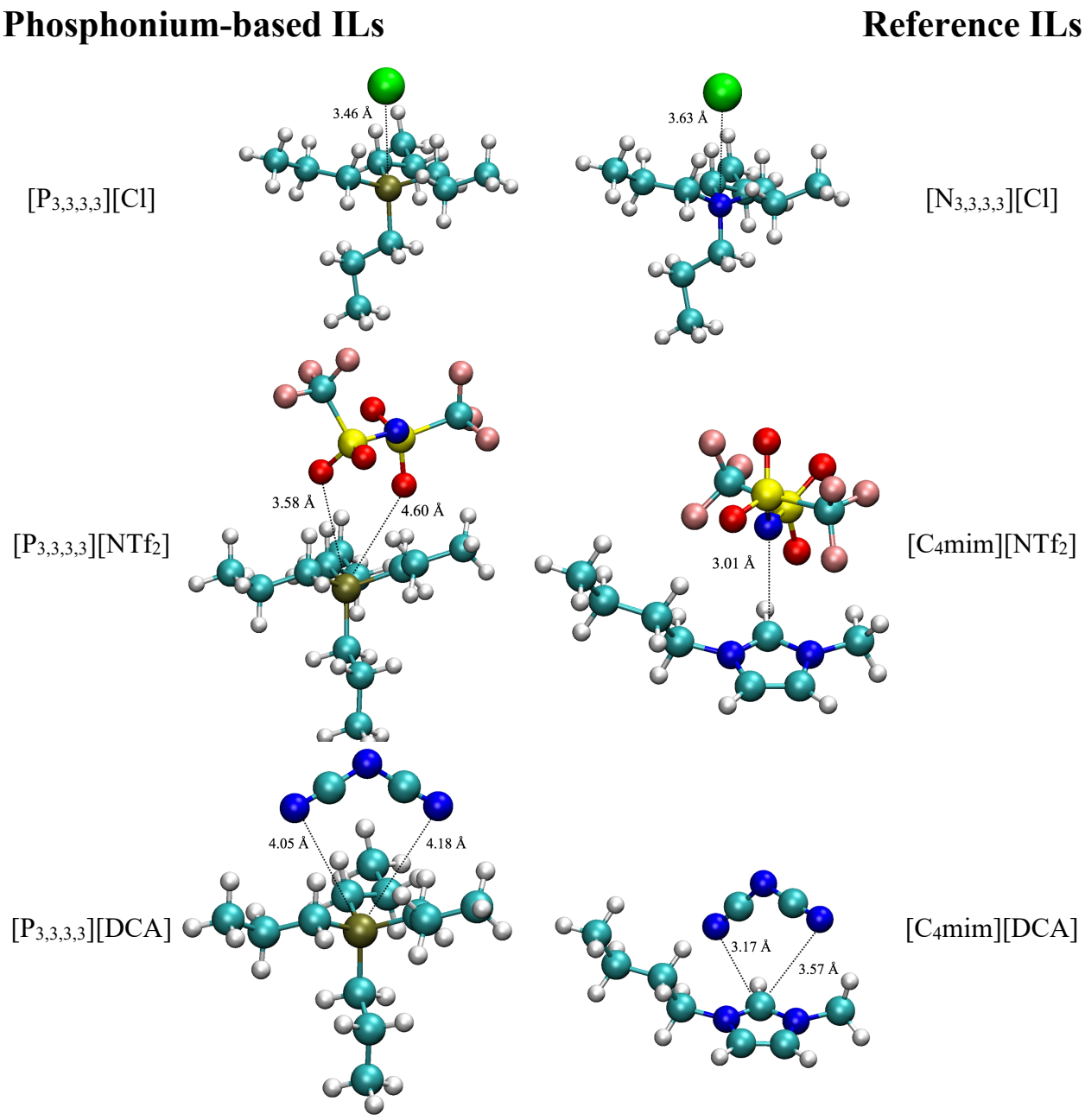

Figure 3.24. Equilibrium geometries of the three $[P_{3,3,3,3}][X]$ ILs and their reference counterparts optimized via DFT. The distance between the cation/anion interaction regions is also depicted in each geometry.

$\varepsilon^{HB}_{\alpha\beta,ii}/k_B$ = 3384 K and $K^{HB}_{\alpha\beta,ii}$ = 2100 Å^3 to $\varepsilon^{HB}_{\alpha\beta,ii}/k_B$ = 3500 K and $K^{HB}_{\alpha\beta,ii}$ = 2000 Å^3 to be consistent with the difference in relative interactions between $[P_{3,3,3,3}][Cl]$ and $[N_{3,3,3,3}][Cl]$.

On the other hand, the anions interact with the CH atom between the two N of $[C_4mim]^+$, and their equilibrium geometries differ from the $[P_{3,3,3,3}][X]$ ILs due to the lower steric hindrance of the small cation. For example, $[NTF_2]^-$ interacts with $[C_4mim]^+$ through its N atom, whereas it binds to the central P atom of $[P_{3,3,3,3}]^+$ through its SO_2 groups. The difference between both cations is also reflected in the calculated DFT interaction energies, where phosphonium-based ILs exhibit

Table 3.9. Cation/anion interaction energies (ΔE) and equilibrium distances (r) of the three phosphonium-based ILs along with the three references obtained through DFT calculations. The new associative parameters derived from the reference values [124,142] are also given.

Property	[$P_{3,3,3,3}$] [Cl]	[$N_{3,3,3,3}$] [Cl]	[$P_{3,3,3,3}$] [NTf_2]	[C_4mim] [NTf_2]	[$P_{3,3,3,3}$] [DCA]	[C_4mim] [DCA]
ΔE / kcal·mol^{-1}	-87.0	-86.4	-69.0	-72.2	-73.3	-78.3
r / Å	3.46	3.63	3.58, 4.60	3.01	4.05, 4.18	3.17, 3.57
$\varepsilon^{HB}_{\alpha\beta,ii}/k_B$ / K	3500	3384	3300	3450	3600	3850
$K^{HB}_{\alpha\beta,ii}$ / Å^3	2000	2100	2700	2250	3000	2450

ΔE values 4.4 % and 6.4 % lower than [C_4mim][NTf_2] and [C_4mim][DCA], respectively. Similarly to the first IL, the associative strengths have been rescaled according to the DFT relative difference: the value of $\varepsilon^{HB}_{\alpha\beta,ii}/k_B$ = 3450 K for [C_4mim][NTf_2] reduces to $\varepsilon^{HB}_{\alpha\beta,ii}/k_B$ = 3300 K for [$P_{3,3,3,3}$][NTf_2] and the value of $\varepsilon^{HB}_{\alpha\beta,ii}/k_B$ = 3850 K for [C_4mim][DCA] becomes $\varepsilon^{HB}_{\alpha\beta,ii}/k_B$ = 3600 K for [$P_{3,3,3,3}$][DCA]. The equilibrium distances among the [$P_{3,3,3,3}$][X] ILs is approximately a 20 % longer than in [C_4mim][X] due to the difference in steric hindrances. To that end the volumes of association have been increased by a 20 % in consistency to the relative DFT equilibrium distances (*i.e.,* the value of $K^{HB}_{\alpha\beta,ii}$ = 2250 Å^3 for [C_4mim][NTf_2] increases to $K^{HB}_{\alpha\beta,ii}$ = 2700 Å^3 for [$P_{3,3,3,3}$][NTf_2] and the value of $K^{HB}_{\alpha\beta,ii}$ = 2450 Å^3 for [C_4mim][DCA] increases to $K^{HB}_{\alpha\beta,ii}$ = 3000 Å^3 for [$P_{3,3,3,3}$][DCA]).

After deriving the associative values (*i.e.,* $\varepsilon^{HB}_{\alpha\beta,ii}$ and $K^{HB}_{\alpha\beta,ii}$) of the three ILs, the m_i, σ_{ii} and ε_{ii} parameters have been fitted to reproduce their densities at different pressure and temperature conditions (*i.e.,* from 303 K to 333 K and 2 atm to 650 atm). Although soft-SAFT EoS is usually adjusted to reproduce VLE curves, ILs present negligible vapor pressures, so only densities are available for the fitting. The experimentally measured densities (ρ) have been obtained from the work of Esperança *et al.,*[122] and Tomé *et al.,*[132] The fitted parameters for all the molecules considered in this work are compiled in Table 3.10. The order of the chain length parameter (m_i) obtained is directly proportional to the size of the anions, being [$P_{6,6,6,14}$][NTf_2] the largest modeled IL, followed by [$P_{6,6,6,14}$][DCA] and finally, [$P_{6,6,6,14}$][Cl]. On the other hand, the cation is large enough to yield very similar adjusted segment diameters (σ_{ii}) for the three ILs, so they have been fixed to the average value of 4.323 Å. Finally, the dispersive energies (ε_{ii}) also give very similar values in all the studied ILs, ranged as [$P_{6,6,6,14}$][$Cl]^-$ > [$P_{6,6,6,14}$][$DCA]^-$ > [$P_{6,6,6,14}$][$NTf_2]^-$. These results show that anions modify noticeably the chain length and associative schemes of the modeled ILs, whereas the segment diameters and dispersive energies are almost entirely due to the

Table 3.10. Soft-SAFT parameters for all species used in this thesis. The parameters of ILs are fitted to experimental density data at temperatures between 303 K and 333 K and pressures between 2 atm and 650 atm.[122,132] The parameters of gas molecules are obtained from previous works.[118]

	m_i	σ_{ii} / Å	ε_{ii}/k_B / K	$\varepsilon^{HB}_{\alpha\beta,ii}/k_B$ / K	$K^{HB}_{\alpha\beta,ii}$ / Å^3	N of sites [1]
$[P_{6,6,6,14}][Cl]$	11.231	4.323	386.25	3500	2000	1+0
$[P_{6,6,6,14}][NTf_2]$	13.773	4.323	369.39	3300	2700	1+2
$[P_{6,6,6,14}][DCA]$	11.836	4.323	379.86	3600	3000	1+2
CO_2 [2]	1.571	3.184	160.2	-	-	-
SO_2	2.444	2.861	228.3	1130	601	2

[1] The number of sites for ILs is separated into dual sites plus negative sites. SO_2 is modeled with both a positive and a negative charged site to reproduce its dipole.
[2] Two additional parameters are used to account for the quadrupolar moment of CO_2: $Q_{exp} = 4.4\text{e-}40$ and $\chi_p = 1/3$.

cation. When comparing the obtained parameters with other ILs already modeled with soft-SAFT,[116–118,125,142] one can see that $[P_{6,6,6,14}][X]$ ILs generally exhibit larger values of m_i due to their longer chains. They also have larger values of σ_{ii}, because the effect on the ramifications around the central P atom was captured with an increase of the average segment diameter. And finally, they have lower ε_{ii} values because the cation has very long aliphatic chains, who weakly interact with other species.

The parameters for gas molecules were obtained from previous soft-SAFT works.[118] In this model CO_2 does not bear any associative site, but its quadrupole is considered by adding an additional A_{polar} term to the soft-SAFT EoS. This term depends on the quadrupole moment of the molecule (Q) that can be calculated through the experimental quadrupolar moment (Q_{exp}) and the fraction of segments of the chain that contains the quadrupole (χ_p), such as: $Q = Q_{exp}\chi_p$. On the other hand, the dipole moment of SO_2 is modeled through two associative sites (*i.e.,* a $[+]$ and a $[-]$ sites). According to the previous definition, $[+]$ sites can interact with $[-]$, and vice versa, creating dipole-dipole associations. Notice that SO_2 sites can also interact with IL sites. The mixing rules for gas-IL associative energies and volumes follow the common Lorentz-Berthelot rules, as detailed in eq. 2.72 and eq. 2.73

The combination of models and parameters obtained are able to fit very accurately the density at different pressures and temperatures (Figure 3.25), giving average absolute deviations (AAD%) lower than 0.05 % in all the modeled ILs. There are some P/T conditions where experimental data were not measured in the abovementioned works; in these situations, the results from soft-SAFT EoS complement it.

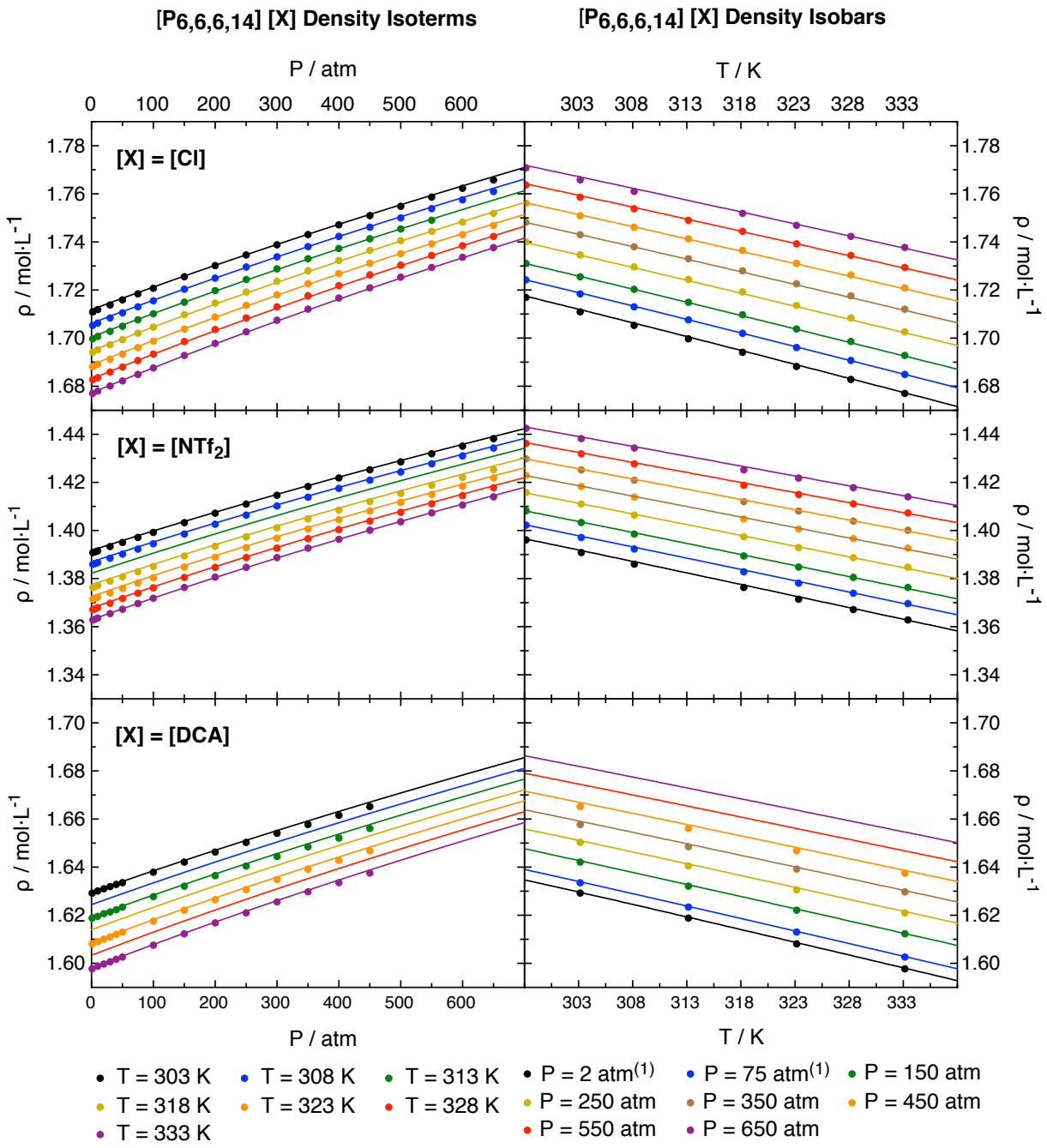

Figure 3.25. Predicted IL densities (ρ) at different pressures and temperatures. Solid lines represent soft-SAFT EoS calculations, whereas dots refer to available experimental data.[122,132]

Three other pure IL properties have been calculated to validate the soft-SAFT models. First, the isothermal compressibilities (κ_T) have also been predicted from the variation of the density with pressure according to eq. 3.17. All the studied ILs, show reasonable agreement to experimental information (Figure 3.26), being $[P_{6,6,6,14}][NTf_2]$ the compound with the highest κ_T followed by $[P_{6,6,6,14}][Cl]$ and $[P_{6,6,6,14}][DCA]$. On the other hand, the thermal expansion coefficients (α_P) are obtained from the variation of the density with temperature as described in eq. 3.18.

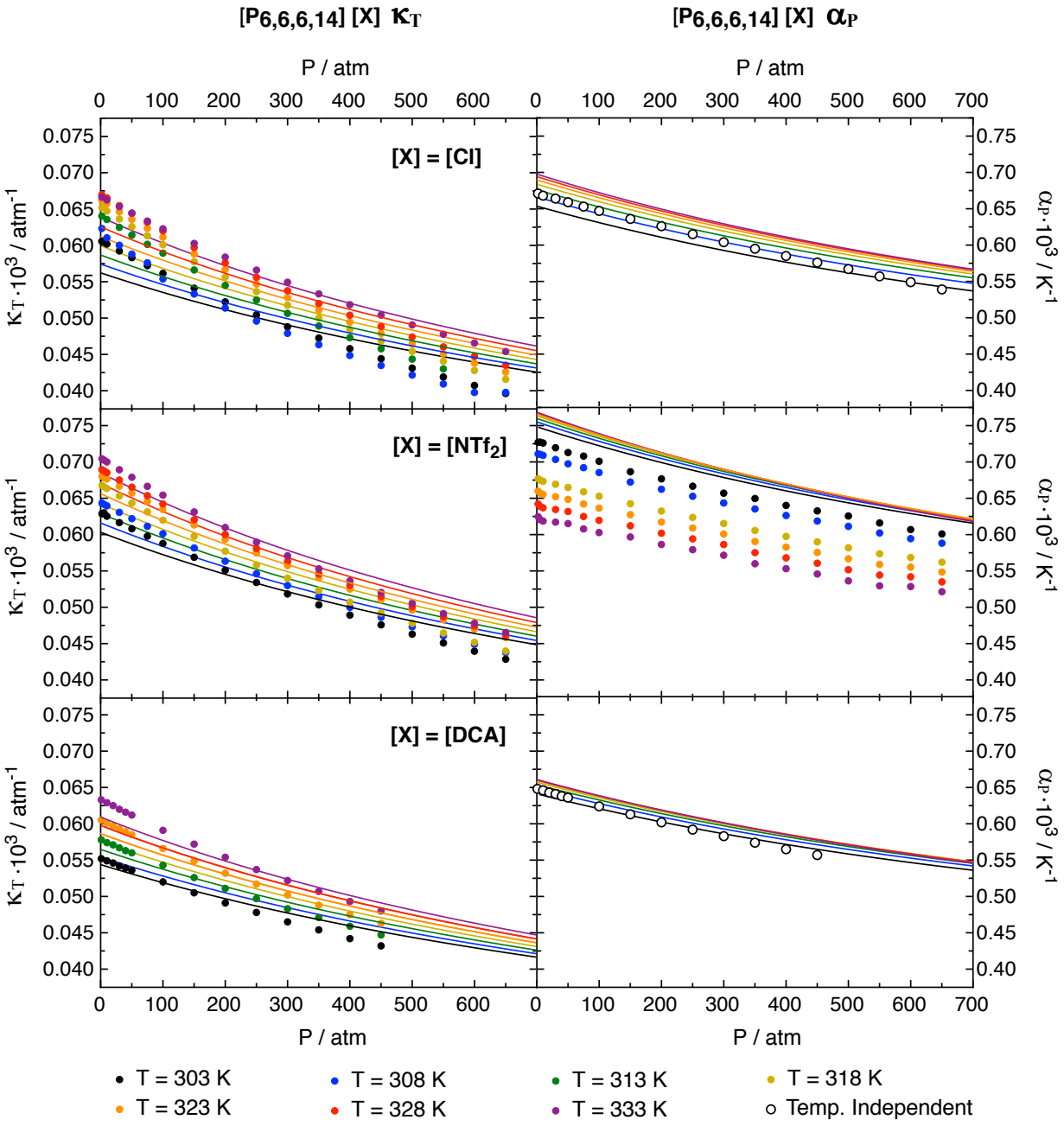

Figure 3.26. Predicted isothermal compressibilities (κ_T) and thermal expansion coefficients (α_P) of the three pure ILs at different pressures and temperatures. Solid lines represent the soft-SAFT calculations, whereas dots refer to available experimental data.[122,132]

$$\kappa_T = \frac{1}{\rho}\left(\frac{\partial \rho}{\partial P}\right)_T = \left(\frac{\partial \ln \rho}{\partial P}\right)_T \qquad 3.17$$

$$\alpha_P = -\frac{1}{\rho}\left(\frac{\partial \rho}{\partial T}\right)_P = -\left(\frac{\partial \ln \rho}{\partial T}\right)_P \qquad 3.18$$

The soft-SAFT EoS predicts a weak temperature dependence for all studied ILs (Figure 3.26). Additionally, the obtained results are in good agreement with experimental information on [$P_{6,6,6,14}$][Cl] and [$P_{6,6,6,14}$][DCA].[122,132] The calculated values of [$P_{6,6,6,14}$][NTf_2] present higher deviations from the experimental results of Esperança *et al.*[122] In this case, soft-SAFT EoS only captures a qualitative higher α_P value but not its temperature dependence. Additionally, higher values of α_P are predicted to be at higher temperatures, whereas the experimental trend is the opposite. This behavior is also observed in other modeling works with associative fluids modeled by soft-SAFT EoS, where the temperature dependence in α_P shows an inversion point at a certain pressure.[146] This inversion is very sensitive to the chosen molecular parameters and, in some situations, it can be only qualitatively reproduced.

Finally, the surface tensions (γ) have been calculated throughout soft-SAFT EoS coupled to the density gradient theory (DGT).[147,148] This theory applies an inhomogeneous corrective term to the local Helmholtz energy density $a_0(\rho)$ to obtain the energy of an inhomogeneous fluid. The correction assumes a planar interface and depends on the local density and the so-called influence parameter (c_{ij}). If the temperature dependence on c_{ij} is neglected, the surface tension within the soft-SAFT EoS/DGT framework can be written as a function of the chemical potential and equilibrium pressure of the system (eq. 3.19).

$$\gamma = \sum_i \sum_j \int_{-\infty}^{\infty} c_{ij} \frac{d\rho_i}{dz} \frac{d\rho_j}{dz} dz = 2 \int_{-\infty}^{\infty} \left[a_0(\rho) - \sum_i \rho_i \mu_{0i} - p_0 \right] dz \qquad 3.19$$

Influence parameters were fitted to the experimental values of Kilaru *et al.*,[149] and the obtained values are collected in Table 3.11. Then, the temperature dependence on the surface tension for [$P_{6,6,6,14}$][Cl], [$P_{6,6,6,14}$][NTf_2] and [$P_{6,6,6,14}$][DCA] is shown in Figure 3.27, where it can be seen the accurate reproduction obtained by soft-SAFT/DGT, further validating the model. According to soft-SAFT results, all values lie close to each other around 33 $mN \cdot m^{-1}$ and 35 $mN \cdot m^{-1}$ at 300 K and decrease with temperature with a similar slope, being [$P_{6,6,6,14}$][DCA] the IL with higher surface tension, followed by [$P_{6,6,6,14}$][Cl] and finally, [$P_{6,6,6,14}$][NTf_2].

Table 3.11. Temperature independent influence parameters c_{ij} adjusted to calculate the surface tension of the three studied ILs.

IL	[$P_{6,6,6,14}$][Cl]	[$P_{6,6,6,14}$][NTf_2]	[$P_{6,6,6,14}$][DCA]
c_{ij} / $J \cdot m^5 \cdot mol^{-2}$	8.998e-18	1.275e-17	1.000e-17

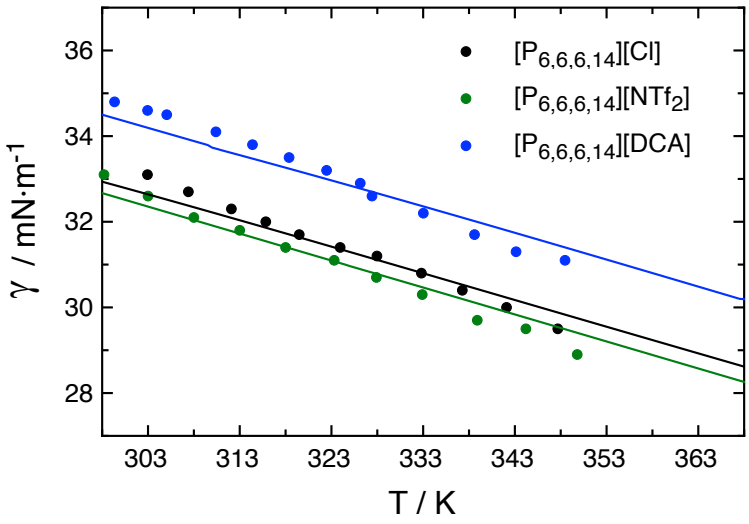

Figure 3.27. Predicted soft-SAFT surface tension (Solid lines) for the three ILs in comparison with available experimental data (dots) of Kilaru *et al.*[149]

3.4.2 Binary Absorption Isotherms from soft-SAFT EoS and COSMO-RS

The previous results show that soft-SAFT EoS is capable of reproducing general thermophysical data of the three tetraakylphosphonium ILs. Then, the prediction of CO_2 and SO_2 absorption isotherms is carried out by both, soft-SAFT EoS and COSMO-RS. The former does not only require experimental data to fit and validate pure IL parameters, but also need to fit gas/IL binary interaction parameters (*i.e.,* k_{ij} in eq. 2.35). On the other hand, the latter uses only the previously calculated σ-profiles to predict binary solubility data.

Six binary k_{ij} values are necessary to reproduce the desired gas/IL interactions with soft-SAFT EoS (*i.e.,* 2 gases in 3 ILs). To that end, experimental isotherms of CO_2 in $[P_{6,6,6,14}][Cl]$, $[P_{6,6,6,14}][NTf_2]$ and $[P_{6,6,6,14}][DCA]$ are used to fit three of them explicitly. The parameters obtained are $k_{CO_2,[P_{6,6,6,14}][Cl]} = 0.940$, $k_{CO_2,[P_{6,6,6,14}][NTf_2]} = 0.932$ and $k_{CO_2,[P_{6,6,6,14}][DCA]} = 0.917$, which are comparable to other ILs already modeled with soft-SAFT EoS (*e.g.,* $k_{CO_2,[N_{4,4,4,4}][Cl]} = 0.947$ [125] or $k_{CO_2,[C_4mim][NTf_2]} = 0.972$ [142]). Similarly, the three SO_2/IL binary parameters are also required to study their absorption properties. Unfortunately, there are no available experimental absorption isotherms of this contaminant in any of the three studied ILs. For this reason, the $k_{SO_2,[P_{6,6,6,14}][X]}$ parameters are derived from similar systems. Specifically, Ojeda *et al.,*[125] studied the absorption of CO_2 and SO_2 in tetraalkylammonium-based ILs and proposed values of $k_{ij} = 0.947$ and $k_{ij} = 0.880$ for both gases, respectively. As tetraalkylammonium and tetraalkylphosphonium-based ILs

have similar chemical structures, it is assumed that the k_{ij} difference in changing the gas from CO_2 to SO_2 will not depend significantly on the IL. Within this approximation, all of the SO_2/IL binary interaction parameters have been approximated by the relationship in eq. 3.20. Finally, an additional $k_{CO_2/SO_2} = 1.065$ parameter is used to account for the binary interaction of CO_2 with SO_2. The latter parameter is only used when modelling ternary mixtures containing CO_2, SO_2 and IL simultaneously, and has been obtained from the previous work of Llovell *et al.*[117] All the parameters mentioned are compiled in Table 3.12.

After obtaining the binary interaction parameters, the absorption isotherms are computed by both, soft-SAFT EoS and COSMO-RS (Figure 3.28). According to soft-SAFT, $[P_{6,6,6,14}][NTf_2]$ exhibits the highest absorption uptake followed by $[P_{6,6,6,14}][Cl]$ and $[P_{6,6,6,14}][DCA]$. This result is in agreement with previous works that state that $[NTf_2]$ is an anion that favors CO_2 capture.[150] Additionally, soft-SAFT EoS is also capable of reproducing the overall shape of the absorption isotherms with a single temperature independent binary interaction parameter. On the other hand, COSMO-RS does not seem to give such a good description of the absorption isotherms because all ILs yield similar uptakes in the studied pressure/temperature range. Additionally, COSMO-RS seems to overestimate the solubility of gases at high pressures, presenting higher saturation points for all ILs except for $[P_{6,6,6,14}][NTf_2]$.

$$k_{SO_2,[P_{6,6,6,14}][X]} = (0.947 / 0.880)\, k_{CO_2,[P_{6,6,6,14}][X]} \qquad 3.20$$

Figure 3.28 also contains a magnification of the low-pressure/composition region within each plot. Thanks to that magnification, it can be seen that in some cases soft-SAFT EoS is unable to reproduce the adequate temperature dependence on the low-pressure absorption

Table 3.12. All binary interaction parameters used in this work. The gas/IL parameters have been explicitly fitted, while gas/gas k are obtained from Llovell *et al.*[117]

j species	$k_{CO_2,j}$	$k_{SO_2,j}$
$[P_{6,6,6,14}][Cl]$	0.940	0.873
$[P_{6,6,6,14}][NTf_2]$	0.932	0.866
$[P_{6,6,6,14}][DCA]$	0.917	0.852
CO_2	-	1.065
SO_2	1.065	-

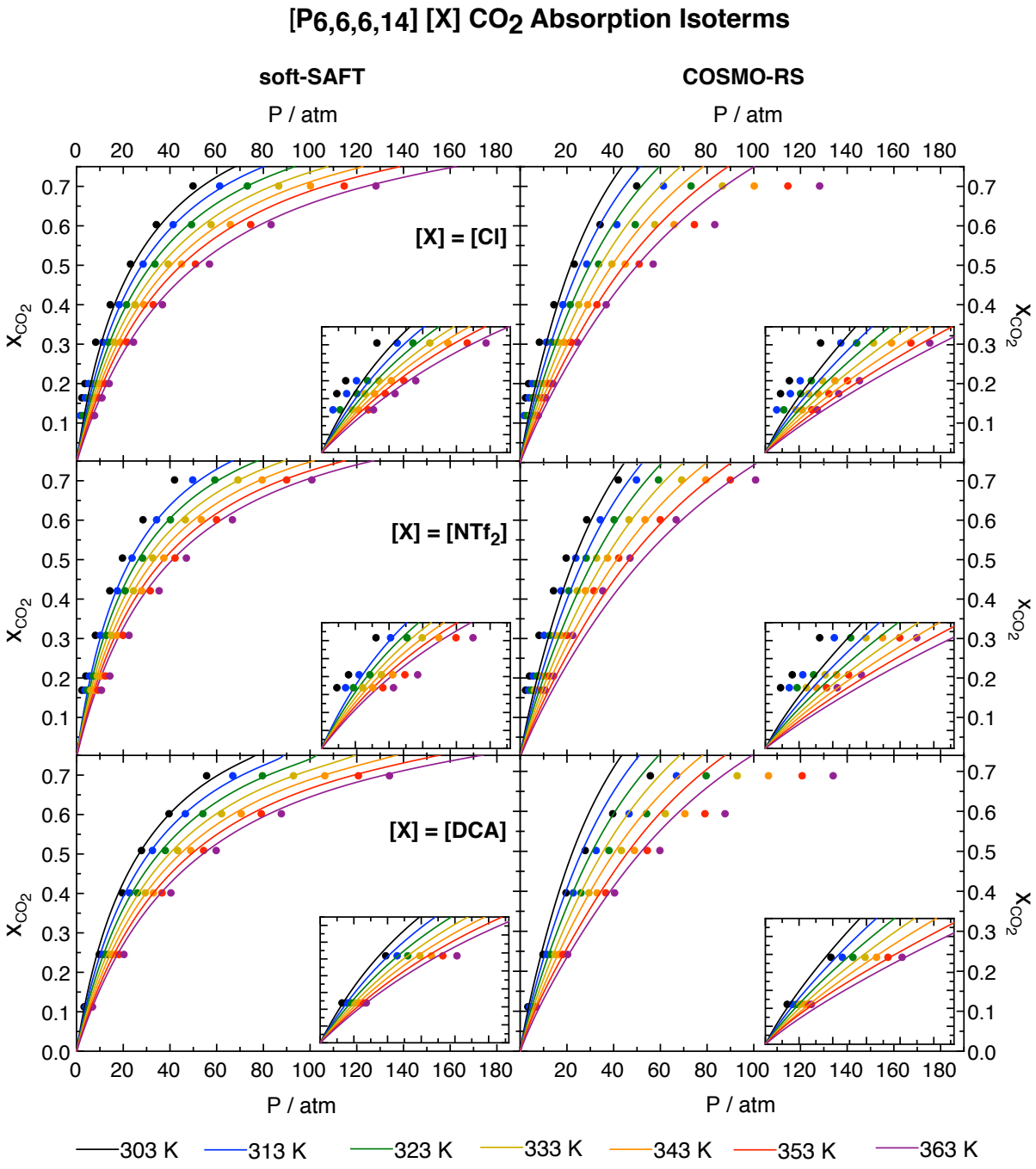

Figure 3.28. CO_2 absorption isotherms calculated with soft-SAFT EoS (left) and COSMO-RS (right) in the three studied ILs. Experimental data are shown in dots,[122,132] and the low-pressure/composition region (*i.e.,* from $x_{CO_2} = 0$ to $x_{CO_2} = 0.35$) is magnified in the subplots.

isotherms. In fact, the EoS was fitted to reproduce the properties of ILs in a wide range of pressures and temperatures, so it is capable of capturing the overall shape of the isotherm at the cost of larger deviations in the low-pressure region.

On the other hand, COSMO-RS reproduces fairly well the correct shape and temperature dependence of the absorption isotherms in this region, without needing to fit any adjustable parameters. In some situations, COSMO-RS even yields better estimates for

some absorption isotherms at low pressures than soft-SAFT EoS. Notice that soft-SAFT EoS could be fitted to reproduce low-pressure absorption isotherms and outperform COSMO-RS. However, the latter does not require any adjustable parameter to capture the low-pressure absorption properties (*i.e.,* it only needs the sigma profile from a DFT calculation, and the general purpose fitted parameters already included in the model). This fact makes COSMO-RS a very appealing tool to work in a framework where soft-SAFT reproduces medium and high-pressure absorption data, whereas COSMO-RS provides low-pressure information.

The absorption of SO_2 in the three ILs is predicted by both methods and compiled in Figure 3.29. The strong dipole moment of SO_2 interacts strongly with all ILs, giving significantly larger uptakes for this gas than for CO_2. The soft-SAFT EoS predicts the highest SO_2 absorption with $[P_{6,6,6,14}][NTf_2]$ and $[P_{6,6,6,14}][Cl]$, followed by $[P_{6,6,6,14}][DCA]$. On the other hand, COSMO-RS predicts similar SO_2 absorptions for either $[P_{6,6,6,14}][Cl]$, $[P_{6,6,6,14}][DCA]$ and $[P_{6,6,6,14}][NTf_2]$, Similarly to CO_2, COSMO-RS seems to overestimate the SO_2 absorption for all of the ILs at high pressures.

When comparing the two gas solubilities, it can be seen that absorption isotherms exhibit an almost linear behavior up to uptakes close to a molar fraction of $x_i = 0.3$ - 0.4. For the case of CO_2, the linear region holds until approximately 10 atm regardless of the IL, whereas SO_2 loses the linear regime at pressures close to 1 atm. This implies that SO_2 has a much stronger absorption onto phosphonium-based ILs than CO_2, which will not allow them to selectively capture CO_2 unless the partial pressure of the pollutant is significantly small. A similar behavior was seen in the previous studies on Mg-MOF-74, where SO_2 could easily poison the adsorbent, preventing it to capture CO_2. It is worth noticing that, although ILs generally show lower absorption capacities than microporous materials, their regenerability is significantly higher. In fact, according to the calculated isotherms, CO_2 can almost be completely released from the phosphonium-based ILs at atmospheric pressure. On the other hand, SO_2 exhibits a significantly large uptake in all ILs at 1 atm but it can be released by heating the solvent from 303 K to 363 K. It is also recommended to create a mild vacuum (*i.e.,* 0.1 atm) after capturing SO_2, to regenerate the IL almost completely. This feature opens the possibility of using ILs for CO_2 separation by either capturing CO_2 or SO_2, which is a hardly applicable practice with Mg-MOF-74 due to its inability to release the adsorbed SO_2.

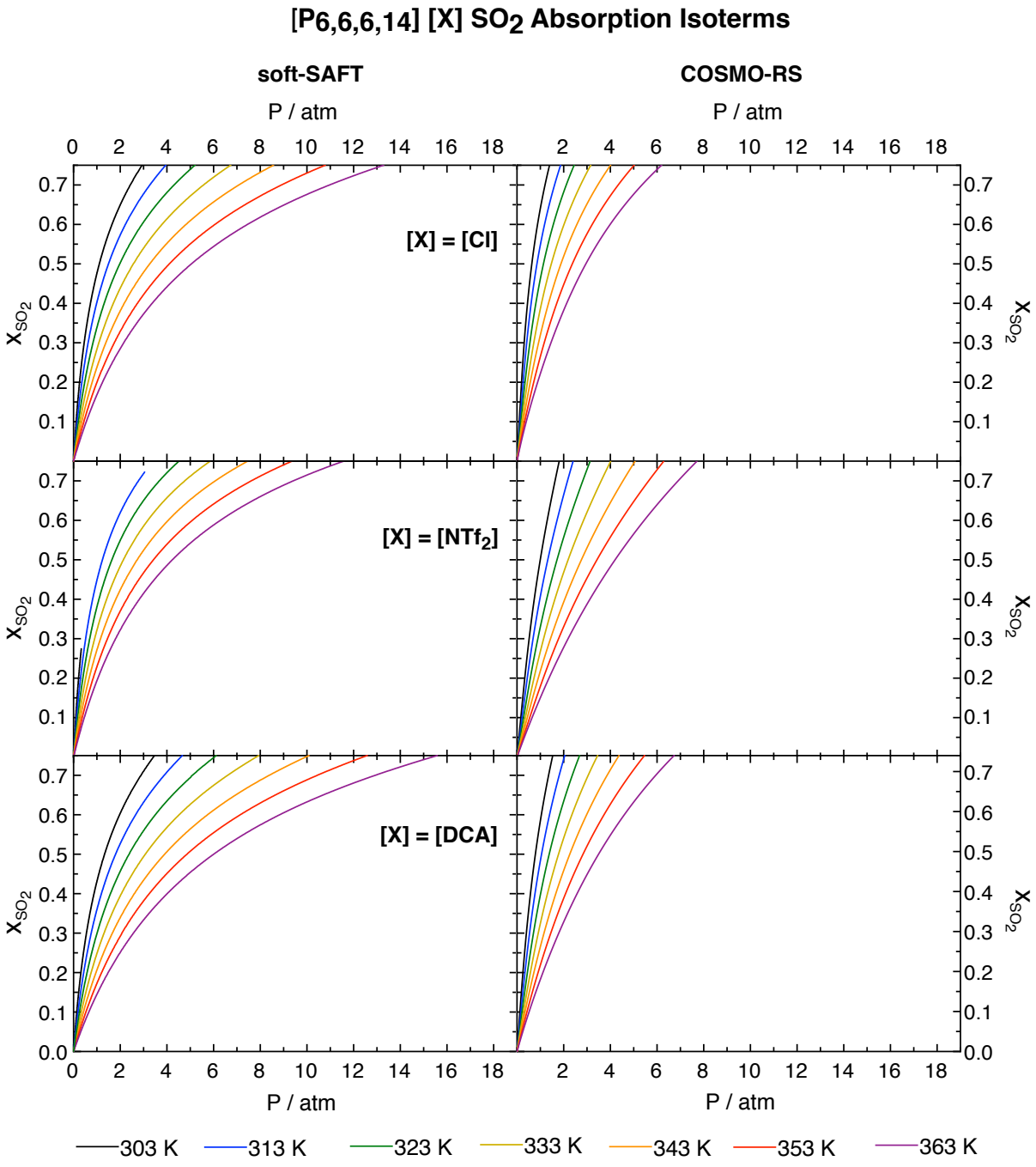

Figure 3.29. SO_2 absorption isotherms calculated with soft-SAFT EoS (left) and COSMO-RS (right) in the three studied ILs. Experimental data are not available for these systems, so it is provided in a purely predictive way.

To evaluate the absorption affinity of both gas molecules into the three ILs, the enthalpy of dissolution (ΔH_i^{dis}), the entropy of dissolution (ΔS_i^{dis}), and the Henry's coefficients (H_i) have been obtained. First, the Clausius-Clapeyron equation (eq. 3.4) has been used to calculate the enthalpy of dissolution of the two gases in all ILs. The effect of the uptake has been evaluated by the calculation of the ΔH_i^{dis} at infinite dilution (*i.e.*, $x_i = 10^{-3}$) and at high gas concentration (*i.e.*, $x_i = 0.75$) to compare with other CO_2 capture technologies (Table 3.13). According to

Table 3.13. Enthalpies and entropies of dissolution at low (x_i = 10^{-3}) and high (x_i = 0.75) molar fractions of CO_2 and SO_2.

			ΔH_i^{dis} / kJ·mol^{-1}		ΔS_i^{dis} / J·(mol·K)$^{-1}$	
	IL		CO_2	SO_2	CO_2	SO_2
soft-SAFT	$[P_{6,6,6,14}][Cl]$	Diluted	-11.5	-24.4	-34.6	-73.6
		Concentrated	-13.1	-23.0	-39.6	-69.4
	$[P_{6,6,6,14}][NTf_2]$	Diluted	-10.6	-23.9	-31.6	-71.0
		Concentrated	-12.1	-23.0	-36.2	-68.4
	$[P_{6,6,6,14}][DCA]$	Diluted	-10.7	-24.1	-32.2	-72.6
		Concentrated	-12.5	-22.9	-37.6	-69.0
COSMO-RS	$[P_{6,6,6,14}][Cl]$	Diluted	-14.1	-18.6	-42.7	-56.0
		Concentrated	-12.7	-22.7	-38.3	-68.6
	$[P_{6,6,6,14}][NTf_2]$	Diluted	-13.9	-19.7	-42.0	-59.4
		Concentrated	-12.5	-22.1	-37.8	-66.6
	$[P_{6,6,6,14}][DCA]$	Diluted	-11.5	-20.5	-34.8	-61.7
		Concentrated	-12.6	-22.6	-37.9	-68.1

soft-SAFT EoS, CO_2 in all ILs has an infinitely diluted enthalpy of dissolution close to -10 kJ·mol^{-1}, that increases to -12/-13 kJ·mol^{-1} at higher CO_2 concentrations. Otherwise, SO_2 has more negative ΔH_i^{dis} values, presenting infinite dilution values close to -24 kJ·mol^{-1} for all ILs that almost do not change with concentration (*i.e.,* it decreases from -24 kJ·mol^{-1} at x_i = 10^{-3} to -23 kJ·mol^{-1} at x_i = 0.75). Contrarily, COSMO-RS gives ΔH_i^{dis} values close to -14 kJ·mol^{-1} for $[P_{6,6,6,14}][Cl]$ and $[P_{6,6,6,14}][NTf_2]$ at x_i = 10^{-3}, which are reduced to -12.5 kJ·mol^{-1} at x_i = 0.75. The COSMO-RS values obtained for CO_2 in $[P_{6,6,6,14}][DCA]$ are in good agreement with soft-SAFT values at both infinite dilution and high gas concentration. Finally, COSMO-RS predicts SO_2 enthalpies of absorption around -19/-20 kJ·mol^{-1} at x_i = 10^{-3} that increase to -22/-23 kJ·mol^{-1} at x_i = 0.75. Both, soft-SAFT and COSMO-RS are in good agreement among each other, especially in the high concentration regime (*i.e.,* around 1 kJ·mol^{-1} difference), and slightly less in the infinite dilution region (*i.e.,* around 4 kJ·mol^{-1}).

From the obtained results, one can see that the enthalpies of dissolution of CO_2 in all ILs range from -10 kJ·mol^{-1} to -14 kJ·mol^{-1}. These values are significantly lower (*i.e.,* in absolute value) than the heats of adsorption of microporous materials such as Mg-MOF-74 (*i.e.,* -44.7 kJ·mol^{-1}) or Faujasites with low Si/Al ratio (*i.e.,* -44.0 kJ·mol^{-1} for NaX). In fact, the obtained enthalpy is similar to the isosteric heat of the DAY Faujasite (*i.e.,* -14.0 kJ·mol^{-1}), which did not exhibit relevant interactions with CO_2. Fortunately, the SO_2 enthalpy of absorption in all ILs range from

-20 kJ·mol^{-1} to -24 kJ·mol^{-1}. If the ΔH_i^{dis} of SO_2 was significantly larger (*e.g.,* between -52.8 kJ·mol^{-1} and -82.5 kJ·mol^{-1} obtained from the q_{st} values of Figure 3.16 for Mg-MOF-74), the separation technology would become poisoned by SO_2 preventing it to capture any additional gas. However, this interaction is relatively weak, which supports the possibility of desorbing SO_2 to recover the solvent.

Similarly to ΔH_i^{dis}, the entropy of dissolution can be calculated from the temperature dependence of the absorption isotherms (eq. 3.21). The obtained results at infinite dilution and high concentration are also compiled in Table 3.13. It can be seen again how soft-SAFT and COSMO-RS agree within 2 J·(mol·K)$^{-1}$ in the high-concentration ΔS_i^{dis} values for [$P_{6,6,6,14}$][Cl], [$P_{6,6,6,14}$][NTf_2] and [$P_{6,6,6,14}$][DCA]. On the other hand, infinite dilution values agree for [$P_{6,6,6,14}$][DCA] in less than 4 J·(mol·K)$^{-1}$, whereas [$P_{6,6,6,14}$][Cl] and [$P_{6,6,6,14}$][NTf_2] give higher deviations (*i.e.,* 8-10 J·(mol·K)$^{-1}$). The obtained results show that both gases lose entropy upon absorption, and SO_2 loses almost the double than CO_2.

$$\Delta S_i^{dis} = -R\left(\frac{\partial \ln P}{\partial \ln T}\right)_{x_i} \qquad 3.21$$

The Henry's coefficients have been obtained from the slope of the absorption isotherms at very low pressure for both methods (Table 3.14). When comparing the CO_2/IL Henry's coefficients predicted by soft-SAFT EoS and COSMO-RS, it can be seen that [$P_{6,6,6,14}$][DCA] is well described regardless the method used. Also, the value of [$P_{6,6,6,14}$][Cl] is slightly higher than the experimental

Table 3.14. CO_2/IL and SO_2/IL Henry's coefficients in the three studied ILs in comparison to the available experimental values for CO_2 as a function of temperature.

		$H_{CO_2}^{exp} \times 10^3$ / atm^{-1}	$H_{CO_2} \times 10^3$ / atm^{-1}			$H_{SO_2} \times 10^3$ /atm^{-1}		
	IL	303 K	303 K	333 K	363 K	303 K	333 K	363 K
soft-SAFT	[$P_{6,6,6,14}$][Cl]	33 ± 2 [121]	37	26	19	1000	400	204
	[$P_{6,6,6,14}$][NTf_2]	30 ± 6 [151]	49	32	24	1250	476	238
	[$P_{6,6,6,14}$][DCA]	34 ± 4 [151]	37	24	18	833	333	169
COSMO-RS	[$P_{6,6,6,14}$][Cl]	33 ± 2 [121]	39	25	16	1000	500	286
	[$P_{6,6,6,14}$][NTf_2]	30 ± 6 [151]	36	23	14	588	270	161
	[$P_{6,6,6,14}$][DCA]	34 ± 4 [151]	36	23	16	833	370	208

H_{CO_2} for both techniques. Notice also that [$P_{6,6,6,14}$][NTf_2] is significantly overestimated by soft-SAFT EoS but not by COSMO-RS. It was previously seen how COSMO-RS provided a reasonably good description in the low-pressure absorption isotherms, and it is now seen again in the prediction of Henry's coefficients. A comparison of the obtained CO_2/IL Henry's coefficients with other families of ILs studied in the bibliography, reveals that tetraalkylphosphonium ILs have large H_{CO_2}, which implies that these ILs have a significantly large affinity for CO_2. Some examples to compare are [C_4mim][PF_6] [152] with a value of $H_{CO_2} \times 10^3 = 18$ atm^{-1}, [C_4mim][BF_4] [153] with a value of $H_{CO_2} \times 10^3 = 16$ atm^{-1} or [C_2mim][DCA] [154] with $H_{CO_2} \times 10^3 = 10$ atm^{-1}. In fact, some of the ILs with the highest CO_2 affinity have Henry's coefficients in the same order than the studied [$P_{6,6,6,14}$][X] ILs. Some examples are [$C_n$mim][NTf_2] [155,156] with n = 2, 4 and 6 that have values of $H_{CO_2} \times 10^3 = 25$ atm^{-1}, 27 atm^{-1} and 29 atm^{-1}, respectively.

Regarding SO_2, the values of H_{SO_2} are significantly higher than H_{CO_2}, denoting its higher affinity towards the three ILs. The increase of temperature from 303 K to 333 K reduce the Henry's coefficients of CO_2 in all IL by approximately a 30-35 %, whereas in the case of SO_2 they are reduced by a 55-60 %. Similarly, the values of H_{CO_2} and H_{SO_2} are reduced by a 45-60 % and a 70-80 % respectively, when increasing the temperature from 303 K to 363 K. High temperatures induce larger penalties in SO_2 absorption than CO_2 due to the higher ΔS_i^{dis} of SO_2. This effect is also reflected in the selectivity values obtained from the ratio of Henry's coefficients (Table 3.15). According to the results obtained, SO_2 absorbs between 15 and 25 times more than CO_2 in the ILs at 303 K. The increase of temperature reduces the selectivity of the material towards SO_2, dropping its selectivity a 55-60 % according to soft-SAFT EoS or a 30-40 % according to COSMO-RS. This favors CO_2 capture, but

Table 3.15. SO_2/CO_2 selectivity values obtained for the three studied ILs as a function of temperature.

		S_{SO_2/CO_2}		
	IL	303 K	333 K	363 K
soft-SAFT	[$P_{6,6,6,14}$][Cl]	27.10	15.24	10.9
	[$P_{6,6,6,14}$][NTf_2]	25.75	14.67	9.93
	[$P_{6,6,6,14}$][DCA]	24.75	13.70	9.37
COSMO-RS	[$P_{6,6,6,14}$][Cl]	25.40	20.25	18.40
	[$P_{6,6,6,14}$][NTf_2]	16.53	11.92	11.21
	[$P_{6,6,6,14}$][DCA]	23.17	16.37	13.13

the selectivity of all ILs towards SO_2 is still between 10 and 20 times higher than CO_2 at 363 K.

3.4.3 Ternary Absorption Isotherms from soft-SAFT EoS

The selectivity of ILs towards CO_2 and SO_2 have been evaluated also in a ternary mixture to determine the effect of pressure and competition between both species. Ternary diagrams have been built at the temperature of 333 K and pressures between 1 atm and 40 atm to model common post-combustion conditions (Figure 3.30). It was previously shown by Llovell *et al.,*[117] that soft-SAFT is capable of reproducing the VLE of a binary mixture of CO_2 and SO_2, which validates the k_{CO_2/SO_2} value. The results of Llovell *et al.,* also shown that the VLE region of the gas mixture is located at pressures higher than 10 atm at 333 K. This is also seen in the calculated ternary diagrams, where the coexistence lines reach the binary CO_2/SO_2 mixture axis at pressures between 10 atm and 20 atm for all ILs. From the coexistence lines, one can see that $[P_{6,6,6,14}][NTf_2]$ is the IL with the largest liquid region (*i.e.,* the area close to the IL axis), which means that it has the largest absorption capacity of the three ILs for a mixture of SO_2/CO_2 gas. Additionally, the coexistence line is positioned more to the right than the other ILs, denoting a higher CO_2 capacity. Finally, $[P_{6,6,6,14}][Cl]$ and $[P_{6,6,6,14}][DCA]$ have a very similar behavior and slightly lower capacities than $[P_{6,6,6,14}][NTf_2]$.

Three different CO_2/SO_2 gas mixtures have been selected, with different compositions, to evaluate the CO_2 and SO_2 selectivity of the ILs at mixture conditions: first, a gas with a 99.9 % of CO_2 and a 0.1 % of SO_2, second, with a 90 % of CO_2 and a 10 % of SO_2, and third, an equimolar gas mixture (*i.e.,* 50 % of CO_2 and 50 % of SO_2). The two former concentrations simulate flue gases with higher amounts of CO_2 than SO_2, which is the common case in flue gas mixtures, whereas the latter composition represents the hypothetical situation where both gases are at the same conditions.

The selectivity values obtained by eq. 3.2 at low pressures (*i.e.,* at 1 atm or 5 atm) are comparable to the ones obtained by the ratio of Henry's coefficients and are compiled in Table 3.16. Additionally, the IL selectivity is not strongly dependent on the CO_2/SO_2 ratio of the gas mixture. On the other hand, the increase of pressure up to 40 atm reduces the SO_2 selectivity with respect CO_2 by approximately a 25-30 %. However, all ILs are between 8 and 11 times more selective towards SO_2 than for CO_2 at 40 atm, which still prevents separation via CO_2 capture. Otherwise, if separation is performed via SO_2 capture, low pressures and temperatures should be

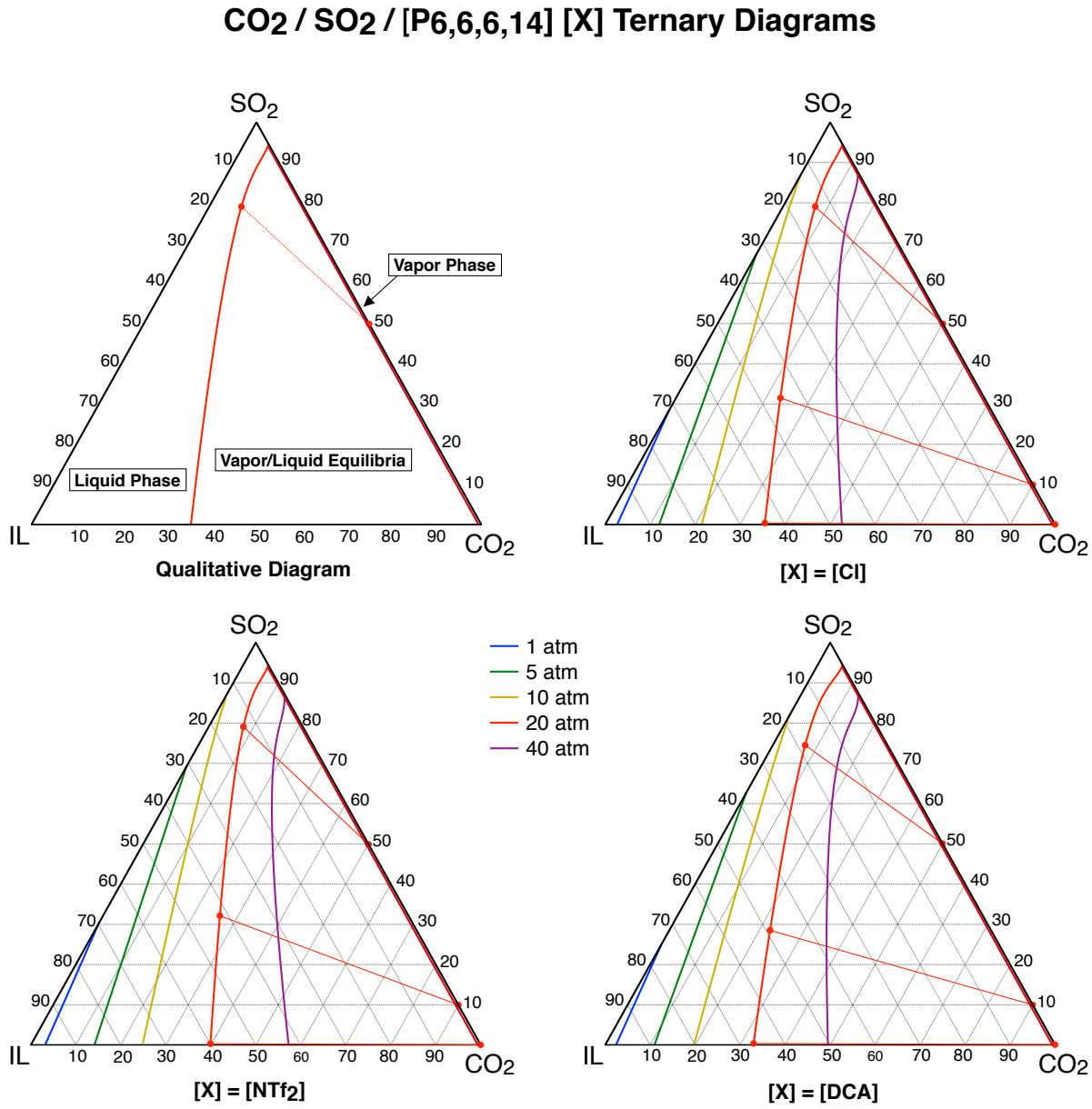

Figure 3.30. CO_2/SO_2/IL ternary absorption diagrams for all studied ILs of this work at 333 K predicted by soft-SAFT EoS. The coexistence VLE curves at a fixed temperature and pressure are represented in solid lines from 1 atm to 40 atm. Additionally, a qualitative ternary diagram is also included for better understanding of the phase equilibria regions. The dots correspond to liquid and vapor phases at 20 atm at equilibrium for three different flue gas compositions (*i.e.,* 99.9 % / 0.1 %, 90 % / 10 % and 50 % / 50 % of CO_2/SO_2).

used to enhance the selectivity of the IL towards SO_2. Also, the most SO_2 selective IL (*i.e.,* the $[P_{6,6,6,14}][Cl]$) should be used to optimize the separation process by capturing the highest amount of SO_2 possible.

Table 3.16. Selectivity of CO_2 and SO_2 in the tree ILs obtained from ternary diagrams. The results are obtained with soft-SAFT EoS at 333 K at different flue gas compositions and pressures.

		S_{SO_2/CO_2}				
	IL	1 atm	5 atm	10 atm	20 atm	40 atm
99.9 % CO_2 0.1 % SO_2	$[P_{6,6,6,14}][Cl]$	-	14.59	14.00	12.92	11.01
	$[P_{6,6,6,14}][NTf_2]$	-	13.04	12.53	11.61	9.95
	$[P_{6,6,6,14}][DCA]$	-	13.36	12.87	11.95	10.30
90 % CO_2 10 % SO_2	$[P_{6,6,6,14}][Cl]$	15.00	14.27	13.51	12.28	10.44
	$[P_{6,6,6,14}][NTf_2]$	13.41	12.83	11.20	11.16	9.54
	$[P_{6,6,6,14}][DCA]$	13.72	13.14	12.50	11.44	9.77
50 % CO_2 50 % SO_2	$[P_{6,6,6,14}][Cl]$	14.71	13.36	12.27	11.09	-
	$[P_{6,6,6,14}][NTf_2]$	13.21	12.16	11.29	10.32	-
	$[P_{6,6,6,14}][DCA]$	13.52	12.43	11.50	10.33	-

3.4.4 Summary and Conclusions

In this part of the thesis two different thermodynamic fluid theories (*i.e.,* soft-SAFT EoS and COSMO-RS) have been used to describe the thermophysical properties of three phosphonium-based ILs and their CO_2 and SO_2 absorption capabilities. Accurate associative models for soft-SAFT EoS have been derived from the combination of DFT interaction energies and ADF/COSMO σ-profiles. It was shown that the selected coarse-grained models permitted a reasonably good reproduction of pure IL properties by soft-SAFT EoS, validating them accordingly.

Binary absorption isotherms have been built with soft-SAFT EoS and COSMO-RS. The results obtained suggest that COSMO-RS is a suitable tool to reproduce the low-pressure/composition region of the absorption isotherms, obtaining good estimates for the Henry's coefficients and selectivity values. Notice that COSMO-RS is, in practice, a predictive method and it does not require any previous experimental data to use it. On the other hand, soft-SAFT EoS is capable of reproducing the overall shape of the absorption isotherms significantly better than COSMO-RS but requires adjusting binary interaction parameters. Additionally, in this thesis, soft-SAFT EoS was fitted to reproduce the isotherms in a wide range of pressures with a single temperature independent binary interaction parameter, so the accurate description of the low-

pressure/composition region can be compromised. For this reason, it seems that a good working procedure to obtain gas/IL absorption properties could be to use COSMO-RS at low pressures to predict Henry's coefficients and use soft-SAFT EoS to obtain high-pressure absorption isotherms.

The three studied solvents have a significantly high CO_2 affinity in comparison to many other ILs, but their higher selectivity for SO_2 hampers the CO_2 capture and separation. If the concentration of SO_2 in the flue gas mixture is very small, they can be used to capture CO_2 at high pressures and entirely recover the solvent reducing the pressure to 1 atm. However, if the concentration of SO_2 is large, it will absorb preferentially in any IL, recovering an impure CO_2 gas. In this situation it can be beneficial to separate the CO_2 by capturing the pollutant with the most SO_2 selective IL (*i.e.,* $[P_{6,6,6,14}][Cl]$). This practice can be carried out because SO_2 is not interacting strong enough with the solvent to effectively poison it, making the recovery step feasible. If the post-combustion flue gas is treated with an IL at relatively low temperatures and atmospheric pressures, the mixture will have its SO_2 stripped, letting only a $CO_2/N_2/O_2$ mixture, which can be separated in a sequential step to recover CO_2 in absence of SO_2.

3.5 Summary and General Conclusions

Three different materials were studied with computational models and methods to evaluate their suitability for CO_2 capture and separation from post-combustion flue gases. In Section 3.2 a set of Zeolites of the Faujasite family were evaluated to separate CO_2 from a flue gas, which also contained N_2 and O_2. To have a wide understanding of these kinds of systems two different techniques were applied: (i) DFT calculations to analyze the most fundamental interactions between gas molecules and the material and (ii) GCMC calculations to obtain collective properties such as equilibrium adsorption isotherms as a function of pressure and temperature.

From DFT it was seen that there are three main adsorption sites in the Faujasite framework: the main pore walls, the sodalite cages and the extra-framework cations. Even though the sodalite cage is a relatively favorable site, as seen by its high interaction energies, the diffusion of gas molecules from the main pore to the sodalite cages is strongly hindered by large energy barriers, in practice limiting the adsorption to the main pores. In fact, the extra-framework cations are usually located at the entrances of sodalite cages potentially making the diffusion harder. On the other hand, the walls of the main pores are not very strongly interacting sites, as revealed by the low interaction energies for all gas molecules. Finally, the extra-framework cations have very localized charges that can strongly interact with polar gas molecules (*i.e.,* either dipolar or quadrupolar), increasing their adsorption energies significantly. In the case of the studied

Faujasites, these are the most stable sites for CO_2 adsorption. Other less polar gases, such as N_2 and O_2 do not interact with cations as strongly as CO_2, which allows a very selective separation.

From GCMC simulations it was possible to build adsorption isotherms of pure CO_2, N_2, O_2 and a ternary gas mixture. The results obtained confirmed the DFT conclusions, showing isosteric heats in good agreement with the DFT interaction energies and higher adsorption for CO_2 than for other gases. Also, the preferential adsorption upon the extra-framework cations allowed the structures to saturate at significantly lower pressures and to be more selective towards CO_2 capture. However, from GCMC it was concluded that the increase of affinity comes at the cost of reducing the total adsorption volume and saturation uptake of the framework. For this reason, depending on the type of swing adsorption process selected for CO_2 recovery it could be more efficient to use structures with different Si/Al ratio. For example, in a PSA at [10 atm/1 atm] of adsorption/desorption pressure, the structure that recovers higher amount of CO_2 per kg and cycle is the Si/Al = 7, whereas if an VSA process with [1 atm/0.1 atm] of adsorption/desorption pressure, the most efficient structure would be the Si/Al = 3. Both structures yield similar purities compared to the reference NaX Faujasite, but with higher working capacities.

After this study, in Section 3.3 the CO_2 separation with Mg-MOF-74 from a mixture with N_2 and SO_2 is evaluated. The O_2 was no longer considered in the post-combustion flue gas mixtures because it behaved similarly to N_2. To that end, the % of O_2 was transferred to N_2 to model the less polar fraction of the flue gas and SO_2 was added in its place. In this section the CO_2 adsorption capacity of Mg-MOF-74 was evaluated along with the negative effect produced by the presence of SO_2 as a pollutant in the $CO_2/N_2/SO_2$ flue gas.

Similarly to the first study, DFT calculations were performed to understand the main fundamental interactions that allow Mg-MOF-74 to effectively capture CO_2. From the results obtained, two main adsorption sites were located: (i) the metal site and (ii) the linker site. The interaction energies of gas molecules at the metal site are significantly strong for molecules of higher polarity, that is $SO_2 > CO_2 > N_2$. In fact, CO_2 exhibits even stronger adsorption energies into the Mg-MOF-74 metal sites than in the Faujasite extra-framework cations. However, it also has very strong adsorption for SO_2 (*i.e.,* almost doubling CO_2), which can poison the metal sites preventing CO_2 capture. The secondary site is a weak linker that, in principle, does not favor the adsorption of SO_2 in front of CO_2. The inclusion of gas-gas lateral interactions (*i.e.,* the effect of the coverage) have a relatively weak effect in CO_2 adsorption but it increases dramatically the adsorption of SO_2 into the linker sites.

The lack of accurate force fields to reproduce the SO_2/MOF interactions forced to use a mean-field thermodynamic fluid theory based on a dual-site Langmuir isotherm equation, where the

equilibrium constant was obtained by the combination of DFT calculations and statistical thermodynamics. This technique permitted the prediction of gas adsorption isotherms for pure CO_2, N_2, SO_2 and several ternary gas mixtures with different SO_2 content. As it was expected from DFT, SO_2 is capable of saturating all Mg^{2+} metal sites at very low pressures, preventing any CO_2 adsorption. In fact, both the isosteric heats and Henry's coefficients of pure SO_2 in Mg-MOF-74 point towards a large selectivity of the material towards SO_2. The modeling of mixtures showed that at SO_2 concentrations higher than 0.002 %, the purity of the adsorbed CO_2 starts dropping due to SO_2 adsorption. Fortunately, when SO_2 adsorbs into the framework it cannot be easily desorbed, so the recovered CO_2 still has a relatively high degree of purity and it has only a small fraction of N_2. Notice that small amounts of SO_2 can be handled depending on the swing adsorption cycle selected. In a VTSA (*i.e.,* with [1 atm, 313 K/0.1 atm, 373 K] of adsorption/desorption pressure and temperature) the desorption step is very effective, recovering high amounts of CO_2 but risking the desorption of SO_2 that would contaminate the recovered mixture. Other cycles such as TSA (*i.e.,* with [313 K/373 K] of adsorption/desorption temperature) or VSA (*i.e.,* with [1 atm/0.1 atm] of adsorption/desorption pressure) have more mild regeneration steps, recovering less CO_2 but allowing to work at higher SO_2 content. However, it is important to eliminate the SO_2 from the gas mixture because it has significant harmful effects on CO_2 adsorption.

A final CO_2 separation technology was studied considering phosphonium-based ILs in Section 3.4. The main advantage of ILs is that they are chemically stable liquid solvents that can be directly implemented as amine substitutes in the current separation by absorption. As SO_2 is the main competitor for CO_2 capture and separation, the gas mixture studied in this section only contained these two gases. Two different methods were applied simultaneously to study gas absorption in ILs (*i.e.,* ADF/COSMO-RS and soft-SAFT EoS). First, DFT calculations with ADF/COSMO-RS were used as an aid to develop a representative coarse-grained model for soft-SAFT EoS. Then, absorption isotherms of pure CO_2 and SO_2 were obtained in a purely predictive way with COSMO-RS. It was seen that COSMO-RS gives reasonable estimates of the absorption properties at the low-pressure/composition region without the need of fitting any parameter. Parallelly, soft-SAFT EoS was validated with pure IL thermophysical data and was then used to obtain pure CO_2 and SO_2 absorption isotherms for the three studied ILs. Only a single temperature independent parameter was enough to reproduce the overall shape of the absorption isotherms at the cost of a low-pressure/composition poorer description. To that end, COSMO-RS can be used to reproduce the low-pressure/composition region whereas soft-SAFT EoS can focus onto the absorption properties at higher pressures.

The combined results obtained show that the studied ILs have relatively strong affinity for CO_2, presenting high Henry's coefficients comparable to some of the reference ILs for CO_2

capture. The previously studied microporous materials exhibit higher affinity for polar gases than ILs. For example, the enthalpies of absorption in the three ILs are comparable to the interaction energies of the inefficient DAY Faujasite. At the light of these results, it seems a better option to use microporous materials instead of ILs to capture CO_2. However, the three ILs have a higher affinity towards SO_2 capture than CO_2, which hampers the applicability of this technology. This conclusion is achieved from the calculated enthalpies of absorption, Henry's coefficients, selectivity and absorption isotherms, where SO_2 always surpasses CO_2. Fortunately, the relatively weak gas/IL interactions are also reflected in an improved regenerability of the material, which potentially allows SO_2 to be quantitatively desorbed from the liquid solvent. This feature opens the possibility of using ILs to separate CO_2 by selective SO_2 capture. Then, CO_2 can be recovered in a future separation step while the IL can be regenerated desorbing the previously captured SO_2.

Compiling the results of the three studies, different CO_2 separation setups can be proposed as a function of the nature of the flue gas mixture. Microporous materials excel in selective capture of CO_2 via strong electrostatic interactions from their metal cations. However, they generally interact more strongly with dipolar molecules (*e.g.,* SO_2) than with molecules with quadrupolar moment (*e.g.,* CO_2). According to the obtained results, at very low % of SO_2 microporous materials can still be used effectively. However, higher SO_2 content totally poisons the structures and do not allow an effective CO_2 separation. For these situations, ILs could be used to selectively capture SO_2 and remove it from the flue gas. Then, a second separation stage could employ microporous materials to capture CO_2 as already proposed.

3.6 References

1 M. M. F. Hasan, E. L. First and C. A. Floudas, Cost-Effective CO_2 Capture Based on in Silico Screening of Zeolites and Process Optimization, *Phys. Chem. Chem. Phys.*, 2013, **15**, 17601–17618.

2 B. P. Spigarelli and S. K. Kawatra, Opportunities and Challenges in Carbon Dioxide Capture, *J. CO2 Util.*, 2013, **1**, 69–87.

3 C. L. Quéré, R. M. Andrew, J. G. Canadell, S. Sitch, J. I. Korsbakken, G. P. Peters, A. C. Manning, T. A. Boden, P. P. Tans, R. A. Houghton, R. F. Keeling, S. Alin, O. D. Andrews, P. Anthoni, L. Barbero, L. Bopp, F. Chevallier, L. P. Chini, P. Ciais, K. Currie, C. Delire, S. C. Doney, P. Friedlingstein, T. Gkritzalis, I. Harris, J. Hauck, V. Haverd, M. Hoppema, K. Klein Goldewijk, A. K. Jain, E. Kato, A. Körtzinger, P. Landschützer, N. Lefèvre, A. Lenton, S. Lienert, D. Lombardozzi, J. R. Melton, N. Metzl, F. Millero, P. M. S. Monteiro, D. R. Munro,

J. E. M. S. Nabel, S. Nakaoka, K. O'Brien, A. Olsen, A. M. Omar, T. Ono, D. Pierrot, B. Poulter, C. Rödenbeck, J. Salisbury, U. Schuster, J. Schwinger, R. Séférian, I. Skjelvan, B. D. Stocker, A. J. Sutton, T. Takahashi, H. Tian, B. Tilbrook, I. T. van der Laan-Luijkx, G. R. van der Werf, N. Viovy, A. P. Walker, A. J. Wiltshire and S. Zaehle, Global Carbon Budget 2016, *Earth Syst. Sci. Data*, 2016, **8**, 605–649.

4 C. P. Morice, J. J. Kennedy, N. A. Rayner and P. D. Jones, Quantifying Uncertainties in Global and Regional Temperature Change Using an Ensemble of Observational Estimates: The HadCRUT4 Data Set, *J. Geophys. Res. Atmos.*, 2012, **117**, D08101:1-22.

5 S. E. Schwartz, Unrealized Global Temperature Increase: Implications of Current Uncertainties, *J. Geophys. Res. Atmos.*, 2018, **123**, 3462–3482.

6 V. J. Fabry, B. A. Seibel, R. A. Feely and J. C. Orr, Impacts of Ocean Acidification on Marine Fauna and Ecosystem Processes, *ICES J. Mar. Sci.*, 2008, **65**, 414–432.

7 J. M. Guinotte and V. J. Fabry, Ocean Acidification and Its Potential Effects on Marine Ecosystems, *Ann. N. Y. Acad. Sci.*, 2008, **1134**, 320–342.

8 *Paris Agreement*, United Nation, Paris, 2016.

9 A. A. Kiss, J. J. Pragt, H. J. Vos, G. Bargeman and M. T. de Groot, Novel Efficient Process for Methanol Synthesis by CO_2 Hydrogenation, *Chem. Eng. J.*, 2016, **284**, 260–269.

10 S. Rönsch, J. Schneider, S. Matthischke, M. Schlüter, M. Götz, J. Lefebvre, P. Prabhakaran and S. Bajohr, Review on Methanation – From Fundamentals to Current Projects, *Fuel*, 2016, **166**, 276–296.

11 B. Haut, V. Halloin, T. Cartage and A. Cockx, Production of Sodium Bicarbonate in Industrial Bubble Columns, *Chem. Eng. Sci.*, 2004, **59**, 5687–5694.

12 G. J. Millar and M. Collins, Industrial Production of Formaldehyde Using Polycrystalline Silver Catalyst, *Ind. Eng. Chem. Res.*, 2017, **56**, 9247–9265.

13 W.-J. Kim, J.-D. Kim and S.-G. Oh, Supercritical Carbon Dioxide Extraction of Caffeine from Korean Green Tea, *Sep. Sci. Technol.*, 2007, **42**, 3229–3242.

14 B. Liu, J. Shi, M. Wang, J. Zhang, B. Sun, Y. Shen and X. Sun, Reduction in Interfacial Tension of Water–Oil Interface by Supercritical CO_2 in Enhanced Oil Recovery Processes Studied with Molecular Dynamics Simulation, *J. Supercrit. Fluids*, 2016, **111**, 171–178.

15 D. P. Rall, Review of the Health Effects of Sulfur Oxides, *Environ. Health Perspect.*, 1974, **8**, 97–121.

16 National Research Council (US), *Assessment of Exposure-Response Functions for Rocket-Emission Toxicants*, National Academies Press, Washington, 1998.

17 A. Fihri, R. Mahfouz, A. Shahrani, I. Taie and G. Alabedi, Pervaporative desulfurization of gasoline: A review, *Chem. Eng. Process. Process Intensif.*, 2016, **107**, 94–105.

18 H. Yang, Z. Xu, M. Fan, R. Gupta, R. B. Slimane, A. E. Bland and I. Wright, Progress in Carbon Dioxide Separation and Capture: a Review, *J. Environ. Sci. China*, 2008, **20**, 14–27.

19 C. Gouedard, D. Picq, F. Launay and P.-L. Carrette, Amine Degradation in CO_2 Capture. I. A Review, *Int. J. Greenh. Gas Control*, 2012, **10**, 244–270.

20 A. Krzemień, A. Więckol-Ryk, A. Duda and A. Koteras, Risk Assessment of a Post-Combustion and Amine-Based CO_2 Capture Ready Process, *J. Sustain. Min.*, 2013, **12**, 18–23.

21 H. M. Stowe and G. S. Hwang, Fundamental Understanding of CO_2 Capture and Regeneration in Aqueous Amines from First-Principles Studies: Recent Progress and Remaining Challenges, *Ind. Eng. Chem. Res.*, 2017, **56**, 6887–6899.

22 Y. X. Lv, G. H. Yan, C. Q. Xu, M. Xu and L. Sun, Review on Membrane Technologies for Carbon Dioxide Capture from Power Plant Flue Gas, *Adv. Mater. Res.*, 2013, **602**, 1140–1144.

23 Ch. Baerlocher and L.B. McCusker, Database of Zeolite Structures, http://www.iza-structure.org/databases/, (accessed March 27, 2019).

24 G. D. Pirngruber, P. Raybaud, Y. Belmabkhout, J. Čejka and A. Zukal, The role of the Extra-Framework Cations in the Adsorption of CO_2 on Faujasite Y, *Phys. Chem. Chem. Phys.*, 2010, **12**, 13534–13546.

25 R. Krishna and J. M. van Baten, A Comparison of the CO_2 Capture Characteristics of Zeolites and Metal–Organic Frameworks, *Sep. Purif. Technol.*, **87**, 120–126.

26 K. N. Marsh, J. A. Boxall and R. Lichtenthaler, Room Temperature Ionic Liquids and their Mixtures—a Review, *Fluid Phase Equilibr.*, 2004, **219**, 93–98.

27 R. D. Rogers and K. R. Seddon, Ionic Liquids--Solvents of the Future?, *Science*, 2003, **302**, 792–793.

28 T. Welton, Room-Temperature Ionic Liquids. Solvents for Synthesis and Catalysis, *Chem. Rev.*, 1999, **99**, 2071–2084.

29 Y.-S. Bae and R. Q. Snurr, Development and Evaluation of Porous Materials for Carbon Dioxide Separation and Capture, *Angew. Chem. Int. Ed.*, 2011, **50**, 11586–11596.

30 F. J. Blas and L. F. Vega, Thermodynamic Behaviour of Homonuclear and Heteronuclear Lennard-Jones Chains with Association Sites from Simulation and Theory, *Mol. Phys.*, 1997, **92**, 135–150.

31 M. Moshoeshoe, M. S. Nadiye-Tabbiruka and V. Obuseng, A Review of the Chemistry, Structure, Properties and Applications of Zeolites, *Am. J. Mater. Sci.*, 2017, **7**, 196–221.

32 H. Prats, D. Bahamon, G. Alonso, X. Giménez, P. Gamallo and R. Sayós, Optimal Faujasite Structures for Post Combustion CO_2 Capture and Separation in Different Swing Adsorption Processes, *J. CO2 Util.*, 2017, **19**, 100–111.

33 T. Armbruster and M.E. Gunter, *Natural Zeolites: Occurrence, Properties, Applications*, Mineralogical Society of America, Chantilly, 2001.

34 R. Castañeda, A. Corma, V. Fornés, F. Rey and J. Rius, Synthesis of a New Zeolite Structure ITQ-24, with Intersecting 10- and 12-Membered Ring Pores, *J. Am. Chem. Soc.*, 2003, **125**, 7820–7821.

35 H. Li and O. M. Yaghi, Transformation of Germanium Dioxide to Microporous Germanate 4-Connected Nets, *J. Am. Chem. Soc.*, 1998, **120**, 10569–10570.

36 T. E. Gier, X. Bu, P. Feng and G. D. Stucky, Synthesis and Organization of Zeolite-like Materials with Three-Dimensional Helical Pores, *Nature*, 1998, **395**, 154–157.

37 B. M. Weckhuysen and J. Yu, Recent Advances in Zeolite Chemistry and Catalysis, *Chem. Soc. Rev.*, 2015, **44**, 7022–7024.

38 C. J. Harpel, P. R. Kyle and N. W. Dunbar, Englacial Tephrostratigraphy of Erebus Volcano, Antarctica, *J. Volcanol. Geotherm. Res.*, 2008, **177**, 549–568.

39 M. Khodayar and H. Franzson, Fracture Pattern of Thjórsárdalur Central Volcano with Respect to Rift-Jump and a Migrating Transform Zone in South Iceland, *J. Struct. Geol.*, 2007, **29**, 898–912.

40 I. Axuma, Geology of Natural Zeolites and Zeolitic Rocks, *Pure & Appl. Chem.*, 1980, **52**, 2115–2130.

41 H. St. Claire-Deville, Reproduction de la Lévyne, *Comptes Rendus Acad. Sci.*, 1862, **54**, 324–327.

42 Ch. Baerlocher, L.B. McCusker and D.H. Olson, *Atlas of Zeolite Framework Types*, Elsevier Science, Amsterdam, 2007.

43 K. Chen, J. Damron, C. Pearson, D. Resasco, L. Zhang and J. L. White, Zeolite Catalysis: Water Can Dramatically Increase or Suppress Alkane C–H Bond Activation, *ACS Catal.*, 2014, **4**, 3039–3044.

44 J. Weitkamp, Zeolites and catalysis, *Solid State Ionics*, 2000, **131**, 175–188.

45 S. Bhatia, J. Beltramini and D. D. Do, Deactivation of Zeolite Catalysts, *Catal. Rev.*, 1989, **31**, 431–480.

46 M. Rožić, Š. Cerjan-Stefanović, S. Kurajica, V. Vančina and E. Hodžić, Ammoniacal Nitrogen Removal from Water by Treatment with Clays and Zeolites, *Water Res.*, 2000, **34**, 3675–3681.

47 A. M. Cardoso, M. B. Horn, L. S. Ferret, C. M. N. Azevedo and M. Pires, Integrated Synthesis of Zeolites 4A and Na–P1 Using Coal Fly Ash for Application in the Formulation of Detergents and Swine Wastewater Treatment, *J. Hazard. Mater.*, 2015, **287**, 69–77.

48 M. Pan, H. M. Omar and S. Rohani, Application of Nanosize Zeolite Molecular Sieves for Medical Oxygen Concentration, *Nanomaterials*, 2017, **7**, 195:1–19.

49 A. Villarreal, G. Garbarino, P. Riani, E. Finocchio, B. Bosio, J. Ramírez and G. Busca, Adsorption and Separation of CO_2 from N_2 -Rich Gas on Zeolites: Na-X Faujasite vs Na-Mordenite, *J. CO2 Util.*, 2017, **19**, 266–275.

50 K. Kusakabe, T. Kuroda, K. Uchino, Y. Hasegawa and S. Morooka, Gas Permeation Properties of Ion-Exchanged Faujasite-type Zeolite Membranes, *AIChE J.*, 1999, **45**, 1220–1226.

51 P. Xiao, J. Zhang, P. Webley, G. Li, R. Singh and R. Todd, Capture of CO_2 from Flue Gas Streams with Zeolite 13X by Vacuum-Pressure Swing Adsorption, *Adsorption*, 2008, **14**, 575–582.

52 W. Löwenstein, The Distribution of Aluminum in the Tetrahedra of Silicates and Aluminates, *Am. Mineral*, 1954, **39**, 92–96.

53 G. Kresse and J. Furthmüller, Efficiency of Ab-Initio Total Energy Calculations for Metals and Semiconductors using a Plane-Wave Basis set, *Comput. Mater. Sci.*, 1996, **6**, 15–50.

54 G. Kresse and J. Furthmüller, Efficient Iterative Schemes for Ab Initio Total-Energy Calculations Using a Plane-Wave Basis Set, *Phys. Rev. B*, 1996, **54**, 11169–11186.

55 J. P. Perdew, K. Burke and M. Ernzerhof, Generalized Gradient Approximation Made Simple, *Phys. Rev. Lett.*, 1996, **77**, 3865–3868.

56 S. Grimme, Semiempirical GGA-type Density Functional Constructed with a Long-Range Dispersion Correction, *J. Comput. Chem.*, 2006, **27**, 1787–1799.

57 S. Grimme, J. Antony, S. Ehrlich and H. Krieg, A Consistent and Accurate Ab Initio Parametrization of Density Functional Dispersion Correction (DFT-D) for the 94 Elements H-Pu, *J. Chem. Phys.*, 2010, **132**, 154104:1–19.

58 C. Beauvais, A. Boutin and A. H. Fuchs, Adsorption of Water in Zeolite Sodium-Faujasite : A Molecular Simulation Study, *C.R. Chimie*, 2005, **8**, 485–490.

59 S. Plimpton, Fast Parallel Algorithms for Short-Range Molecular Dynamics, *J. Comput. Phys.*, 1995, **117**, 1–19.

60 A. García-Sánchez, C. O. Ania, J. B. Parra, D. Dubbeldam, T. J. H. Vlugt, R. Krishna and S. Calero, Transferable Force Field for Carbon Dioxide Adsorption in Zeolites, *J. Phys. Chem. C*, 2009, **113**, 8814–8820.

61 A. Martin-Calvo, J. J. Gutiérrez-Sevillano, J. B. Parra, C. O. Ania and S. Calero, Transferable Force Fields for Adsorption of Small Gases in Zeolites, *Phys. Chem. Chem. Phys.*, 2015, **17**, 24048–24055.

62 A. Martín-Calvo, E. García-Pérez, A. García-Sánchez, R. Bueno-Pérez, S. Hamad and S. Calero, Effect of Air Humidity on the Removal of Carbon Tetrachloride from Air Using Cu–BTC Metal–Organic Framework, *Phys. Chem. Chem. Phys.*, 2011, **13**, 11165–11174.

63 G. Maurin, R. Bell, B. Kuchta, T. Poyet and P. Llewellyn, Adsorption of Non Polar and Quadrupolar Gases in Siliceous Faujasite: Molecular Simulations and Experiments, *Adsorption*, 2005, **11**, 331–336.

64 J. A. Dunne, M. Rao, S. Sircar, R. J. Gorte and A. L. Myers, Calorimetric Heats of Adsorption and Adsorption Isotherms. 2. O_2, N_2, Ar, CO_2, CH_4, C_2H_6, and SF_6 on NaX, H-ZSM-5, and Na-ZSM-5 Zeolites, *Langmuir*, 1996, **12**, 5896–5904.

65 Y.-J. Park, S.-J. Lee, J.-H. Moon, D.-K. Choi and C.-H. Lee, Adsorption Equilibria of O_2, N_2, and Ar on Carbon Molecular Sieve and Zeolites 10X, 13X, and LiX, *J. Chem. Eng. Data*, 2006, **51**, 1001–1008.

66 A. D. Wiersum, J.-S. Chang, C. Serre and P. L. Llewellyn, An Adsorbent Performance Indicator as a First Step Evaluation of Novel Sorbents for Gas Separations: Application to Metal–Organic Frameworks, *Langmuir*, 2013, **29**, 3301–3309.

67 A. H. Berger and A. S. Bhown, Comparing Physisorption and Chemisorption Solid Sorbents for use Separating CO_2 from flue gas using Temperature Swing Adsorption, *Energy Proced.*, 2011, **4**, 562–567.

68 T.-H. Bae, M. R. Hudson, J. A. Mason, W. L. Queen, J. J. Dutton, K. Sumida, K. J. Micklash, S. S. Kaye, C. M. Brown and J. R. Long, Evaluation of Cation-Exchanged Zeolite Adsorbents for Post-Combustion Carbon Dioxide Capture, *Energy Environ. Sci.*, 2012, **6**, 128–138.

69 H. K. Chae, D. Y. Siberio-Pérez, J. Kim, Y. Go, M. Eddaoudi, A. J. Matzger, M. O'Keeffe and O. M. Yaghi, A Route to High Surface Area, Porosity and Inclusion of Large Molecules in Crystals, *Nature*, 2004, **427**, 523–527.

70 S. M. Moosavi, P. G. Boyd, L. Sarkisov and B. Smit, Improving the Mechanical Stability of Metal–Organic Frameworks Using Chemical Caryatids, *ACS Cent. Sci.*, 2018, **4**, 832–839.

71 M. Eddaoudi, J. Kim, N. Rosi, D. Vodak, J. Wachter, M. O'Keeffe and O. M. Yaghi, Systematic Design of Pore Size and Functionality in Isoreticular MOFs and Their Application in Methane Storage, *Science*, 2002, **295**, 469–472.

72 V. V. Butova, M. A. Soldatov, A. A. Guda, K. A. Lomachenko and C. Lamberti, Metal-

Organic Frameworks: Structure, Properties, Methods of Synthesis and Characterization, *Russ. Chem. Rev.*, 2016, **85**, 280–307.

73 L. Jiao, J. Y. R. Seow, W. S. Skinner, Z. U. Wang and H.-L. Jiang, Metal–Organic Frameworks: Structures and Functional Applications, *Mater. Today*, 2018, In Press.

74 N. C. Burtch, H. Jasuja and K. S. Walton, Water Stability and Adsorption in Metal–Organic Frameworks, *Chem. Rev.*, 2014, **114**, 10575–10612.

75 S. Yuan, L. Feng, K. Wang, J. Pang, M. Bosch, C. Lollar, Y. Sun, J. Qin, X. Yang, P. Zhang, Q. Wang, L. Zou, Y. Zhang, L. Zhang, Y. Fang, J. Li and H.-C. Zhou, Stable Metal–Organic Frameworks: Design, Synthesis, and Applications, *Adv. Mater.*, 2018, **30**, 1704303:1–35.

76 K. Lee, J. D. Howe, L.-C. Lin, B. Smit and J. B. Neaton, Small-Molecule Adsorption in Open-Site Metal–Organic Frameworks: A Systematic Density Functional Theory Study for Rational Design, *Chem. Mater.*, 2015, **27**, 668–678.

77 K. Yu, K. Kiesling and J. R. Schmidt, Trace Flue Gas Contaminants Poison Coordinatively Unsaturated Metal–Organic Frameworks: Implications for CO_2 Adsorption and Separation, *J. Phys. Chem. C*, 2012, **116**, 20480–20488.

78 R. Poloni, B. Smit and J. B. Neaton, CO_2 Capture by Metal–Organic Frameworks with van der Waals Density Functionals, *J. Phys. Chem. A*, 2012, **116**, 4957–4964.

79 M. Abu-Ghalia and Y. Dahman, Development and Evaluation of Zeolites and Metal–Organic Frameworks for Carbon Dioxide Separation and Capture, *Energy Technol.*, 2017, **5**, 356–372.

80 L. F. Vega and D. Bahamon, Comparative Study of MOFs and Zeolites For CO_2 Capture and Separation at Process Conditions. In: Abu Dhabi International Petroleum Exhibition & Conference, Abu Dhabi, 2016.

81 J. A. Mason, K. Sumida, Z. R. Herm, R. Krishna and Jeffrey. R. Long, Evaluating Metal–Organic Frameworks for Post-Combustion Carbon Dioxide Capture via Temperature Swing Adsorption, *Energy Environ. Sci.*, 2011, **4**, 3030–3040.

82 S. R. Caskey, A. G. Wong-Foy and A. J. Matzger, Dramatic Tuning of Carbon Dioxide Uptake via Metal Substitution in a Coordination Polymer with Cylindrical Pores, *J. Am. Chem. Soc.*, 2008, **130**, 10870–10871.

83 M. Dion, H. Rydberg, E. Schröder, D. C. Langreth and B. I. Lundqvist, Van der Waals Density Functional for General Geometries, *Phys. Rev. Lett.*, 2004, **92**, 246401:1–4.

84 K. Lee, É. D. Murray, L. Kong, B. I. Lundqvist and D. C. Langreth, Higher-Accuracy van der Waals Density Functional, *Phys. Rev. B*, 2010, **82**, 081101:1–4.

85 B. Vlaisavljevich, J. Huck, Z. Hulvey, K. Lee, J. A. Mason, J. B. Neaton, J. R. Long, C. M.

Brown, D. Alfè, A. Michaelides and B. Smit, Performance of van der Waals Corrected Functionals for Guest Adsorption in the M2(dobdc) Metal–Organic Frameworks, *J. Phys. Chem. A*, 2017, **121**, 4139–4151.

86 J. Park, H. Kim, S. S. Han and Y. Jung, Tuning Metal–Organic Frameworks with Open-Metal Sites and Its Origin for Enhancing CO_2 Affinity by Metal Substitution, *J. Phys. Chem. Lett.*, 2012, **3**, 826–829.

87 K. Tan, S. Zuluaga, H. Wang, P. Canepa, K. Soliman, J. Cure, J. Li, T. Thonhauser and Y. J. Chabal, Interaction of Acid Gases SO_2 and NO_2 with Coordinatively Unsaturated Metal Organic Frameworks: M-MOF-74 (M = Zn, Mg, Ni, Co), *Chem. Mater.*, 2017, **29**, 4227–4235.

88 L. Ding and A. Ö. Yazaydin, How Well Do Metal–Organic Frameworks Tolerate Flue Gas Impurities?, *J. Phys. Chem. C*, 2012, **116**, 22987–22991.

89 W. L. Queen, M. R. Hudson, E. D. Bloch, J. A. Mason, M. I. Gonzalez, J. S. Lee, D. Gygi, J. D. Howe, K. Lee, T. A. Darwish, M. James, V. K. Peterson, S. J. Teat, B. Smit, J. B. Neaton, J. R. Long and C. M. Brown, Comprehensive Study of Carbon Dioxide Adsorption in the Metal–Organic Frameworks M2(dobdc) (M = Mg, Mn, Fe, Co, Ni, Cu, Zn), *Chem. Sci.*, 2014, **5**, 4569–4581.

90 T. M. Becker, J. Heinen, D. Dubbeldam, L.-C. Lin and T. J. H. Vlugt, Polarizable Force Fields for CO_2 and CH_4 Adsorption in M-MOF-74, *J. Phys. Chem. C*, 2017, **121**, 4659–4673.

91 K. Sillar, A. Kundu and J. Sauer, Ab Initio Adsorption Isotherms for Molecules with Lateral Interactions: CO_2 in Metal–Organic Frameworks, *J. Phys. Chem. C*, 2017, **121**, 12789–12799.

92 I. Langmuir, The Adsorption of Gases on Plane Surfaces of Glass, Mica and Platinum, *J. Am. Chem. Soc.*, 1918, **40**, 1361–1403.

93 W. Sun, L.-C. Lin, X. Peng and B. Smit, Computational Screening of Porous Metal-Organic Frameworks and Zeolites for the Removal of SO_2 and NO_x from Flue Gases, *AIChE J.*, 2014, **60**, 2314–2323.

94 A. Ö. Yazaydın, R. Q. Snurr, T.-H. Park, K. Koh, J. Liu, M. D. LeVan, A. I. Benin, P. Jakubczak, M. Lanuza, D. B. Galloway, J. J. Low and R. R. Willis, Screening of Metal−Organic Frameworks for Carbon Dioxide Capture from Flue Gas Using a Combined Experimental and Modeling Approach, *J. Am. Chem. Soc.*, 2009, **131**, 18198–18199.

95 I.D. Masel, *Principles of Adsorption and Reaction on Solid Surfaces*, John Wiley & Sons, New York, 1996.

96 A. Milchev and K. Binder, Monte Carlo Study of a Lattice Gas Model with Non-Additive Lateral Interactions, *Surf. Sci.*, 1985, **164**, 1–18.

97 A. Milchev and M. Paunov, A Unified Model Description of Mobile and Localized Adsorption: I. MFA with Nonadditive Lateral Interactions — an Application to Disordered Adsorbed Monolayer on a Structureless Substrate, *Surf. Sci.*, 1981, **108**, 25–37.

98 K. Sillar and J. Sauer, Ab Initio Prediction of Adsorption Isotherms for Small Molecules in Metal–Organic Frameworks: The Effect of Lateral Interactions for Methane/CPO-27-Mg, *J. Am. Chem. Soc.*, 2012, **134**, 18354–18365.

99 A. Kundu, G. Piccini, K. Sillar and J. Sauer, Ab Initio Prediction of Adsorption Isotherms for Small Molecules in Metal–Organic Frameworks, *J. Am. Chem. Soc.*, 2016, **138**, 14047–14056.

100 X. Wu, Z. Bao, B. Yuan, J. Wang, Y. Sun, H. Luo and S. Deng, Microwave Synthesis and Characterization of MOF-74 (M=Ni, Mg) for Gas Separation, *Microporous Mesoporous Mater.*, 2013, **180**, 114–122.

101 P. D. C. Dietzel, V. Besikiotis and R. Blom, Application of Metal–Organic Frameworks with Coordinatively Unsaturated Metal Sites in Storage and Separation of Methane and Carbon Dioxide, *J. Mater. Chem.*, 2009, **19**, 7362–7370.

102 E. J. Granite and H. W. Pennline, Photochemical Removal of Mercury from Flue Gas, *Ind. Eng. Chem. Res.*, 2002, **41**, 5470–5476.

103 E. D. Bloch, L. J. Murray, W. L. Queen, S. Chavan, S. N. Maximoff, J. P. Bigi, R. Krishna, V. K. Peterson, F. Grandjean, G. J. Long, B. Smit, S. Bordiga, C. M. Brown and J. R. Long, Selective Binding of O_2 over N_2 in a Redox–Active Metal–Organic Framework with Open Iron(II) Coordination Sites, *J. Am. Chem. Soc.*, 2011, **133**, 14814–14822.

104 B. A. Oyenekan and G. T. Rochelle, Energy Performance of Stripper Configurations for CO_2 Capture by Aqueous Amines, *Ind. Eng. Chem. Res.*, 2006, **45**, 2457–2464.

105 M. Doble and A.K. Kruthiventi, *Green Chemistry and Engineering*, Academic Press, San Diego, 2007.

106 S. N. V. K. Aki, B. R. Mellein, E. M. Saurer and J. F. Brennecke, High-Pressure Phase Behavior of Carbon Dioxide with Imidazolium-Based Ionic Liquids, *J. Phys. Chem. B*, 2004, **108**, 20355–20365.

107 M. J. Muldoon, S. N. V. K. Aki, J. L. Anderson, J. K. Dixon and J. F. Brennecke, Improving Carbon Dioxide Solubility in Ionic Liquids, *J. Phys. Chem. B*, 2007, **111**, 9001–9009.

108 J. E. Bara, C. J. Gabriel, S. Lessmann, T. K. Carlisle, A. Finotello, D. L. Gin and R. D. Noble, Enhanced CO_2 Separation Selectivity in Oligo(ethylene glycol) Functionalized Room-Temperature Ionic Liquids, *Ind. Eng. Chem. Res.*, 2007, **46**, 5380–5386.

109 O. M. Basha, M. J. Keller, D. R. Luebke, K. P. Resnik and B. I. Morsi, Development of a

Conceptual Process for Selective CO_2 Capture from Fuel Gas Streams Using [hmim][Tf_2N] Ionic Liquid as a Physical Solvent, *Energ. Fuel.*, 2013, **27**, 3905–3917.

110 M. B. Shiflett and A. Yokozeki, Solubility of CO_2 in Room Temperature Ionic Liquid [hmim][Tf_2N], *J. Phys. Chem. B*, 2007, **111**, 2070–2074.

111 W. G. Chapman, K. E. Gubbins, G. Jackson and M. Radosz, New Reference Equation of State for Associating Liquids, *Ind. Eng. Chem. Res.*, 1990, **29**, 1709–1721.

112 S. H. Huang and M. Radosz, Equation of State for Small, Large, Polydisperse, and Associating Molecules, *Ind. Eng. Chem. Res.*, 1990, **29**, 2284–2294.

113 G. Zarca, I. Ortiz, A. Urtiaga and F. Llovell, Accurate Thermodynamic Modeling of Ionic Liquids/Metal Salt Mixtures: Application to Carbon Monoxide Reactive Absorption, *AIChE J.*, 2017, **63**, 3532–3543.

114 M. B. Oliveira, E. A. Crespo, F. Llovell, L. F. Vega and J. A. P. Coutinho, Modeling the Vapor–Liquid Equilibria and Water Activity Coefficients of Alternative Refrigerant-Absorbent Ionic Liquid–Water Pairs for Absorption Systems, *Fluid Phase Equilibr.*, 2016, **426**, 100–109.

115 N. Mac Dowell, F. Llovell, N. Sun, J. P. Hallett, A. George, P. A. Hunt, T. Welton, B. A. Simmons and L. F. Vega, New Experimental Density Data and Soft-SAFT Models of Alkylimidazolium ($[CnC_1im]^+$) Chloride (Cl^-), Methylsulfate ($[MeSO_4]^-$), and Dimethylphosphate ($[Me_2PO_4]^-$) Based Ionic Liquids, *J. Phys. Chem. B*, 2014, **118**, 6206–6221.

116 F. Llovell, E. Valente, O. Vilaseca and L. F. Vega, Modeling Complex Associating Mixtures with [C_n-mim][Tf_2N] Ionic Liquids: Predictions from the Soft-SAFT Equation, *J. Phys. Chem. B*, 2011, **115**, 4387–4398.

117 F. Llovell, M. B. Oliveira, J. A. P. Coutinho and L. F. Vega, Solubility of Greenhouse and Acid Gases on the [C_4mim][$MeSO_4$] Ionic Liquid for Gas Separation and CO_2 Conversion, *Catal. Today*, 2015, **255**, 87–96.

118 M. B. Oliveira, F. Llovell, J. A. P. Coutinho and L. F. Vega, Modeling the [NTf_2] Pyridinium Ionic Liquids Family and Their Mixtures with the Soft Statistical Associating Fluid Theory Equation of State, *J. Phys. Chem. B*, 2012, **116**, 9089–9100.

119 J. L. Anthony, J. L. Anderson, E. J. Maginn and J. F. Brennecke, Anion Effects on Gas Solubility in Ionic Liquids, *J. Phys. Chem. B*, 2005, **109**, 6366–6374.

120 T. Altamash, T. S. Haimour, M. A. Tarsad, B. Anaya, M. H. Ali, S. Aparicio and M. Atilhan, Carbon Dioxide Solubility in Phosphonium-, Ammonium-, Sulfonyl-, and Pyrrolidinium-

Based Ionic Liquids and their Mixtures at Moderate Pressures up to 10 bar, *J. Chem. Eng. Data*, 2017, **62**, 1310–1317.

121 D. Camper, P. Scovazzo, C. Koval and R. Noble, Gas Solubilities in Room-Temperature Ionic Liquids, *Ind. Eng. Chem. Res.*, 2004, **43**, 3049–3054.

122 J. M. S. S. Esperança, H. J. R. Guedes, M. Blesic and L. P. N. Rebelo, Densities and Derived Thermodynamic Properties of Ionic Liquids. 3. Phosphonium-Based Ionic Liquids over an Extended Pressure Range, *J. Chem. Eng. Data*, 2006, **51**, 237–242.

123 P. J. Carvalho, V. H. Álvarez, I. M. Marrucho, M. Aznar and J. A. P. Coutinho, High Carbon Dioxide Solubilities in Trihexyltetradecylphosphonium-Based Ionic Liquids, *J. Supercrit. Fluids*, 2010, **52**, 258–265.

124 J. O. Lloret, L. F. Vega and F. Llovell, Accurate Description of Thermophysical Properties of Tetraalkylammonium Chloride Deep Eutectic Solvents with the soft-SAFT Equation of State, *Fluid Phase Equilibr.*, 2017, **448**, 81–93.

125 R. M. Ojeda and F. Llovell, Soft-SAFT Transferable Molecular Models for the Description of Gas Solubility in Eutectic Ammonium Salt-Based Solvents, *J. Chem. Eng. Data*, 2018, **63**, 2599–2612.

126 A. Klamt and G. Schüürmann, COSMO: a New Approach to Dielectric Screening in Solvents with Explicit Expressions for the Screening Energy and its Gradient, *J. Chem. Soc. Perkin Trans. 2*, 1993, **0**, 799–805.

127 A. Klamt, Conductor-like Screening Model for Real Solvents: A New Approach to the Quantitative Calculation of Solvation Phenomena, *J. Phys. Chem.*, 1995, **99**, 2224–2235.

128 C. B. Bavoh, B. Lal, O. Nashed, M. S. Khan, L. K. Keong and Mohd. A. Bustam, COSMO-RS: An Ionic Liquid Prescreening Tool for Gas Hydrate Mitigation, *Chin. J. Chem. Eng.*, 2016, **24**, 1619–1624.

129 Z. Lei, C. Dai and B. Chen, Gas Solubility in Ionic Liquids, *Chem. Rev.*, 2014, **114**, 1289–1326.

130 X. Zhang, Z. Liu and W. Wang, Screening of Ionic liquids to Capture CO_2 by COSMO-RS and Experiments, *AIChE J.*, 2008, **54**, 2717–2728.

131 C. E. Ferreira, N. M. C. Talavera-Prieto, I. M. A. Fonseca, A. T. G. Portugal and A. G. M. Ferreira, Measurements of pVT, viscosity, and surface tension of trihexyltetradecylphosphonium tris(pentafluoroethyl)trifluorophosphate ionic liquid and modelling with equations of state, *J. Chem. Thermodyn.*, 2012, **47**, 183–196.

132 L. I. N. Tomé, R. L. Gardas, P. J. Carvalho, M. J. Pastoriza-Gallego, M. M. Piñeiro and J. A.

P. Coutinho, Measurements and Correlation of High-Pressure Densities of Phosphonium Based Ionic Liquids, *J. Chem. Eng. Data*, 2011, **56**, 2205–2217.

133 F. Mozaffari and S. M. R. Mousavi, PVT properties of imidazolium-, phosphonium-, pyridinium- and pyrrolidinium-based ionic liquids using critical point constants, *Phys. Chem. Liq.*, 2017, **55**, 11–18.

134 F. Mozaffari, Modeling the volumetric properties of some imidazolium and phosphonium based ionic liquids from surface tension, *J. Mol. Liq.*, 2015, **212**, 461–466.

135 S. M. Hosseini, J. Moghadasi, M. M. Papari and F. Fadaei Nobandegani, Modeling the Volumetric Properties of Ionic Liquids Using Modified Perturbed Hard-Sphere Equation of State: Application to Pure and Binary Mixtures, *Ind. Eng. Chem. Res.*, 2012, **51**, 758–766.

136 T. Banerjee and A. Khanna, Infinite Dilution Activity Coefficients for Trihexyltetradecyl Phosphonium Ionic Liquids: Measurements and COSMO-RS Prediction, *J. Chem. Eng. Data*, 2006, **51**, 2170–2177.

137 M. S. Manic, A. J. Queimada, E. A. Macedo and V. Najdanovic-Visak, High-pressure solubilities of carbon dioxide in ionic liquids based on bis(trifluoromethylsulfonyl)imide and chloride, *J. Supercrit. Fluids*, 2012, **65**, 1–10.

138 M. Ramdin, T. Z. Olasagasti, T. J. H. Vlugt and T. W. de Loos, High pressure solubility of CO2 in non-fluorinated phosphonium-based ionic liquids, *J. Supercrit. Fluids*, 2013, **82**, 41–49.

139 P. Scovazzo, D. Camper, J. Kieft, J. Poshusta, C. Koval and R. Noble, Regular Solution Theory and CO2 Gas Solubility in Room-Temperature Ionic Liquids, *Ind. Eng. Chem. Res.*, 2004, **43**, 6855–6860.

140 C. C. Pye, T. Ziegler, E. van Lenthe and J. N. Louwen, An Implementation of the Conductor-Like Screening Model of Solvation within the Amsterdam Density Functional Package — Part II. COSMO for Real Solvents, *Can. J. Chem.*, 2009, **87**, 790–797.

141 *ADF2017 COSMO-RS, SCM, Theoretical Chemistry, Vrije Universiteit, Amsterdam, The Netherlands, http://www.scm.com*, .

142 L. M. C. Pereira, M. B. Oliveira, F. Llovell, L. F. Vega and J. A. P. Coutinho, Assessing the N_2O/CO_2 High Pressure Separation Using Ionic Liquids with the soft-SAFT EoS, *J. Supercrit. Fluids*, 2014, **92**, 231–241.

143 A. D. Becke, Density-Functional Exchange-Energy Approximation with Correct Asymptotic Behavior, *Phys. Rev. A*, 1988, **38**, 3098–3100.

144 A. D. Becke, Density-Functional Thermochemistry. III. The Role of Exact Exchange, *J. Chem.*

Phys., 1993, **98**, 5648–5652.

145 G. García, M. Atilhan and S. Aparicio, Assessment of DFT Methods for Studying Acid Gas Capture by Ionic Liquids, *Phys. Chem. Chem. Phys.*, 2015, **17**, 26875–26891.

146 E. A. Crespo, J. M. L. Costa, Z. B. M. A. Hanafiah, K. A. Kurnia, M. B. Oliveira, F. Llovell, L. F. Vega, P. J. Carvalho and J. A. P. Coutinho, New Measurements and Modeling of High Pressure Thermodynamic Properties of Glycols, *Fluid Phase Equilibr.*, 2017, **436**, 113–123.

147 J. D. van der Waals, Thermodynamische Theorie der Kapillarität unter Voraussetzung Stetiger Dichteänderung, *Z. Für Phys. Chem.*, 1894, **13**, 657–725.

148 J. D. van der Waals, The Thermodynamic Theory of Capillarity under the Hypothesis of a Continuous Variation of Density, *J. Stat. Phys.*, 1979, **20**, 200–244.

149 P. Kilaru, G. A. Baker and P. Scovazzo, Density and Surface Tension Measurements of Imidazolium-, Quaternary Phosphonium-, and Ammonium-Based Room-Temperature Ionic Liquids: Data and Correlations, *J. Chem. Eng. Data*, 2007, **52**, 2306–2314.

150 S. Zeng, X. Zhang, L. Bai, X. Zhang, H. Wang, J. Wang, D. Bao, M. Li, X. Liu and S. Zhang, Ionic-Liquid-Based CO_2 Capture Systems: Structure, Interaction and Process, *Chem. Rev.*, 2017, **117**, 9625–9673.

151 L. Ferguson and P. Scovazzo, Solubility, Diffusivity, and Permeability of Gases in Phosphonium-Based Room Temperature Ionic Liquids: Data and Correlations, *Ind. Eng. Chem. Res.*, 2007, **46**, 1369–1374.

152 J. Jacquemin, P. Husson, V. Majer and M. F. C. Gomes, Low-Pressure Solubilities and Thermodynamics of Solvation of Eight Gases in 1-Butyl-3-Methylimidazolium Hexafluorophosphate, *Fluid Phase Equilibr.*, 2006, **240**, 87–95.

153 J. Jacquemin, M. F. Costa Gomes, P. Husson and V. Majer, Solubility of Carbon Dioxide, Ethane, Methane, Oxygen, Nitrogen, Hydrogen, Argon, and Carbon Monoxide in 1-Butyl-3-Methylimidazolium Tetrafluoroborate Between Temperatures 283K and 343K and at Pressures Close to Atmospheric, *J. Chem. Thermodyn.*, 2006, **38**, 490–502.

154 D. Camper, C. Becker, C. Koval and R. Noble, Low Pressure Hydrocarbon Solubility in Room Temperature Ionic Liquids Containing Imidazolium Rings Interpreted Using Regular Solution Theory, *Ind. Eng. Chem. Res.*, 2005, **44**, 1928–1933.

155 A. Finotello, J. E. Bara, D. Camper and R. D. Noble, Room-Temperature Ionic Liquids: Temperature Dependence of Gas Solubility Selectivity, *Ind. Eng. Chem. Res.*, 2008, **47**, 3453–3459.

156 R. E. Baltus, B. H. Culbertson, S. Dai, H. Luo and D. W. DePaoli, Low-Pressure Solubility of

Carbon Dioxide in Room-Temperature Ionic Liquids Measured with a Quartz Crystal Microbalance, *J. Phys. Chem. B*, 2004, **108**, 721–727.

CHAPTER 4

Oil/Water/Rock Wettability for Enhanced Oil Recovery

According to the projections made by the Organization for Economic Cooperation and Development (OECD) and the International Energy Agency (IEA), the energy demand will be steadily increasing yearly by approximately a 1.6 % up to 2030.[1,2] That increase has been successfully tackled by renewable and clean energy sources, even slightly reducing the demands of fossil fuels. However, the 2030 perspectives consider that fossil fuels will still be the source of the 80 % of the total energy produced in the near future. In fact, the highest demands are centered on the transport sector, where alternative energy sources (*e.g.,* electric or hydrogen fuel cars) are still not widely implemented. To satisfy the high energy demand, fossil fuels still need to be extracted, while the energy generation efficiency is optimized. Specifically, the fossil fuels used to produce this 80 % of the energy can be divided into three main groups: (i) solid fuels (*e.g.,* coal), which are still used in the 15-20 % of the total production, (ii) liquid fuels (*e.g.,* petroleum), satisfying a 35-40 % of the energy demands, and (iii) gas fuels (*e.g.,* propane, butane, etc.), who are responsible of the remaining 20-25 % needs.

Both, gas and liquid fuels can be found in underground traps, either onshore or offshore, known as petroleum reservoirs. After the standard process of extraction, there is still a significantly large amount of crude oil that cannot be recovered, even with the best available technologies. For this reason, even though oil reservoirs are never entirely depleted, it is more economically viable to find new oil reservoirs than completing the exploitation of the already known ones. Unfortunately, the new reservoirs that are being discovered are located in hardly accessible regions,[3] which require large economical investment to obtain the crude oil. For this reason, there is a large interest in improving the available technologies for oil recovery to make the extraction of currently known reservoirs economically viable.

The work developed in this Chapter is part of a project carried out to understand the oil/water and oil/water/rock interfacial properties of different model crude oils in collaboration with the oil company REPSOL. The conclusions achieved during this part of the thesis can be mainly used to better understand the crude oil interfacial phenomena under different conditions.

4.1 Introduction to Oil Recovery

Oil reservoirs are naturally created from a set of chemical reactions of organic matter in anoxic conditions through a long geological time.[4] This organic matter, coming mostly from aquatic plants and dead animals, starts an oxygen driven decomposition at the floor of the sea. The fraction of matter that became buried before total decomposition becomes protected from oxygen by an earth layer. In fact, the oil reservoir precursor is a mud that contains inorganic matter, partially decomposed organic matter and water (*i.e.,* also known as formation water). Throughout millions of years, Earth movements begin burring the sediment deeper underground, where temperature and pressure rise. At the first stages of the process, organic matter polymerizes onto a waxy and heavy compound known as kerogen. A cracking process starts when the kerogen is deeper enough to reach temperatures up to 90 ºC. During the cracking its bonds break homolitically creating radicals that undergo a series of chain reactions, yielding a final enormous mixture of organic compounds. The final mixture is currently known as crude oil, and it contains moieties with very different molecular weights and functional groups. Finally, for the oil to become trapped, there must be a thick impermeable layer of rock that seals the reservoir. These reservoirs can be relocated closer to the surface by earth movements and then drilled to produce crude oil. Recall that the precursor of crude oil was a mud, where organic matter was mixed with water and inorganic materials. This means that after the successive chemical reactions of the organic matter, the crude oil and the formation water, along with all the inorganic electrolytes in solution, are trapped in a matrix of microporous rocks.

The crude oil, after all the successive reactions carried out during the timespan of its formation, has become a mixture of countless different species with different natures.[5] In fact, the crude oil contains at the same time liquid, gaseous and solid organic compounds, which gives an idea of the range of different species present in a reservoir. Due its complex composition, the accurate determination of its individual components is almost an impossible task to the available technologies. Additionally, all analyses show similar chemical properties regardless of the crude oil. For this reason, two different systems were created to classify its fractions onto simplified pseudocompounds with similar properties.

The first system is used in refineries and consists in separating the crude oil by boiling point ranges.[6] At low temperature boiling points one can find light compounds such as liquified petroleum gases or short-chained hydrocarbons, commonly used as chemicals. Then, different kinds of fuels become separated at intermediate temperatures (*i.e.,* petrol for vehicles, kerosene for planes or diesels). After that, waxes and lubricants or fuels for ships can be obtained from the high

temperature fraction of distillation. Finally, the remaining compounds that do not boil are used for asphalts.

The second system classifies oil fractions by polarity difference, and it is known as SARA,[7,8] which stands for Saturate, Aromatic, Resin and Asphaltene. The first step of the SARA analysis consists on solving the crude oil in n-heptane, in which the insoluble part of the oil is separated and assigned to asphaltenes. Asphaltenes are a family of large molecules, with extended π systems and a large number of heteroatoms. These features make asphaltenes to strongly attach to rocks and to aggregate among each other, which lowers its solubility and increase the viscosity of the crude oil. In fact, asphaltenes are one of the main issues in oil extraction due to its precipitation during recovery.[9] The remaining separation was performed in the past via elution using different polarity solvents, but it is currently carried out by high pressure liquid chromatography (HPLC).[10] The fraction of saturates corresponds to non-polar hydrocarbons, either linear, ramified or cyclic. Aromatics refer to non-polar molecules with one or more aromatic rings, which can be fused or separated by hydrocarbon chains. Finally, resins are defined as the polar fraction of oil, and can contain either aliphatic or aromatic compounds with heteroatoms such as N, O or S in forms of acid, basic or neutral functional groups. A summary of the SARA fractionation scheme can be seen in Figure 4.1 and some examples of possible crude oil components that would fit in either saturates, aromatics, resins and asphaltenes can be seen in Figure 4.2.

Two very different species are compiled in Figure 4.2 under the label of asphaltenes. In reality, their molecular formulas are unknown because asphaltene characterization is a very difficult task. In fact, there are several studies nowadays focused on determining the physicochemical properties of asphaltenes with the aim of shed light onto this topic.[11–14] However, up to date, only partial information about the average aromaticity and functional groups present in the asphaltene mixture can be obtained. From that information two different models of asphaltenes were proposed:[15,16] (i) the archipelago asphaltenes, which are defined as relatively small fused aromatic regions

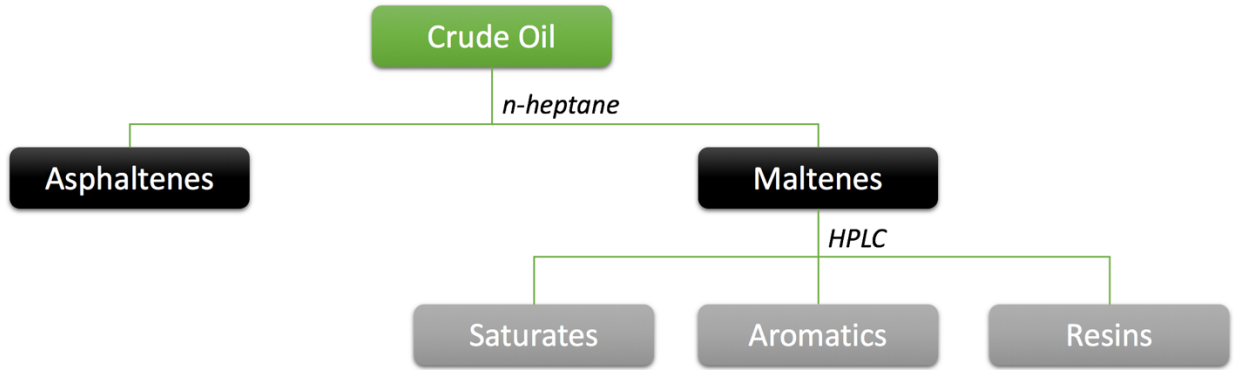

Figure 4.1. SARA fractionation scheme from a crude oil.

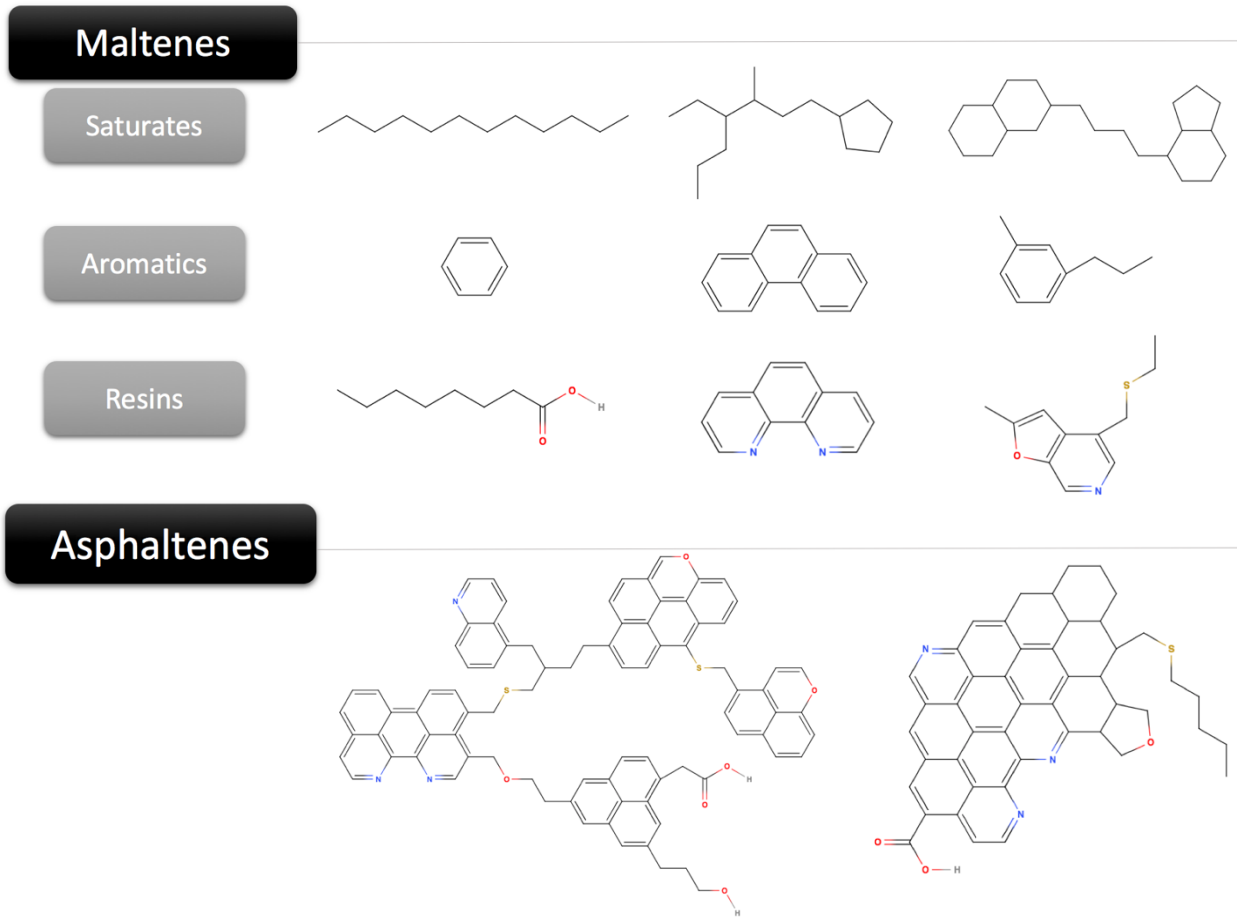

Figure 4.2. Examples of possible chemical compounds present in crude oil that could fit in each SARA fraction.

connected by hydrocarbon chains and (ii) the continental asphaltenes, that have a very large aromatic region in the center and some hydrocarbon chains / aliphatic rings connected to it. According to elemental analyses, asphaltenes usually contain heteroatoms in their structure, which gives them a certain polarity and makes them share some common features with resins. In fact, a simplified way of picturing asphaltenes is to consider them as resins large enough, that they start precipitating and can no longer boil in the distillation fractionation. So, even though in Figure 4.2 there are asphaltene examples of these two models, the real structure of asphaltenes is not unequivocally defined. In fact, they can be formed by combinations of both archipelago and continental regions connected to each other.

Apart from the difficulty in characterization, the recovery of crude oil from reservoirs is not a simple task. This process is commonly divided in three main stages (Figure 4.3).[17,18] The first stage (*i.e.,* primary recovery) consists on drilling the reservoir and let the crude oil to flow through the newly created production well by the natural high underground pressure. This method is capable of recovering between a 5 % and a 10 % of the total oil present in the reservoir. When the production of oil by the primary recovery is insufficient, the pressure at the reservoir is increased

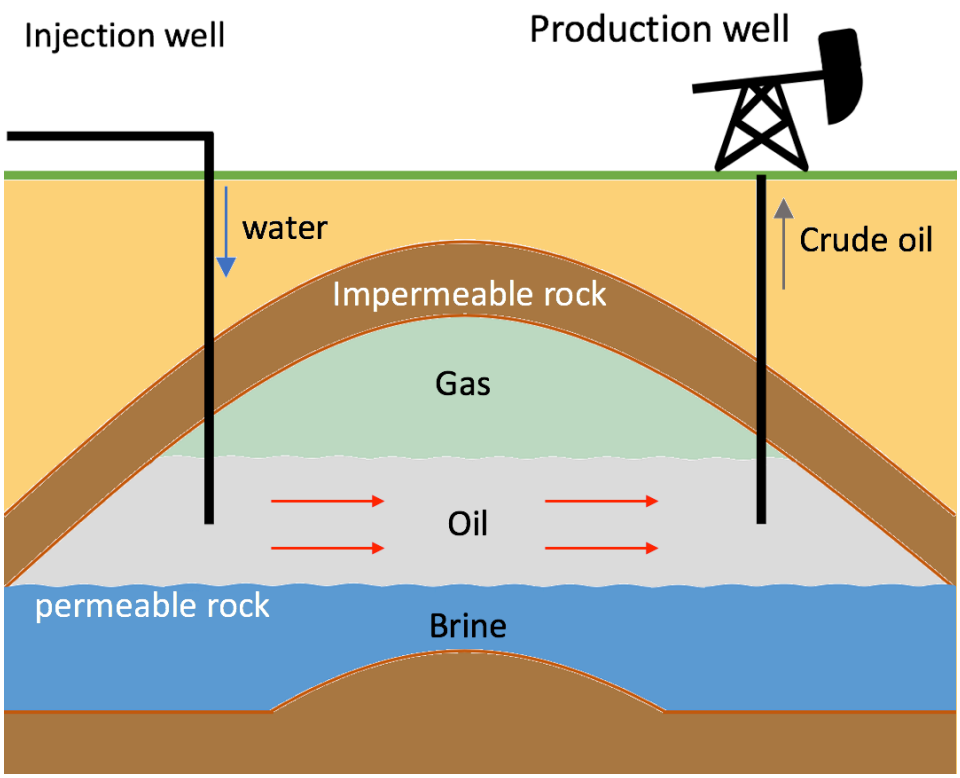

Figure 4.3. Simplified structure crude oil trapped under an impermeable rock forming a petroleum reservoir. The injection and production wells are also shown as an example of the water-flooding extraction process.

by injection of water or gas. This stage is known as secondary recovery and is usually carried out by pumping seawater in an injection well to drag the oil towards the production well (*i.e.,* water-flooding). Even though the pressure of the reservoir is maintained with water-flooding, only a 25-30 % of the crude oil can be effectively recovered. The final stage is often referred to tertiary or enhanced oil recovery (EOR) stage. This term encompasses all the different techniques with higher operational cost that target specific properties to allow recovering roughly an additional 30 % of oil. Some of these methods include, reduction of oil viscosity via thermal recovery,[19] solubilization via CO_2 injection,[20,21] increase of the injection water viscosity through addition of polymers,[22] reduction of interfacial tension and change of wettability by the action of surfactants and nanofluids[23–27] or modifying the salinity of the injection water to weaken the oil/rock interactions.[28,29]

All of these techniques require a deep knowledge of both the different mechanisms behind and the physicochemical interactions that can occur at pore conditions. For this reason, this chapter focuses on understanding the most fundamental interactions among water, crude oil and different rocks, as well as how they are affected by the presence of additives. This comprehension can serve in future applications for chemical enhanced oil recovery (cEOR), which intends to modify specific molecular interactions by changing the chemical composition of the injection water. Specifically,

cEOR tries to optimize two main properties: the oil/water interfacial tension (IFT) and the oil/water/rock contact angle (CA).

The IFT is defined as the energy needed to create an interface by connecting two independent bulk phases. The term "IFT" is used when the connection is made through two liquid phases, whereas the term surface tension (ST) is employed when the interface is created between a liquid and its vapor at equilibrium. In an interfacial system, the molecules located at the interface feel attracted by its own bulk. These attractive interactions are known as cohesive forces and are responsible of contracting the system to the minimum interfacial area. For this reason, the creation of any interface (*i.e.,* either liquid/vapor or liquid/liquid) requires overcoming the cohesion forces of the bulk phases. Apart from cohesion, interfacial molecules can also be attracted by the other bulk phase. These interactions are known as adhesive forces and fight against the cohesive forces to spread out the fluid, increasing the interfacial area. The resulting surface or interfacial tension (γ) comes from the balance between the cohesive and adhesive interactions (*i.e.,* $\gamma \propto F_{coh} - F_{adh}$).

Notice that systems with high adhesive forces will have low γ and a strong tendency to mix. On the other hand, systems with very strong cohesive forces yield high γ, and they will rapidly separate into two phases. For this reason, aiming at increasing the solubility of oil in the injected water and increase production, cEOR focuses on study techniques that allow to reduce the IFT in the most effective and economical way. However, the IFT study at pore conditions is hard to carry out experimentally due to the high temperatures and pressures involved in the extraction of crude oil. Alternatively, these kinds of studies can be made via molecular simulations, which are capable of describing fluid interactions at a molecular level and working under any pressure of temperature range.

The ST or IFT is a collective property that can also be calculated computationally, and similarly to their definitions, it can be obtained in two different manners: through the thermodynamic route of Gloor *et al.,*[30] which relates the IFT to the energy needed to increase the interfacial area, or through the mechanical route of Kirkwood *et al.,*[31,32] that quantifies the IFT according to the imbalance of forces at the interface. Despite their differences, both methods require to model two bulk phases in equilibrium connected by an interface via molecular simulations. Then, in the thermodynamic route, the system is perturbed at each timestep with an infinitesimal area increase, and an infinitesimal area decrease, at constant volume. The variation of the internal energy between the reference and the perturbed systems (*i.e.,* ΔU_+ and ΔU_- for the area increase and decrease, respectively) is used to calculate the variation of Helmholtz free energy (A) necessary to modify the interfacial area (S), which is the definition of IFT (eq. 4.1).

$$\gamma = \left(\frac{\partial A}{\partial S}\right)_{NVT} = \lim_{\Delta S \to 0}\left(-\frac{k_B T}{2\,\Delta S}\left[\ln\langle e^{-\Delta U_+/k_B T}\rangle - \ln\langle e^{-\Delta U_-/k_B T}\rangle\right]\right) \quad 4.1$$

Otherwise, in the mechanical route, the components of the pressure tensor are computed during the time evolution of the system. At any position of the fluid bulk, the pressure tensor is diagonal, their values are equal and they correspond to the pressure of the system, which means that the forces are isotropic in all directions of the space. However, at the interface, there is an imbalance between the normal and tangential forces with respect to the plane of the interface. This anisotropy is also reflected in the pressure tensor and can be used to obtain the interfacial tension via eq. 4.2. The term $P_N - P_T$ vanishes in bulk phases, so an integral over all the simulation cell can be performed to obtain the IFT of a system with N equivalent interfaces. The definition used here for the mechanical route requires to use a planar interface, the normal component of the pressure tensor is chosen as the z-direction by convention (*i.e.,* $P_N = P_{zz}$) and the tangential component is the average between the P_{xx} and P_{yy} components (*i.e.,* $P_T = (P_{xx} + P_{yy})/2$). A visual representation of the pressure tensor method can be seen in Figure 4.4

$$\gamma = \int_{z=-\infty}^{z=\infty} [P_N(z) - P_T(z)]\, dz = \frac{L_Z}{N}\left(\langle P_N\rangle - \langle P_T\rangle\right) \quad 4.2$$

The second key property for cEOR is the oil/water/rock CA. This magnitude quantifies the capacity of a fluid to wet a surface and is represented by a balance among the cohesive forces of all bulks and the oil/water, oil/rock and water/oil adhesive interactions, as expressed in the Young equation (eq. 4.3).[33] Recall that in reservoirs, crude oil and formation water are trapped in matrixes of capillary rocks. This means that there are many non-negligible fluid/rock interactions that determine the behavior of petroleum during its recovery. If rocks interact more strongly with the organic compounds than with water the surface becomes oil wet, and the water-flooding is not capable of effectively displacing the crude oil to the production well. On the other hand, if rocks interact strongly with water, they become water wet, the oil easily detaches from the rock surface and it can be effectively recovered in the water-flooding process.

$$\cos(\theta) = \frac{\gamma_{Sf_1} - \gamma_{Sf_2}}{\gamma_{f_1 f_2}} \quad 4.3$$

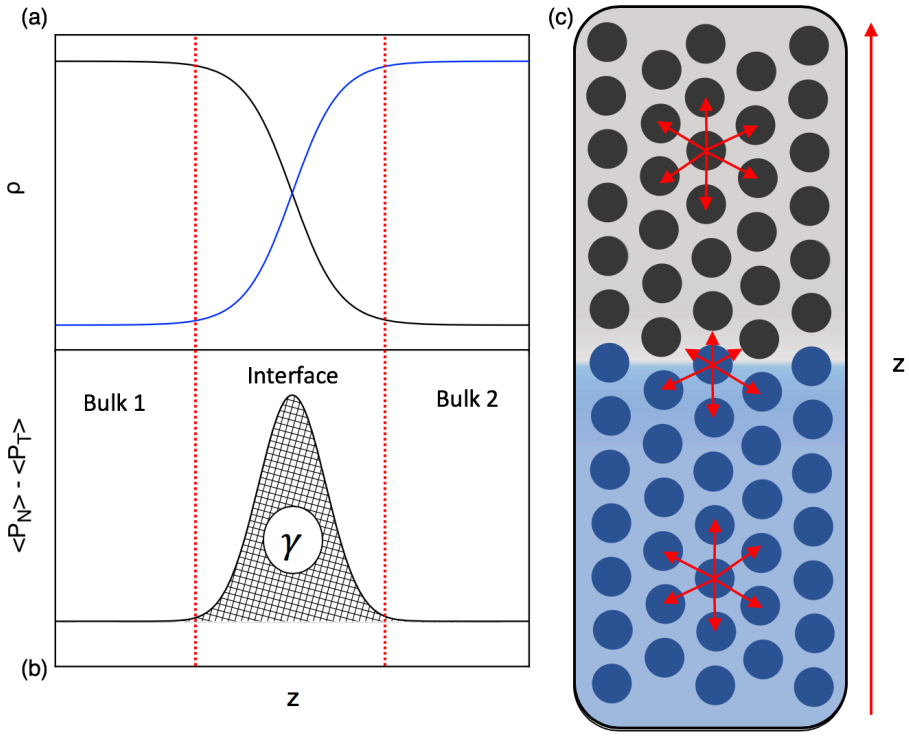

Figure 4.4. Visual interpretation of the IFT calculated from the mechanical route of Kirkwood *et al.*,[31,32] with the z-axis located perpendicular to the planar interface. (a) The density profile of a system with two bulk phases (*i.e.,* blue and black lines, respectively) connected by an interface limited by the red dotted line. (b) The value of $\langle P_N \rangle - \langle P_T \rangle$ as a function of the z-coordinate, where the highlighted integral gives the value of γ. (c) Schematization of the forces at different positions of the system.

The CA is explicitly defined as the angle that forms the interface of a fluid droplet (f_1) with a solid surface (S) when putting them in contact, both embedded in a second fluid (f_2). The first fluid is generally a liquid with a well-defined boundary (*e.g.,* water or oil) and the embedding fluid can either be a liquid or a gas (*e.g.,* air). The value of the CA is obtained by the tangent of the droplet at the triple $f_1/f_s/S$ contact point. When a fluid is not capable of wetting a surface, it becomes spherical and it yields a low CA (*i.e.,* $\theta < 90º$), whereas wetting fluids spread over the surface giving large CA values (*i.e.,* $\theta > 90º$) as it can be seen in Figure 4.5.

The most common method of obtaining the CA of an oil/water/rock system is by direct molecular simulation.[34–37] With this technique, a large simulation cell is built with a droplet placed on a solid surface embedded in a second fluid (*e.g.,* an oil droplet placed on a reservoir rock surrounded by brine), and it is evolved to an equilibrium state. Then, the angle is obtained by fitting the average geometry of the droplet to a circle and obtaining its tangent at the triple point. Alternatively, after fitting the droplet profile into a circle, the ratio between the radius of the droplet (r) and the distance between the center and the surface (h) also gives an estimate of the CA as

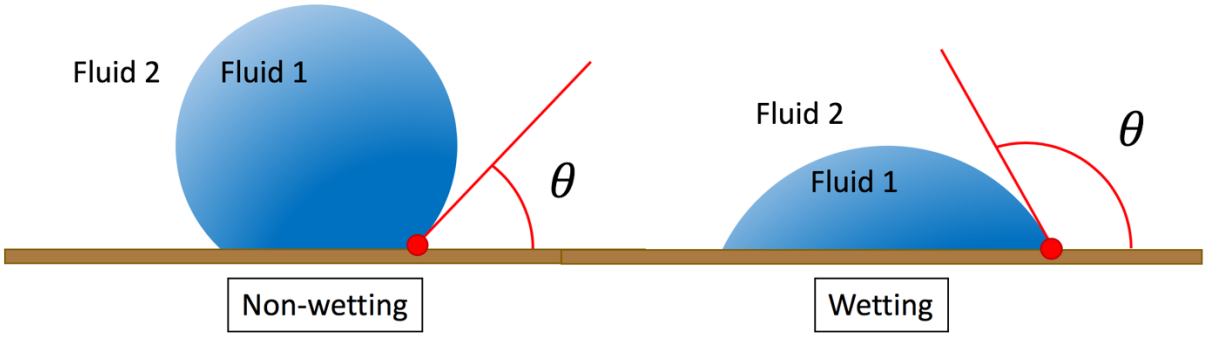

Figure 4.5. Representation of a wetting (left) and a non-wetting (right) droplet, along with their CA as defined by the Young equation (eq. 4.3). The red dots represent the fluid 1/fluid 2/solid triple point.

shown in Figure 4.6. Notice that spherical fittings are good approximations in molecular simulations because the effect of gravity, which could flatten the droplet, is neglected.

All properties in this part of the thesis have been calculated via MD simulations with classical force fields using the LAMMPS code.[38] Intramolecular interactions (*i.e.,* bonds, angles, etc.) have been treated with expressions equivalent to eq. 2.27, eq. 2.28 and eq. 2.29. On the other hand, intermolecular interactions are treated with the combination of a Lennard-Jones (LJ) + Coulomb potentials (*i.e.,* eq. 2.30 and eq. 2.31). A spherical cutoff distance for intermolecular interactions of 14 Å has been selected and the neglected tail contribution for LJ interactions has been accounted through an analytic tail correction[39], whereas the long-range coulomb interactions have been considered via the Particle-Particle/Particle-Mesh Ewald summation.[40] Periodic boundary conditions (PBCs) have been imposed in the three directions of the space to prevent finite size effects created by the boundaries of the box.

The simulation cells to calculate the IFTs have been built as rectangular boxes with $Lx = Ly < Lz$. Half of the box has been filled with molecules relative to the water phase (*i.e.,* from $z = 0$ to $z = Lz/2$) and the other half with molecules relative to the oil phase (*i.e.,* from $z = Lz/2$

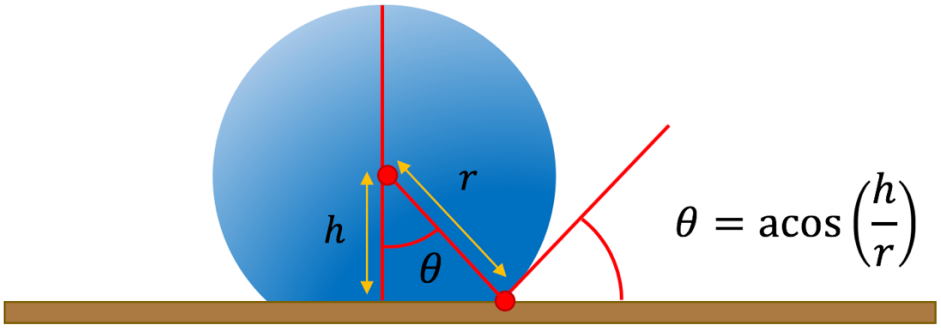

Figure 4.6. Calculation of the equilibrium CA of a droplet based on the relationship between its height and radius.

to $z = Lz$). The insertion of molecules is performed following a uniform random distribution of positions and orientations within the respective defined regions. In such configuration, two interfaces appear naturally in the simulation cell: the first is visible in $z = Lz/2$ and the second is in the border of the cell, which by PBCs is explicitly located at $z = 0$ and $z = Lz$ at the same time. Both are oil/water interfaces, which implies that there are two equivalent interfaces (N) in eq. 4.2. The length of the simulation cell (Lz) is selected long enough to minimize the interactions between the two simulated interfaces, while Lx and Ly are virtually infinite due to PBCs.

As abovementioned, the simulation cells for CA calculations have been constructed as rectangular boxes with $Lx \approx Ly < Lz$. The rock bulk molecular structures have been taken from crystallographic data and have been cut through the most stable faces according to experimental surface energy data. The width of the rock has been selected between 20 Å and 25 Å depending on the cell parameter of the bulk to ensure that the inner layers of the rock behave like the solid bulk. The solid structure has been placed on the $z = 0$ position of the simulation cell and an equivalent inverted layer has been added at $z = Lz/2$ to delimit the wetting region. The length from $z = Lz/2$ to $z = Lz$ did not include any molecules and is added to prevent any species to interact with image surfaces in the z-direction due to PBCs. A semispherical region close to the surface at $z = 0$ has been defined to contain the molecules relative to the oil phase, whereas the remaining space between the two layers (*i.e.,* from $z = 0$ to $z = Lz/2$ excluding the volumes occupied by the surfaces and the oil) has been filled with molecules relative to the water phase, both of them following a uniform random distribution in positions and orientations. The length of the simulation cell in the x and y direction and the distance between the two layers in $z = 0$ and $z = Lz/2$ has been chosen large enough to prevent interactions between the droplet with its periodic images, and the droplet with the upper surface, respectively. Finally, the most outer layers of the rocks have been allowed to move during the simulation to reproduce the molecular vibrations of the solid surfaces, whereas the most inner solid layer has been fixed at its bulk geometry. A representation of the two kinds of simulation cells is shown in Figure 4.7.

All simulations of this work have been conducted in five stages: (i) create the system by placing molecules in different regions as aforementioned, according to the desired property to calculate; (ii) perform an energy minimization to prevent molecular overlaps during the first steps of the MD simulation due to the random creation of molecules; (iii) heat the system to the working temperature in the NVT ensemble using a Langevin thermostat [41] during 20 ps followed by a 100 ps of thermal equilibration with the Nosé-Hoover thermostat;[42] (iv) bring the system to the working pressure by coupling a Berendsen barostat [43] only to the z-direction of the simulation cell during 500 ps (*i.e.,* the z-direction was selected by convention to be the perpendicular to the

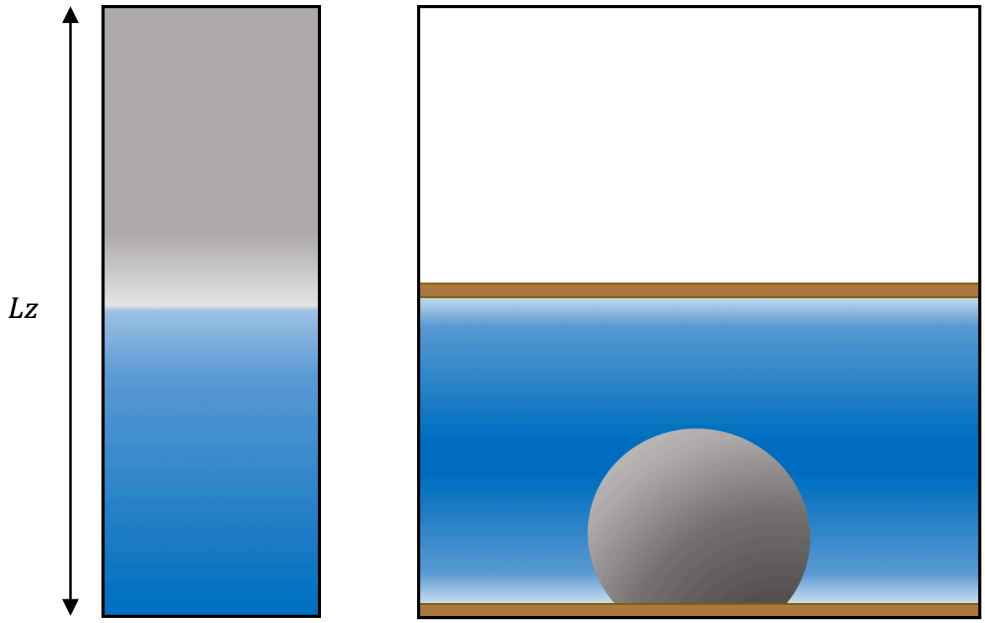

Figure 4.7. Sketches of the IFT (left) and CA (right) simulation cells used in this thesis. Blue represents water phase, grey represents oil phase and rocks are shown in brown.

interfacial planes, so this barostat keeps the interfacial area constant during the entire simulation and updates the cell volume via modifying *Lz*); and (v) change the Berendsen barostat by the Nosé-Hoover barostat [44] (*i.e.,* still coupled to the z-direction) and evolve the system enough time so that the equilibration is over and the production stage is long enough to obtain the average of the properties of interest.

4.2 The SARA Fractionation and Molecular Models

This is the first time that the Applied Computational Chemistry & Molecular Modeling group under supervision of Prof. Ramón Sayós models this kind of interfacial systems and the computational resources at the beginning of the project were insufficient to yield results at the rate demanded by the company. To complete the calculations in the lowest possible time frame, relatively small simulation cells have been used at the beginning of the project and have been enlarged when more computational power was acquired. Additionally, the crude oil modeling is a rather complex goal that requires many approximations. For this reason, this study does not intend to reproduce quantitative results but seeks to qualitatively identify the behavior of crude oils under different pressure, temperature and salinity conditions.

A real crude oil is a combination of an enormous number of organic molecules with very different properties. For this reason, it is a general practice to employ the SARA fractionation

method to characterize the oil into saturates, aromatics, resins and asphaltenes. The molecules belonging within each of these groups have similar moieties in their structure, which gives them common chemical properties. In this regard, it is a reasonable approximation to model each of the fractions with a single molecule that represents the average behavior of the complete group.

In this thesis, each crude oil fraction has been simulated through one or two simple molecules with representative properties of its group. The interfacial properties of these model oil fractions are analyzed through MD simulations at different pressure/temperature conditions and the impact on the IFT/CA induced by each fraction of the model oil is evaluated at the molecular level. Although almost any compound can be modeled with MD, the selection of molecules to reproduce each crude oil fraction has been limited by experimental constraints, such as their commercial availability, toxicity and their possible experimental manipulation. The decision was driven by the possibility of obtaining comparable experiment/simulation results if similar molecules were selected in both parts of the project, because REPSOL disposed of adequate equipment to perform measurements of both: the oil/water IFT (*i.e.,* through the pendant drop and spinning drop techniques)[45] and the oil/water/rock CA.

The saturated fraction is formed by linear or ramified hydrocarbons, usually at liquid phase. Saturates do not contain any kind of functional group, which make them a non-polar fraction. They also have a relatively low chemical reactivity because all the bonds are strong and have no acid/base character. The selected molecule to represent this fraction is dodecane (*i.e.,* $C_{12}H_{26}$), which is a linear hydrocarbon with all of the beforementioned features. However, the selection of the hydrocarbon does not seem to be critical in determining the interfacial properties of crude oil because they exhibit similar oil/water interfacial tensions regardless of their molecular weight and structure.[46]

On the other hand, the aromatic fraction is formed by molecules built with fused benzene rings. It is generally a fraction without heteroatoms but with some polarity given by the quadrupolar momenta of the π-ring electronic distribution. These compounds are usually found in liquid phase or in solution in a crude oil at pore conditions. However, many of these species have relatively high melting points (*e.g.,* naphthalene 354 K,[47] anthracene 490 K,[47] chrysene 373 K [48] or coronene 710 K,[49] among others) and, unless dissolved on other organic compounds, they are solid at laboratory conditions. This fact forces to select the toluene molecule as the representative species of the aromatic fraction, which is a liquid that can be used experimentally as a pure compound at 300 K and 1 atm.

The resin fraction contains the group of polar compounds. Many molecules are present in this group, each of them with different heteroatoms responsible for their polarity. For example, species

with O atoms could contain acid groups (*i.e.,* R-COOH), whereas other species can contain basic aromatic N atoms (*e.g.,* pyridinium ring). For this reason, instead of using a single molecule to model the fraction, a part of the resins is reproduced with quinoline (*i.e.,* to account for the aromatic/basic part of the fraction) and the other is modeled with 3-(3-ethylcyclopentyl) propanoic acid, also known as 3-naphthenic acid (*i.e.,* to account for the aliphatic/acid part of the fraction). The acid corresponds to the typical structure of a naphthenic acid, which contains an aliphatic cycle and a carboxylic acid group connected via a saturated carbon chain.

Finally, an adequate reproduction of the asphaltene fraction would require using several molecules with different shapes and functional groups (*i.e.,* some archipelago and some continental regions with different distributions of O, N and S atoms). As asphaltenes are very large molecules, this practice rapidly becomes computationally prohibitive, so other researchers developed alternative "average" molecules based on chemical analysis of different crude oils. The obtained molecules are relatively small versions of asphaltenes that contain at the same time different heteroatoms in their structure to keep the computational cost at a reasonable level. Some of the most relevant works in the field were carried out by Boek *et al.,*[15] who developed the Quantum Molecular Representation (QMR) code to generate model asphaltene structures that can reasonably fit experimental chemical analyses of different crude oils. Up to two asphaltene structures are used to model the heaviest fraction of crude oils based on the molecules elucidated by the QMR code and published by Boek *et al.,*[15] Both structures are derived from the same continental-type asphaltene: the first one, with an aromatic basic N and a thioether group, and the second one with an aromatic basic N, a thioether group and a COOH group. All the molecules used as representatives of the different SARA fractions are compiled in Figure 4.8.

Notice that real crude oils are formed by molecules with many different functional groups, exposed to high pressures and temperatures at pore conditions, which is a favorable environment for chemical reactions to occur. However, the modeling of such a complex system is already challenging enough without considering that the chemical species are continuously reacting among each other. For this reason, all molecular models have been assumed to be non-reactive and only the physical interactions between all of the different crude oil fractions, the water, the solved electrolytes and the rocks have been considered.

Within this modeling framework, the United-Atom (UA) molecular representation has been selected as the best compromise between accuracy and computational cost to model the oil phase. Intramolecular and intermolecular interactions of organic molecules have been calculated using the TraPPE-UA force field,[50] because it was specifically fitted to reproduce phase equilibria of organic molecules and its quality in predicting surface tension was already tested by other

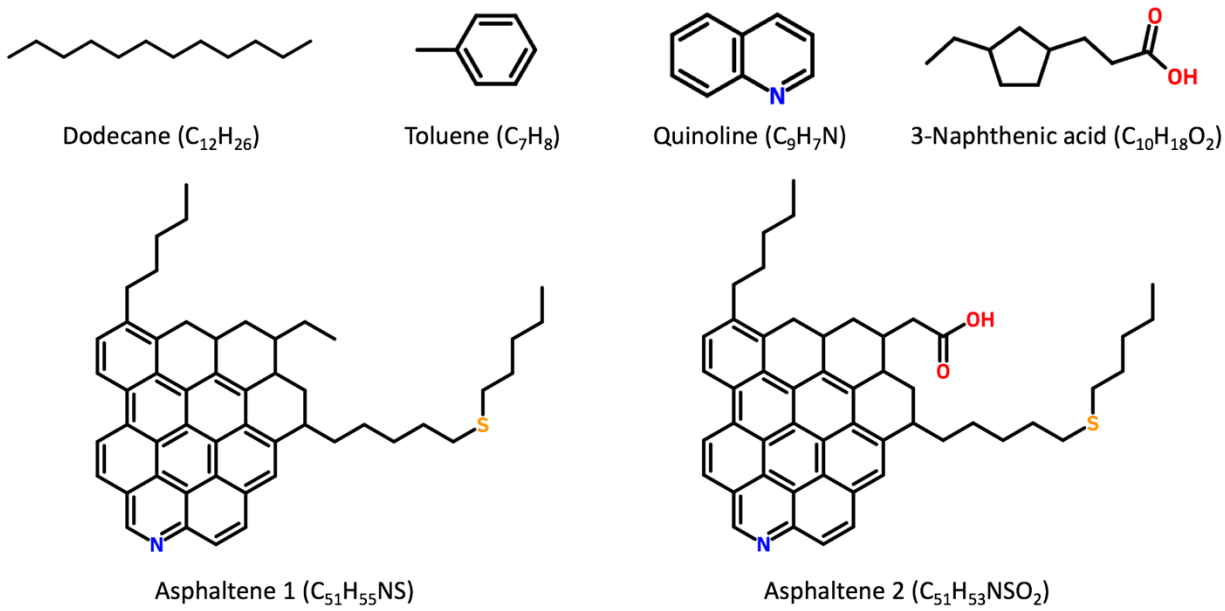

Figure 4.8. The six molecules used to represent the different SARA fractions in the studied model crude oils.

authors.[51] Regarding the intramolecular interactions, TraPPE-UA considers bonds to be fixed at their equilibrium bond lengths, angles constrained by a quadratic potential (eq. 2.28) and dihedral angles restricted to follow a Fourier series expression (eq. 2.29) to allow the multiple torsion minima exhibited by hydrocarbons. To include the effect of bond vibration in the simulations, the equilibrium spring constants of AMBER force field [52] have been used in a quadratic expression (eq. 2.27), according to the recommendations of TraPPE-UA developers.

The liquid density of dodecane, toluene, quinoline and 3-naphthenic acid at laboratory conditions have been calculated with MD using a 45 Å x 45 Å x 45 Å simulation cell filled with 250 dodecane, 500 toluene, 450 quinoline or 300 3-naphthenic acid molecules. The initial number of molecules of each simulation cell correspond to the experimental pure densities of each compound at 300 K. The system is evolved in time up to 500 ps in an NPT simulation fixing the temperature and the pressure to 300 K and 1 atm, respectively. The results are compiled in Table 4.1, where one can see that the force field is capable of describing the densities of the pure compounds used to represent the maltene fraction, which partially serves as validation of the oil models.

Additionally, different water models have been tested to select the most adequate force field to reproduce oil/water interactions. The validation has been carried out based on their ability to reproduce the available dodecane/water and toluene/water IFTs,[46,53–55] (*i.e.,* the only data available in the bibliography). From all the available water models for MD, four of them have been selected for validation: the three site (i) SPC,[56] (ii) SPC/E [56] and (iii) TIP3P [57] models

Table 4.1. Experimental and calculated liquid densities at 300 K and 1 atm for all molecules representing the maltene fraction of the model crude oil. Asphaltenes are not simulated because they are not liquid at these conditions and no experimental information is available for validation.

	Dodecane	Toluene	Quinoline	3-Naphthenic Acid
ρ_{MD} / g·cm^{-3}	0.75	0.84	1.02	0.91
ρ_{exp} / g·cm^{-3}	0.74 [60]	0.86 [60]	1.09 [61]	0.91-0.96 [62,63]

and the four site (iv) TIP4P [58] model. The four water force fields were developed as rigid models, so all bonds and angles have been constrained to their equilibrium geometry by means of the SHAKE algorithm.[59] All of these force fields are relatively simple and have been successfully used by many researchers to reproduce general liquid water properties.

The oil/water IFT calculations of each pure fluid have been carried out in a 45 Å x 45 Å x 100 Å simulation box with 300 dodecane, 600 toluene, 500 quinoline or 350 3-naphthenic acid molecules filling half of the simulation cell, and 3000 water molecules filling the rest of the box. The system has been evolved in time up to 10 ns in an NPT simulation fixing the temperature and the z-component of the pressure to 300 K and 1 atm, respectively. Finally, the IFT has been calculated using the mechanical route of Kirkwood *et al.,*[31,32]

Although these models exhibit significant differences in the prediction of the pure water ST,[64] the calculated oil/water IFTs lay all in a range of 5 mN·m^{-1} among each other, with a general trend of $\gamma_{TIP4P} \geq \gamma_{SPC/E} > \gamma_{TIP3P} > \gamma_{SPC}$. In fact, the four water models are in a reasonably good agreement with the experimental dodecane/water IFT (Table 4.2).[46,53] However, the model that better reproduces the toluene/water IFT is the three site SPC model.[54,55] For this reason, even though SPC is one of the simplest water models available, it has been selected to reproduce the oil/water interfacial properties in this part of the thesis.

Table 4.2. Experimental and calculated oil/water IFT (*i.e.,* γ_{exp} and γ_{MD}, respectively) at 300 K and 1 atm of dodecane and toluene with four different water models.

	γ / mN·m^{-1}	SPC	SPC/E	TIP3P	TIP4P
Dodecane	γ_{MD}	48.4	54.6	49.2	54.1
	γ_{exp}	51.0, 52.3 [46,53]			
Toluene	γ_{MD}	39.5	45.3	43.1	46.4
	γ_{exp}	36.0, 36.1 [54,55]			

4.3 Model Oil/Water/Rock Interfacial Properties (Pure Compounds)

After the adequate selection of oil/water models and force fields, this section focuses on computationally studying the oil/water and oil/water/rock interfacial properties of each model fraction of the crude oil individually, as well as their interaction with other additives such as salts. To that end, both the IFT and the CA have been calculated through MD simulations using the four average maltene molecules (*i.e.,* dodecane, toluene, quinoline and 3-naphthenic acid), water and calcite as a support when needed. Although the majority of calculations have been carried out at room conditions (*i.e.,* T = 300 K and P = 1 atm) to compare with the measurements performed in REPSOL laboratories, some higher temperatures, pressures and salinities have also been employed to simulate reservoir conditions.

4.3.1 Oil/Water Interfacial Tensions

The first part of this section involves the calculation of different oil/water IFTs. The simulation cell employed is equivalent to the one used in the previous force field validation stage and the obtained results for each fraction are compiled in Table 4.3, along with the measured experimental values provided by REPSOL.[65] As it can be seen, dodecane/water interface has the highest IFT value among the four fractions, followed by toluene/water, quinoline/water and finally, the 3-naphthenic acid/water. This ranking follows the inverse trend with respect the polarity of the compounds, being dodecane the least polar molecule, followed by toluene, quinoline and 3-naphthenic acid. Notice that 3-naphthenic acid exhibits a relatively low IFT because its molecular structure resembles that of a pseudo-surfactant: a polar head containing a COOH group and a non-polar tail with a 5-membered aliphatic ring.

The experimental data supplied by REPSOL [65] at the same conditions of pressure and temperature for the four model molecules are also shown in Table 4.3. As it can be seen,

Table 4.3. Calculated oil/water IFT at 300 K and 1 atm of the four molecules chosen to represent the maltene fraction in comparison to the experimental data supplied by REPSOL [65] and other studies. Recall that the value of 7.0 mN·m^{-1} yielded by quinoline may be incorrect due to contamination.

γ / mN·m^{-1}	Dodecane	Toluene	Quinoline	3-naphthenic acid
γ_{MD}	48.4	39.5	25.5	17.6
γ_{exp}	50.0 - 53.0 [65]	35.0 - 37.0 [65]	7.0, 33.0 [65]	11.0 - 13.0 [65]
γ_{exp}	51.0, 52.3 [46,53]	36.0, 36.1 [54,55]	-	-

dodecane/water, toluene/water and 3-naphthenic acid/water experimental IFTs are in good agreement with the simulated IFTs. On the other hand, REPSOL supplied two different values for pure quinoline/water IFT: (i) a value of 33 $mN \cdot m^{-1}$, which is in reasonably good agreement with the simulated value and (ii) 7 $mN \cdot m^{-1}$, which is even lower than the 3-naphthenic acid/water value. Regarding the molecular structures of the four simulated compounds, it seems unprovable that a pure quinoline/water interface yields a lower IFT than the 3-naphthenic acid/water value, which has a pseudo-surfactant structure and can interact strongly with water via hydrogen bonding. In fact, according to the qualitative behaviour observed in MD simulations, the IFT of the quinoline/water interface should be between the toluene/water and 3-naphthenic acid/water values, which is in better agreement with the provided IFT value of 33 $mN \cdot m^{-1}$. For this reason, molecular simulations have been used to confirm that the value of 7 $mN \cdot m^{-1}$ is not reliable, and the IFT measurements with quinoline might be contaminated with other highly polar compounds.

The dependence of the IFT with temperature and pressure has also been calculated via molecular simulations (Figure 4.9). Temperatures from 280 K to 360 K and pressures from 1 atm to 100 atm have been considered to model the systems from lab to pore conditions. The obtained results show that the IFT decreases with temperature at a different rate depending on the studied compound. Dodecane/water interface exhibits the largest decrease in IFT with temperature (*i.e.,* 8.6 $mN \cdot m^{-1}$ when increasing 80 K the temperature), followed by toluene/water (*i.e.,* 6.8 $mN \cdot m^{-1}$), 3-naphthenic acid/water (*i.e.,* 5.8 $mN \cdot m^{-1}$) and finally quinoline/water (*i.e.,* 1.7 $mN \cdot m^{-1}$), whose IFT has a weak temperature dependence. Otherwise, due to the low compressibility of liquids, the pressure dependence of the four components from 1 atm to 100 atm is practically negligible, showing only slight increases of 1-3 $mN \cdot m^{-1}$.

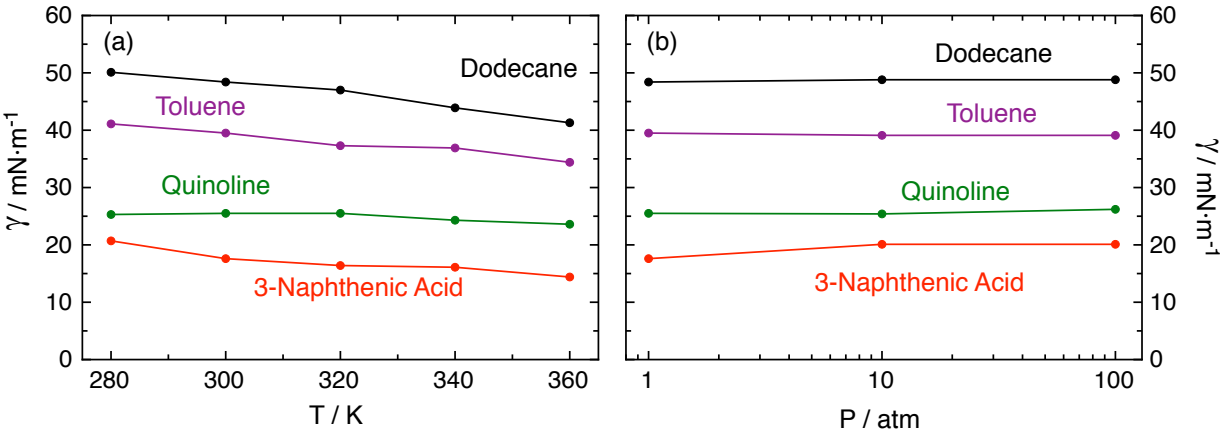

Figure 4.9. (a) Variation of oil/water IFT with temperature from 280 K to 360 K with the pressure fixed at 1 atm. (b) Variation of oil/water IFT with pressure from 1 atm to 100 atm with the temperature fixed at 300 K.

The distribution of molecules along the z-direction of the simulation cell (z-distributions) have been calculated in all of the beforementioned calculations to characterize the oil/water interfaces at a molecular level. To that end, the cell has been divided in bins of 1 Å width along the z direction (*i.e.,* $Lx_{bin} = Lx$, $Ly_{bin} = Ly$, $Lz_{bin} = 1$ Å) and the molecular position was averaged along the 2 last ns of the simulation. Recall that the simulation cells were divided into two regions filled with the respective molecules of the oil phase (*i.e.,* between z= 0 and $z = Lz/2$) and the water phase (*i.e.,* between $z = Lz/2$ and $z = Lz$), so the interfaces were originally located at $z = Lz/2$ and $z = 0$, the latter being equivalent to $z = Lz$ by PBCs. To better represent the two oil/water interfaces, the z-distributions have been displaced by $Lz/4$ in the z-direction, which moves the interfaces initially located at $z = 0$ and $z = Lz/2$ to $z = Lz/4$ and $z = 3Lz/4$, respectively. Then, the resulting distribution is shown as an oil bulk virtually surrounded by two water phases. An example of a z-distribution at 300 K and 1 atm for each of the studied liquid molecules is compiled in Figure 4.10.

As it can be seen in the z-distributions, all bulk water and oil regions exhibit a flat pattern giving the density of the pure compounds shown previously in Table 4.1. Additionally, the water and oil phases have such low reciprocal solubilities that no water molecules are found in the oil

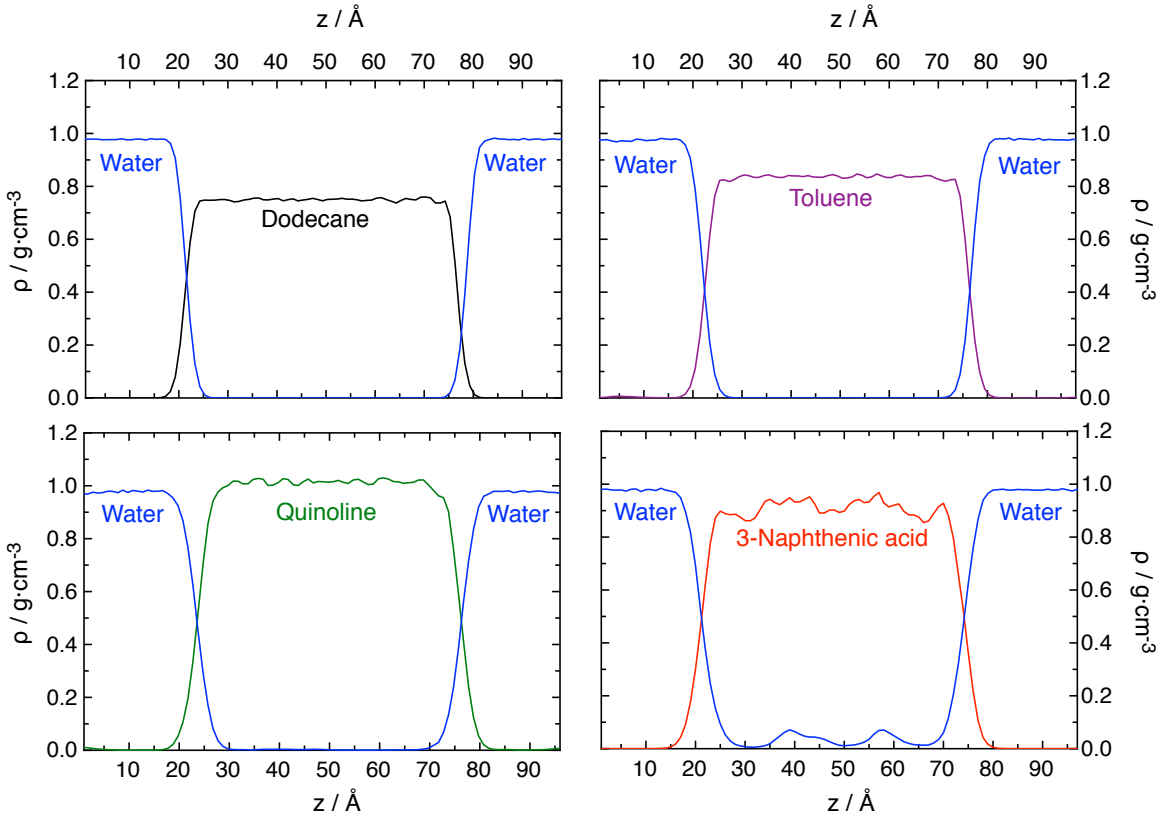

Figure 4.10. Pure oil/water interfacial z-distributions for the four molecules used to reproduce the maltene fraction of crude oil at 300 K and 1 atm.

phase and vice versa. The exception is the 3-naphthenic acid system, which has some water molecules solved within the oil phase, denoted by the blue peaks centered at z = 39 Å and z = 57 Å. The presence of water in the oil phase combined with the strong tendency of carboxylate acids to form hydrogen bonds slightly disrupts the homogeneity of the density pattern along the z-direction. In fact, two maxima of the 3-naphthenic acid density are found close to the water peaks, which suggests that the acid could be interacting and accumulating around the solved water via hydrogen bonds.

The width of the interface (ΔI) has also been analyzed from the z-distributions. To do so, the water phase bulk is assigned to the z-positions where the water density is constant, and the density of the oil phase is lower than 0.01 g/cm^3. Similarly, the oil bulk is assigned to the region where the oil density is constant, and the density of water is lower than 0.01 g/cm^3. Finally, the interface width is assumed to be the distance between the two bulk phases. According to the obtained results, this magnitude depends on the nature of the oil species and the temperature of the simulation. In that sense, the interfacial widths between 280 K and 360 K of the four oil/water systems has been calculated, giving values ranging from 6.8 Å to 8.0 Å for dodecane/water, from 7.7 Å to 9.1 Å for toluene/water, from 11.1 Å to 13.4 Å for quinoline/water and from 11.1 Å to 17.7 Å for 3-naphthenic acid/water.

The wider interfaces are also the ones with lower tension and vice versa, which is the expected trend because low IFTs usually tend to favor the mixing of the two phases in contact. In fact, from the obtained results a correlation can be built where the IFT is inversely proportional to the square of ΔI regardless of the species modeled (i.e., $\gamma = a/(\Delta I - b)^2$). In Figure 4.11 the correlation between the calculated IFT with the interfacial widths obtained from the z-distributions can be seen. Five IFT vs. ΔI points are plotted for each species referring to five different temperatures (*i.e.,* from 280 K to 360 K).

To conclude, the four model crude oil molecules are insoluble in water, specially the most non-polar fraction (*i.e.,* dodecane and toluene), which have relatively high IFTs and stiff interfaces. On the other hand, the most polar fractions of oil are more water-like, so their oil/water interfaces are the most diffuse and they have the lowest IFT. In fact, some cEOR techniques try to activate the naphthenic acids of crude oil (*i.e.,* the most polar fraction) to turn them onto "surfactant-like molecules", which reduce the oil/water IFTs and significantly improve oil/water mixing and oil recovery.[66,67] So, based only on oil/water IFT data, crude oils with higher resin content should be more easily recovered than oils with high content of non-polar compounds.

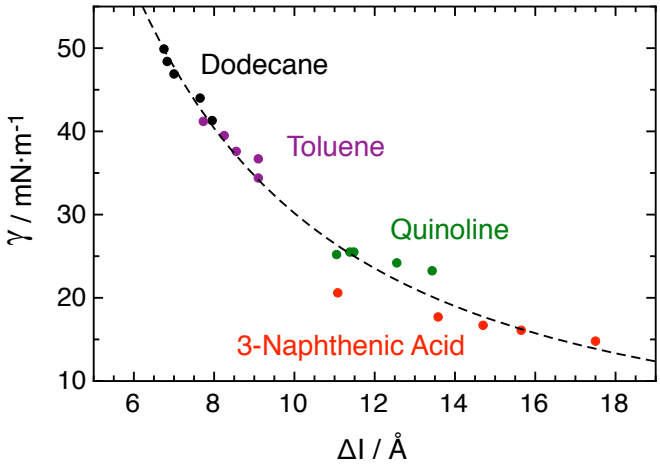

Figure 4.11. Correlation between the calculated IFT vs. the interfacial widths obtained from the z-distributions. Each dot corresponds to an independent simulation at a different temperature (*i.e.,* from 280 K to 360 K) and a pressure of 1 atm. Black, purple, green and red symbols refer to dodecane/water, toluene/water, quinoline/water and 3-naphtenic acid/water interfacial systems. Finally, the dashed black line correlates the data as $\gamma \propto \Delta I^{-2}$.

4.3.2 Oil/Water/Rock Contact Angles

In the previous section the most fundamental interactions between the different oil fractions and water have been evaluated. However, the interaction of these compounds with the porous rock is also key for the oil recovery process, which makes the understanding of the involved solid/liquid interfacial phenomena necessary. To that end, the CA of four nanodroplets, each of them containing a single pure oil component, immersed in water and placed on top of a crystalline $CaCO_3(10\bar{1}4)$ surface have been calculated. This specific face has been selected because it has the lowest surface energy,[68] so it should be the predominant face exposed in crystalline $CaCO_3$.

The calcite bulk unit cell has been obtained from X-ray crystallographic data,[69] and then cut through the most stable $(10\bar{1}4)$ face. A slab containing 7 layers has been replicated in the x and y directions to reach $Lx \approx Ly \approx 200$ Å and located at $Lz = 0$ Å. Then, an inverted copy of the slab has been placed at $Lz = 200$ Å to limit the size of the simulation cell. To prevent interactions between the upper and lower slabs due to PBCs the Lz cell parameter has been set to 400 Å, so at the end both surfaces are separated either by 200 Å of water or vacuum. Finally, the region between both surfaces has been filled with an oil nanodroplet, which has been placed on top of the surface located at $Lz = 0$ Å, and the remaining free volume has been filled with water molecules. The number of oil and water molecules depend on each simulation but are in the order of $1.5\text{-}2.0 \cdot 10^5$ water molecules and 1500-5000 oil molecules, scaling up to a total of 0.5-1.0 million atoms.

Although MD simulations with UA force fields have a relatively fine molecular representation, the computational time required to equilibrate and calculate properties of such large systems limits the number of simulations that can be performed in the time frame of the project. In this situation, one would ideally use a coarser molecular representation (*e.g.,* CG) to reduce the computational cost, but there are not many parameters that adequately capture the physics behind molecular solid surfaces yet. For this reason, the UA representation is still used with the atomistic force field of Xiao *et al.,*[70] to model the $CaCO_3$ surface, which uses a LJ potential to account for the interatomic interactions of calcite. This approach favors the integration of the mineral force field with other water or organic FFs that also use the same function to calculate the van der Waals interactions. Additionally, it accelerates the simulations giving similar results due to the faster calculation of the LJ 12-6 terms, in contrast to the exponential Buckingham term found commonly in mineral force fields.[71]

The CA simulations of pure oil components have been evolved in time during 5-10 ns, depending on the system, to ensure that the equilibration stage was over. The average geometry of the droplet has been monitored at each ns by averaging the molecular distributions in bins of 1 Å^2 of area along the xz plane (*i.e.,* $Lx_{bin} = 1$ Å, $Ly_{bin} = Ly$, $Lz_{bin} = 1$ Å). The equilibrium CA has been calculated by fitting its average profile to a circle to obtain the radius and height of the droplet as shown in Figure 4.6.

It is worth noticing that the Young equation (eq. 4.3), which relates the contact angle of a macroscopic droplet with the three interfacial tensions (*i.e.,* s/f_1, s/f_2 and f_1/f_2), is not exactly valid at the nanoscale. In fact, there is an evidence that the CA of nanodroplets placed on planar homogeneous surfaces exhibit deviations from the values predicted by Young equation.[72–74] The reason is that the wetting of nanodroplets depends not only on the balance of IFTs but also on an additional term known as line tension, which is defined as the excess free energy per unit length of a three phase contact line. This line tension is negligible for macroscopic droplets but as the size of a nanodroplet decreases, the relative amount of molecules at the vicinity of the three-phase contact line increases, along with the line tension. To take this effect into consideration, the Young equation can be modified as in eq. 4.4, where the angle of a nanodroplet (θ) becomes related to the angle of a macroscopic droplet (θ_∞), its radius (R) and the line tension (τ).[75]

$$\cos(\theta) = \frac{\gamma_{Sf_1} - \gamma_{Sf_2}}{\gamma_{f_1f_2}} - \frac{\tau}{\gamma_{f_1f_2}}\frac{1}{R} = \cos(\theta_\infty) - \frac{\tau}{\gamma_{f_1f_2}}\frac{1}{R} \qquad 4.4$$

The calculated CAs for the four model oil fractions are compiled in Table 4.4. Additionally, the effect of the line tension has been evaluated in the abovementioned setup using dodecane and toluene nanodroplets containing between 1500 and 5000 oil molecules. According to the results obtained, 3-naphthenic acid strongly competes with water in interacting with the calcite surface, as shown by a CA around 80º. The CAs of 60º for quinoline, 40º-50º for toluene and 20º-30º for dodecane reveal weaker oil/rock interactions that can be easily overcome by the strong water/calcite adhesion forces. These results show that even though from the IFT information it seems that the presence of polar oil molecules should help to recover oil from a reservoir, the most polar molecules also attach strongly to the rock surface. This fact implies that unless the polar molecule is capable of significantly reducing the IFT of the oil mixture, the overall trend will be to increase the oil/water/rock CA and hamper oil production.

Although the CAs of dodecane and toluene increase with the size of the droplet, thus denoting the effect of the line tension, the qualitative difference between the obtained results do not change. Additionally, the predicted CAs at a fixed size are already in agreement with the available experimental data regardless of the droplet size. On the other hand, the calculation of a macroscopic CA requires at least three or four calculations at different drop sizes, which rapidly becomes computationally prohibitive in the currently working framework. For this reason, instead of trying to reproduce the equilibrium CA of a macroscopic droplet, only nanodroplets with approximately 3000 oil molecules were used as shown in Figure 4.12 (*i.e.,* the largest that could be simulated in a reasonable amount of time according to the available computational power) to qualitatively compare the obtained angles at equality of oil molecules.

Table 4.4. Calculated oil/water/calcite CA at 300 K and 1 atm of the four molecules chosen to represent the maltene fraction at different nanodroplet sizes. The results are compared with experimentally measured macroscopic CAs of decane/water/calcite in ref 76 and toluene/water/calcite from REPSOL.[65]

	Oil Molecules	Droplet Radius / Å	θ / º	θ_{exp} / º
Dodecane	1500	55.2	20.6	21-38 [76]
	2000	59.5	23.8	
	2500	64.0	25.7	
	5000	81.5	36.4	
Toluene	2000	46.5	40.9	27-49 [65]
	2500	49.3	40.4	
	5000	57.5	48.0	
Quinoline	3000	55.0	63.8	
3-Naphthenic acid	3000	68.5	80.8	

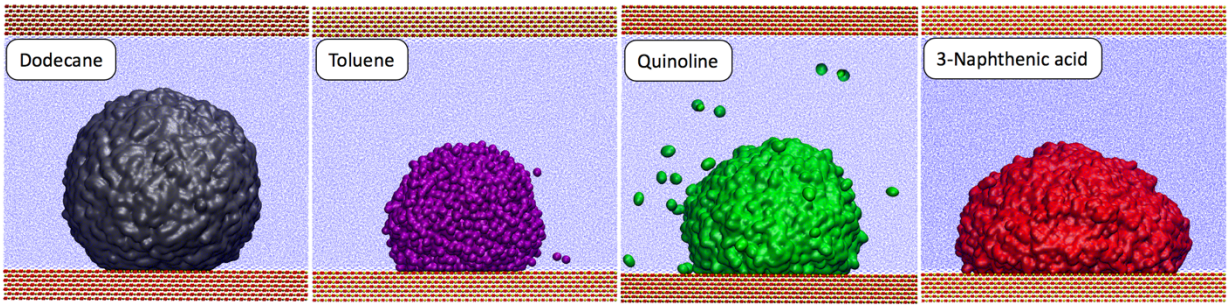

Figure 4.12. Final snapshot of the dodecane, toluene, quinoline and 3-naphthenic acid CA simulations on a calcite $(10\bar{1}4)$ surface embedded in water at 300 K and 1 atm. The vacuum above the upper layer is not represented in this figure and the droplets correspond to 2500/3000 molecules in size according to Table 4.4.

To analyze the functional groups involved in the oil/water/rock interactions, the Radial Distribution Functions (RDFs) of some relevant molecular segments with either Ca or O from $CaCO_3$ have been computed. The results show that the O atoms of water strongly interact with the Ca^{2+} ions of calcite (Figure 4.13b), as it can be seen by the sharp peak around 2.5 Å, and similarly its H atoms interact with the negatively charged CO_3^{2-} group via O-H hydrogen bonding (*i.e.,* the narrow peak at 2 Å). Water/calcite interactions are favored because the dipole moment of water is capable of strongly interacting with the charges of the ionic surface.

On the other hand, dodecane does not orient significantly towards the oil/rock interface (Figure 4.13c), due to its negligible dipole moment, which suggests that their mutual interaction is weak. For this reason, in the water/calcite vs. dodecane/calcite competition, water is capable of displacing dodecane from the surface and calcite becomes water wet. Similarly to dodecane, toluene does not show a strong orientation pattern with the surface because it lacks a strong polar moment (Figure 4.13d). The only noticeable interaction is a peak located at relatively lower distance involving aromatic carbon atoms and Ca^{2+} ion. This distribution suggests that toluene might be interacting slightly stronger than dodecane with the surface through the π region, which is also reflected in the resulting CAs.

Otherwise, both molecules used to represent the resin fraction are interacting strongly with the surface. Specifically, the partially negative N atom of quinoline confers it a significant dipole moment that points towards the Ca^{2+} ion of calcite, as it can be seen in the narrow peak at 2.5 Å (Figure 4.13e). Charge-dipole interactions are usually more intense than π-charge, so the aromatic rings of this molecule are not playing a role in its interaction with the surface and are positioned at a farther distance. Due to the stronger quinoline/calcite interactions water is not capable of displacing it as efficiently as dodecane or toluene and the CA of this species is higher than the other two.

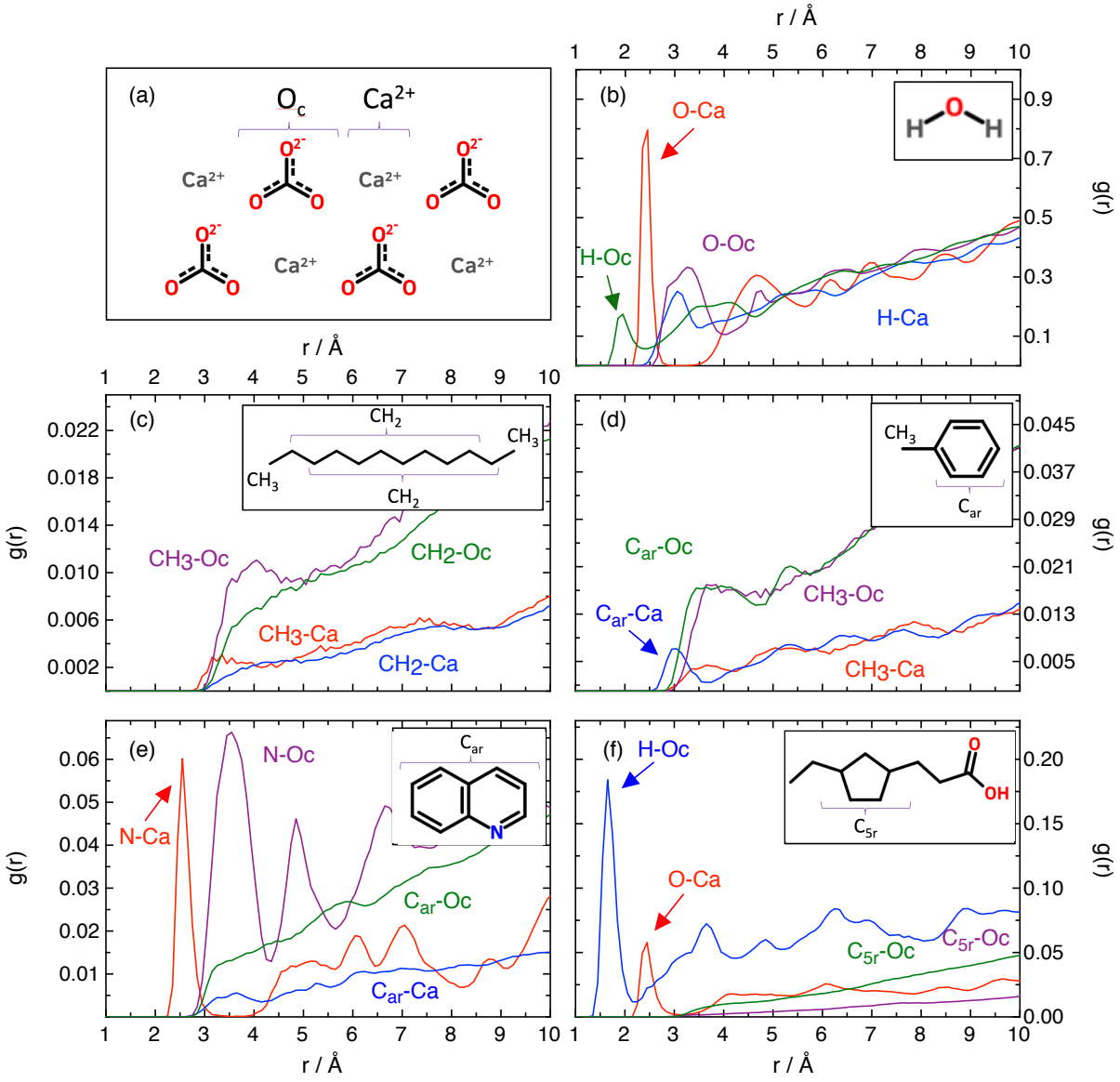

Figure 4.13. (a) Representation of the calcite $(10\bar{1}4)$ side view and (b-f) RDFs of some relevant molecular groups of water (b), dodecane (c), toluene (d), quinoline (e) and 3-naphthenic acid (f) with $CaCO_3$ obtained from the CA simulations at 300 K and 1 atm.

Similarly, 3-naphthenic acid has a COOH group that gives a strong dipole moment to the molecule. The O atoms have a partial negative charge located on them due to their electronegativity with respect the carboxylate C and H, which both bear a partial positive charge. This electronic distribution makes H and O atoms to interact with the negatively charged CO_3^{2-} and the positively charged Ca^{2+} ions of calcite, respectively (Figure 4.13f), whereas the organic non-polar part of the molecule is farther away, probably pointing towards the oil bulk (*i.e.,* similarly to a surfactant behavior). This is the strongest interaction seen among the four compounds, which is also reflected on a significantly high CA value, denoting the difficulty of water to displace naphthenic acids from carbonate reservoirs.

To conclude, this section shows that although the information obtained by oil/water IFT calculations is important, it is also not enough because the oil/rock interactions are also key in understanding the oil recovery phenomenon. In fact, according to the IFT results it seems that polar components solved in oil should help in recovering crude oil from reservoirs, whereas CA simulations showed that they attach strongly to the oil/rock surface, preventing water to displace them effectively. Fortunately, $CaCO_3$ is a very hydrophilic rock and water tends to displace any oil molecule on top of it except 3-naphthenic acid, which is capable of attaching to the surface via the H atom and the O atoms of the COOH group.

4.3.3 Salinity Effects on Interfacial Tensions and Contact Angles

Recall that during the formation process of a petroleum reservoir a highly concentrated brine is also trapped along with the crude oil. This fact opens another possible set of oil/brine and oil/brine/rock relevant interactions that may affect the oil recovery. For this reason, after evaluating the IFT of pure oil components with water, the effect of salinity has been assessed by adding different electrolytes to the water bulk. To that end, two different brines have been modeled using NaCl as a monovalent electrolyte and $CaCl_2$ as a divalent salt. The IFT MD simulations have been performed at 300 K and at 1 atm exactly as in pure oil/water systems, but adding a total of 11, 54 and 108 NaCl or $CaCl_2$ units randomly distributed within the water bulk region to simulate brine concentrations of 0.2 $mol \cdot kg^{-1}$, 1.0 $mol \cdot kg^{-1}$ and 2.0 $mol \cdot kg^{-1}$, respectively. On the other hand, the total number of electrolytes added for the CA calculations range from 550 to 7000 depending on the amount of water and the salinity concentration modeled. NaCl has been modeled with the force field of Smith *et al.,,*[77] whereas divalent cation parameters have been obtained from the work of Åqvist.[78]

All ions interact strongly with water dipoles, which makes them more soluble in water rather than in any of the four model oils simulated. The presence of ions in the water phase increases the ionic strength of the solution, which in turn enhances its polarity, making the differences between the water and oil phases more noticeable. As expected, this effect is also reflected in an approximately linear increase of the oil/water IFTs when adding either NaCl or $CaCl_2$ (Figure 4.14), being the latter more prejudicial to oil recovery due to the stronger ionic strength. Finally, the effect of salts seems to be independent of the oil fraction, because either dodecane/water, toluene/water, quinoline/water and 3-naphthenic acid/water exhibit similar increases between 3 and 5 $mN \cdot m^{-1}$ when adding a maximum of 2.0 $mol \cdot kg^{-1}$ of NaCl and between 7 and 9 $mN \cdot m^{-1}$ when adding the same amount of $CaCl_2$. The predicted trend adequately agrees

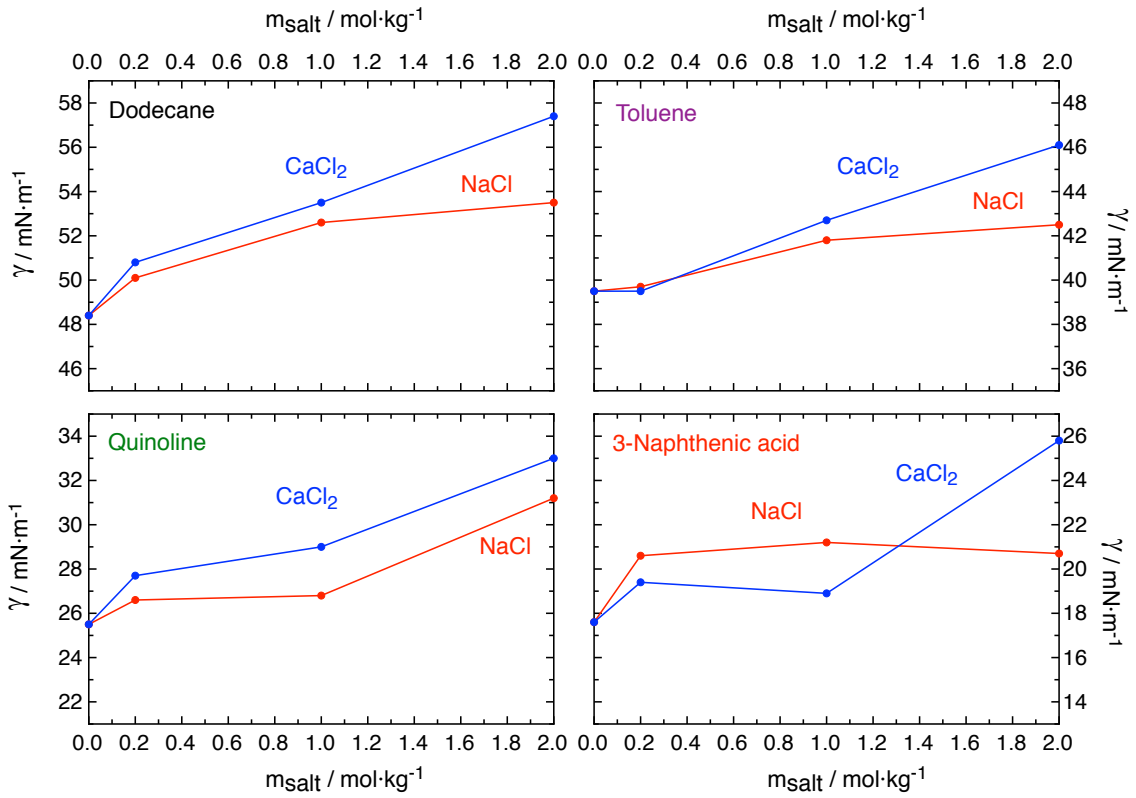

Figure 4.14. Oil/water IFT increase produced by the presence of NaCl and $CaCl_2$ as monovalent and divalent salts, respectively. The effect is evaluated for dodecane, toluene, quinoline and 3-naphthenic acid at 300 K and 1 atm.

with other experimental works on pure oil/water interfaces, which validates the results obtained. Some examples are the studies performed by Lima *et al.*,[79] who added 2.0 mol·kg^{-1} of NaCl to a cyclohexane/water interface to increase 3 mN·m^{-1} the IFT and also added 1.0 mol·kg^{-1} of $CaCl_2$ to linearly increase the IFT to 3.5 mN·m^{-1} (*i.e.,* that can be extrapolated to 7 mN·m^{-1} at a $CaCl_2$ concentration of 2.0 mol·kg^{-1}). Or similarly, Aveyard *et al.*,[80] measured a linear increase of 1.5 mN·m^{-1} per each 1.0 mol·kg^{-1} of NaCl in the decane/water IFT, whose extrapolated value of 3.0 mN·m^{-1} at 2.0 mol·kg^{-1} of NaCl also agrees to the result of Lima *et al.*,[79]

The z-distributions of the oil/water/salt (2.0 mol·kg^{-1}) systems have also been computed and are displayed in Figure 4.15. In these plots the water phase has been centered (*i.e.,* instead of the oil phase) to better analyze the behavior of the salt. Any of the four oil bulks are perturbed by the presence of salt, so they keep the pattern shown in the distributions of Figure 4.10. On the other hand, at equilibrium, the water phase contains the totality of the ions in solution homogeneously distributed along its bulk, but none of them is located close to the interface. This is explained because electrolytes are even more polar than water molecules, so oil/water interfaces should be less energetic than oil/electrolyte interfaces.

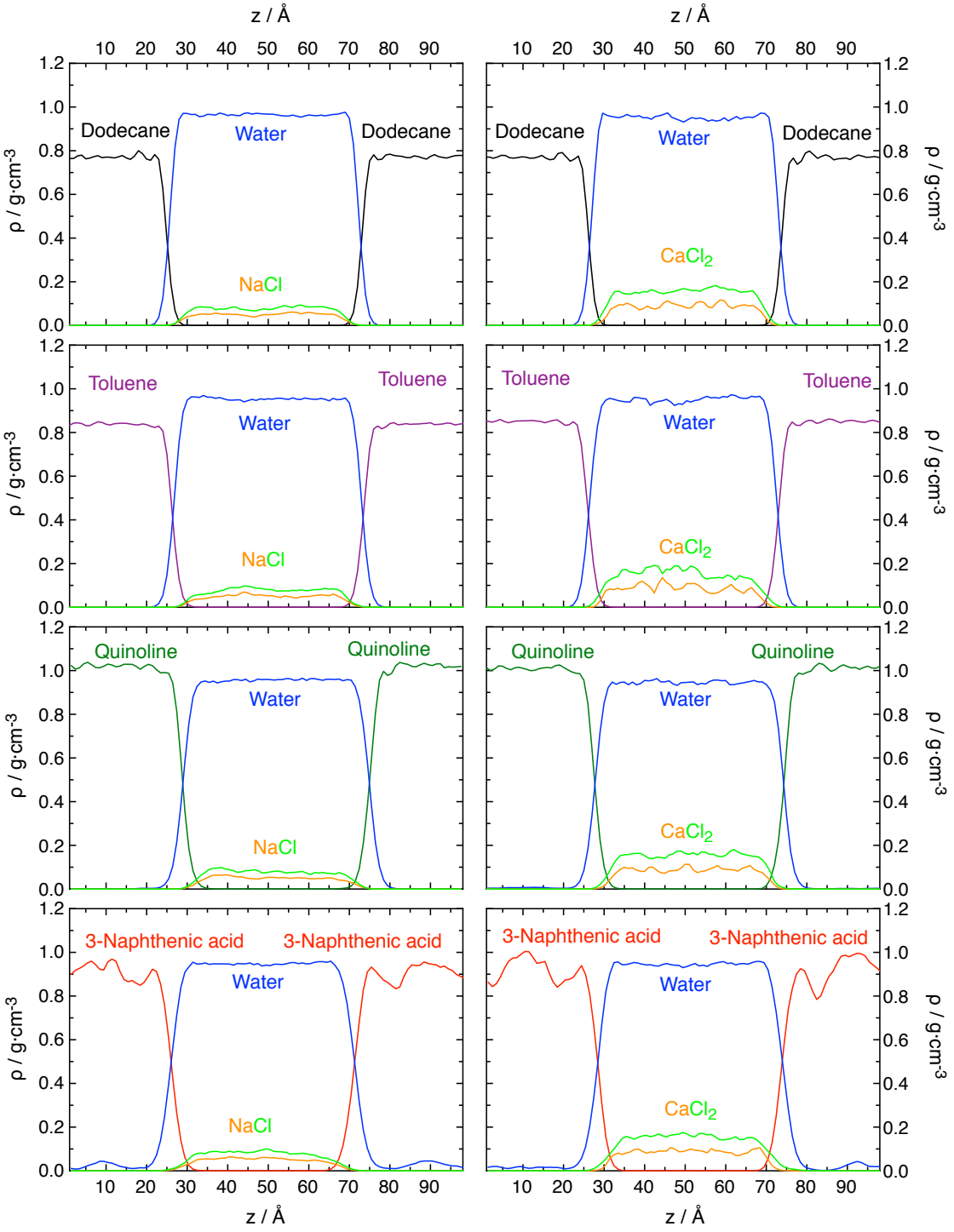

Figure 4.15. Oil/water/NaCl (2.0 mol·kg^{-1}) and oil/water/$CaCl_2$ (2.0 mol·kg^{-1}) interfacial z-distributions for the four molecules used to reproduce the maltene fraction of crude oil.

On the other hand, the behavior exhibited by the oil/brine/carbonate CAs measured experimentally is significantly scattered. In fact, some studies show that carbonates become more water wet when increasing salinity concentration, possibly because water can interact more favorably with the surface if the oil is not significantly affected by the presence of brine.[81,82] Alternatively, other studies found that carbonates turn more oil wet because ions may help the

Table 4.5. Salinity effect on the CA of a 2500 dodecane nanodroplet on top of a calcite surface embedded in water at 300 K and 1 atm.

	Pure water	0.2 m NaCl	2.0 m NaCl
θ / º	25.7	18.4	22.4

polar fractions of oil to attach to $CaCO_3$ and hamper oil recovery.[83] For this reason, the saline effect on CA has also been analyzed via MD simulations. The interactions between salinity and the four oil components are very similar among each other, as seen by the IFT patterns of Figure 4.14, so the saline effect on the CA has not been replicated in all molecules and has only been studied with dodecane and NaCl. The obtained results show that the effect of the electrolytes seems to be slightly reducing the oil/water/rock CA, but the effect is not very significant (Table 4.5). Although the oil/water IFT is increasing by the presence of the salt, the water/calcite interactions become enhanced due to the increased polarity of the water phase. In this new system, the stronger water/calcite adhesion forces, that favors oil extraction, compete against the IFT increase that hampers it, concluding in a positive slight CA reduction.

The compilation of results in this section show that salinity does not interact significantly with any of the four pure model oil components used in this work. In fact, the oil/water IFT is increased by approximately the same amount regardless of the system simulated and their molecular distributions are not significantly affected by salinity. Additionally, the CA of a dodecane droplet on top of a calcite surface is slightly reduced when adding electrolytes to water, which increase the polarity of the phase and enhance the water/calcite interactions without affecting oil/rock interactions.

4.3.4 Summary and Conclusions

To conclude, the selected force fields are capable of reproducing the oil/water IFT and CA in a reasonable agreement with the available experimental information, either published in the bibliography or supplied by REPSOL. The obtained results show that the interfaces of the most polar oil compounds (*i.e.,* the most hydrophilic) have the lowest IFTs because they interact favorably with water, whereas the interfaces with the least polar compounds (*i.e.,* the most hydrophobic) are highly energetic. Temperature reduces the IFT of all studied systems linearly, but the effect of pressure is negligible due to the incompressibility of liquids. It is also worth noticing that systems with high oil/water IFTs tend to minimize the oil/water contact, which is related to a thinner and stiffer interface, whereas a low oil/water IFT yield wider interfaces. Additionally, the most polar compounds also have a higher affinity for the oil/rock interface, which

increases the CA as dodecane < toluene < quinoline < 3-naphthenic acid. Specifically, 3-naphthenic acid attaches as a bidentate species to the calcite surface with the H atoms interacting with the CO_3^{2-} groups of calcite via hydrogen bonding and the O atoms interacting with the Ca^{2+} ion. On the other hand, quinoline attaches as a monodentate species, only interacting with the Ca^{2+} ion via the dipole moment produced by the N atom. Finally, the interactions of toluene and dodecane with calcite are weaker as reflected by the lower CA. These results imply that, even though the most polar compounds are showing the lowest oil/water IFTs they attach strongly to the carbonate surface impeding the efficient oil recovery.

Finally, the selected force fields are also shown to be capable of qualitatively reproduce the oil/water interfacial behavior without salt and when adding either NaCl or $CaCl_2$. The latter species tend to solve onto polar liquids and flee from interfaces, so they accumulate at the water bulk, which increases the ionic strength and polarity of water. This fact makes oil to be much lesser polar than water, which should hamper the oil extraction because it reduces the oil/water affinity and strengthens their interfaces. As a result, the IFT of the liquid/liquid system is increased approximately the same amount regardless of the oil model used (*i.e.,* 3-5 $mN \cdot m^{-1}$ with a 2.0 $mol \cdot kg^{-1}$ of NaCl and 7-9 $mN \cdot m^{-1}$ with a 2.0 $mol \cdot kg^{-1}$ of $CaCl_2$). On the other hand, the oil/water/rock CA is slightly reduced with the presence of salt, which suggests that the competition between the enhanced brine/rock and the weakened oil/brine interactions slightly balance the carbonate surface to water wet conditions, as shown by some published experimental results.

4.4 Model Oil/Water/Rock Interfacial Properties (Mixtures)

The study of pure model oil components is useful to understand the most fundamental interactions and affinities of each compound with water and different brines as well as the main driving forces that yield high or low IFTs and CAs. However, a closer representation of a real crude oil comes from modeling a mixture containing all of the proposed average molecules. Specifically, to analyze how changing the polarity of the oil phase affects the oil/water IFT and the oil/water/rock CA, different species have been combined to analyze the impact of each fraction one by one. In that sense, the work compiled in the following sections includes the IFT and CA simulations with different model oil mixtures with and without the effect of salinity.

4.4.1 Oil/Water Interfacial Tensions

The oil/water IFT of binary, ternary and quaternary mixtures of maltene molecules (*i.e.,* dodecane, toluene, quinoline and 3-naphthenic acid) is analyzed in this section, followed by the modeling of complex mixtures containing all of the representative crude oil average molecules (*i.e.,* including asphaltenes). The previous 45 Å x 45 Å x 100 Å simulation cell has become too small to model a statistically significant number of each oil component in mixtures. For this reason, the size of the oil region was almost doubled, keeping the length of the water phase constant, which forced to enlarge the simulation cells to 45 Å x 45 Å x 135 Å for the mixtures without asphaltenes and to 80 Å x 80 Å x 210 Å for the asphalted crude oil models. Additionally, the simulation time has been increased from 10 ns to 20-40 ns to ensure the equilibrium in the molecular distributions for mixtures without and with asphaltenes, respectively.

(i) Organic binary mixtures 1: the dodecane/toluene and quinoline toluene model oils

The first maltene oil mixtures of this part of the thesis have been selected with the aim to reproduce the experimental results that REPSOL measured at that moment. First, the binary dodecane/toluene and toluene/quinoline mixtures have been modeled through MD simulations at different concentrations to quantify the oil/water IFT variation from their pure state. Regarding the first mixture, the addition of toluene onto a dodecane matrix lowers the oil/water IFT from the pure dodecane/water to the pure toluene/water values (Figure 4.16a). The experimental results of REPSOL denote two different regions in the IFT vs. % toluene plot: (i) from 0 % to 30 % of toluene the oil/water IFT falls from approximately 50 $mN \cdot m^{-1}$ to 36 $mN \cdot m^{-1}$ and (ii) the oil/water IFT almost does not change when increasing toluene content from 30 % of toluene to 100 % toluene.

Similarly, the addition of quinoline onto a toluene matrix reduces the oil/water IFT from the pure toluene/water to the pure quinoline/water values (Figure 4.16c). In this case, the experimental REPSOL values drop onto an abnormal value of 7 $mN \cdot m^{-1}$ for the pure quinoline/water interface, probably due to an unknown contamination, as previously explained. Qualitatively, the trend reproduced by REPSOL is commonly seen in other experimental works,[84,85] where the oil/water IFT is significantly reduced when adding a low concentration of a more polar compound to the mixture. In fact, Kim *et al.,*[84] proposed an empiric expression to fit the IFT of an oil binary mixture with water from the IFT of the pure components, which describes an exponential decay from the highest to the lowest IFT. The steep slope at low concentrations is attributed to the diffusion of

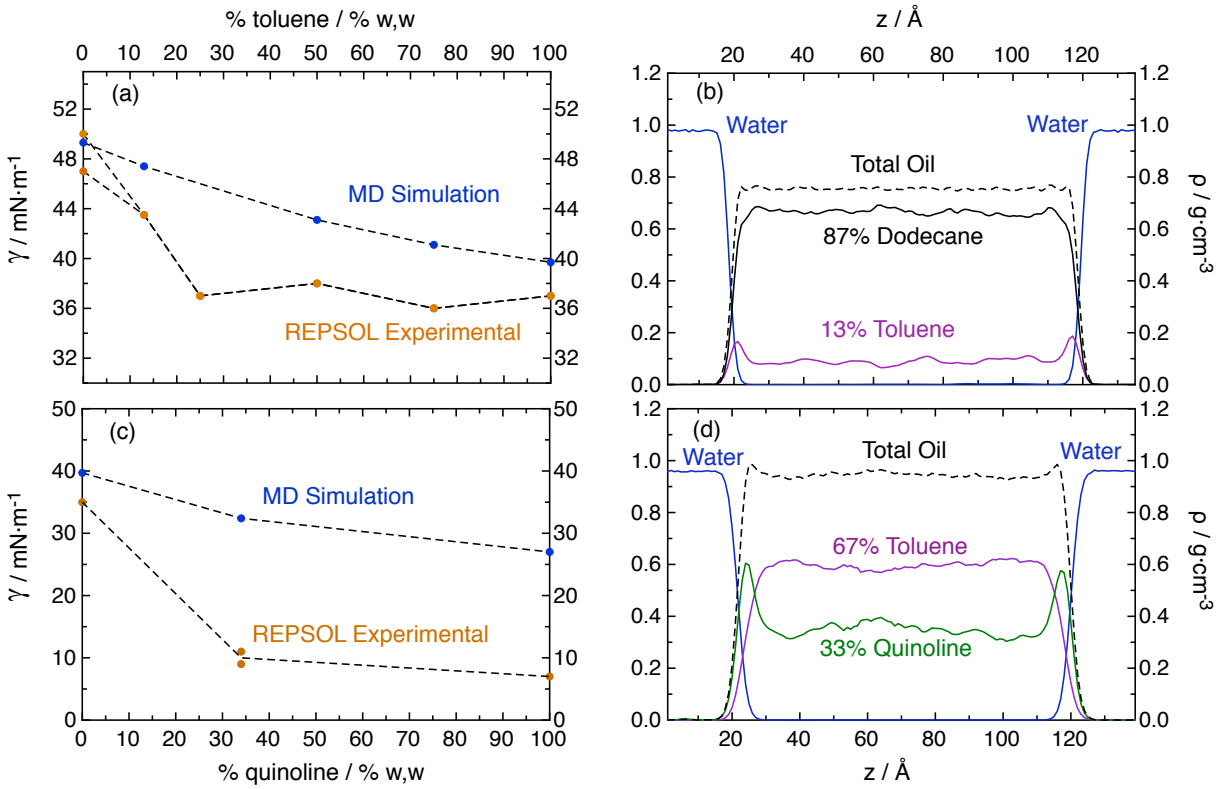

Figure 4.16. Comparison between the experimentally measured and the MD calculated oil/water IFTs for (a) dodecane/toluene and (c) toluene/quinoline systems at different compositions of organic binary mixtures at 300 K and 1 atm. Also, z-distributions for all species of a simulation with (b) an 87 % of dodecane and 13 % of toluene and (d) a 67 % of toluene and 33 % of quinoline are also shown as examples.

polar oil species to the oil/water interface and is followed by a flatter pattern when the interface is almost saturated.

Otherwise, the simulation results seem to reduce the oil/water IFT with concentration, with a lower slope than the experimentally measured dodecane/toluene and toluene/quinoline mixtures. Even though the oil/water IFT reduction is underestimated, the accumulation at the interface of the most polar oil components is correctly captured (*i.e.,* toluene for the dodecane/toluene mixture and quinoline in the toluene quinoline/mixture). According to Figure 4.16b the concentration of toluene and dodecane is homogeneous in the bulk phase, but two toluene peaks appear at $z \approx 20$ Å and $z \approx 115$ Å. These peaks denote that dodecane is being pushed onto the bulk phase and toluene is accumulating at the oil/water interface because it has slightly higher polarity and stronger adhesive interactions with water. Similarly, as quinoline is much more polar than toluene due to the well-defined dipole moment given by the N atom, it is capable of accumulating at the oil/water interface (*i.e.,* the quinoline accumulation peaks in $z \approx 25$ Å and $z \approx 115$ Å of Figure 4.16d) and displace toluene to the oil bulk.

(ii) Organic binary mixtures 2: the analysis of quinoline impurities

At this point of the study, the large discrepancies between the experimental and simulated oil/water quinoline IFTs motivated to perform an analysis of the main possible contaminants present in the commercial quinoline acquired by REPSOL. According to a HPLC carried out to a quinoline sample (Table 4.6), it was observed that the many of the higher concentration impurities either had significant less polarity (*i.e.,* naphthalene derivatives), or a quinoline-like structure (*i.e.,* quinoxaline, dimethylquinoline). For this reason, two trace compounds that differed significantly from the quinoline structure (*i.e.,* benzoisothiazole and methylbenzothiophene) were analyzed through MD simulations. The impact on the pure quinoline/water IFT induced by these impurities has been evaluated by modeling binary mixtures with a 95 % of quinoline and a 5 % of contaminant. This concentration is significantly larger than in the HPLC analysis, but as previously seen in the dodecane/toluene mixture, MD simulations predict a weaker IFT decrease in the low concentration region. For this reason, a higher impurity concentration intends to magnify the effects to give a qualitative description of the behavior of both contaminants.

The resulting oil/water IFT of the system with benzoisothiazole was reduced from 25.5 $mN \cdot m^{-1}$ to 22.3 $mN \cdot m^{-1}$, whereas methylbenzothiphene could not affect the quinoline IFT and yielded 25.1 $mN \cdot m^{-1}$. The z-distributions of the impurities are compiled in Figure 4.17, where one can see that benzoisothiophene accumulates significantly at the oil/water interface, while methylbenzothiophene stays in the quinoline bulk. This result implies that the former is significantly more polar than quinoline and it is expected to affect the interfacial properties even at low concentrations. On the other hand, the latter is not an active compound because the sulphur atom is less polar than the nitrogen of quinoline. The conducted MD simulations allow to propose benzoisothiophene as a possible contaminant in the quinoline/water IFT, showing the capacity of simulations to predict useful information even though only qualitative trends are reproduced.

Table 4.6. HPLC analysis carried out by REPSOL [65] of the main possible contaminants of commercial quinoline.

Compound	Retention time	% Area	Compound	Retention time	% Area
Quinoxaline	10.819	0.004	methylbenzotiophene	11.889	0.025
Benzoisothiazole	11.046	0.002	methylnaphthalene	12.001	1.744
Quinoline	11.256	98.198	dimethylquinoline	14.204	0.010

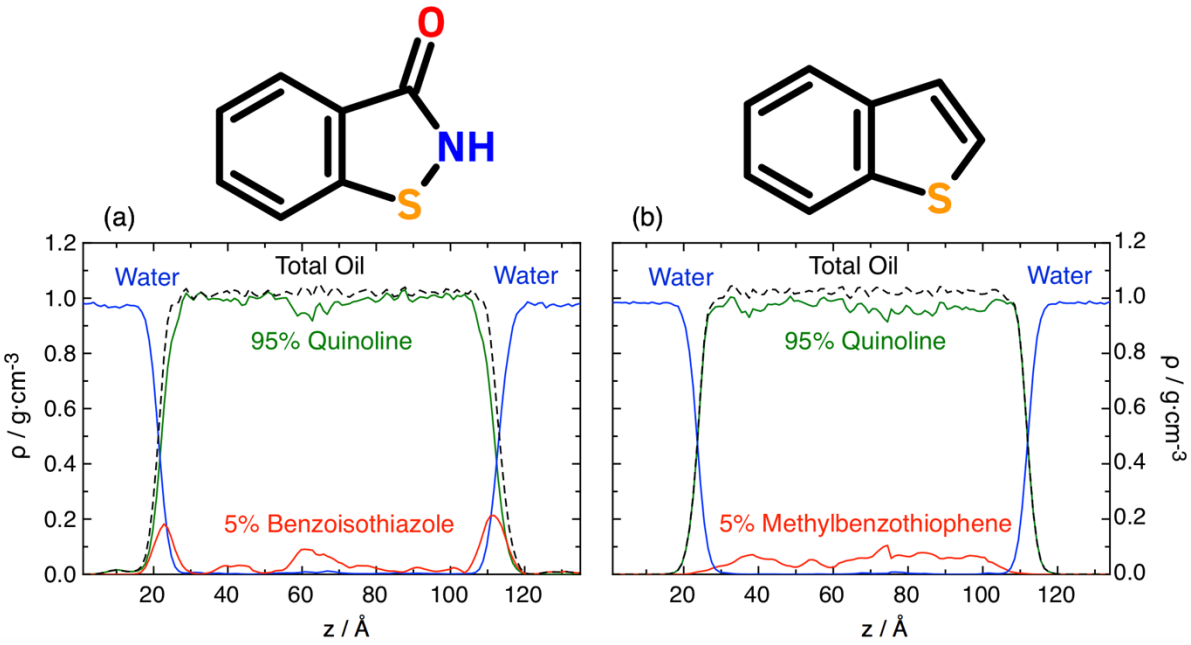

Figure 4.17. Equilibrium z-distributions for all species in quinoline/water/impurities simulations at lab conditions (*i.e.,* 300 K and 1 atm). The molecular structure of each impurity is shown above its distribution.

(iii) Organic ternary mixtures: the dodecane/toluene/3-naphthenic acid oil models

Apart from the quinoline impurity analysis, the previous binary mixtures evaluate the interfacial impact of the saturate, aromatic and basic resin fractions. The effect of 3-naphthenic acid has been evaluated through some ternary oil models containing dodecane, toluene and 3-naphthenic acid. In this mixture, the dodecane/toluene ratio is kept constant to the initial 87 % dodecane / 13 % toluene and different amounts of 3-naphthenic acid are added onto the system. Specifically, the initial concentrations of the mixtures studied in this section using both experiments and MD simulations are compiled in Table 4.7.

The experimental measurements shown in Figure 4.18a suggest that the 3-naphthenic acid accumulates at the oil/water interface, dropping the dodecane/toluene/water IFT significantly to the value of 20 $mN \cdot m^{-1}$ in the concentration range from 0 % to 10 %. Then, the slope of the IFT vs. acid concentration becomes flatter until achieving the value of pure 3-naphthenic acid. The same qualitative behavior is seen when modeling the mixture with MD, where the IFT vs. acid concentration decreases more rapidly at low acid composition due to the high interfacial activity of this species. In fact, the large polarity difference between 3-naphthenic acid and the dodecane/toluene matrix makes the former to migrate significantly to the oil/water interface (Figure 4.18b).

Table 4.7. Initial composition (*i.e.,* in % w,w) of the different ternary mixtures in which the oil/water IFT was either measured experimentally or calculated via MD simulations, both of them at laboratory conditions (*i.e.,* 300 K and 1 atm).

Ternary mixture	Studied via	Dodecane	Toluene	3-Naphthenic acid
1	MD and Exp.	87.0 %	13.0 %	-
2	MD and Exp.	86.1 %	12.9 %	1.0 %
3	Exp.	85.3 %	12.7 %	2.0 %
4	Exp.	85.3 %	12.7 %	5.0 %
5	MD and Exp.	78.3 %	11.7 %	10.0 %
6	MD	43.5 %	6.5 %	50.0 %
7	MD and Exp.	-	-	100.0 %

Notice, that the initial concentrations compiled in Table 4.7 do not coincide with the simulation concentrations of Figure 4.18a. The reason is that 3-naphthenic acid feels very attracted to water, which favors the migration of many acid molecules to the oil/water interface. When this happens, the bulk concentration of species at the end of the MD simulation becomes lower than the initial values. Then, to correctly evaluate the effect on the IFT, the concentration of all species has to be recalculated at the end of the simulation. This is a consequence of the finite size of the system modeled, which contains only a few amount of molecules at each bulk phase (*i.e.,* in the order of 10^2 molecules). This is generally not an issue in experiments because even a dilute solution has an order of 10^{20} molecules, which is an almost infinitely large molecule reservoir. So, if some molecules migrate from the bulk to the interface, the initial concentration almost does not change.

For this reason, the simulation data in Figure 4.18a refer to the ternary mixtures labeled in Table 4.7 as 1, 2, 5, 6 and 7 but with the bulk concentration of 3-naphthenic acid recalculated

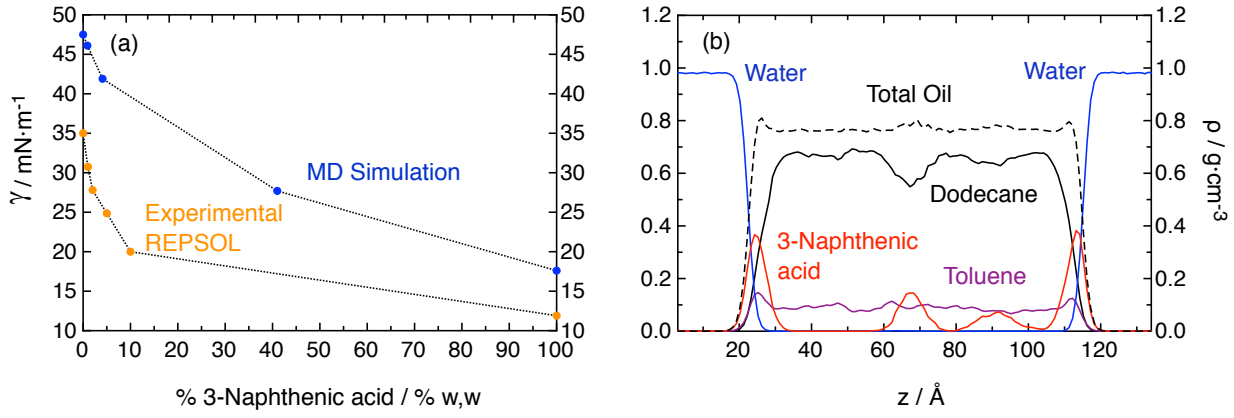

Figure 4.18. (a) Comparison between the experimentally measured IFT and the simulation data for the different ternary mixtures as a function of 3-naphthenic acid concentration. (b) The z-distribution for all species of ternary mixture 5. All data shown are at 300 K and 1 atm.

according to each equilibrium configuration. Additionally, in Figure 4.18b the z-distribution of ternary mixture 5 is shown to exemplify the large interfacial accumulation of 3-naphthenic acid at the interface. In this case, there is a 10 % of initial acid bulk concentration, but when the system achieves the equilibrium state, the final bulk concentration becomes roughly a 4 %. It is important to remark that this effect is only seen when 3-naphthenic acid is present in the mixture and not in the previous dodecane/toluene and toluene/quinoline models.

(iv) Organic quaternary mixtures: the equimolar model

A final quaternary mixture has been modeled containing an equimolar composition of the four molecules studied up to now. The aim of this simulation is to characterize the nature of the interface in the presence of a complete maltene crude oil model. To that end, the same number of dodecane, toluene, quinoline and 3-naphthenic acid molecules have been initially added to the oil bulk and the system has been equilibrated at 300 K and 1 atm. The resulting oil/water IFT of the quaternary system becomes 23.6 $mN \cdot m^{-1}$, which is relatively close to the values of 25.5 $mN \cdot m^{-1}$ and 17.6 $mN \cdot m^{-1}$ of the interfaces of pure polar fractions with water. This result suggests that all polar molecules are effectively occupying the interface, while dodecane and toluene are present only in the bulk phase. In fact, the z-distribution of this system at equilibrium (Figure 4.19a) shows that 3-naphthenic acid migrates from the bulk phase and occupies a large amount of interfacial volume, almost preventing quinoline accumulation.

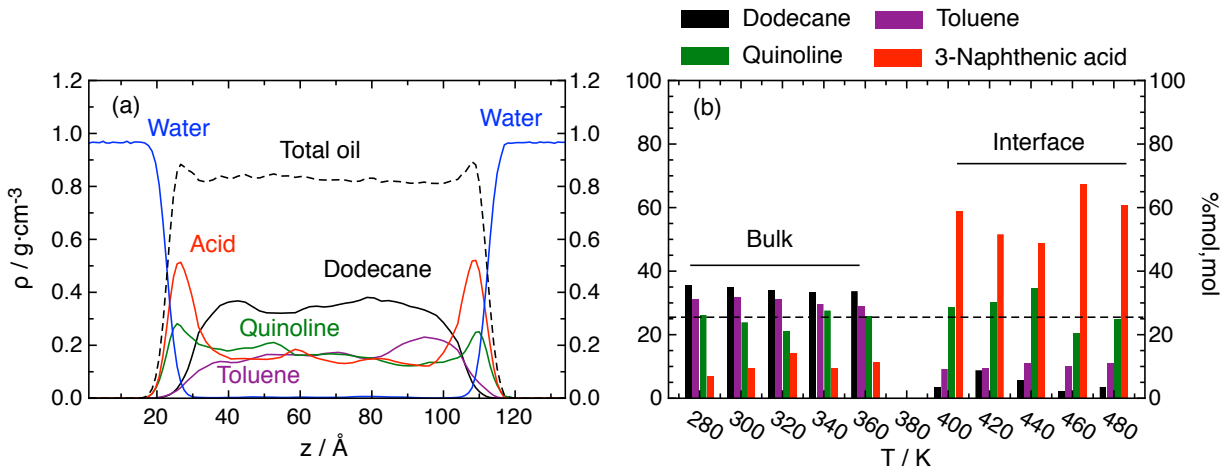

Figure 4.19. (a) Calculated z-distributions for all species of the quaternary equimolar mixture at 300 K and 1 atm. (b) Comparison between the bulk and the interfacial composition (*i.e.,* in % mol,mol) of each simulated species as a function of temperature. The dashed line corresponds to the input bulk composition (*i.e.,* 25 %).

Apart from the equilibrium bulk concentration, the interfacial accumulation of all species has been calculated in these simulations. The interface has been defined as the regions where the 3-naphthenic acid makes large peaks (*i.e.,* located at z = 20-40 Å, and z = 100-120 Å in Figure 4.19a) and the bulk is selected as the whole volume between the interfaces with homogeneous density patterns (*i.e.,* from z = 40 Å to z = 100 Å). The simulation results determine that the concentration at the interface of 3-naphthenic acid is slightly higher than 50 %, which is the double of the input concentration, followed by a 30 % for quinoline and 10 % for dodecane and toluene, respectively. The bulk concentrations of all species follow an inverse trend with respect the interfacial values, with 35 %, 32 %, 24 % and 9 % for dodecane, toluene, quinoline and 3-naphthenic acid, respectively. Finally, the effect of temperature in the molecular distributions has been analyzed by performing five different simulations from 280 K to 360 K. The results are compiled in Figure 4.19b, where it can be seen that all concentrations at the bulk and at the interface oscillate around the same values regardless of the temperature.

The oil/water IFT of a mixture is not an average of the pure oil/water IFTs weighted by their initial bulk concentration because some species have a strong tendency to accumulate at the interface, which reduces the IFT of the mixture. Otherwise, if the average is performed with the equilibrium concentration of species at the interface, the resulting IFT (γ_{ave}) correlates almost perfectly with the calculated value of the mixture from MD (γ_{MD}). To denote this correlation, the pure oil/water IFT of the four maltene molecules and the equimolar quaternary mixture at different temperatures have been compiled in Table 4.8, along with the equilibrium interfacial concentration in % mol,mol and the interfacial averaged IFT (γ_{ave}). These results suggest that the IFT of an oil with water is only dependent on the species accumulated at the interface, and not on the bulk components.

(v) Complex model oils: the mixtures with asphaltenes

Up to this point the interfacial behavior of several oil models has been studied, by only considering the effect of the different maltene fractions. However, the presence of asphaltenes usually affects the interfacial and rheological properties of crude oils.[86,87] Thus, in the following IFT simulations, asphaltenes have been included in the simulation cell aiming at qualitatively understanding and characterizing the interfacial behavior of this model fraction in different crude oil mixtures. Additionally, the asphaltene content (*i.e.,* 10.8 % w,w) and the molecules used to represent the fraction have been selected to specifically mimic the chemical properties of the Carabobo crude oil, according to the experimental characterization performed by REPSOL.[65] The

Table 4.8. Calculated oil/water IFTs for the pure maltene molecules at different temperatures from 280 to 360 K and 1 atm (*i.e.,* the data of Figure 4.9). Also, the calculated oil/water IFT (γ_{MD}) for the quaternary equimolar mixture and the interfacial averaged oil/water IFT (γ_{ave}) from pure components is shown along with the interfacial concentration of all species in the simulation for the same temperatures.

		γ_{MD} / mN·m^{-1}			
	T / K	Dodecane	Toluene	Quinoline	3-Naphthenic acid
Pure Compounds	280	50.1	41.1	25.3	20.7
	300	48.4	39.5	25.5	17.6
	320	47.0	37.3	25.5	16.4
	340	43.9	36.9	24.3	16.1
	360	41.3	34.4	23.6	14.4

		Interfacial concentration / % mol,mol				γ / mN·m^{-1}	
	T / K	Dodecane	Toluene	Quinoline	3-Naphthenic acid	γ_{MD}	γ_{ave}
Equimolar mixture	280	3.6 %	9.2 %	28.5 %	58.7 %	22.6	24.9
	300	8.8 %	9.5 %	30.1 %	51.6 %	23.6	24.8
	320	5.8 %	10.9 %	34.5 %	48.8 %	21.2	23.6
	340	2.1 %	10.1 %	20.5 %	67.3 %	20.7	20.5
	360	3.6 %	11.0 %	24.8 %	60.6 %	20.0	19.8

information regarding the Carabobo crude oil composition is strictly confidential, but it is known to be a heavy crude oil. For this reason, a set of model oils containing high amounts of asphaltenes have been selected to try to qualitatively predict the interfacial properties of average heavy crude oils with different polarity.

The asphaltene fraction has been modeled using two different asphaltene molecules to match the chemical analysis carried out by REPSOL. The molecule used to represent the asphaltene 1 was initially elucidated by Boek *et al.,*,[15] and already accounts for some of the reported asphaltene features, so it is selected as an average asphaltene molecule in this thesis. The second molecule (*i.e.,* asphaltene 2) is a modified version of asphaltene 1 with an additional COOH group to account for the contribution of oxygen heteroatoms in the average asphaltene fraction. Recall that asphaltenes are very large molecules, so the simulation cells have been increased from 45 Å x 45 Å x 135 Å to 80 Å x 80 Å x 210 Å and the simulation time has been increased from 20 ns to 40 ns to have relevant statistics of the oil phase.

Four different model oils with the same total asphaltene content have been considered: (i) a low-polarity oil based on a dodecane/toluene mixture and a negligible amount of resins (*i.e.,* 0.2 % of quinoline and 0.5 % of 3-naphthenic acid); (ii) the representative model of Carabobo

crude oil, which has a high amount of resins and their correspondent acidity; (iii) a high-polarity oil with relatively high concentration of the resin average molecules; and (iv) a variation of the second model, where the asphaltenes are represented only by the molecule of Boek *et al.,*[15] The compositions of these four model oils are listed in Table 4.9.

The first model oil is very similar to the maltene dodecane/toluene system studied in Figure 4.16a and Figure 4.16b. In fact, the dodecane/toluene ratio of model 1 lays between the already studied 50 %/50 % and the 25 %/75 % dodecane/toluene mixtures, which gave oil/water IFTs between 43 $mN \cdot m^{-1}$ and 41 $mN \cdot m^{-1}$ depending on the toluene content. According to the simulation results, the presence of asphaltenes is slightly reducing the equilibrium oil/water IFT of the maltene mixture (*i.e.,* from 43-41 $mN \cdot m^{-1}$ to 40 $mN \cdot m^{-1}$). The difference in IFTs is not very significant, but as it can be seen in Figure 4.20a, it is the result of the asphaltene accumulation at both interfaces. This result suggests that the heteroatoms of asphaltenes confer them a higher polarity and a larger affinity than dodecane or toluene for the oil/water surface.

Similarly, the second model exhibits an asphaltene interfacial accumulation (Figure 4.20b) but lower than model oil 1 due to the presence of quinoline, which competes for the interface and is capable of partially displacing some asphaltene molecules into the bulk phase. In this model, the few toluene molecules located at the interface have been completely expelled, and the resulting oil/water IFT of 31.6 $mN \cdot m^{-1}$ is mainly governed by the contributions of quinoline and both asphaltene molecules. Finally, the molecular interfacial distribution of model oil 2 is capable of reproducing an IFT in good agreement with the reported real crude oil/water IFT range (*i.e.,* 15-30 $mN \cdot m^{-1}$).[88–91]

The third model contains a high amount of both acid and basic fractions (*i.e.,* 34 % of quinoline and 8.6 % of 3-naphthenic acid), which confer the highest polarity and the lowest oil/water IFT of the four model oils studied. The interfacial distribution of this oil (Figure 4.20c) reveals that 3-naphthenic acid has migrated to the interface occupying it almost entirely. In fact, the well-defined accumulation peaks of quinoline have partially disappeared and the more modest asphaltene surface activity becomes negligible.

Table 4.9. Composition (*i.e.,* in % w,w) and equilibrium IFTs of the four model oils simulated.

Model	Dodecane	Toluene	Quinoline	3-Naphthenic acid	Asphaltene 1+2	γ_{MD} / $mN \cdot m^{-1}$
1	27.8 %	60.7 %	0.2 %	0.5 %	8.9 + 1.9 %	40.0
2	17.2 %	37.5 %	34.0 %	0.5 %	8.9 + 1.9 %	31.6
3	14.7 %	31.9 %	34.0 %	8.6 %	8.9 + 1.9 %	26.7
4	17.2 %	37.5 %	33.6 %	0.9 %	10.8 + 0 %	31.6

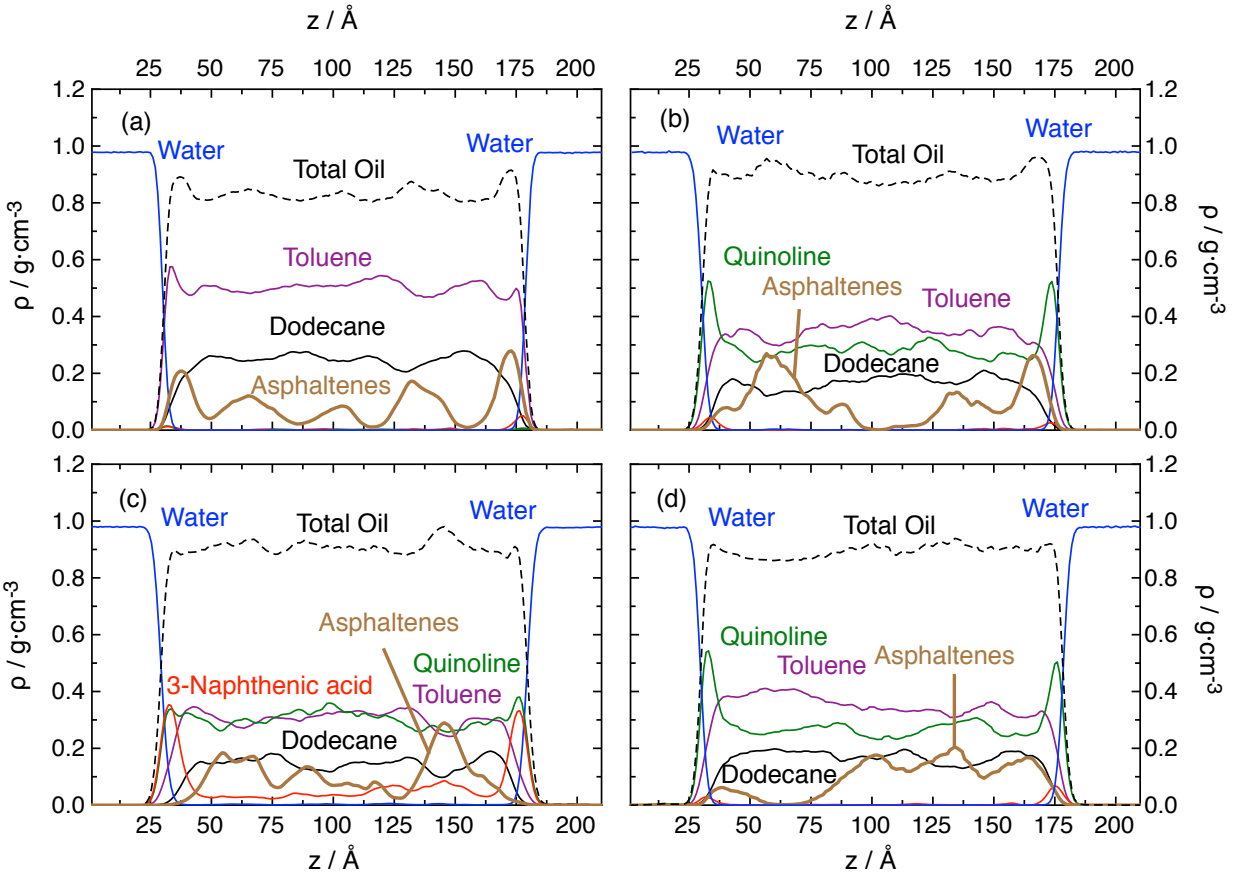

Figure 4.20. Equilibrium z-distributions of the four model oils studied at 300 K and 1 atm. The models exposed in Table 4.9 from 1 to 4 are ordered from a to d, respectively. The labels of the most diluted compounds have been omitted for clarity because they do not have a significant impact on the interfacial properties.

Finally, the fourth model is very similar to the oil 2 but instead of using two asphaltene molecules, only the structure without COOH is considered, with the same total 10.8 % concentration. Although carboxylate groups are usually very surface active due to its high polarity and hydrogen bonding capability, removing the acid asphaltene does not change the equilibrium oil/water IFT. On the other hand, the z-distribution (Figure 4.20d) seems to yield a lower interfacial accumulation and a higher bulk concentration of asphaltenes in absence of COOH groups.

To conclude, the polarity ranking of oil species within the simulation cell is 3-naphthenic acid > quinoline ≈ asphaltene 2 > asphaltene 1 > toluene > dodecane. This trend is maintained in the oil/water interfacial accumulation, as well as in their ability to reduce the IFT. According to the systems modeled, the most interfacial-active species (*i.e.,* 3-naphthenic acid) is still dominant in determining the oil/water IFT, pushing any other polar molecule (*i.e.,* quinoline and both asphaltenes) to the bulk phase.

Notice that the bulk concentration of asphaltenes shown in all model oils in Figure 4.20 is not very homogeneously distributed along the z-direction of the simulation cell. This pattern contrasts

with the other smaller molecules (*e.g.,* dodecane, water, etc.) and reveals the capacity of asphaltenes to agglomerate. Due to their molecular structure the agglomeration of asphaltenes is produced mainly via π-π interactions of their large aromatic centers.[92,93] To evaluate their capacity to agglomerate, the distances between all the asphaltene aromatic centers of mass (CM_{ar}) have been computed at each timestep during the simulation. Then, each asphaltene molecule has been assigned to a cluster if its CM_{ar} is close to any other asphaltene CM_{ar}. The threshold distance to consider two asphaltene molecules agglomerated is chosen as 6.5 Å as determined by the CM_{ar} radial distribution function (RDF) shown in Figure 4.21a. This distribution suggests that the average distance between two asphaltene π-stacking regions is between 3.5 and 5 Å when forming a cluster, with a maximum of probability around 4 Å. This result is in good agreement with the values predicted by Carauta *et al.,*,[94] and Boek *et al.,*,[15] which determined the distance between aromatic cores of asphaltene molecules as 5 Å and 5-8 Å in pure toluene, respectively. Additionally, secondary and tertiary peaks appear at 8 Å and 12 Å, denoting the presence of at least asphaltene trimers and tetramers in the simulation.

Clusters with different sizes have been defined according to the number of the asphaltene molecules they contain. Then, the distribution of asphaltene molecules in each cluster size has been calculated through the time average of the last 10 ns of simulation (*i.e.,* from 30 to 40 ns). The analysis has been conducted in the two model oils with different asphaltene distribution (*i.e.,* Model oil 2 and 4). The results obtained (Figure 4.21b) show that the majority of asphaltene molecules are forming similar agglomeration patterns regardless of their structure (*i.e.,* tetramers/hexamers in model oil 2 and pentamers in model oil 4). The association obtained from experimental results indicate aggregation numbers of common asphaltenes between 4 and 8,[95,96] and other simulation studies predict a cluster size around 4 units in toluene solution.[16] Both

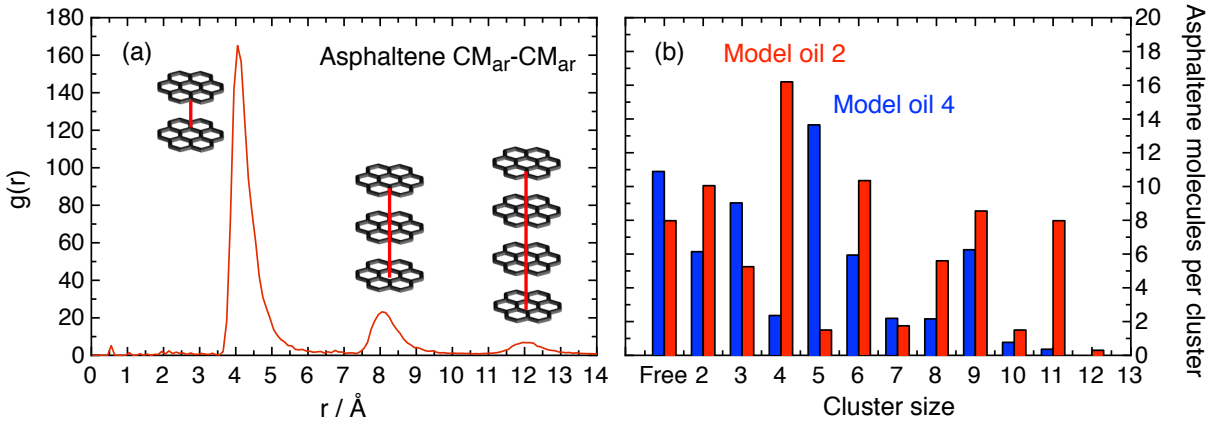

Figure 4.21. (a) RDF between asphaltene aromatic centers of mass and (b) aggregation distribution as a function of cluster size.

results are in good agreement with the here presented MD simulations further validating the asphaltene model and explaining the bulk inhomogeneity of asphaltenes in Figure 4.20.

To conclude, in this section it was seen how the most polar fractions of oil are capable of migrating from the oil bulk to the interface to interact with water and reduce the oil/water IFT. If oil molecules are very interfacially active, they are capable of displacing other less active molecules to the bulk phase, reducing their contribution to the interfacial properties of the system. According to MD simulations the interfacial activity of the average oil molecules are ranged from 3-naphthenic acid > quinoline ≈ asphaltene 2 > asphaltene 1 > toluene > dodecane, which is the same order of interfacial accumulation affinity.

4.4.2 Oil/Water/Rock Contact Angles

The analysis of model oils is also extended to the calculation of CA to improve the qualitative description provided by the pure oils section. Previously, it was seen that only 3-naphthenic acid attaches strongly to the surface, which yields a relatively high CA value, while the other three maltene average molecules interact with the surface in the order: quinoline > toluene > dodecane. Due to the high computational cost of CA simulations some of the previous models defined in Section 4.4.1 (*i.e.,* specially the maltene mixtures) have not been considered in this work to be able to adequately model the more complex asphaltenic mixtures. Specifically, the only maltene mixture studied is the dodecane/toluene/3-naphthenic acid mixture (*i.e.,* with an 87/13 dodecane/toluene ratio and a 1 % of acid fraction) to evaluate the effect of the acidity in a simple model oil on a calcite surface. Then, the CA of model oils 1, 2 and 3 have been simulated to determine the capacity of complex crudes, with different acidity/basicity in the maltene matrix, to interact with the carbonate rock. Model oil 4 has been neglected because as seen in the IFT calculations, both asphaltenes with and without COOH groups behave similarly, so the results would be equivalent to Model oil 2. Finally, the CA of model oil 2 has been calculated also on top of a kaolinite surface (*i.e.,* not modeled in Section 4.3.2) to address the difference between oil/water/carbonate and oil/water/clay interactions.

The CA simulation of oil mixtures, similarly to the IFT calculations, ideally requires larger simulation cells (*i.e.,* to have more oil molecules of each type) and longer simulation times (*i.e.,* to ensure that all species migrate to the bulk phase or to the respective oil/water or oil/rock interfaces). The high computational cost of these calculations did not permit to increase the simulation cell size, which was already significantly large, and only the time evolution could be extended to 10-20 ns. The additional simulation time allowed to see the formation of a water layer below the

oil droplet, which was previously unseen in pure compounds due to shorter simulation times. With this additional time, it is seen that the CA of oil droplets is stabilized around a constant value (*i.e.,* as seen in pure compounds) and then, water slowly starts displacing the oil molecules attached to the surface until a thin water layer of approximately 5 Å is formed between the oil and the surface. According to the performed simulations, the formation of the layer has a characteristic time of 5-10 ns after the CA of the droplet achieved a constant value (Figure 4.22a), which is the reason why it was unseen in the shorter simulations of pure compounds (*i.e.,* maximum of 10 ns).

In the simulations where droplets are not directly in contact with the surface, the base line disappears and the height/radius ratio of the droplet can no longer be calculated, as well as the CA. However, Jiménez-Ángeles *et al.,*[34] realized that oil droplets are still attracted by the rock even when screened by a water layer. For this reason, they proposed to redefine the position of the base line to the highest z-position where the droplet still feels a significant oil/rock interaction. This interaction induces a distortion from the ideal spherical shape of the lower part of the droplet, which can be used to find the new base line from the droplet profiles. The CA has been determined by building block averages of the droplet density profile at each 1 ns to monitor the shape of the droplet through time. Then, from each density profile, the upper half (*i.e.,* from $z = 40$ Å to $z = 76$ Å in the example of Figure 4.22b) has been fitted to a circle with radius (R_{fit}). Next, the unfitted radius of the droplet ($R_{drop}(Z)$), which can be calculated at different z-positions is subtracted from the constant R_{fit} value to build Figure 4.22b. In the upper part of the droplet (*i.e.,* from $z = 40$ Å to $z = 76$ Å) both radii are equal, which keeps the sphericity of the droplet, in part due to the fitting and in part because the surface does not interact with the oil at this distance.

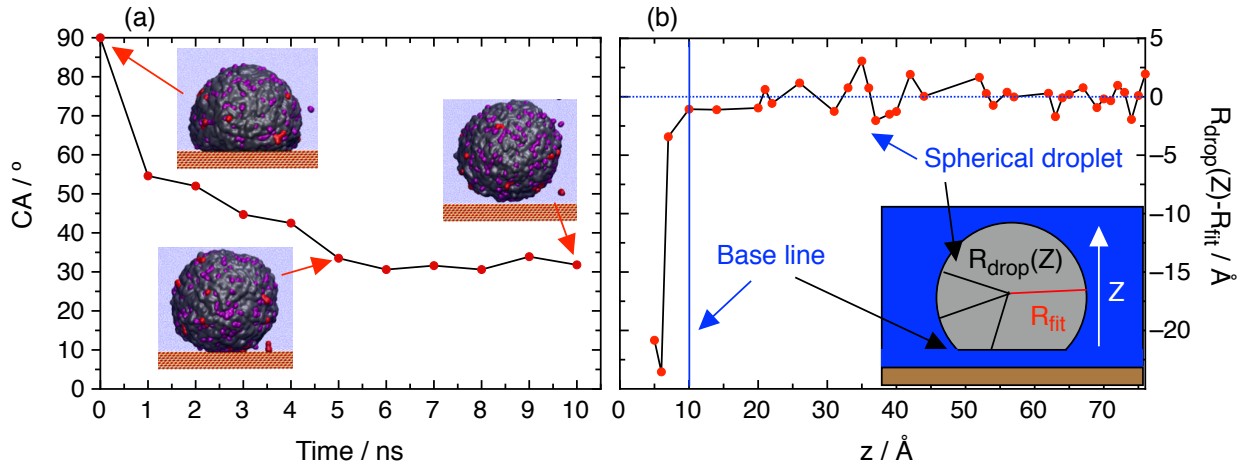

Figure 4.22. (a) Equilibration of the ternary mixture 2 CA on calcite embedded in water at 300 K and 1 atm with time, along with snapshots that show the formation of the thin water layer under the droplet. (b) Difference between the radius of the average droplet profile obtained from the 9-10 ns time frame ($R_{drop}(Z)$) and the circular fit (R_{fit}) used to redefine the base line. The $z = 0$ Å corresponds to the position of the $CaCO_3$ surface.

However, at z-positions closer to the surface (*e.g.,* at 10 Å) the droplet becomes flatter and R_{fit} becomes smaller than R_{drop}. Finally, the new base line has been placed at the transition from spherical to non-spherical droplet, and the CA can be calculated from the height/radius ratio as usual.

Specifically, the data shown in Figure 4.22 correspond to the equilibration of the maltene ternary mixture 2 (*i.e.,* 86.1 % dodecane, 12.9 % toluene, 1.0 % 3-naphthenic acid) The calculated CA for this mixture is 34.3º, which is in between the 25.7º and the 40.4º obtained in pure dodecane and pure toluene, respectively. Even though the nanodroplet contains more than 85 % of dodecane, the CA is closer to the pure toluene value. The reason is that toluene migrates to the oil/rock interface to interact with $CaCO_3$ displacing dodecane to the bulk phase. This fact makes the final CA to resemble the pure toluene value. Additionally, the CA is also increased by the presence of acid molecules, which migrates to the oil/rock interface to interact with their polar heads either with the water layer or the mineral surface. These accumulations can be seen in z-distributions depicted in Figure 4.23a, where a peak of both 3-naphthenic acid and toluene appear around z = 10 Å of the $CaCO_3$ surface. Notice that the oil species are not in contact with the rock, which

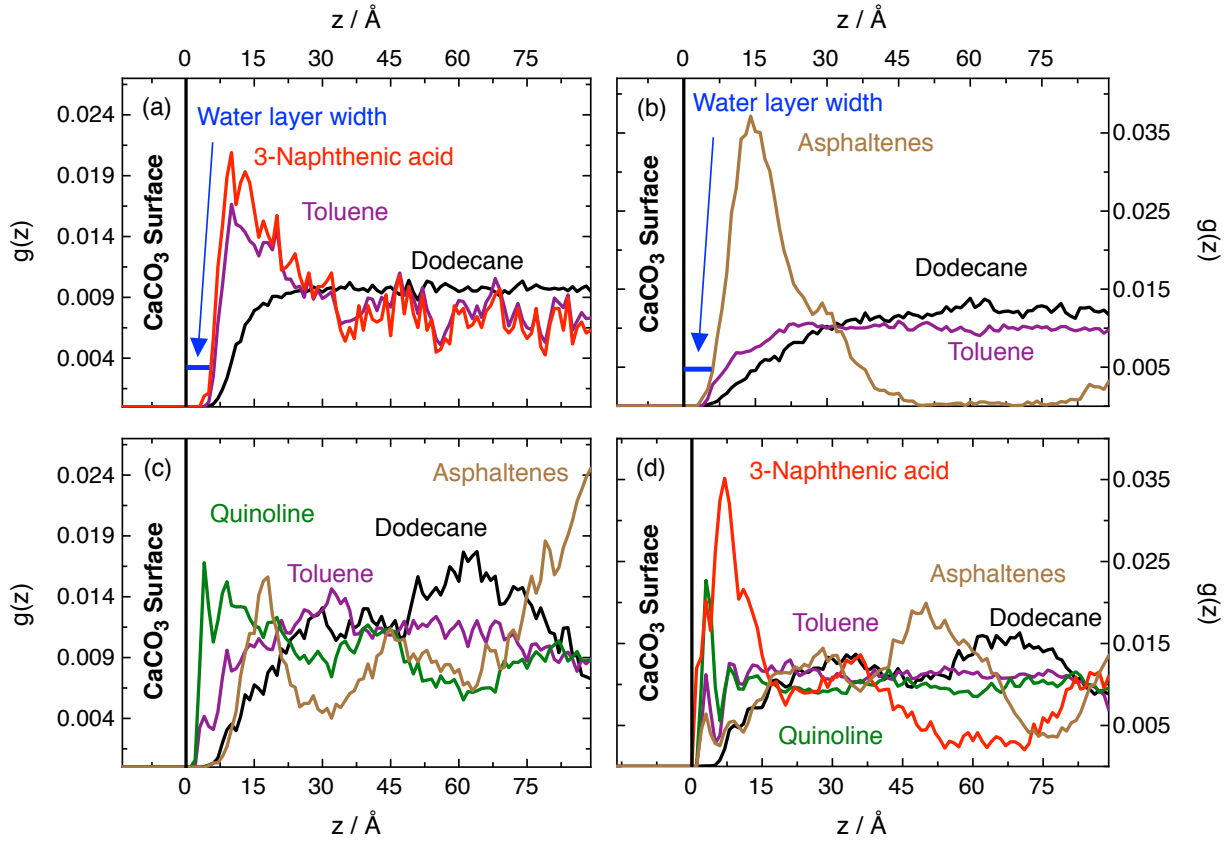

Figure 4.23. Equilibrium z-distributions of (a) the ternary mixture 2 and model oils 1 (b), 2 (c) and 3 (d) over a calcite surface at 300 K and 1 atm. All complex model oils (b-d) contain the six average molecules to represent the four oil fractions, but molecules with very low concentration have been hidden for clarity purposes.

means that there is a water layer between the nanodroplet and the carbonate. The z-distributions depicted in Figure 4.23 have been constructed by averaging during 1 ns all molecules located in a cylindrical region from $z = 0$ to $z = Lz$ crossing the center of the oil droplet. In this cylinder the molecules located close to $z = 0$ are interacting with the oil/rock interface whereas higher values of z refer to molecules in the bulk phase.

Model oil 1 is a complex mixture with very low concentration of acid and base resins, which means that the mostly present species are dodecane, toluene and the mixture of asphaltenes. In this model both dodecane and toluene interact weakly with the surface, but the more polar asphaltenes are capable of migrating to the oil/rock interface as denoted by the large peak seen in Figure 4.23b. The presence of asphaltenes yields a CA of 34.2º similarly to the value of the maltene acid mixture, suggesting that a relatively high concentration of model asphaltenes have a similar effect than the 1 % of 3-naphthenic acid. These simulations imply that the modeled asphaltenes are not significantly active to the interface, and although they can accumulate when mixed within a non-polar oil matrix, the presence of any other polar species diminishes their interfacial activity. In fact, the z-distributions of model oil 2 (*i.e.,* with low acid and high base concentrations) show that asphaltene accumulates in a second molecular layer, preceded by quinoline (Figure 4.23c). However, the obtained CA for this model is statistically equivalent to model oil 1 (*i.e.,* 33.7º). Finally, the most polar oil model (*i.e.,* with high acid and high base content) shows accumulation of both polar species at the interface, as denoted by the peaks at z = 5-7 Å from the surface (Figure 4.23d). This model has the highest CA of all the model crude oils explored, with a value of 48.3º, which suggests that the acid fraction has the strongest impact in defining the oil/rock interactions. All the results mentioned here are compiled in Table 4.10.

Table 4.10. Composition (*i.e.,* in % w,w) of all model oils simulated along with their equilibrium CA on calcite and kaolinite surfaces (*i.e.,* the latter in both the silicon and aluminum faces) embedded in pure water at 300 K and 1 atm.

Model	Dodecane	Toluene	Quinoline	3-Naphthenic acid	Asphaltene 1+2	CA / º
Maltene on $CaCO_3$	86.1 %	12.9 %	-	1.0 %	-	34.3
1 on $CaCO_3$	27.8 %	60.7 %	0.2 %	0.5 %	8.9 + 1.9 %	34.2
2 on $CaCO_3$	17.2 %	37.5 %	34.0 %	0.5 %	8.9 + 1.9 %	33.7
3 on $CaCO_3$	14.7 %	31.9 %	34.0 %	8.6 %	8.9 + 1.9 %	48.3
2 on Si-Kao	17.2 %	37.5 %	34.0 %	0.5 %	8.9 + 1.9 %	95.0
2 on Al-Kao	17.2 %	37.5 %	34.0 %	0.5 %	8.9 + 1.9 %	75.0

Apart from the study on carbonate rocks, model oil 2 has also been simulated on top of a clay surface to compare the relative affinities of both rocks for the crude oil. Kaolinite, with general molecular formula $Si_2Al_2O_5(OH)_4$, has been chosen as a model clay surface and its bulk structure has been obtained from crystallographic data, equivalently to $CaCO_3$.[97] Then, the bulk has been cut through the most stable (001) face, according to the available experimental data.[97] The kaolinite (001) is a non-expansive layered aluminosilicate, whose layers are connected via hydrogen bonds. Each layer is formed by a silica tetrahedron and an alumina octahedron directly connected via covalent bonds to each other (Figure 4.24a), forming the structure Si-Al—Si-Al—Si-Al, and where the interlayer interactions are due to hydrogen bonds. According to this structure, the (001) cut is carried out breaking the hydrogen bonds and leading to two possible terminations: (i) the silicon termination (Si-Kao), which is known to be relatively hydrophobic, and (ii) the aluminum termination (Al-Kao), which is more hydrophilic.[98]

The intermolecular and intramolecular interactions of kaolinite have been treated with the ClayFF force field developed by Cygan *et al.*,[99] which was specifically fitted to reproduce the structure and water/solid interfaces of hydrated minerals (*i.e.,* specially clays). The water/clay interactions in both terminations have been addressed by building a three-layered slab of kaolinite (001) located in the center of a rectangular box with dimensions $Lx \approx Ly \approx 25$ Å and $Lz = 100$ Å. The slab is extended through the xy plane and the upper part of the simulation cell (*i.e.,* $z > Lz/2$) exposes the Al-Kao termination, whereas the lower part (*i.e.,* $z < Lz/2$) exhibits the Si-Kao termination. The whole simulation cell has been filled with water molecules and the system has been equilibrated at 300 K and 1 atm. The RDFs of water/kaolinite were computed between water oxygen atoms and the most external O atoms of either Al-Kao and Si-Kao. The

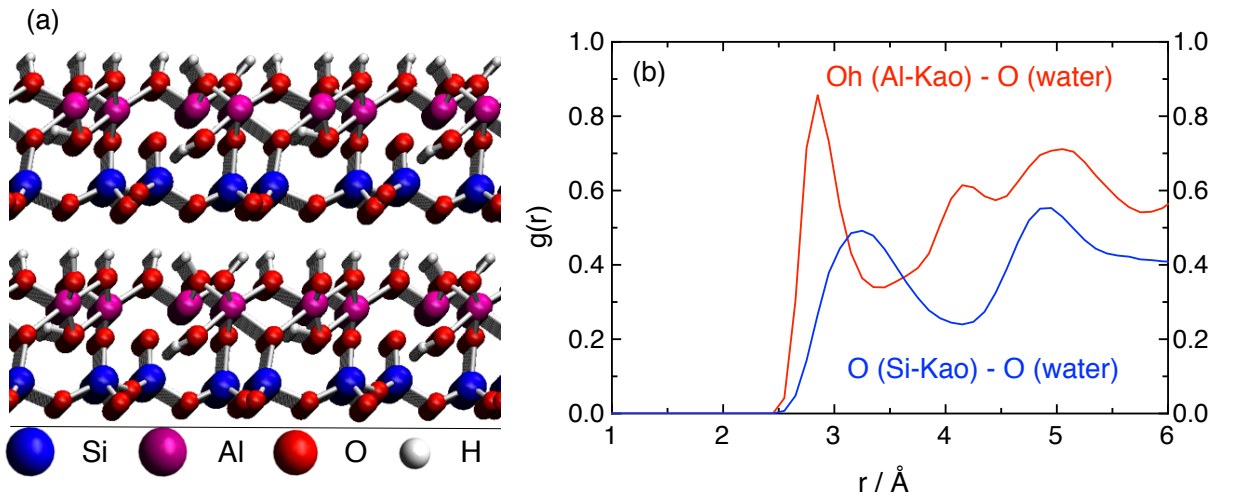

Figure 4.24. (a) Molecular structure of two layers of kaolinite where the respective layers of tetrahedral silica connected to octahedral alumina can be seen. (b) RDFs of the most external O atoms of kaolinite with water in both terminations.

results are shown in Figure 4.24b, where it can be seen that water molecules orient at a closer distance to Al-Kao termination (*i.e.,* around 2.7 Å) in contrast to Si-Kao (*i.e.,* around 3.2 Å). This orientation agrees with the expected behavior since the Al-Kao termination is more hydrophilic than the Si-Kao termination.

The CA of model oil 2 has been calculated in the Si-Kao and the Al-Kao terminations (Table 4.10). The equilibrium values obtained are significantly larger than those obtained for calcite, which suggest kaolinite is less hydrophilic than $CaCO_3$ and exhibits an almost oil wet behavior. Specifically, the CA in the Al-Kao termination is lower than in Si-Kao (*i.e.,* 75.0º and 95.0º, respectively) due to the higher hydrophilicity of the surface (*i.e.,* less oil wet). This fact implies that the Al-Kao termination interacts more favorably with water than oil, whereas Si-Kao termination prefers the interaction with oil in front of water. The obtained results propose that a heavy crude oil trapped onto a calcite pore should be more easily recoverable than the same oil interacting within a kaolinite pore, especially if kaolinite exposes its Si-Kao surface.

The z-distributions of all model crude oil molecules in both terminations have been computed at equilibrium equivalently to $CaCO_3$ simulations. The results are compiled in Figure 4.25, where it can be seen a strong accumulation of quinoline at the oil/clay interface. Additionally, all other oil components also become ordered close to the kaolinite surface, as denoted by the peaks of all compounds at $z < 5$ Å in both terminations. The most notable difference between the z-distributions on top of the Si-Kao and Al-Kao surfaces is that Si-Kao allows the asphaltene fraction to be in contact with the surface, whereas Al-Kao exhibits an interfacial depletion of this oil component. As a consequence, the model oil 2 on top of the Si-Kao surface achieves higher equilibrium CA. Finally, no water layer is created over this surface after the equilibration of the oil droplet. This is

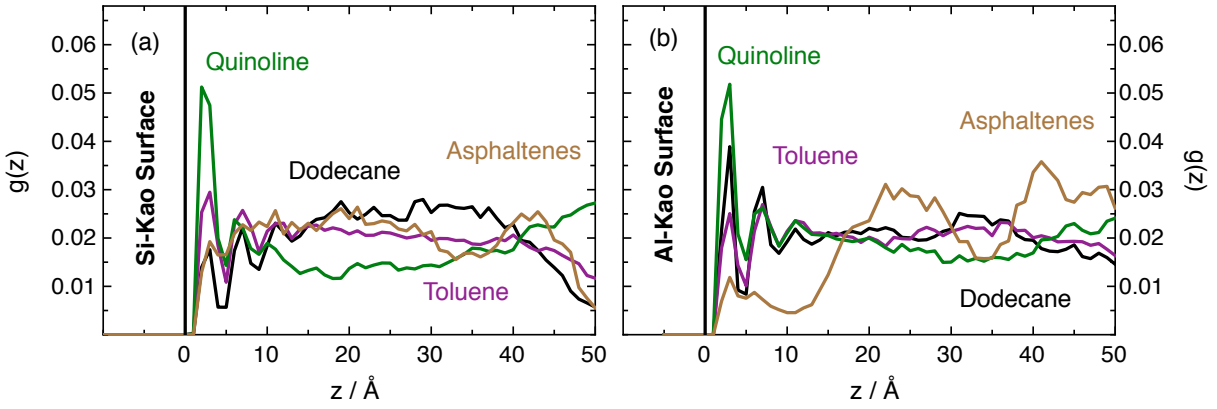

Figure 4.25. Equilibrium z-distributions of model oil 2 on top of a kaolinite surface in the Si-Kao (a) and Al-Kao terminations (b). 3-Naphthenic acid is also part of the mixture in a very low concentration, so it has been hidden for clarity purposes.

due to the combination of a weaker water/kaolinite and a stronger oil/kaolinite set of interactions with respect the calcite surface, either in the Al-Kao or in the Si-Kao terminations, that do not allow water to displace oil effectively.

To conclude, the CA of different model oils were analyzed on top of two different surfaces: (i) a calcite surface and (ii) the both terminations of a kaolinite surface. From the results obtained it has been concluded that the most polar components in oil mixtures not only migrate to the oil/water interface, but also to the surface of the rock, increasing the average oil/rock interaction strength and the CA. Additionally, the simulation times have been increased to give enough time for molecules to migrate and distribute adequately in these mixtures, allowing to see the formation of a water layer in calcite surfaces. This water layer (*i.e.,* around 5 Å width) does not prevent the oil droplet to interact with the surface and starts forming after the CA achieves an equilibrium value.

4.4.3 Salinity Effects on Interfacial Tensions and Contact Angles

The salinity effect in pure oil components basically increases the oil/water IFT linearly and exhibits a little reduction on the oil/water/rock CA. However, different behaviors were seen experimentally when using simple models or real crude oils. Specifically, salinity increases the oil/water IFT of simple model oils, such as pure alkanes.[79,80] However, measurements on real crude oils sometimes showed different behaviors, such as a reduction, a negligible effect[100,101] or a decrease followed by an increase (*i.e.,* non-monotonic trend) of the oil/water IFT.[102,103] Similarly, electrolytes affect the oil/water/rock CA differently depending on the nature of the crude oil: sometimes turning the surface to water wet[81,82] or oil wet behavior.[83]

For this reason, both properties are reanalyzed in a set of different oils, starting with simpler maltene mixtures and ending with model oil 2. Specifically, the effect of salinity on the IFT is analyzed using three different maltene mixtures (*i.e.,* all % are given in % w,w) at laboratory conditions: (i) the 87 % dodecane/13 % toluene mixture, (ii) the ternary maltene mixture 2, which contains a 1 % of 3-naphthenic acid and (iii) the equimolar quaternary mixture. The addition of either 2.0 $mol \cdot kg^{-1}$ of NaCl and 2.0 $mol \cdot kg^{-1}$ of $CaCl_2$ increases the oil/water IFTs of any of the three systems by 3-4 $mN \cdot m^{-1}$ and 6-7 $mN \cdot m^{-1}$, respectively (Figure 4.26a-c). These increases are statistically equivalent to the oil/water IFT change induced by electrolytes in pure components and similar to the abovementioned experimental works that report an increase of the oil/water IFT with salinity.[79,80] In fact, this result was expected because all of the different pure oil/water/salt systems exhibited the same IFT increase with salt molality concentration, which implies that the oil in

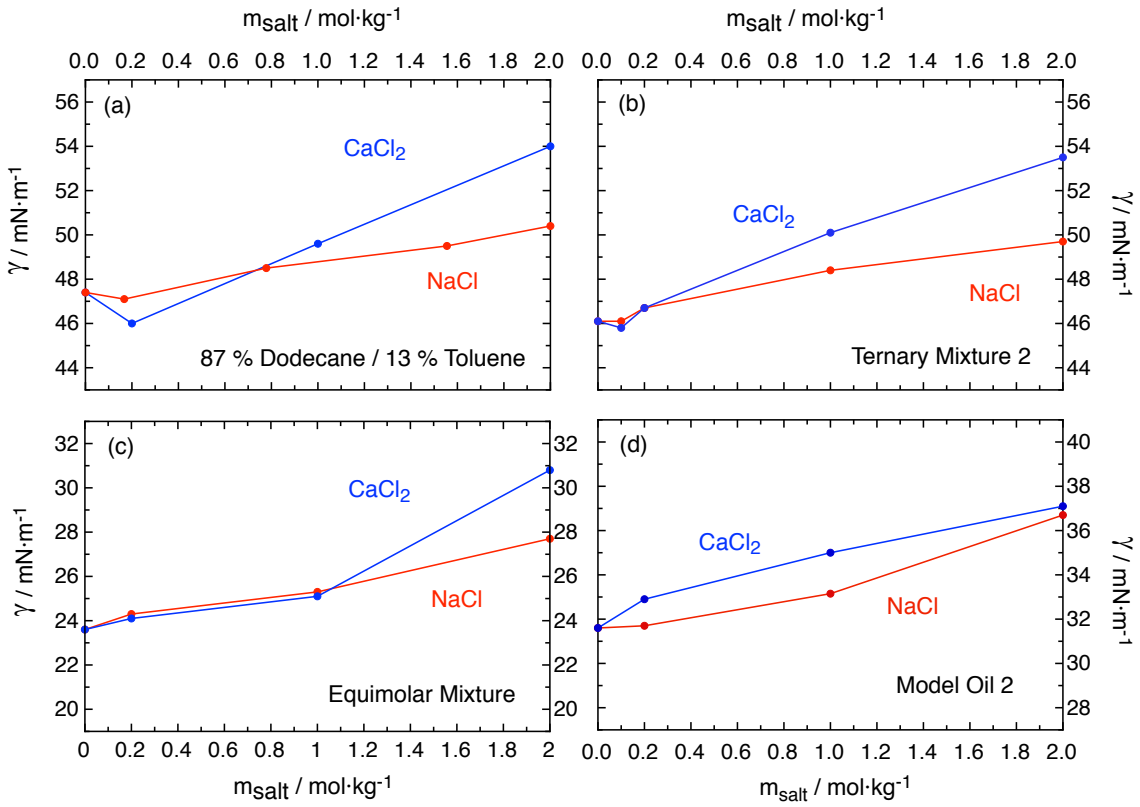

Figure 4.26. Variation of the simulated oil/water IFTs of three different maltene model oils (a-c) and model oil 2 (d) as a function of NaCl and $CaCl_2$ molality at 300 K and 1 atm.

general does not interact significantly with salinity. Similarly, the inclusion of asphaltenes did not affect the usual trend of the oil/water IFT observed up to now (Figure 4.26d). In fact, the oil/water IFT of model oil 2 increases by 5.0 $mN \cdot m^{-1}$ and 5.5 $mN \cdot m^{-1}$ in presence of a 2.0 $mol \cdot kg^{-1}$ of NaCl or $CaCl_2$, respectively. The difference between the IFT increase of both salts is less noticeable than in pure compounds or maltene mixtures, but the general qualitative trend of IFT $CaCl_2$ > NaCl is still maintained.

The equilibrium z-distributions of the four systems have also been analyzed in Figure 4.27. However, as the oil/salt interactions are relatively weak, the molecular distributions of the maltene oil mixtures (Figure 4.27a-f) with a 2.0 $mol \cdot kg^{-1}$ of salt and in pure water are very similar. The only remarkable difference is an enhanced accumulation of 3-naphthenic acid molecules to the oil/water interface, denoted by the higher acid peaks at $z \approx 25$ Å and $z \approx 110$ Å in Figure 4.27e and 4.27f with respect the system without salt. This fact suggests that salinity should be able to interact with polar components of oil to favor their migration to the oil/water interface. However, the migration is not strong enough to observe any reduction on the IFT.

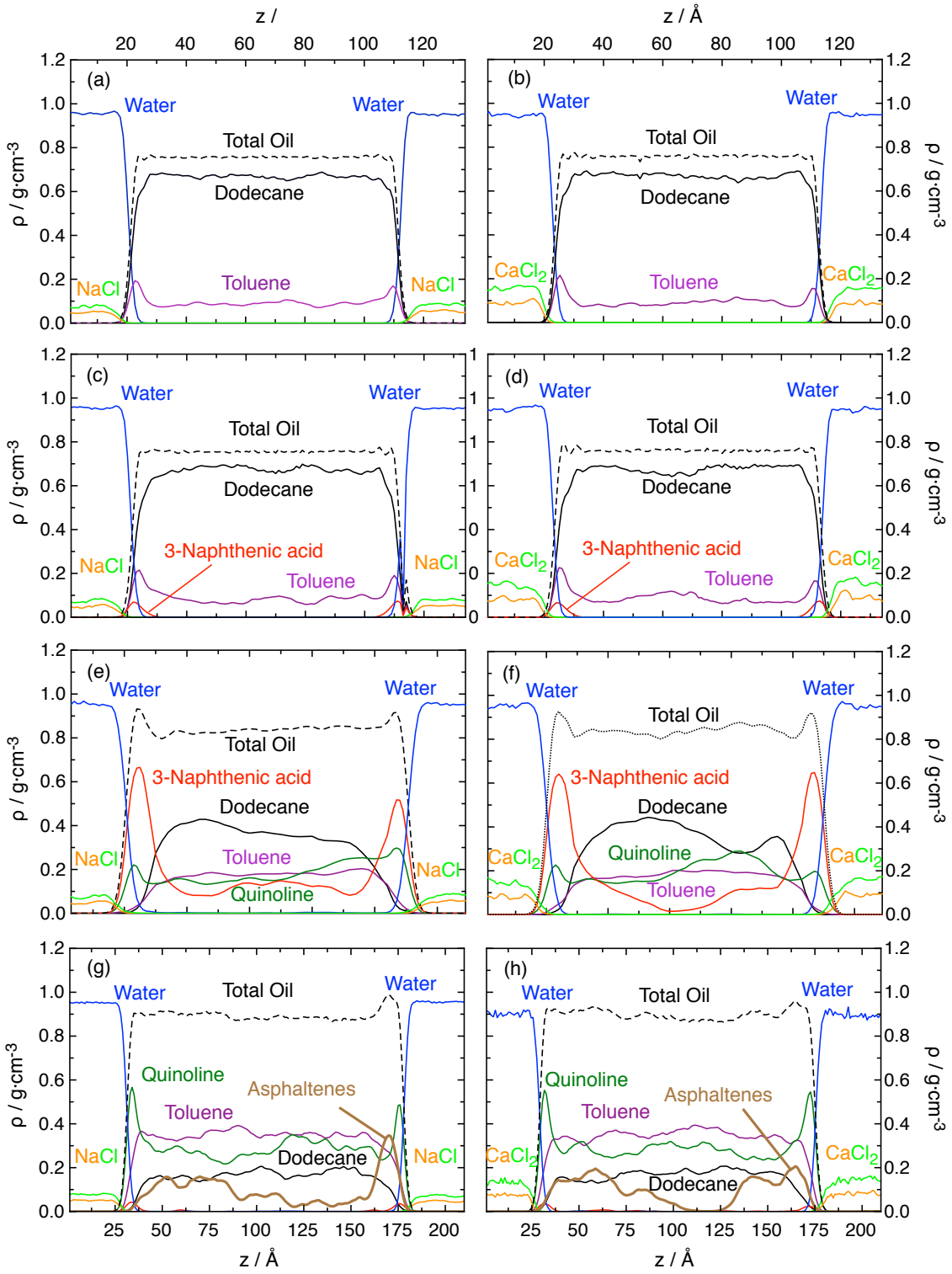

Figure 4.27. Equilibrium z-distributions of the (a,b) 87 % dodecane/ 13 % toluene mixture, (c,d) maltene ternary mixture 2, (e,f) the equimolar mixture and (g,h) model oil 2 in presence of 2.0 mol·kg^{-1} of NaCl (left panels) and $CaCl_2$ (right panels).

On the other hand, the system with asphaltenes (*i.e.,* model oil 2 shown in Figure 4.27g-h) has a very low concentration of acid molecules, and they were already totally accumulated at the interface in absence of salt. This means that the addition of electrolytes is not affecting the

molecular distribution of 3-naphthenic acid, resulting in z-distributions statistically equivalent to the systems without salt. The only exception is that in the presence of NaCl only a peak of interfacial accumulation of asphaltenes is located at the right interface (*i.e.,* at $z \approx 170$ Å in Figure 4.27g), whereas $CaCl_2$ seems to slightly push the asphaltenes back to the bulk (*i.e.,* the same peak is significantly lower in Figure 4.27h). This distribution suggest that salinity hampers the ability of asphaltenes to migrate towards the oil/water interface, especially when divalent salts are used.

Regarding the CA simulations, the saline effect with a 2.0 mol·kg^{-1} of NaCl has been evaluated in the maltene ternary mixture 2 on a calcite surface. In this simulation, both ions (*i.e.,* Na^+ and Cl^-) diffuse into the water layer located under the oil droplet, as it can be seen by the accumulation peaks at $z < 5$ Å in Figure 4.28. In this position, ions are capable of interacting with the most polar components of oil and attract them to the interface, which was previously seen in the IFT simulations of mixtures compiled in Figure 4.27e-f and now in Figure 4.28 (*i.e.,* the 3-naphthenic acid peak is higher with NaCl than in pure water). The enhanced acid/calcite attraction induced by the salt is also reflected in an increase of the oil/water/rock CA with salt concentration as it can be seen in Table 4.11.

Recall that in pure oil components the saline effect was enhancing calcite/water interactions without affecting the oil/rock behavior, which resulted in a slight reduction of the oil/water/rock CA. However, in this mixture the ions of salt can diffuse into the thin water layer below the droplet and increase the acid concentration close to the mineral surface, thus increasing the oil/rock interactions and ultimately, the CA. This mechanism could explain the reason why pure model oils behave differently with respect mixtures in the abovementioned experiments.

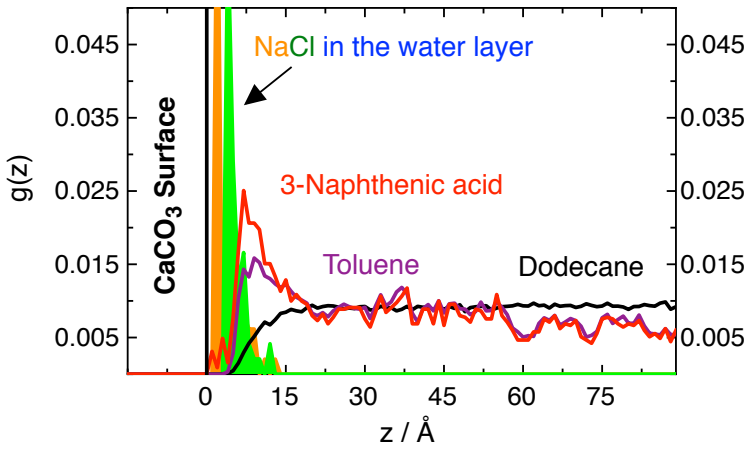

Figure 4.28. Equilibrium z-distributions of the ternary maltene mixture 2 on top of a calcite surface surrounded by a 2.0 mol·kg^{-1} NaCl brine at 300 K and 1 atm.

Table 4.11. CA results at different NaCl or $CaCl_2$ salinity concentration of the dodecane/toluene/3-naphthenic acid mixture and model oil 2 on calcite and kaolinite Al termination at 300 K and 1 atm.

Model	$CA_{Pure\ water}$ / º	$CA_{2.0\ m\ NaCl}$ / º	$CA_{2.0\ m\ CaCl_2}$ / º
Maltene on $CaCO_3$	34.3	48.1	-
Model oil 2 on $CaCO_3$	33.7	29.9	16.6
Model oil 2 on Al-Kao	75.0	74.1	73.2

On the other hand, the CA simulations of model oil 2 on top of the calcite surface reveal that the ions in solution promote the formation of the water layer, previously unseen in absence of salt (Figure 4.29a-b). However, this water layer does not favor the attachment of any oil component to the calcite surface due to the very low concentration of 3-naphthenic acid and the low salt/oil interactions with all other model fractions. This fact results in a reduction of the oil/water/rock CA by the presence of salt because water/calcite interactions become enhanced while oil/rock behavior is unchanged, equivalently to pure compounds behavior.

Alternatively, the CA of model oil 2 has also been calculated on top of the Al termination of the kaolinite surface, for being the most hydrophilic face and the one with higher probability to

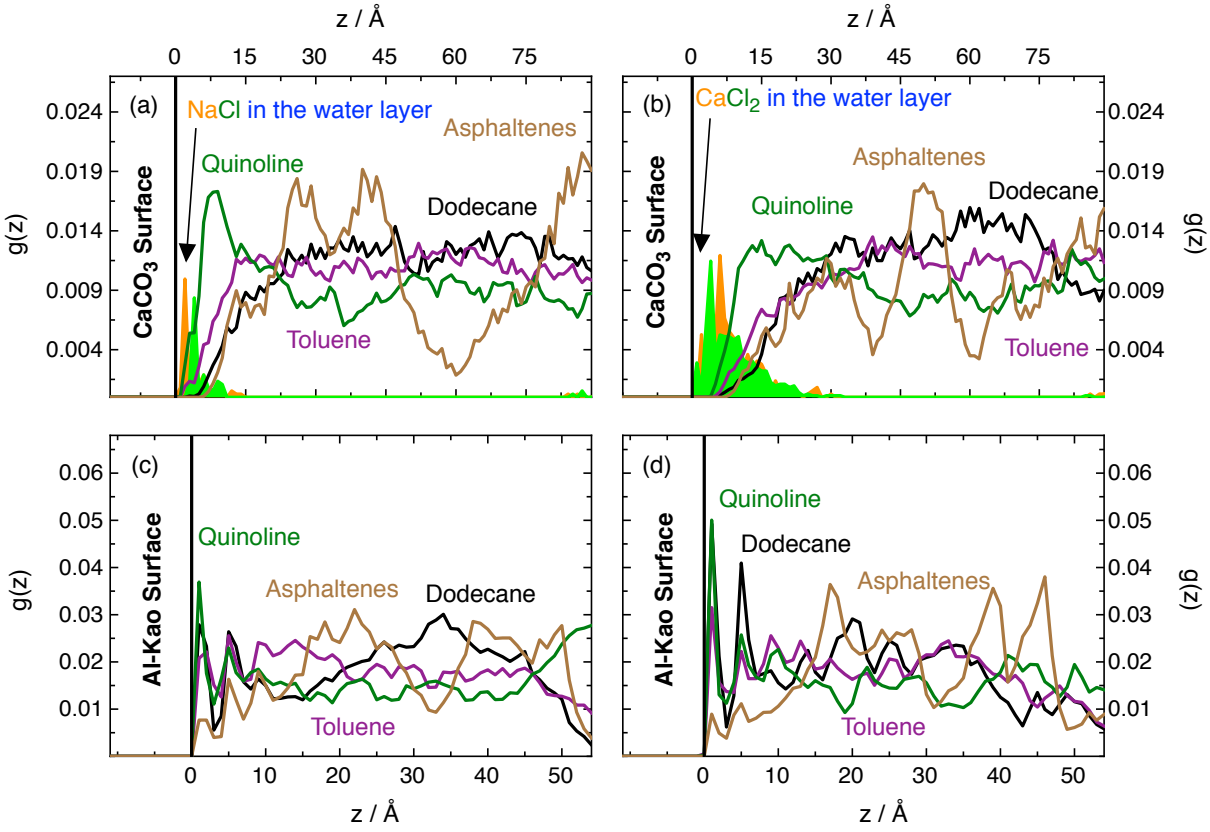

Figure 4.29. Equilibrium z-distributions of model oil 2 on top of calcite embedded in 2.0 mol·kg^{-1} of NaCl (a) and $CaCl_2$ brines (b), along with its counterparts in the Al-Kao surface with 2.0 mol·kg^{-1} of NaCl (c) and $CaCl_2$ brines (d).

form a water layer in the presence of 2.0 $mol \cdot kg^{-1}$ of salt. The resulting CA when adding NaCl or $CaCl_2$ to the system remains completely unchanged with respect pure water denoting that salinity does not affect significantly the oil/water/rock interactions. In fact, oil and kaolinite interact strongly enough that the water layer cannot be formed, and no salt can diffuse under the droplet to enhance oil/clay interactions, as seen in the z-distributions that remain statistically unchanged with respect those of pure water (Figure 4.29c-d).

4.4.4 Summary and Conclusions

In this section, different model oils were simulated using representative molecules capable of accounting for the average properties of the four SARA fractions to evaluate the behavior of the IFT and CA in oil mixtures. From the results obtained in this part of the thesis it is concluded that when the polar fractions of oil are part of a mixture, they tend to migrate from the bulk to the interfaces effectively reducing the oil/water IFT and increasing the oil/water/rock CA. The interfacial accumulation of each species depends on the relative polarity of all of the present compounds, which means that a low-polarity molecule such as toluene can accumulate at the dodecane/toluene interfaces, whereas it cannot in presence of 3-naphthenic acid. The results obtained by the MD simulations carried out in this part of the thesis show that they are capable of qualitatively reproducing the IFT trends under many different water and oil environments, which can be used to identify the most interfacially active species. Finally, the modeled asphaltenes have an interfacial activity slightly lower than quinoline, which means that these asphaltene molecules do not contribute significantly to the oil/water IFT or the oil/water/rock CA in polar oil matrixes. Although one could think that the asphaltenes should accumulate at the interface because they have more functional groups than quinoline, their tendency to aggregate among each other hampers they capability of migrating and occupying the interfacial volume.

As abovementioned, different model oils have different behaviors regarding both the oil/water IFT and oil/water/rock CA when interacting with electrolytes. These experimental results could suggest that there might be components in some real crude oils capable of interacting with salinity and revert its natural oil/water IFT increasing effect. However, a real crude oil is a combination of several different species, while the present study uses only a relatively small set to model many different behaviors. In fact, due to that limitation, the aim of this study was to describe, only in a qualitative way, the interfacial behavior of the different crude oil fractions when modeled simultaneously. For this reason, the model is only capable of reproducing the IFT increase with salinity concentration, and not the other mechanisms determined in the bibliography for some

heavy crude oils (*i.e.,* the IFT decrease or the non-monotonic trend). Other molecules with stronger interfacial activity should be added, either in the asphaltene or in the resin fractions of the oil, to simulate them accordingly. Alternatively, the different possible chemical reactions occurring in a real crude oil could also be playing a role (*e.g.,* an acid/base reaction involving the COOH groups of 3-naphthenic acid and asphaltene 2, which would increase their polarity). However, investing additional time in further increasing the complexity of the crude oil model was out of the scope in the frame of the time-sensitive project with REPSOL.

Regarding CA simulations, different behaviors were seen depending on the composition of the model crude oil employed. Specifically, the increase of the simulation time required to equilibrate the system on calcite allowed to see the formation of a water layer of 5 Å width between the oil droplet and the surface. This water layer could be filled with ions in the brine solution and could attract the most polar fractions of oil to the calcite surface, increasing its CA (*e.g.,* the 3-naphthenic acid of a dodecane/toluene/3-naphthenic acid mixture). However, if the oil does not have fractions with high polarity (*e.g.,* the model oil 2) this attraction effect is negligible and the CA either remains unchanged or is reduced by enhanced water/rock interactions. This mechanism is capable of explaining why different oil/rock combinations interact differently with salinity.

4.5 Summary and General Conclusions

This chapter of the thesis was focused on studying the fundamental interactions of several model crude oils with water, different minerals and salts, to better comprehend the mechanisms under the oil recovery processes. To that end, a set of different molecules were selected to represent the average behavior of each oil fraction according to the SARA fractionation (*i.e.,* dodecane for saturates, toluene for aromatics, quinoline for basic/aromatic resins, 3-naphthenic acid for acid/aliphatic resins and two similar continental asphaltene molecules for asphaltenes). First, the two interfacial properties of interest (*i.e.,* the oil/water IFT and the oil/water/rock CA) were analyzed using pure oil components to evaluate the interfacial behavior of each fraction on its own. Then, different simple binary, ternary or quaternary oil mixtures were built to assess the interfacial properties of oils that combine different SARA fractions simultaneously. Finally, complex model oils containing all SARA fractions in different proportions were simulated to mimic as reliably as possible the behavior of real crude oils.

Regarding the study of pure molecules, it was seen that the most polar components of oil can interact with water via electrostatic or hydrogen bond interactions that make the oil/water interface more stable. When these interactions are relevant the interfaces become wider (*i.e.,* ΔI 3-

naphthenic acid/water > quinoline/water > toluene/water > dodecane/water) and the IFT becomes lower (*i.e.,* IFT dodecane/water > toluene/water > quinoline/water > 3-naphthenic acid/water). In fact, there is a correlation where the IFT is inversely proportional to the square of the interfacial width. Increasing temperature reduces the oil/water IFT in all compounds, whereas pressure variations around 100 atm almost do not affect the resulting IFT.

The understanding of water affinities of pure compounds is critical when modeling mixtures, because the most polar components of oil tend to migrate from the oil bulk to the oil/water interface and reduce the IFT. Specifically, the polar compounds accumulate at the interface relegating any other less polar molecules to the oil bulk, as seen with dodecane in the binary dodecane/toluene mixture, toluene in the toluene/quinoline mixture or all other compounds when 3-naphthenic acid is present. The molecules located at the interface are the ones that contribute to the oil/water IFT, regardless of the oil bulk, as specifically determined by MD simulations. The effect of model asphaltenes was also analyzed, but the average molecules selected did not seem to be very interfacially active, especially in the presence of other smaller polar molecules (*e.g.,* quinoline or 3-naphthenic acid). Additionally, the natural agglomeration of asphaltenes makes them to form clusters with 4 to 6 units that reduce their mobility and diminish their interfacial activity.

From all of the compiled results regarding the oil/water IFT it seems that the inclusion of polar molecules, such as 3-naphthenic acid, to the oil matrix is beneficial to oil recovery because it reduces the oil/water IFT, but when including the effect of the mineral substrate these compounds tend to attach strongly to the rock preventing recovery. This conclusion was achieved by modeling different pure oil nanodroplets immersed in water on top of a $CaCO_3(10\bar{1}4)$ surface. This particular surface is highly hydrophilic and has a water wet behavior when non-polar oils are placed on top of it. However, 3-naphthenic acid is capable of strongly interacting simultaneously with both the Ca^{2+} and CO_3^{2-} ions of calcite, turning the surface almost oil wet. These results have been analyzed throughout CA simulations, where CA dodecane < toluene < quinoline < 3-naphthenic acid.

In highly hydrophilic surfaces (*e.g.,* calcite), a thin water layer of 5 Å width is formed below the oil droplets, whereas in less hydrophilic surfaces (*e.g.,* kaolinite) the water layer is not necessarily formed. However, the addition of salinity to the medium increases the polarity of the water phase, which in turn favors its interactions with the ionic mineral surface. In this situation, salinity helps in promoting the formation of the water layer between the oil droplet and the surface. Then, the CA of the system is reduced due to stronger water/rock adhesion forces unless the oil contains highly polar compounds that can interact with the electrolytes located in the water layer, which can become attracted via electrostatic interactions and then reinforce the oil/rock interactions by proximity. All of these effects could not be seen in kaolinite, whose stronger

oil/rock interactions prevented the formation of any water layer, and thus the saline effect to the CA was negligible.

On the other hand, the effect of salinity increased the oil/water IFT due to a higher polarity of brine with respect pure water, which increases the polarity difference between the water and oil phases. Even though a small attractive effect could be intuited in the z-distributions of mixtures containing high concentrations of 3-naphthenic acid, the salt interactions with the selected average molecules are not strong enough to provoke any noticeable effect on the oil/water IFT.

Finally, this part of the work has shown how MD simulations can aid in the comprehension of complex problems like oil recovery, unveiling some of the phenomena occurring in oil reservoirs at a molecular level. Even though the obtained results not always provided accurate values of IFTs or CAs, the qualitative trends of these properties at different oil and water compositions were successfully reproduced, allowing to help in experimental misconceptions (*e.g.,* the effect of quinoline impurities), the reproduction of the relative oil/water or oil/rock interactions or the explanation of the different saline effects on the CA of non-polar and polar oils.

4.6 References

1 *Second Strategic Energy Review - An EU Energy Security And Solidarity Action Plan*, Brussels, 2008.

2 *An Energy Policy For Europe*, Brussels, 2007.

3 L. Guoyu, *World Atlas of Oil and Gas Basins*, Wiley-Blackwell, Oxford, 2011.

4 Schobert, H., *Chemistry of Fossil Fuels*, Cambridge University Press, Cambridge, 2013.

5 I. A. Wiehe and K. S. Liang, Asphaltenes, Resins, and Other Petroleum Macromolecules, *Fluid Phase Equilibr.*, 1996, **117**, 201–210.

6 H. Devold, *Oil and Gas Production Handbook: An Introduction to oil and Gas Production, Transport, Refining and Petrochemical Industry*, ABB Oil and Gas, Oslo, 2013.

7 D. M. Jewell, J. H. Weber, J. W. Bunger, H. Plancher and D. R. Latham, Ion-Exchange, Coordination, and Adsorption Chromatographic Separation of Heavy-end Petroleum Distillates, *Anal. Chem.*, 1972, **44**, 1391–1395.

8 T. Fan, J. Wang and J. S. Buckley, Evaluating Crude Oils by SARA Analysis. In: Oklahoma Society of Petroleum Engineers, Oklahoma, 2002.

9 L. Carbognani, M. Orea and M. Fonseca, Complex Nature of Separated Solid Phases from Crude Oils, *Energ. Fuel.*, 1999, **13**, 351–358.

10 J. C. Suatoni and R. E. Swab, Rapid Hydrocarbon Group-Type Analysis by High Performance Liquid Chromatography, *J. Chromatogr. Sci.*, 1975, **13**, 361–366.

11 E. Rogel, M. Roye, J. Vien and T. Miao, Characterization of Asphaltene Fractions: Distribution, Chemical Characteristics, and Solubility Behavior, *Energ. Fuel.*, 2015, **29**, 2143–2152.

12 C. Ovalles, E. Rogel, M. Moir, L. Thomas and A. Pradhan, Characterization of Heavy Crude Oils, Their Fractions, and Hydrovisbroken Products by the Asphaltene Solubility Fraction Method, *Energ. Fuel.*, 2012, **26**, 549–556.

13 P. Wattana, H. S. Fogler, A. Yen, M. C. Garcìa and L. Carbognani, Characterization of Polarity-Based Asphaltene Subfractions, *Energ. Fuel.*, 2005, **19**, 101–110.

14 K. L. Gawrys, G. A. Blankenship and P. K. Kilpatrick, On the Distribution of Chemical Properties and Aggregation of Solubility Fractions in Asphaltenes, *Energ. Fuel.*, 2006, **20**, 705–714.

15 E. S. Boek, D. S. Yakovlev and T. F. Headen, Quantitative Molecular Representation of Asphaltenes and Molecular Dynamics Simulation of Their Aggregation, *Energ. Fuel.*, 2009, **23**, 1209–1219.

16 T. F. Headen, E. S. Boek, G. Jackson, T. S. Totton and E. A. Müller, Simulation of Asphaltene Aggregation through Molecular Dynamics: Insights and Limitations, *Energ. Fuel.*, 2017, **31**, 1108–1125.

17 J. Sheng, *Modern Chemical Enhanced Oil Recovery; Theory and Practice*, Elsevier Science, Burlington, 2010.

18 J.G. Speight, *Chemistry and Technology of Petroleum*, Taylor and Francis, Hoboken, 2006.

19 E. M. A. Mokheimer, M. Hamdy, Z. Abubakar, M. R. Shakeel, M. A. Habib and M. Mahmoud, A Comprehensive Review of Thermal Enhanced Oil Recovery: Techniques Evaluation, *J. Energy Resour. Technol.*, 2019, **141**, 030801.

20 M. Arif, S. A. Abu-Khamsin and S. Iglauer, Wettability of Rock/CO_2/Brine and Rock/Oil/CO_2-Enriched-Brine Systems: Critical Parametric Analysis and Future Outlook, *Adv. Colloid Interfac.*, 2019, **268**, 91–113.

21 C. Esene, N. Rezaei, A. Aborig and S. Zendehboudi, Comprehensive Review of Carbonated Water Injection for Enhanced Oil Recovery, *Fuel*, 2019, **237**, 1086–1107.

22 E. Manrique, M. Ahmadi and S. Samani, Historical and Recent Observations in Polymer Floods: An update review, *CTF - Cienc. Tecnol. Futuro*, 2017, **6**, 17–48.

23 M. A. Mousavi and S. M. Baghban, Enhancing Hydrocarbon Productivity Via Wettability Alteration: a Review on the Application of Nanoparticles, *Rev. Chem. Eng.*, 2019, **35**, 531–563.

24 S. Ko and C. Huh, Use of Nanoparticles for Oil Production Applications, *J. Pet. Sci. Eng.*, 2019,

172, 97–114.

25 A. A. Umar, I. B. M. Saaid, A. A. Sulaimon and R. B. M. Pilus, A Review of Petroleum Emulsions and Recent Progress on Water-in-Crude Oil Emulsions Stabilized by Natural Surfactants and Solids, *J. Pet. Sci. Eng.*, 2018, **165**, 673–690.

26 S. Pal, M. Mushtaq, F. Banat and A. M. Al Sumaiti, Review of Surfactant-Assisted Chemical Enhanced Oil Recovery for Carbonate Reservoirs: Challenges and Future Perspectives, *Pet. Sci.*, 2018, **15**, 77–102.

27 M. S. Kamal, I. A. Hussein and A. S. Sultan, Review on Surfactant Flooding: Phase Behavior, Retention, IFT, and Field Applications, *Energ. Fuel.*, 2017, **31**, 7701–7720.

28 M. A. Sohal, G. Thyne and E. G. Søgaard, Review of Recovery Mechanisms of Ionically Modified Waterflood in Carbonate Reservoirs, *Energ. Fuel.*, 2016, **30**, 1904–1914.

29 A. Katende and F. Sagala, A Critical Review of Low Salinity Water Flooding: Mechanism, Laboratory and Field Application, *J. Mol. Liq.*, 2019, **278**, 627–649.

30 G. J. Gloor, G. Jackson, F. J. Blas and E. de Miguel, Test-Area Simulation Method for the Direct Determination of the Interfacial Tension of Systems with Continuous or Discontinuous Potentials, *J. Chem. Phys.*, 2005, **123**, 134703.

31 J. G. Kirkwood and F. P. Buff, The Statistical Mechanical Theory of Surface Tension, *J. Chem. Phys.*, 2004, **17**, 338.

32 J. H. Irving and J. G. Kirkwood, The Statistical Mechanical Theory of Transport Processes. IV. The Equations of Hydrodynamics, *J. Chem. Phys.*, 1950, **18**, 817–829.

33 T. Young, III. An Essay on the Cohesion of Fluids, *Philos. Trans. R. Soc. Lond.*, 1805, **95**, 65–87.

34 F. Jiménez-Ángeles and A. Firoozabadi, Contact Angle, Liquid Film, and Liquid–Liquid and Liquid–Solid Interfaces in Model Oil–Brine–Substrate Systems, *J. Phys. Chem. C*, 2016, **120**, 11910–11917.

35 R. Raj, S. C. Maroo and E. N. Wang, Wettability of Graphene, *Nano Lett.*, 2013, **13**, 1509–1515.

36 B. Ramos-Alvarado, S. Kumar and G. P. Peterson, Wettability of Graphitic-Carbon and Silicon Surfaces: MD Modeling and Theoretical Analysis, *J. Chem. Phys.*, 2015, **143**, 044703.

37 L. S. de Lara, T. Voltatoni, M. C. Rodrigues, C. R. Miranda and S. Brochsztain, Potential Applications of Cyclodextrins in Enhanced Oil Recovery, *Colloid. Surface. A*, 2015, **469**, 42–50.

38 S. Plimpton, Fast Parallel Algorithms for Short-Range Molecular Dynamics, *J. Comput. Phys.*, 1995, **117**, 1–19.

39 H. Sun, COMPASS: An ab Initio Force-Field Optimized for Condensed-Phase Applications Overview with Details on Alkane and Benzene Compounds, *J. Phys. Chem. B*, 1998, **102**, 7338–

7364.

40 J. W. Eastwood and R. W. Hockney, Shaping the Force Law in Two-Dimensional Particle-Mesh Models, *J. Comput. Phys.*, 1974, **16**, 342–359.

41 T. Schneider and E. Stoll, Molecular-Dynamics Study of a Three-Dimensional One-Component Model for Distortive Phase Transitions, *Phys. Rev. B*, 1978, **17**, 1302–1322.

42 S. Nosé, A Molecular Dynamics Method for Simulations in the Canonical Ensemble, *Mol. Phys.*, 1984, **52**, 255–268.

43 H. J. C. Berendsen, J. P. M. Postma, W. F. van Gunsteren, A. DiNola and J. R. Haak, Molecular Dynamics With Coupling to an External Bath, *J. Chem. Phys.*, 1998, **81**, 3684–3690.

44 W. G. Hoover, Constant-Pressure Equations of Motion, *Phys. Rev. A*, 1986, **34**, 2499–2500.

45 S. Hartland, *Surface and Interfacial Tension: Measurement, Theory and Applications*, Marcel Dekker, Inc., New York, 2004.

46 S. Zeppieri, J. Rodríguez and A. L. López de Ramos, Interfacial Tension of Alkane + Water Systems, *J. Chem. Eng. Data*, 2001, **46**, 1086–1088.

47 D.R. Lide, *CRC Handbook of Chemistry and Physics (90th ed.)*, CRC Press, Boca Raton, 2009.

48 F. Casellato, C. Vecchi, A. Girelli and B. Casu, Differential Calorimetric Study of Polycyclic Aromatic Hydrocarbons, *Thermochim. Acta*, 1973, **6**, 361–368.

49 G. W. Smith, Phase Behavior of some Condensed Polycyclic Aromatics, *Mol. Cryst. Liq. Cryst.*, 1980, **64**, 15–17.

50 M. G. Martin and J. I. Siepmann, Transferable Potentials for Phase Equilibria. 1. United-Atom Description of n-Alkanes, *J. Phys. Chem. B*, 1998, **102**, 2569–2577.

51 F. N. Mendoza, R. López-Rendón, J. López-Lemus, J. Cruz and J. Alejandre, Surface Tension of Hydrocarbon Chains at the Liquid–Vapour Interface, *Mol. Phys.*, 2008, **106**, 1055–1059.

52 J. Wang, R. M. Wolf, J. W. Caldwell, P. A. Kollman and D. A. Case, Development and Testing of a General Amber Force Field, *J. Comput. Chem.*, 2004, **25**, 1157–1174.

53 Z. Hu, S. Ballinger, R. Pelton and E. D. Cranston, Surfactant-Enhanced Cellulose Nanocrystal Pickering Emulsions, *J. Colloid Interface Sci.*, 2015, **439**, 139–148.

54 A. Yeung, T. Dabros and J. Masliyah, Does Equilibrium Interfacial Tension Depend on Method of Measurement?, *J. Colloid Interface Sci.*, 1998, **208**, 241–247.

55 K. Moran, A. Yeung and J. Masliyah, Measuring Interfacial Tensions of Micrometer-Sized Droplets: A Novel Micromechanical Technique, *Langmuir*, 1999, **15**, 8497–8504.

56 H. J. C. Berendsen, J. R. Grigera and T. P. Straatsma, The Missing Term in Effective Pair

Potentials, *J. Phys. Chem.*, 1987, **91**, 6269–6271.

57 W. L. Jorgensen, J. Chandrasekhar, J. D. Madura, R. W. Impey and M. L. Klein, Comparison of Simple Potential Functions for Simulating Liquid Water, *J. Chem. Phys.*, 1983, **79**, 926–935.

58 W. L. Jorgensen and J. D. Madura, Temperature and Size Dependence for Monte Carlo Simulations of TIP4P Water, *Mol. Phys.*, 1985, **56**, 1381–1392.

59 J.-P. Ryckaert, G. Ciccotti and H. J. C. Berendsen, Numerical Integration of the Cartesian Equations of Motion of a System with Constraints: Molecular Dynamics of n-Alkanes, *J. Comput. Phys.*, 1977, **23**, 327–341.

60 P.J. Linstrom and W.G. Mallard (ed.), NIST Chemistry WebBook, Nist Standard Reference Database Number 69, National Institute of Standards and Technology, Gaithersburg MD.

61 J. Gurnos, *The Chemistry of Heterocyclic Compounds: Quinolines, Part I*, John Wiley & Sons, Staffordshire, 1977.

62 *3-Cyclohexanepropionic Acid. Safety Data Sheet*, Sigma-Aldrich, St. Louis, 2014.

63 *3-Cyclohexanepentanoic Acid. Safety Data Sheet*, Sigma-Aldrich, St. Louis, 2018.

64 C. Vega and E. de Miguel, Surface Tension of the Most Popular Models of Water by Using the Test-Area Simulation Method, *J. Chem. Phys.*, 2007, **126**, 154707.

65 *Experimental Measurements by REPSOL, Internal Report*, 2017.

66 J. Ge, A. Feng, G. Zhang, P. Jiang, H. Pei, R. Li and X. Fu, Study of the Factors Influencing Alkaline Flooding in Heavy-Oil Reservoirs, *Energ. Fuel.*, 2012, **26**, 2875–2882.

67 J. J. Sheng, Status of Alkaline Flooding Technology, *J. Pet. Eng. Technol.*, 2019, **5**, 44–50.

68 S. C. Parker, S. Kerisit, A. Marmier, S. Grigoleit and G. W. Watson, Modeling Inorganic Solids and their Interfaces: A Combined Approach of Atomistic and Electronic Structure Simulation Techniques, *Faraday Discuss.*, 2003, **124**, 155–170.

69 D. L. Graf, Crystallographic Tables for the Rhombohedral Carbonates, *Am. Mineral.*, 1961, **46**, 1283–1316.

70 S. Xiao, S. A. Edwards and F. Gräter, A New Transferable Forcefield for Simulating the Mechanics of $CaCO_3$ Crystals, *J. Phys. Chem. C*, 2011, **115**, 20067–20075.

71 T. D. Perry, R. T. Cygan and R. Mitchell, Molecular Models of a Hydrated Calcite Mineral Surface, *Geochim. Cosmochim. Acta*, 2007, **71**, 5876–5887.

72 J. Zhang, P. Wang, M. K. Borg, J. M. Reese and D. Wen, A Critical Assessment of the Line Tension Determined by the Modified Young's Equation, *Phys. Fluids*, 2018, **30**, 082003.

73 T. Werder, J. H. Walther, R. L. Jaffe, T. Halicioglu and P. Koumoutsakos, On the Water−Carbon

Interaction for Use in Molecular Dynamics Simulations of Graphite and Carbon Nanotubes, *J. Phys. Chem. B*, 2003, **107**, 1345–1352.

74 J. H. Weijs, A. Marchand, B. Andreotti, D. Lohse and J. H. Snoeijer, Origin of Line Tension for a Lennard-Jones Nanodroplet, *Phys. Fluids*, 2011, **23**, 022001.

75 B. V. Toshev, D. Platikanov and A. Scheludko, Line Tension in Three-Phase Equilibrium Systems, *Langmuir*, 1988, **4**, 489–499.

76 C. O. Metin, J. R. Baran and Q. P. Nguyen, Adsorption of Surface Functionalized Silica Nanoparticles onto Mineral Surfaces and Decane/Water Interface, *J. Nanoparticle Res.*, 2012, **14**, 1246:1–16.

77 D. E. Smith and L. X. Dang, Computer simulations of NaCl association in polarizable water, *J. Chem. Phys.*, 1998, **100**, 3757–3766.

78 J. Åqvist, Ion-water interaction potentials derived from free energy perturbation simulations, *J. Phys. Chem.*, 1990, **94**, 8021–8024.

79 E. R. A. Lima, B. M. de Melo, L. T. Baptista and M. L. L. Paredes, Specific Ion Effects on the Interfacial Tension of Water/Hydrocarbon Systems, *Braz. J. Chem. Eng.*, 2013, **30**, 55–62.

80 R. Aveyard and S. M. Saleem, Interfacial Tensions at Alkane-Aqueous Electrolyte Interfaces, *J. Chem. Soc., Faraday Trans. 1*, 1976, **72**, 1609–1617.

81 Y. Chen, Q. Xie, A. Sari, P. V. Brady and A. Saeedi, Oil/Water/Rock Wettability: Influencing Factors and Implications for Low Salinity Water Flooding in Carbonate Reservoirs, *Fuel*, 2018, **215**, 171–177.

82 H. H. Al-Attar, M. Y. Mahmoud, A. Y. Zekri, R. Almehaideb and M. Ghannam, Low-Salinity Flooding in a Selected Carbonate Reservoir: Experimental Approach, *J. Pet. Explor. Prod. Technol.*, 2013, **3**, 139–149.

83 H. Mahani, A. L. Keya, S. Berg, W.-B. Bartels, R. Nasralla and W. R. Rossen, Insights into the Mechanism of Wettability Alteration by Low-Salinity Flooding (LSF) in Carbonates, *Energ. Fuel.*, 2015, **29**, 1352–1367.

84 H. Kim and D. J. Burgess, Prediction of Interfacial Tension between Oil Mixtures and Water, *J. Colloid Interface Sci.*, 2001, **241**, 509–513.

85 R. G. Martins, L. S. Martins and R. G. Santos, Effects of Short-Chain n-Alcohols on the Properties of Asphaltenes at Toluene/Air and Toluene/Water Interfaces, *Colloids Interfaces*, 2018, **2**, 13:1–9.

86 S. Mozaffari, P. Tchoukov, J. Atias, J. Czarnecki and N. Nazemifard, Effect of Asphaltene Aggregation on Rheological Properties of Diluted Athabasca Bitumen, *Energ. Fuel.*, 2015, **29**,

5595–5599.

87 Yeung A., Dabros T., Czarnecki J. and Masliyah J., On the Interfacial Properties of Micrometre–Sized Water Droplets in Crude Oil, *Proc. R. Soc. Lond. Ser. Math. Phys. Eng. Sci.*, 1999, **455**, 3709–3723.

88 W. Karnanda, M. S. Benzagouta, A. AlQuraishi and M. M. Amro, Effect of Temperature, Pressure, Salinity, and Surfactant Concentration on IFT for Surfactant Flooding Optimization, *Arab. J. Geosci.*, 2013, **6**, 3535–3544.

89 M. Lashkarbolooki and S. Ayatollahi, Effects of Asphaltene, Resin and Crude Oil Type on the Interfacial Tension of Crude Oil/Brine Solution, *Fuel*, 2018, **223**, 261–267.

90 L. Han, Z. Ye, H. Chen and P. Luo, The Interfacial Tension Between Cationic Gemini Surfactant Solution and Crude Oil, *J. Surfactants Deterg.*, 2009, **12**, 185–190.

91 J. S. Buckley and T. Fan, Crude Oil/Brine Interfacial Tensions1, *Petrophysics*, 2007, **48**, 175–185.

92 R. Z. Syunyaev, R. Z. Safieva and R. R. Safin, The Influence of the Internal Structure and Dispersity to Structural–Mechanical Properties of Oil systems, *J. Pet. Sci. Eng.*, 2000, **26**, 31–39.

93 G. K. Wong and T. F. Yen, An Electron Spin Resonance Probe Method for the Understanding of Petroleum Asphaltene Macrostructure, *J. Pet. Sci. Eng.*, 2000, **28**, 55–64.

94 A. N. M. Carauta, P. R. Seidl, E. C. A. N. Chrisman, J. C. G. Correia, P. de O. Menechini, D. M. Silva, K. Z. Leal, S. M. C. de Menezes, W. F. de Souza and M. A. G. Teixeira, Modeling Solvent Effects on Asphaltene Dimers †, *Energ. Fuel.*, 2005, **19**, 1245–1251.

95 H. Zeng, Y.-Q. Song, D. L. Johnson and O. C. Mullins, Critical Nanoaggregate Concentration of Asphaltenes by Direct-Current (DC) Electrical Conductivity, *Energ. Fuel.*, 2009, **23**, 1201–1208.

96 N. V. Lisitza, D. E. Freed, P. N. Sen and Y.-Q. Song, Study of Asphaltene Nanoaggregation by Nuclear Magnetic Resonance (NMR), *Energ. Fuel.*, 2009, **23**, 1189–1193.

97 D. L. Bish, Rietveld Refinement of the Kaolinite Structure at 1.5 K, *Clay. Clay Miner.*, 2006, **41**, 738–744.

98 R. Šolc, M. H. Gerzabek, H. Lischka and D. Tunega, Wettability of Kaolinite (001) Surfaces — Molecular Dynamic Study, *Geoderma*, 2011, **169**, 47–54.

99 R. T. Cygan, J.-J. Liang and A. G. Kalinichev, Molecular Models of Hydroxide, Oxyhydroxide, and Clay Phases and the Development of a General Force Field, *J. Phys. Chem. B*, 2004, **108**, 1255–1266.

100 B. Kumar, PhD Thesis, University of Calgary, 2012.

101 M. M. Salehi, P. Omidvar and F. Naeimi, Salinity of Injection Water and its Impact on Oil Recovery Absolute Permeability, Residual Oil Saturation, Interfacial Tension and Capillary

Pressure, *Egypt. J. Pet.*, 2017, **26**, 301–312.

102 F. Moeini, A. Hemmati-Sarapardeh, M.-H. Ghazanfari, M. Masihi and S. Ayatollahi, Toward Mechanistic Understanding of Heavy Crude Oil/Brine Interfacial Tension: The Roles of Salinity, Temperature and Pressure, *Fluid Phase Equilibr.*, 2014, **375**, 191–200.

103 C. S. Vijapurapu and D. N. Rao, Compositional Effects of Fluids on Spreading, Adhesion and Wettability in Porous Media, *Colloid. Surface. A*, 2004, **241**, 335–342.

CHAPTER 5

Interaction of Surfactants with Oil/Water/Salt Systems for Enhanced Oil Recovery

In Chapter 4 the behavior of oil, brine and rocks have been assessed to better understand some of the interfacial phenomena occurring during oil recovery processes. When the collaboration with the previously mentioned company was over, a new project was formulated within the oil recovery framework aiming at better understanding the interactions of surfactants at the oil/water interface (*i.e.,* extended through Chapter 5). Surfactants (*i.e.,* the usual term for "surface active agents") are amphiphilic molecules, which consist of a non-polar hydrophobic segment called "tail group" or simply "tail" and a polar or ionic region called "head group" or simply "head".[1] The tail is usually built with a linear or ramified hydrocarbon chain, that interacts favorably with other non-polar phases (*e.g.,* an oil). Otherwise, the head can be cationic, anionic, zwitterionic or non-ionic, all of which interact strongly with polar phases (*e.g.,* water).[2]

This dual affinity of surfactants makes them migrate to any interface (*e.g.,* the oil/water interface) and orient their polar and non-polar parts to the respective polar and non-polar regions of the interface, respectively. Due to this orientation, each segment of the surfactant can interact with a bulk phase to increase its adhesive force, which reduce the IFT (*i.e.,* $\gamma \propto F_{coh} - F_{adh}$).[3–5] Additionally, surfactants can also interact with the surface of the porous rock usually displacing the oil and favoring recovery. However, recall that the temperature, pressure and salinity conditions, as well as the oil characteristics, depend significantly on each reservoir, so surfactants may not be equally efficient in all petroleum reservoirs. For this reason, the understanding of all phenomena involving surfactant interactions at the molecular level is fundamental for the future design of better surfactants for cEOR. Specifically, at pore conditions, surfactants can interact with many different species (*i.e.,* with water, many different electrolytes, the enormous amount of oil components and the porous rock), which makes the modeling and understanding of these kinds of systems very challenging. For this reason, in this part of the thesis the effect of the rock is completely removed, and only the effect of surfactants at the oil/brine IFT is evaluated.

The different types of surfactants known are defined according to the type of head group they contain.[1,6] First, the polar head of a cationic surfactant is usually formed by a quaternary

ammonium group with the general formula NR_4^+. The positive charge of the head group is accompanied by a negative anion, such as Cl^- or Br^-. Similarly, anionic surfactants have a negatively charged head group based on carboxylates (COO^-), sulphates (OSO_3^-), sulphonates (SO_3^-) or phosphates ($OP(OH)O_2^-$), all of them paired with a positively charged counterion (*e.g.,* Na^+). Surfactants can also contain at the same time a positively charged and a negatively charged polar head groups (*i.e.,* normally with a betaine functional group).[7] These surfactants are known as zwitterionic surfactants and they have a cationic, anionic or almost non-ionic behavior depending on the pH of the solution. Finally, the non-ionic surfactants do not contain any charged species and their polar head groups are generally based on large regions of alcohol ethoxylates (*i.e.,* $-(OCH_2CH_2)_n - OH$ with no counterion). A summary with some examples of these kinds of surfactants can be seen in Figure 5.1.

5.1 Introduction to the Salt/Surfactant Synergistic Effect

Although the IFT of an oil/water system is reduced by effect of the surfactants, their application in EOR is usually expensive. For this reason, in the recent years, different alternative techniques to lower the oil/water IFT have been explored to obtain the lowest possible value and reduce the necessary surfactant concentration.[8–10] For example, when the injection water is designed by mixing seawater with fresh water, which contains a low concentration of certain electrolytes, an improved recovery with respect standard waterflooding can be observed in certain reservoirs.[11,12] Even though the recovery can be increased with this technique, the ultralow IFT values needed for efficient EOR cannot be achieved by solely tuning the water salinity. For this reason, the most common procedure is based on using combinations of surfactants with other additives that act synergistically to yield a lower IFT, which may allow to reduce the amount of surfactant used or directly increase the amount of produced oil. These additives can either be other

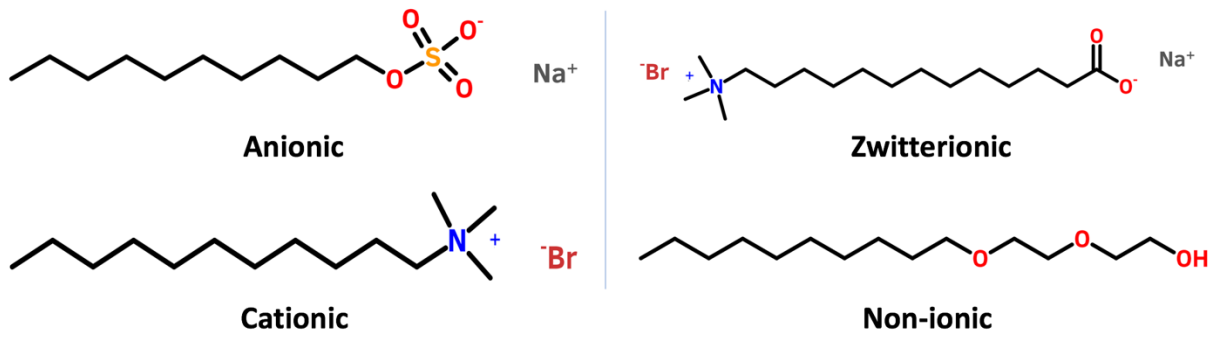

Figure 5.1. Examples of four different types of surfactants classified according to their head groups.

surfactants or non-surfactant species with high interfacial activity such as alcohols (*i.e.,* also grouped under the name of co-surfactants). When the adequate concentration of surfactants and additives are combined, the IFT of the system can potentially achieve ultralow IFT values (*i.e.,* 10^{-2} - 10^{-4} $mN \cdot m^{-1}$), which favors the formation and stabilization of oil/water microemulsions.[13]

Another additive that can be used in surfactant cEOR are electrolytes. They are usually cheap compounds, and many of them are already found in the petroleum reservoir. Electrolytes are capable of strongly interacting with polar segments of molecules and change their microscopical arrangement, which affects the fluid properties (*e.g.,* the dipoles of water orient towards the salt generating solvation shells around each ion, which modify the melting point, the boiling point, the density, the surface tension, the viscosity and the vapor pressure of the fluid [14–16]). In particular, surfactants can be also affected by salinity modifying properties such as the Critical Micelle Concentration (CMC) or the IFT. These properties vary differently depending on the types of surfactants and salts that are combined, so it is important to understand the mechanisms underneath to predict how surfactants behave under a determined salinity environment. Notice that, even though no modifications are applied to injection water, petroleum reservoirs already contain a high concentration of electrolytes, so this specific salt/surfactant interaction will always be present at reservoir conditions, which increases the significance of its understanding.

To illustrate the complexity of salt/surfactant interactions, consider that their CMC usually decrease when increasing salinity concentration,[17,18] but Seredyuk *et al.,*[19] showed a steady increase with zwitterionic gemini surfactants in NaBr. Similarly, the IFT variation also depends on the salt/surfactant combination, but many works showed that electrolytes can act synergistically with surfactants to reduce the oil/water dynamic and static IFT.[20–33] This effect does not follow the usual experimental and computational trend observed, where many oil/water IFTs increase with salinity concentration.[34–38]

The static oil/water IFT is the value measured at equilibrium, which requires the time of all species to diffuse either to the interface, to the oil bulk or to the water bulk (*i.e.,* depending on the system it can take from minutes to hours or days). The static IFT of several systems exhibited lower values in presence of salinity, such as: zwitterionic surfactant mixtures with water and NaCl by Staszak *et al.,*[32] cationic surfactants with water and potassium halides by Koelsch *et al.,*[28] anionic surfactants in monovalent and divalent brines by Fainerman *et al.,*[24] among others.[21–23,25,26] Finally, some of these works specifically show that stronger IFT reduction effects are achieved at surfactant concentrations below the CMC.[28,32,33]

On the other hand, the dynamic oil/water IFT is conformed by the whole set of IFT values measured during the equilibration process, and it can be beneficial in cEOR if the dynamic pattern achieves a minimum at lower IFT values than the static IFT. Some examples are the works of Liu *et al.,*[30,31] where the dynamic IFT pattern of anionic surfactants and combinations of anionic/non-ionic surfactants were measured in the presence of salts. Their analysis showed that the IFT in absence of salinity changes smoothly with time, whereas divalent salts allow the system to achieve an ultralow IFT in the first minutes of measuring, after which the IFT increases again until it meets the static IFT value. Additionally, Witthayapanyanon *et al.,*[33] measured a similar behavior with anionic surfactants and NaCl.

Different mechanisms were proposed from the experimental evidences to explain both the dynamic and static IFT (Figure 5.2).[30,31,39,40] Regarding dynamic IFT, it is proposed that the water solubility of a surfactant soluble in the two phases is reduced by addition of salts via a salting out effect. The surfactants then need to migrate from the water to the oil through the interface to be effectively dissolved. In the time when surfactants are crossing the interface, their interfacial accumulation increases, which produces a temporal reduction of the oil/water IFT.[39] Otherwise, if the solubility of the surfactant in the non-polar phase is low they might only diffuse and stay at the interface, reducing the oil/water IFT at equilibrium (*i.e.,* static IFT).[40] Additionally, the electrolytes can also interact with the surfactants and screen the electrostatic interactions between different

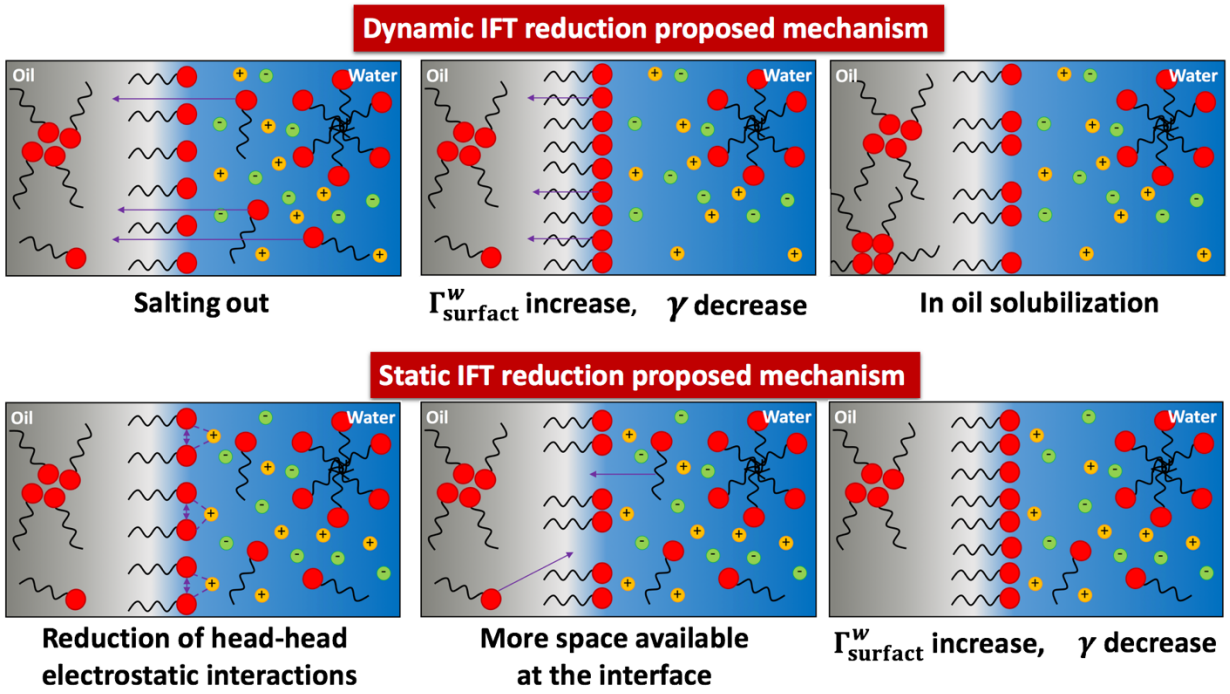

Figure 5.2. Visual representations of two possible mechanisms to explain the dynamic and static IFT reduction, respectively.

head groups, which improves the packing of these species and allow additional molecules to fit at the interface.[30,31]

In summary, the previous mechanisms used to explain the dynamic or static IFT reductions assume that the effect is due to an increase of the number of surfactants at the interface. This behavior is defined by the Gibbs isotherm (eq. 5.1), where the IFT (γ) decreases linearly with the Gibbs interfacial excess concentration (*i.e.,* Γ_i called interfacial excess from now on) and μ_i is the chemical potential of species i at a given temperature.[41] To adequately apply eq. 5.1 an infinitesimal volume of interface located at a position σ (*i.e.,* called the Gibbs dividing surface) must be assumed, and the values of Γ_i depend on the position of σ. For this reason, the Gibbs dividing surface is conveniently located at the position where the Γ_i of a reference component (*i.e.,* water in this thesis) becomes zero. Then, all other Γ_i are referred to that component (Γ_i^{R}) and the expression is rearranged as in eq. 5.2.

$$d\gamma = -\sum_i \Gamma_i \, \mu_i \qquad 5.1$$

$$\Gamma_i^R = -\frac{1}{RT}\left(\frac{\partial \gamma}{\partial \ln(a_i)}\right)_{T,a_{j\neq i}} \qquad 5.2$$

where for diluted solutions the activity (a_i) can be simply taken as the concentration. From the eq. 5.2 one can see that the interfacial excess can be positive if the IFT is reduced when increasing concentration or negative if the IFT increases instead. This fact implies that the higher amount of species accumulating at the interface (*i.e.,* more surface active compounds) the lower the oil/water IFT. On the other hand, when species deplete from the interface to migrate to any bulk phase the IFT will increase.

There are already some studies focused on performing MD simulations with some ionic surfactants and salts at the air/water and oil/water interfaces, which intend to give a molecular perspective of the intermolecular interactions that drive the salt/surfactant synergistic effect.[42–44] However, all of these works show how the ionic head groups of the surfactant (*i.e.,* either positive or negative) are capable of exchanging their counterions with compatible divalent ions present in the brine solution (*e.g.,* Na^+ counterions are exchanged by a Ca^{2+}). This exchange is favored because divalent charges can interact more strongly with charged surfactant head groups than the monovalent charges of a common counterion. According to the published results, the salt/surfactant interactions are capable of changing the molecular distributions of the surfactants at

the interface but none of these works characterized the IFT reduction via molecular simulations. This fact implies that the IFT reduction due to the salt/surfactant synergistic effect cannot be directly related to the effects produced by the described ionic exchange.

In this thesis, MD simulations of a specific interfacial system containing oil, water, salt and non-ionic surfactants have been prepared to better understand the mechanism involved in the IFT reduction due to salt/surfactant synergistic effect. In order to simplify the system, the oil phase has been modeled using only pure dodecane and the water phase is simulated with water molecules and either NaCl, $CaCl_2$ or $MgCl_2$ to evaluate the salt/surfactant synergistic effect on different brines. Finally, two non-ionic surfactants have been modeled in this part of the work. The first surfactant has a linear tail containing 12 CH_x groups and a triethyleneglycol head group (*i.e.,* $CH_3(CH_2)_{11} - (OCH_2CH_2)_3 - OH$ also known as $C_{12}E_3$). On the other hand, the second surfactant is a version of the first but with a ramified non-polar tail with the same molecular weight as the linear surfactant (*i.e.,* $(CH_3(CH_2)_5)(CH_3(CH_2)_4) > CH - (OCH_2CH_2)_3 - OH$, or $C_6C_5CE_3$). The election allows to evaluate the impact of the non-polar tail shape in the salt/surfactant synergistic effect. Alcohol ethoxylate surfactants do not bear a counterion, in contrast to other ionic compounds, so the ionic exchange observed by other works cannot be the driving force of any effect observed in the conducted MD simulations.

Finally, recall that although the IFT reduction due to the salt/surfactant synergistic effect has direct application in EOR (*i.e.,* a reduction of the IFT implies an increase of oil production), the real system involving a microporous rock with many different oil fractions, water and electrolytes has been simplified to give an explanation of the salt/surfactant mechanism only at the oil/water interface. In the real system, electrolytes can also interact with the rock activating other mechanisms that can potentially hamper the oil extraction. For example, depending on the rock matrix and oil composition, positively charged electrolytes can attach to the mineral surface attracting the negatively charged fractions of oil, and retaining the oil attached to the rock.[45] This means that unless the IFT reduction shown by the salt/surfactant combination achieves significantly low values (*e.g.,* ultralow IFT) other mechanisms can still compete to prevent oil recovery. However, the interactions of surfactants and salts are completely unavoidable in petroleum reservoirs, so their understanding can help to shed some light into the complex process of oil recovery.

5.2 Molecular Dynamics Simulations of Salt/Surfactant Interactions

Oil/water/salt/surfactant systems have been modeled via MD simulations using LAMMPS code.[46] The initial simulation cell (Figure 5.3) has been built as described in the IFT simulation setup of Section 4.1 (*i.e.,* a rectangular box half filled with oil molecules and half filled with water molecules), with cell parameters $Lx = Ly = 80$ Å and $Lz = 210$ Å). A surfactant concentration below the CMC has been modeled by adding a relatively low amount of surfactants directly into the oil/water interface, to represent an interfacial excess of $\Gamma_i^R = 1.50$ μmol·m^{-2} (*i.e.,* or equivalently $(\Gamma_i^R)^{-1} = 110$ Å^2·molecule^{-1}). This concentration intends to reproduce the experiments that characterized some of the strong IFT reductions due to salt/surfactant synergistic effects.[26,30–32] Finally, some electrolytes (*i.e.,* either NaCl, $CaCl_2$ or $MgCl_2$) have been included in random positions of the water bulk. The rest of the simulation procedure has been carried out as specified in Section 4.1, evolving the system a total of 20 ns. The 10 last ns of simulations have been used to calculate the average of the equilibrium oil/water IFT and the last 2 ns have served to build properties related to molecular distributions. Finally, the IFT has been calculated via the pressure tensor method (eq. 4.2) of Kirkwood *et al.*[47,48]

Notice that in this setup, no surfactant molecules can be found in any bulk because they are all initially located at the interface at a concentration below the CMC. During the whole simulation time all surfactants remain at the interface even in absence of salinity, so the surfactant migration mechanism proposed experimentally (Figure 5.2) cannot occur in these simulations. In particular, the study here conducted is helpful to characterize other synergistic mechanisms that depend

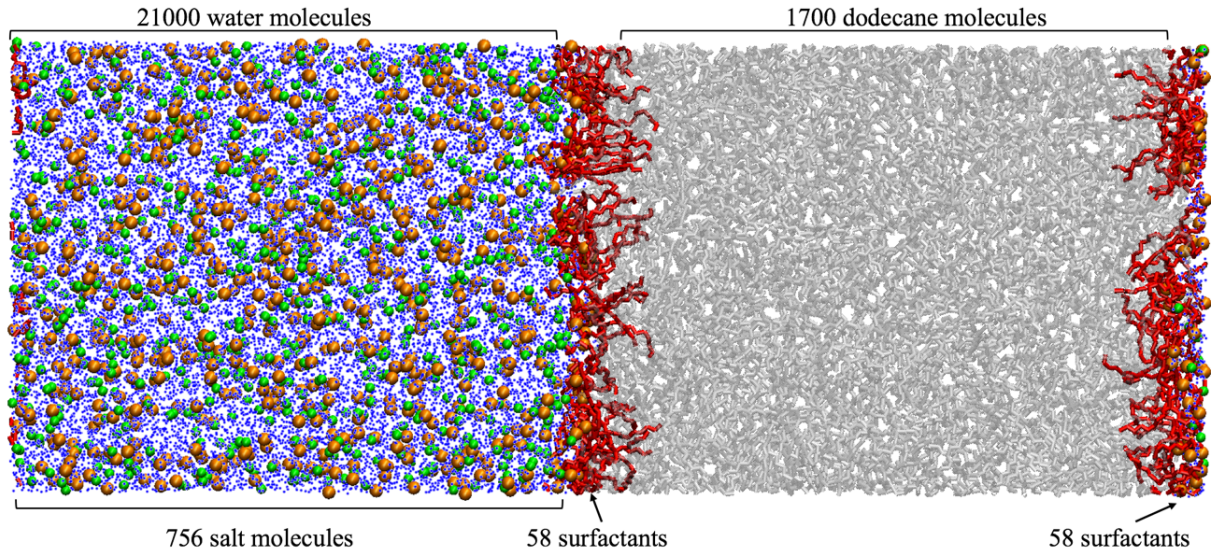

Figure 5.3. Representation of the oil (gray)/water (blue)/salt (orange and green)/surfactant (red) system used in this part of the thesis.

specifically on salt/surfactant interactions and molecular rearrangements, which also might play an important role in the IFT reduction.

The interfacial excess of each simulated species has been obtained from the MD calculated density profile in the direction perpendicular to the interface (*i.e.,* z-distributions) and the ideal density profile of a Gibbs interfacial system. The former has been obtained by dividing the simulation cell in bins with 1 Å width along the z-direction and averaging the position of all species within each bin during the last 2 ns of the simulation. On the other hand, the latter corresponds to the density distribution of the ideal Gibbs interfacial model (*i.e.,* an interface with infinitesimal volume). To better understand the difference between these two density profiles at the oil/water interface, both of them have been depicted for a single species in Figure 5.4a as an example. The solid lines correspond to the MD z-distribution profile, whereas the dashed lines refer to the ideal Gibbs profile. Both density profiles converge to the $\bar{\rho}^{w}$ value at the water bulk and to the $\bar{\rho}^{o}$ value at the oil bulk, which are the average densities of these species in their respective phases. However, the Gibbs profile makes an abrupt transition from $\bar{\rho}^{w}$ to $\bar{\rho}^{o}$ at the σ position (*i.e.,* the red vertical line), while the transition obtained by the MD profile is smoother. Then, the interfacial excess of a single species i (*i.e.,* normalized per unit area) can be calculated from the difference of the two density profiles through eq. 5.3.

$$\Gamma_i^R = \int_{L_w}^{L_o} \frac{\rho_i^{MD}(z) - \rho_i^{Gibbs}(z)}{A} dz = \int_{L_w}^{L_o} \frac{\rho_i^{MD}(z)}{A} dz - \frac{\bar{\rho}_i^{w} \cdot |\sigma^R - L_w| + \bar{\rho}_i^{o} \cdot |L_o - \sigma^R|}{A} \qquad 5.3$$

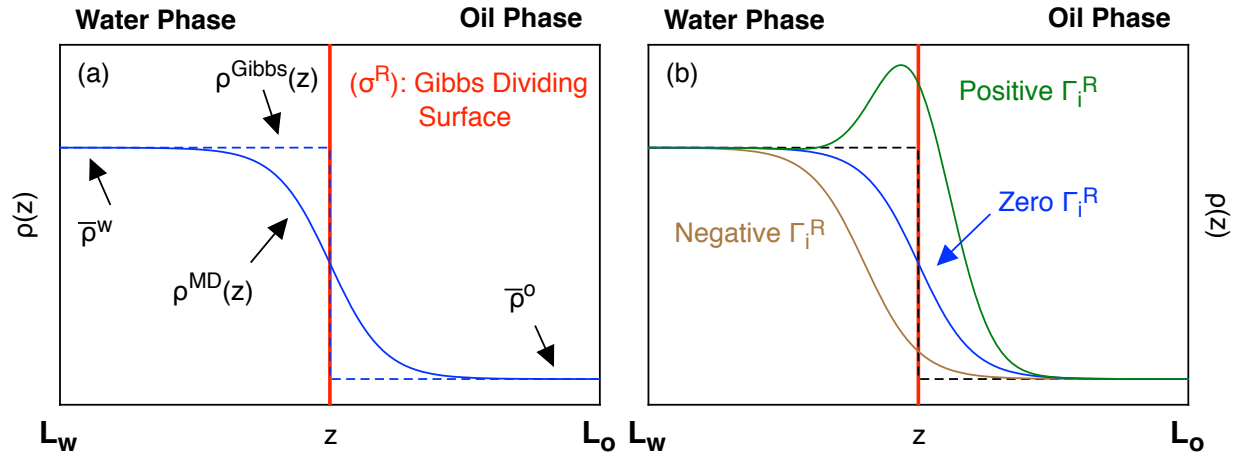

Figure 5.4. (a) Density profiles (*i.e.,* z-distributions) representation of the ideal Gibbs interfacial systems ($\rho^{Gibbs}(z)$) and a more realistic interface ($\rho^{MD}(z)$). (b) Density profiles of a species that depletes from / accumulates at the interface (brown/green) and a reference compound with $\Gamma_i^R = 0$ (blue).

The shape of the Gibbs density profile allows to change the $\int_{L_w}^{L_o} \rho_i^{Gibbs}(z)dz$ integral of eq. 5.3 for the area below two rectangles: one in the water phase (*i.e.,* $\bar{\rho}_i^w \cdot |\sigma^R - L_w|$) and another in the oil phase (*i.e.,* $\bar{\rho}_i^o \cdot |L_o - \sigma^R|$), where the integration limits L_w and L_o are, in practice, the center of the water and oil bulks respectively. Equivalently to eq. 5.2, the Gibbs dividing surface is conveniently chosen to be at the position where the Γ_i of the reference component (*i.e.,* water in this thesis) becomes zero. Then, all other interfacial excesses (Γ_i^R) are referred to the reference component by using the same Gibbs dividing surface (σ^R).

Intermolecular and intramolecular interactions of organic species have been represented by means of the TraPPE-UA force field,[49] which considers all bonds to be fixed at their equilibrium bond lengths. However, the AMBER force field spring constants have been used to permit all bonds to vibrate around its equilibrium position as suggested by TraPPE developers.[50] This force field is specifically fitted to reproduce the liquid/vapor equilibrium of organic molecules and is already capable of capturing the correct surface and interfacial tension of hydrocarbons, as already seen elsewhere [49] and in Chapter 4 of this thesis. However, a validation stage has been carried out to verify the capability of the force field in reproducing the IFT/ST reduction with surfactant concentrations below the CMC.

The ST of water at different $C_{12}E_3$ concentrations below the CMC has been selected as target property for surfactant force field validation. To ensure this validation is not affected by the water model, it is critical to select a water force field capable of reproducing the experimentally measured ST as closely as possible. This is usually not achievable with many three-point models, such as SPC [51] or TIP3P,[52] so more sophisticated four-point force fields must be used.[53] Specifically, the TIP4P/Ew,[54] which was already shown to capture a reasonably good ST of water,[53] has been employed to carry out the validation of the surfactant force field. The variation of the water ST ($\Delta\gamma$) with surfactant interfacial excess ($\Gamma^R_{\text{Surfactant}}$) is shown in Figure 5.5a in comparison with the experimental measurements of Lu *et al.*[55] The excellent agreement between the experimental measurements and the simulation results verify that TraPPE-UA force field is adequate to reproduce the effect of surfactants at the interface.

Although there are significant differences on the ST of water depending on water model used, this variation is less important when modeling an oil/water interface. In fact, in Chapter 4 it was seen that either SPC, SPC/E, TIP3P and TIP4P were all reasonable models to predict the oil/water IFT at laboratory conditions. However, the TIP4P models are computationally more expensive than SPC, SPC/E and TIP3P. For this reason, after using TIP4P/Ew to validate the surfactant force field, TIP3P was selected in this part of the thesis because it is a relatively cheap water model, that

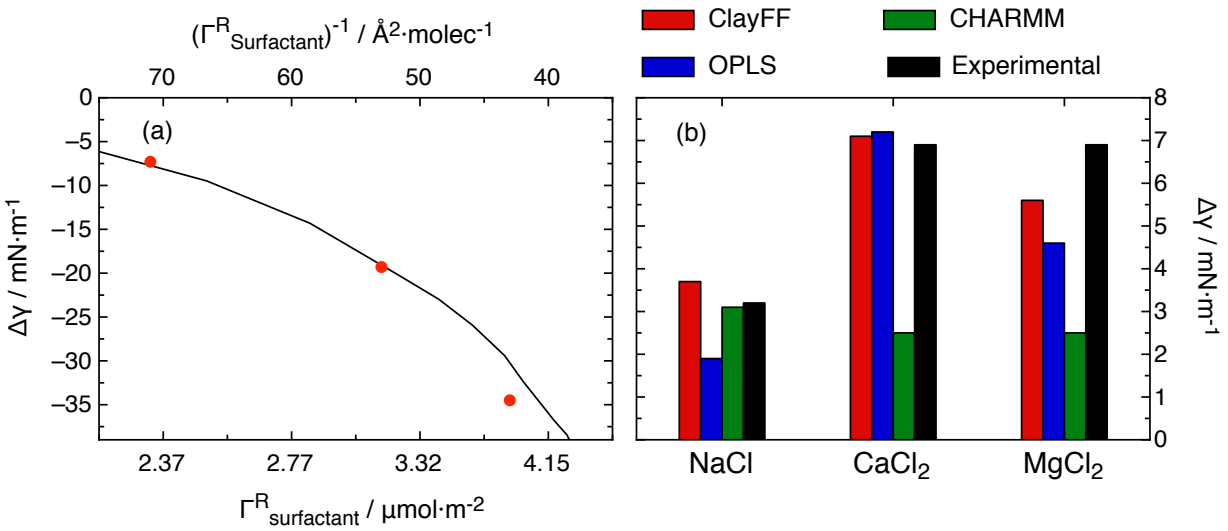

Figure 5.5. (a) Calculated water surface pressure variation as a function of the surfactant interfacial excess (red dots) at 300 K in comparison to the smoothed experimental measurements (black line) of Lu *et al.*[55] (b) Dodecane/water IFT increase with 2.0 mol·kg^{-1} NaCl, $CaCl_2$ and $MgCl_2$ concentration with the three non-polarizable electrolyte force fields tested in this thesis at 300 K and 1 atm. The results are compared with the experimental results of Lima *et al.*,[38] at the same conditions.

allows to simulate a relatively large system, and to reproduce better than any other three-point model the dodecane/water IFT (*i.e.*, γ_{TIP3P} = 50.0 mN·m^{-1}, while the experimental results are 51.0 mN·m^{-1} and 52.3 mN·m^{-1}, all at 300 K and 1 atm [49,50]).

Finally, electrolytes are very polar compounds with strong coulombic interactions, which means that many of its properties depend on the electronic distribution around the ions. For this reason, their behavior is not easy to simulate with single point charge models, which incited many researchers to develop a large amount of force fields over the last years. To ensure that the obtained results are not subject to the selection of the electrolyte parameters, three different non-polarizable models were used and compared in this part of the thesis: (i) the force field from Smith and Dang (*i.e.,* currently implemented in ClayFF)[58], (ii) the force field from Åqvist (*i.e.,* used in OPLS) and the force field of Beglov and Roux (*i.e.,* compiled in CHARMM)[60]. Finally, all crossed interactions have been calculated with the standard Lorentz-Berthelot mixing rules.[61] The cutoff range for intermolecular interactions has been selected as 14 Å and the truncation error in the LJ potential has been coped with an analytic tail correction (eq. 2.52),[62] whereas the long-range Coulomb potential has been treated with the PPPM method.[63]

To evaluate the difference between the three force fields in reproducing the usual linear increase of the oil/water IFT either with NaCl, $CaCl_2$ and $MgCl_2$,[34,38] three different systems were modeled, each with a single salt at a concentration of 2.0 mol·kg^{-1}. The results with the three force fields are compiled in Figure 5.5b, where it can be seen that even though these force fields are not

specifically fitted to reproduce the oil/water IFT variation with salinity concentration, the qualitative behavior is adequately captured by the three of them. However, in average ClayFF seems to more accurately reproduce the IFT increase than OPLS or CHARMM. Specifically, OPLS is slightly underestimating the dodecane/water/NaCl IFT increase effect but it reasonably reproduces the behavior for divalent ions, whereas CHARMM yields a good value for the dodecane/water/NaCl IFT but significantly underestimates the IFT increase produced by divalent ions.

In the following sections, all of the salt/surfactant interactions have been calculated using the three abovementioned force fields obtaining qualitatively the same results, but with differences equivalent to the trends observed in the dodecane/water/salt IFTs (*i.e.,* any effect shown by NaCl is weaker when modeled with OPLS than with the other force fields, as well as the effects on divalent salts are weaker when modeled with CHARMM than with the other force fields). For this reason, many data shown in the following sections correspond only to ClayFF force field and the rest of information calculated with OPLS or CHARMM has been omitted to simplify the discussion.

5.2.1 Determination of the IFT Cooperative Reduction

After the force field validation and evaluation, IFT calculations of oil/water/salt/surfactant systems were conducted to find the optimum salinity concentration capable of magnifying the IFT reduction due to salt/surfactant synergistic effect. To contextualize, some of abovementioned experimental salt/surfactant studies showed that higher salinity concentrations may enhance the static IFT reduction effect, sometimes even up to 2.0 $mol \cdot kg^{-1}$.[26,30–32] However, there is usually a concentration limit where the cooperative effect is lost,[64] which defines the optimum salinity concentration for the salt/surfactant synergistic effect.

To find the optimum salinity for the modeled oil/water/surfactant systems, four different NaCl concentrations were used to explore (i) a reference system without salinity (*i.e.,* 0 $mol \cdot kg^{-1}$), (ii) a low salinity (*i.e.,* 0.5 $mol \cdot kg^{-1}$), (iii) an intermediate salinity (2.0 $mol \cdot kg^{-1}$) and (iv) a high salinity environment (6.0 $mol \cdot kg^{-1}$). To reduce the number of calculations of this preliminary screening, only the ramified surfactant was used along with ClayFF for being the force field that better reproduced the $\Delta\gamma$ values of oil/water/salt systems. In absence of salt (Table 5.1), the surfactant occupies the oil/water interface throughout the whole simulation time (*i.e.* with the polar heads facing the water phase and the non-polar tails oriented towards the dodecane phase), which reduces the IFT from 50.0 $mN \cdot m^{-1}$ to 39.0 $mN \cdot m^{-1}$. After the addition of NaCl, the IFT is not increased

Table 5.1. Equilibrium dodecane/water/surfactant/NaCl IFT at different NaCl concentrations, 300 K and 1 atm.

Surfactant	$\gamma_{No\ Salt}$ / mN·m^{-1}	0.5 mol·kg^{-1} / mN·m^{-1}	2.0 mol·kg^{-1} / mN·m^{-1}	6.0 mol·kg^{-1} / mN·m^{-1}
$(C_6C_5)CE_3$	39.0	39.3 (0.3)	35.5 (-3.5)	41.4 (2.4)

equivalently to the system without surfactant (*i.e.,* approximately 1.5 mN·m^{-1} per 1.0 mol·kg^{-1} of NaCl). This implies that all of these interfaces are showing a synergistic effect, but some of them are too weak to exhibit an absolute IFT reduction. Specifically, the salt/surfactant synergy is very weak at low and high salinities (*i.e.,* the IFT is not reduced in either condition) and relatively strong at 2.0 mol·kg^{-1} of NaCl for the modeled system, achieving even negative $\Delta\gamma$ values. This result implies that the optimum salinity concentration that maximizes the salt/surfactant synergistic effect should be around 2.0 mol·kg^{-1} of salt, which has been selected for the rest of the work.

Following the same procedure, the oil/water IFT of all systems simulated in this part of the thesis have been calculated and compiled in Table 5.2, either without surfactant, with the linear surfactant (*i.e.,* $C_{12}E_3$) or the ramified surfactant (*i.e.,* $(C_6C_5)CE_3$) and all the electrolytes/force field combinations. In absence of surfactant the addition of any salt increases the oil/water IFT regardless of the force field. However, when modeling the electrolytes with ClayFF, NaCl/surfactant interactions seem to be strong enough to be capable of reducing the oil/water IFT instead (*i.e.,* $\Delta\gamma_{\mathrm{NaCl}}$ = -0.3 mN·m^{-1} and $\Delta\gamma_{\mathrm{NaCl}}$ = -3.5 mN·m^{-1} for the linear and ramified surfactant, respectively), whereas the divalent salts/surfactant interactions are not relevant enough to achieve a significant IFT reduction. The same qualitative conclusions are drawn from the CHARMM results, where NaCl/surfactant interactions exhibit zero or negative $\Delta\gamma$ values (*i.e.,* $\Delta\gamma_{\mathrm{NaCl}}$ = 0.1 mN·m^{-1} and $\Delta\gamma_{\mathrm{NaCl}}$ = -2.1 mN·m^{-1} for the linear and ramified surfactant, respectively), while divalent ions do not exhibit negative $\Delta\gamma$ values. On the other hand, when the OPLS parameters are used, the NaCl/surfactant interactions are weaker than with the other force fields and the IFT reduction does not occur (*i.e.,* $\Delta\gamma_{\mathrm{NaCl}}$ = 1.9 mN·m^{-1} and $\Delta\gamma_{\mathrm{NaCl}}$ = 1.0 mN·m^{-1} for the linear and ramified surfactant, respectively). Finally, the cooperative interactions of the salt with the ramified surfactant seem stronger than with the linear surfactant, ranking the $\Delta\gamma$ values in the order of $\Delta\gamma_{\mathrm{ramified}} < \Delta\gamma_{\mathrm{linear}} < \Delta\gamma_{\mathrm{no\ surfactant}}$.

To assess the impact of the water model on the obtained results, some additional calculations have been carried using the four-point TIP4P/Ew model instead of the three-point TIP3P. For this test, the linear surfactant (*i.e.,* $C_{12}E_3$) has been selected along with the ClayFF parameters. Before adding any salt (*i.e.,* only in the oil/water/surfactant system) the obtained IFT is 40.0 mN·m^{-1}, which is almost equivalent to the 39.0 mN·m^{-1} predicted with TIP3P. However, when adding either

Table 5.2. Equilibrium IFT results for the dodecane/water/salt systems using the three different force fields for electrolytes at 2.0 mol·kg^{-1} and the two surfactants. The values in parentheses correspond to $\Delta\gamma$ with respect the value without salt. All results correspond to 300 K and 1 atm.

	Additives	$\gamma_{No\ Salt}$ / mN·m^{-1}	γ_{NaCl} / mN·m^{-1}	γ_{CaCl_2} / mN·m^{-1}	γ_{MgCl_2} / mN·m^{-1}
ClayFF	Without surfactant	50.0	53.7 (3.7)	57.1 (7.1)	55.6 (5.6)
	$C_{12}E_3$	39.0	38.7 (-0.3)	45.4 (6.4)	43.4 (4.4)
	$(C_6C_5)CE_3$	39.0	35.5 (-3.5)	43.6 (4.6)	43.7 (4.7)
OPLS	Without surfactant	50.0	51.9 (1.9)	57.2 (7.2)	54.6 (4.6)
	$C_{12}E_3$	39.0	40.9 (1.9)	43.1 (4.1)	44.0 (5.0)
	$(C_6C_5)CE_3$	39.0	40.0 (1.0)	42.4 (3.4)	41.7 (2.7)
CHARMM	Without surfactant	50.0	53.1 (3.1)	52.5 (2.5)	52.5 (2.5)
	$C_{12}E_3$	39.0	39.1 (0.1)	43.0 (4.0)	41.7 (2.7)
	$(C_6C_5)CE_3$	39.0	36.9 (-2.1)	41.4 (2.4)	41.0 (2.0)

NaCl, $CaCl_2$ or $MgCl_2$ the IFT values dropped to 35.7 mN·m^{-1}, 38.0 mN·m^{-1} and 38.6 mN·m^{-1}, respectively. The results obtained with TIP4P/Ew propose stronger salt/surfactant interactions than with respect TIP3P in the form of IFT reductions (*i.e.,* $\Delta\gamma_{NaCl}$ = -4.3 mN·m^{-1}, $\Delta\gamma_{CaCl_2}$ = -2.0 mN·m^{-1} and $\Delta\gamma_{MgCl_2}$ = -1.4 mN·m^{-1}). Even though the IFT is reduced by the three salts when using TIP4P/Ew, the qualitative effects among the three salts are still equivalent to the results compiled in Table 5.2 (*i.e.,* $\Delta\gamma_{NaCl} > \Delta\gamma_{CaCl_2} > \Delta\gamma_{MgCl_2}$). To summarize, regardless of the water or salt force fields selected, the strongest salt/surfactant effect is due to NaCl, followed by $CaCl_2$ and finally $MgCl_2$, which has the weakest effect of the three salts. For this reason, the TIP3P water model has been ultimately chosen for its computational efficiency and its adequate qualitative description of the oil/water/salt/surfactant interface.

The IFT reduction found in these simulations is relatively weak, when compared to the needed IFTs for efficient cEOR. This might be due to several factors such as the selection of the salt/surfactant combination or concentrations as well as other mechanisms that are not possible in the simulation setup (*i.e.,* the diffusion of additional surfactant molecules to the interface, as previously explained). Even with these limitations, the obtained results are still comparable to some of the experimental works that measure the oil/water IFT in presence of salts and surfactants. Al-Sahhaf *et al.,*[21] studied the addition of electrolytes to systems with cationic and anionic surfactants finding IFT reductions of 2-3 mN·m^{-1}, or Fainerman *et al.,*[24] showed that NaCl reduced the oil/water/surfactant IFT between 5 mN·m^{-1} and 18 mN·m^{-1} depending on surfactant

concentration. This effect was also experimentally seen in the combination of NaCl/non-ionic surfactants at the interface, as described by Bera *et al.,*[22] achieving IFTs lower than 0.1 mN·m^{-1}.

To conclude, the MD simulations carried out in this chapter reveal that increasing the surfactant interfacial concentration by effect of salts is not the only way to reduce the IFT of a system, and other molecular rearrangements, orientations or specific microscopical interactions can also have a significant effect. In that sense, the following sections are focused on unraveling the different factors that involve salts and surfactants to affect the oil/water IFT besides the experimental mechanisms depicted in Figure 5.2.

5.2.2 Perturbation of the Salt in the Presence of Surfactant

According to the Gibbs isotherm equation (eq. 5.1 and eq. 5.2) the IFT of a system is reduced when species accumulate at the interface according to their interfacial excess. This magnitude can be either positive or negative when a compound accumulates at or depletes from the interface. To analyze the interfacial behavior of all species, the interfacial excess of salts and surfactants have been calculated by using eq. 5.3, where the integration limits are chosen at the center of each liquid phase. All surfactant molecules stay at the interface for the whole simulation time, so their densities at any bulk are equal to 0 (*i.e.,* $\bar{\rho}_i^w = \bar{\rho}_i^o = 0$), which makes $\rho_i^{Gibbs}(z) = 0$ and the interfacial excess constant and equal to 1.50 μmol·m^{-2}.

The interfacial excess of salts at the oil/water interface in absence of surfactants is always negative, denoting an interfacial depletion, which justifies the increase of the IFT (Table 5.3). According to the MD simulations, there is a correlation between ions having a more negative interfacial excess and a larger increase of the IFT (*e.g.,* when Na^+ is modeled with ClayFF, CHARMM or OPLS it exhibits Γ_i^R values of -0.83, -0.54 and -0.38 μmol·m^{-2} and $\Delta\gamma$ values of 3.7, 3.1 and 1.9 mN·m^{-1}, respectively). However, this correlation is not maintained when comparing two different salts (*e.g.,* when using ClayFF force field, Ca^{2+} exhibits an interfacial excess of Γ_i^R = -0.45 μmol·m^{-2} and a $\Delta\gamma$ = 7.1 mN·m^{-1}, while Mg^{2+} has a Γ_i^R = -0.92 μmol·m^{-2} and a $\Delta\gamma$ = 5.6 mN·m^{-1}).

Otherwise, when adding salts to a system with surfactants, in general, their interfacial excesses are increased as: no surfactant < $C_{12}E_3$ < $(C_6C_5)CE_3$, which implies that electrolytes are capable of interacting with the surfactant polar head groups to slightly attract them to the interface. Regardless of the force field used, it is seen that the ramified surfactant is more effective in attracting electrolytes, and thus reducing the IFT, than the linear surfactant. Also, the ions of NaCl, who

Table 5.3. Gibbs interfacial excess concentration at the oil/water interface for all electrolytes at 300 K and 1 atm using the three salt force fields.

	Additives	NaCl		$CaCl_2$		$MgCl_2$	
		Γ_{Na}^{w} μmol·m^{-2}	Γ_{Cl}^{w} μmol·m^{-2}	Γ_{Ca}^{w} μmol·m^{-2}	Γ_{Cl}^{w} μmol·m^{-2}	Γ_{Mg}^{w} μmol·m^{-2}	Γ_{Cl}^{w} μmol·m^{-2}
ClayFF	Without surfactant	-0.83	-0.82	-0.45	-0.89	-0.92	-1.83
	$C_{12}E_3$	0.20	0.23	-0.29	-0.57	-0.89	-1.75
	$(C_6C_5)CE_3$	0.22	0.29	-0.19	-0.46	-0.76	-1.51
OPLS	Without surfactant	-0.38	-0.40	-0.85	-1.64	-0.99	-1.99
	$C_{12}E_3$	-0.51	-0.54	-0.17	-0.34	-0.61	-1.12
	$(C_6C_5)CE_3$	-0.31	-0.30	-0.14	-0.29	-0.45	-0.95
CHARMM	Without surfactant	-0.54	-0.51	-0.54	-1.12	-1.07	-2.11
	$C_{12}E_3$	0.25	0.31	-0.58	-1.19	-1.19	-2.40
	$(C_6C_5)CE_3$	0.47	0.44	-0.66	-1.35	-0.93	-1.87

reduced the oil/water IFT, have a positive interfacial excess, suggesting an interfacial accumulation of this species. Divalent salts do not exhibit absolute positive Γ_i^R values, but in the presence of surfactants they are in general more positive than in absence of surfactants. This fact implies that all salts can interact with the surfactant head groups but their attraction ranges in the order of NaCl > $CaCl_2$ > $MgCl_2$.

After finding different interfacial behavior of electrolytes in absence and presence of surfactants, the z-distributions of all studied systems have been calculated focusing on the description given by ClayFF force field. Specifically, Figure 5.6 contains the z-distribution of all species in the simulation cell when adding NaCl for the systems with and without surfactants. The density profiles of the three salts have been computed but only one of them is shown for simplicity. As one can see, either $C_{12}E_3$ and $(C_6C_5)CE_3$ totally accumulate at the interface, and both dodecane and water have very similar behaviors in the three displayed distributions.

On the other hand, before adding the surfactant, all salts deplete from the interface and stay at the water bulk, forming a distribution equivalent to the negative Γ_i^R previously seen in Figure 5.4b, which is consistent to the value calculated at Table 5.3. This effect can also be seen in Figure 5.6, but a magnification of the salt region has been applied and shown in Figure 5.7a for clarity, compiling this time also the systems containing $CaCl_2$ (Figure 5.7d) and $MgCl_2$ (Figure 5.7g). Additionally, from the density profiles it can be seen that all cations and anions are paired and the average local charge at any position of the box is equal to zero. However, the addition of NaCl to an oil/water/non-ionic surfactant system makes the ionic distribution to change significantly. First,

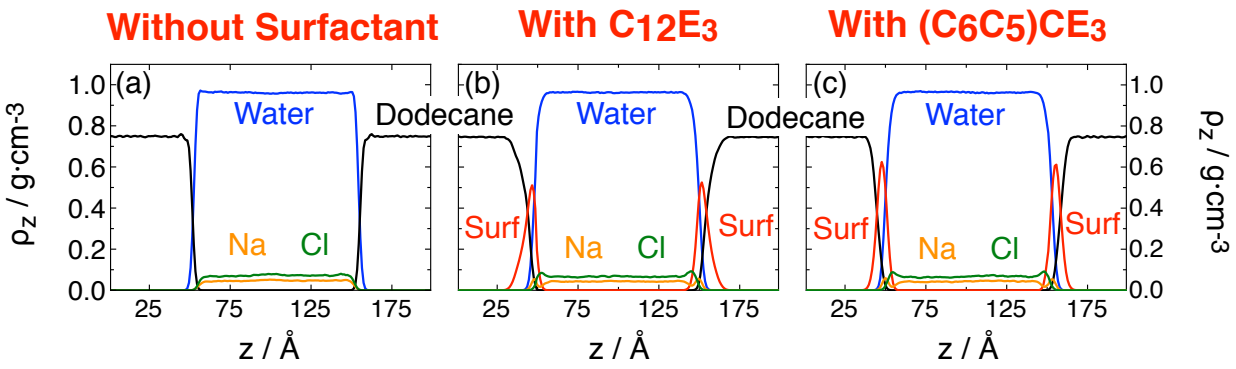

Figure 5.6. Equilibrium z-distributions of all species in the simulation box for the oil/water/NaCl systems (a) without surfactant, (b) with $C_{12}E_3$ and (c) with $(C_6C_5)CE_3$ at 300 K and 1 atm

the Na^+ cation exhibits a positive Γ_i^R according to Table 5.3 and it is reflected with an interfacial accumulation pattern in the z-distributions of both the linear (Figure 5.7b) and the ramified (Figure 5.7c) surfactant. Then a second peak corresponding to Cl^- is also formed, located approximately at 5 Å from the Na^+ accumulation and closer to the water bulk. This suggests that Na^+ seems to be capable of strongly interacting with the newly added surfactant head groups, which favor the migration of this electrolyte towards the interface.

Otherwise, the Cl^-/surfactant interactions seem to be significantly weaker and Cl^- are only driven to the interface by the coulombic attraction of Na^+. To conclude, the different intermolecular interactions between these ions at the interface induce the formation of an electric double layer, which polarizes the interface and affects the resulting oil/water IFT. Regarding divalent cations, the interfacial excess of salts in the presence of surfactant is also increased with respect the system without surfactants, as seen in Table 5.3. However, this increase is not relevant enough to effectively see the formation of the electric double layer, so all distributions (Figure 5.7d-i) keep the same negative Γ_i^R pattern equivalent to the system without surfactant.

The attraction felt by cations due to surfactants also changes their molecular environment. In bulk, water molecules orient its dipoles towards the ions and coordinate with them forming coordination spheres (*i.e.,* also known as solvation spheres). However, the interaction with surfactants bring cations (*i.e.,* specially Na^+) to the interface and its solvation sphere is modified. Specifically, some of the coordination waters of Na^+ are lost and become substituted by Na^+/head interactions. The coordination spheres of cations with water have been evaluated by comparing the water/cation radial distribution functions (RDFs) of electrolytes at the bulk region, and at the interface. To that end, the distance between each cation to the O atom of water (*i.e.,* for being close to the center of mass) have been considered to build the pair-wise distribution.

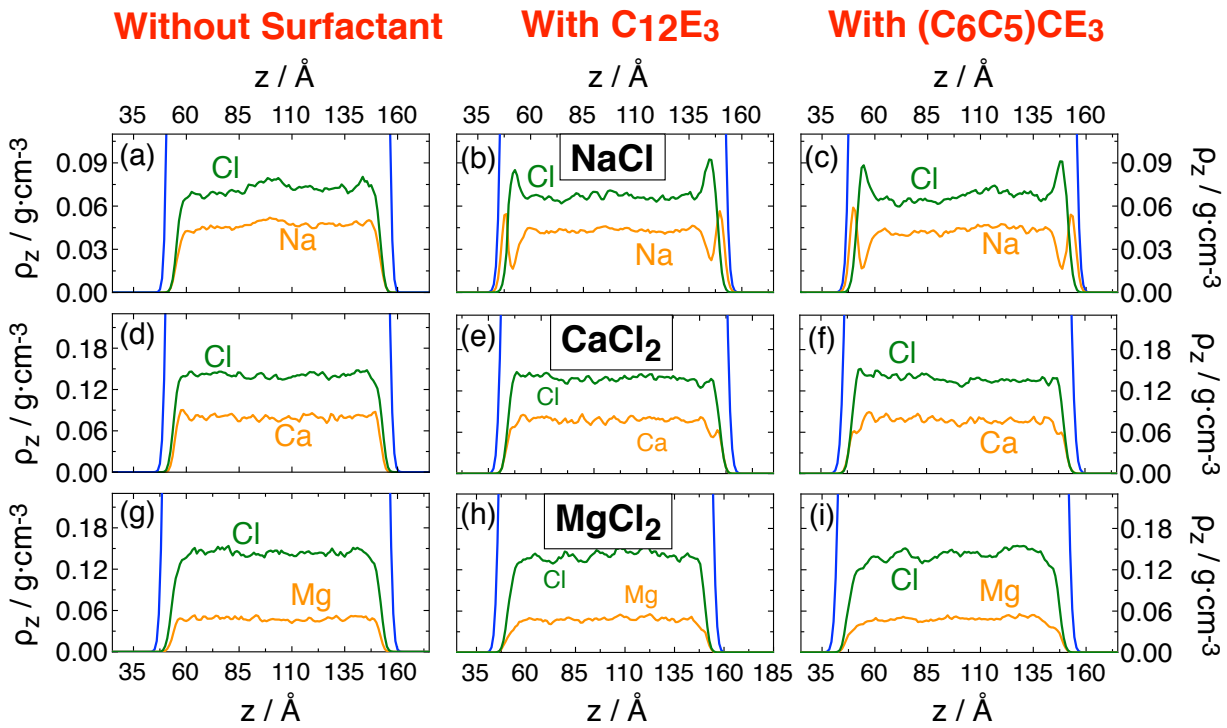

Figure 5.7. Magnification of the salt equilibrium z-distributions at 300 K and 1 atm for (a-c) NaCl, (d-f) $CaCl_2$ and (g-i) $MgCl_2$. The left column represents the systems without surfactant, the center column with $C_{12}E_3$ and the right column with $(C_6C_5)CE_3$.

The interfacial cations have been chosen as all Na^+, Ca^{2+} or Mg^{2+} located at less than 15 Å from the interface, while the rest are assigned as bulk cations. Before adding any surfactant (Figure 5.8a-b) the RDFs of cations do not change whether on bulk or at the interface, denoting that the solvation spheres are not perturbed. However, after adding either $C_{12}E_3$ (Figure 5.8c-d) or $(C_6C_5)CE_3$ (Figure 5.8e-f), the first water/Na^+ peak (*i.e.,* the first solvation sphere) is reduced approximately a 30 % - 40 %. This implies that the Na^+/head interactions are strong enough to break part of the cation solvation sphere. This effect is not seen with Ca^{2+} or Mg^{2+} because the water/cation interactions are significantly stronger than with Na^+ due to their divalent charge, so the simulated surfactant is unable to break them. To illustrate the previous statement with some experimental results, Na^+ has a relatively weak solvation sphere with a hydration enthalpy of 98 kcal·mol^{-1}.[65] On the other hand, the divalent charge strengthens the water/cation interactions up to hydration enthalpies of 337 kcal·mol^{-1} and 459 kcal·mol^{-1} for Ca^{2+} and Mg^{2+}, respectively.[65] The different strength of the three solvation spheres follow the trend of interfacial activity, being Na^+ the most active, followed by Ca^{2+} and finally Mg^{2+}, which is the weakest interacting species.

The obtained results in this section show that the oil/water IFT reduction induced by the salt/surfactant synergistic effect is not only due to the diffusion of additional surfactant molecules onto the interface, but to the accumulation of small ions that were initially depleting from the

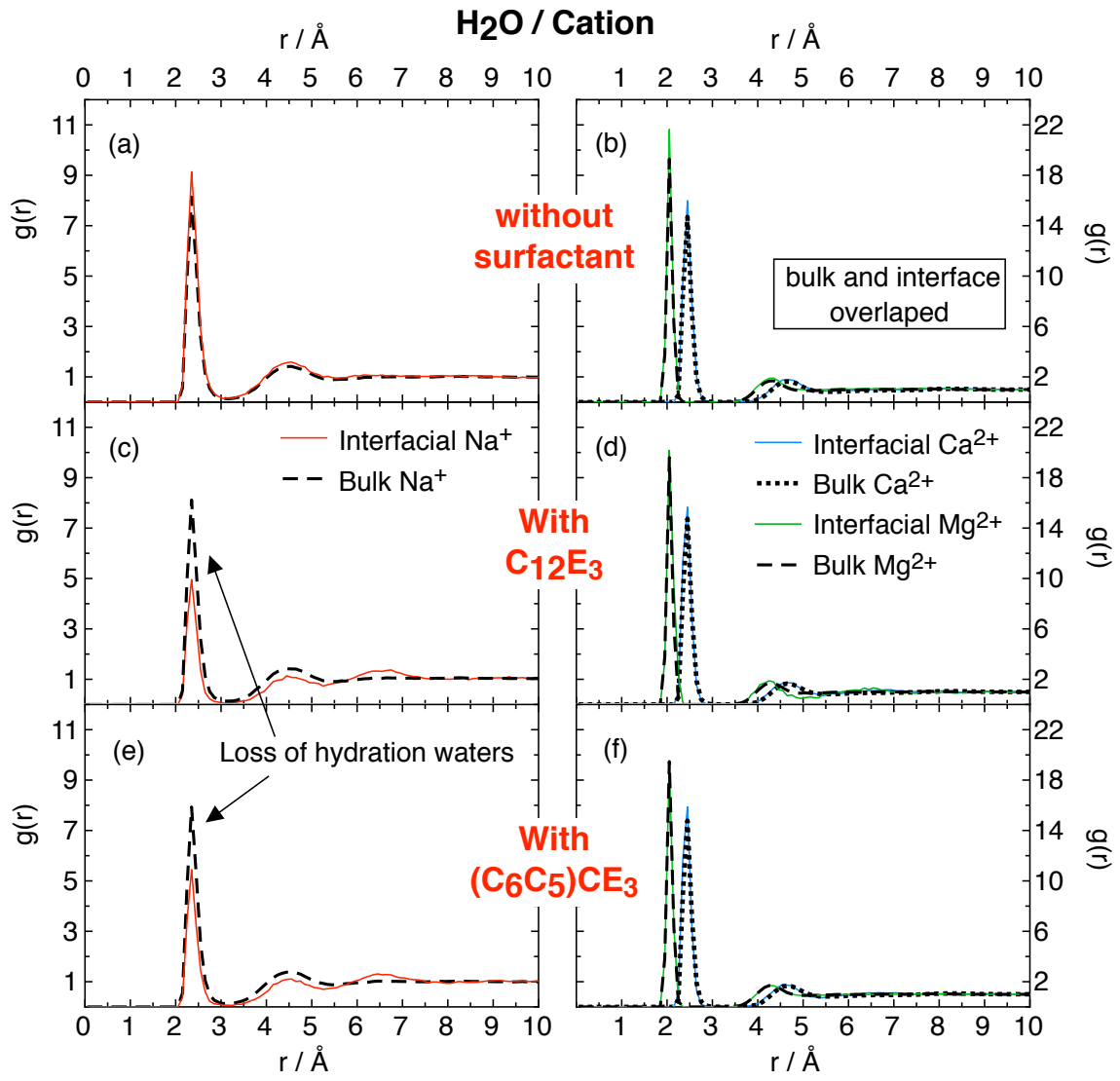

Figure 5.8. Evaluation of cation hydration spheres at 300 K and 1 atm through RDFs for the system without surfactant and the two systems with surfactants. The solid lines correspond to the solvation spheres of cations close to the interface, whereas the dashed/dotted lines refer to the coordination of cations at the bulk.

interface in absence of surfactants. Furthermore, the cations capable of strongly interacting with surfactants polarize the interface via the formation of an electric double layer, which can be affecting the resulting oil/water IFT. Precisely, the only salt that forms consistently an electric double layer is NaCl, which suggests that Na^+ interacts more strongly with the surfactant head groups than the other divalent cations. Particularly, the surfactants are only capable of breaking the solvation spheres of Na^+ (*i.e.,* and not Ca^{2+} or Mg^{2+}), because it has the weakest solvation sphere. And finally, the ramified surfactant is attracting cations more effectively than the linear surfactant, which was previously reflected by a larger IFT reduction and Γ_i^R. This implies that the non-polar tail must be also playing a role in the salt/surfactant synergistic effect.

5.2.3 Perturbation of the Surfactant in the Presence of Salt

The previous section determines how salts may be perturbed by the presence of surfactants and modify their distribution, accumulating at the oil/water interface and forming an electric double layer. However, electrolytes are very polarizing species and can also affect the molecular arrangements of surfactants. In fact, this was already proposed by one of the experimental mechanisms shown in Figure 5.2, which assumed that ions could interact with the polar head groups to screen their electrostatic repulsion.[30,31] In experiments this phenomenon leads to a better interfacial packing of the polar head groups, letting some free space that additional surfactants can occupy. Alternatively, the orientation of molecules at the interface can also affect the IFT, as seen in other works regarding liquid crystals.[66,67] For this reason, to evaluate the effect that electrolytes produce in the surfactant orientation towards the interface the angular distribution of the head and tail groups with respect to the z-axis (*i.e.,* the axis perpendicular to the interface) has been analyzed.

Both surfactants have respectively 12 tail and 9 head UA groups. These molecules are significantly large and have many torsional angles, so they are not exactly linear species. For this reason, the orientational angle of the head and tail groups have been determined separately, as shown in Figure 5.9, to treat smaller moieties and minimize the error in the angular distributions. The angle of all surfactants have been monitored during the last 2 ns of simulation and averaged to create the distribution following the next steps: (i) obtain the coordinates of a surfactant head

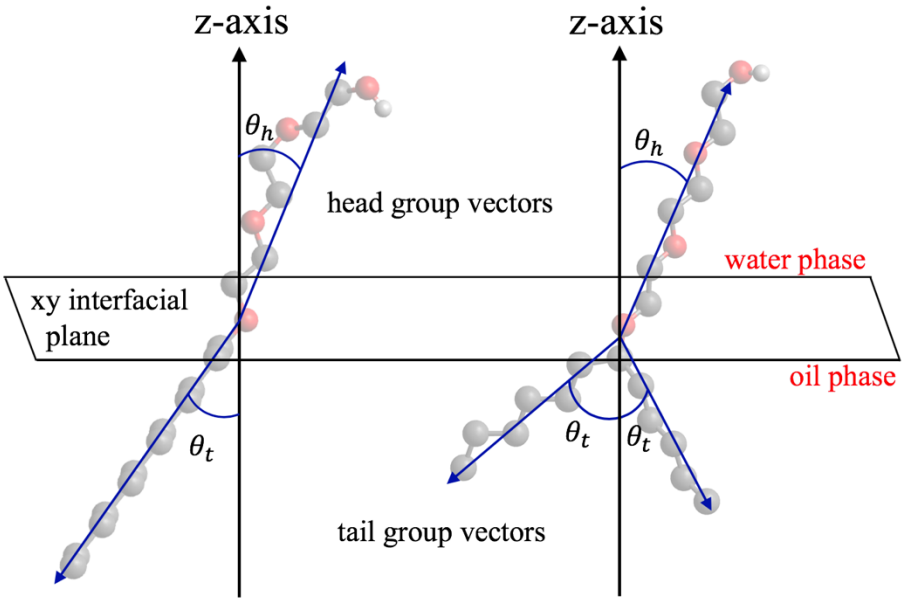

Figure 5.9. Intramolecular reference framework used to obtain the angles between the surfactant head groups and the perpendicular to the interface (θ_h) and the tail groups with the z-axis (θ_t) for both the linear and ramified surfactant.

group, (ii) calculate the vector of the molecular axis that goes in the direction from the first oxygen atom (*i.e.,* the closest to the tail group) to the terminal OH group, (iii) repeat the previous two steps for the tail group to obtain the vector that starts at the carbon atom connected to the first oxygen atom and end at the terminal CH_3, (iv) obtain the desired angles from a dot product with the vector perpendicular to the interface, (v) repeat the process for all surfactants and time steps and (vi) normalize the distribution. As a special case, two different tail groups have been considered for the ramified surfactant (*i.e.,* one for each ramification). Finally, to get information about the conformation of surfactants at the interface, the angle between the head and tail groups within each surfactant has also been computed.

The results obtained for the linear and the ramified surfactant are compiled in Figure 5.10a-c and Figure 5.10d-f, respectively. In absence of salinity, both surfactants have a higher probability to orient their head groups (θ_h) around 70º - 90º with respect to the perpendicular axis (*i.e.,* almost parallel to the interface), as it can be seen in Figure 5.10a and Figure 5.10d. On the other hand, the tail (θ_t) of $C_{12}E_3$ exhibits a similar uniform random distribution from 40º to 90º, denoting certain freedom of orientation (Figure 5.10b), whereas the tail groups of $(C_5C_6)CE_3$ have a larger probability to be at 70º - 90º with respect to the interface. This means that the shorter tail groups

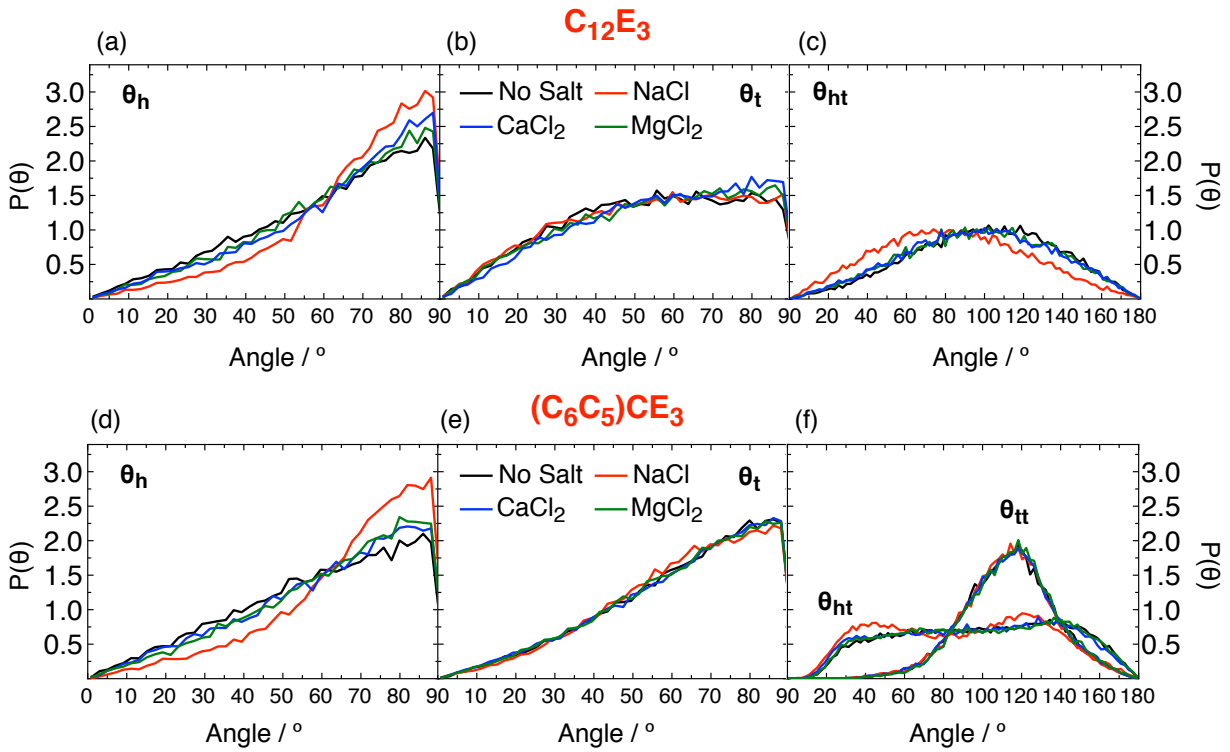

Figure 5.10. Probability angular distributions for the linear (a-c) and the ramified (d-f) surfactant at 300 K and 1 atm in absence and presence of salt. θ_h refers to the head group angle with respect to the interface perpendicular, θ_t is the tail group angle with respect the same perpendicular, θ_{ht} corresponds to the angle between the head and tail groups and θ_{tt} refers to the angle between the two tail groups of the ramified surfactant.

of the ramified surfactant are spreading more through the interface and occupying more area than the single long tail of the linear surfactant. This effect can also be intuited in the z-distributions of Figure 5.6, where the surfactant distribution is wide for $C_{12}E_3$ and narrow for $(C_6C_5)CE_3$.

Otherwise, the angular distribution of surfactant heads with tail groups (θ_{ht}) for $C_{12}E_3$ exhibit a symmetrical pattern with a maximum probability between 60º and 120º (Figure 5.10c), where 180º refers to completely linear. This result suggests that the two moieties of the surfactant are significantly bent among each other. Otherwise, the ramified surfactant exhibits a wider distribution than the linear surfactant, having the highest probabilities between 30º and 150º approximately (Figure 5.10f). Finally, the tail/tail (θ_{tt}) angular distribution of $(C_6C_5)CE_3$ forms a clear maximum around 110º - 120º, which is the expected value of 120º observed in any triangular-like molecules similar to the ramified surfactant. All of the angular distributions shown in this thesis are relatively flat because the surfactant concentration employed is very low, which prevents surfactant molecules to be restricted by the presence of other surface-active species and permit them to orient freely at the interface.

After adding salt to the oil/water/surfactant systems, the orientational peak around 70º - 90º of the head groups are increased, while the probability at angles below 50º becomes reduced (Figure 5.10a and Figure 5.10d). These new distributions suggest that electrolytes are capable of interacting with the surfactant head groups to make them become, in average, more planar towards the interface. This effect is observed with the three salts modeled but it is more intense with NaCl, followed by $CaCl_2$ and finally $MgCl_2$, who almost do not change the surfactant orientation. This follows the same trend previously observed in the other calculated properties, such as the IFT reduction the interfacial excess or the z-distributions.

From the data compiled in Figure 5.10b and 5.10e, one can see that the orientation of the tail groups remains totally unchanged, regardless of the surfactant analyzed. However, since θ_h is changing and θ_t is not, the angle between head and tail groups in each surfactant is affected as seen in Figure 5.10c and Figure 5.10f. Specifically, the surfactants become in average more bent due to the presence of interfacial ions.

If surfactants become more planar towards the interface, they occupy more interfacial area, which separates more effectively the oil phase from the water phase. To confirm that hypothesis, the average distance between oil and water phases have been evaluated through the dodecane/water RDF, and how it changes by addition of salt. All CHx groups in dodecane have been considered to build the pair-wise RDF against the O atoms of water. Additionally, all dodecane or water molecules that are further than 10 Å from the interface have not been considered, to focus only on the effects around the interfacial region. The results obtained show that in absence of surfactant,

the dodecane/water average distance is not modified regardless of the salt used (Figure 5.11a). However, when either the linear (Figure 5.11b) or the ramified (Figure 5.11c) surfactants are present, the addition of NaCl generates a lower dodecane/water RDF. This suggests that both phases are slightly more separated due to the higher planarity of surfactants, confirming the previous hypothesis. Finally, since the $CaCl_2$ is also capable of making the linear surfactants slightly more planar towards the interface (Figure 5.10a), it is also promoting the separation of the oil/water phases.

Besides the change of orientation, surfactants also exhibit a modification of molecular environment due to the presence of the interfacial salt. This modifies only the coordination spheres of the surfactant head groups and not the tail groups, who are in contact with the dodecane phase and are relatively far away from water. The effects are comparable to surfactant orientations, where the head groups could be perturbed by salinity, but the tail distributions remained unchanged. Additional RDFs of surfactant head groups with water have been built to evaluate the ability of cations to affect the solvation sphere of surfactants. The three O atoms of the head group have been selected to build the pair-wise distribution against the water oxygen.

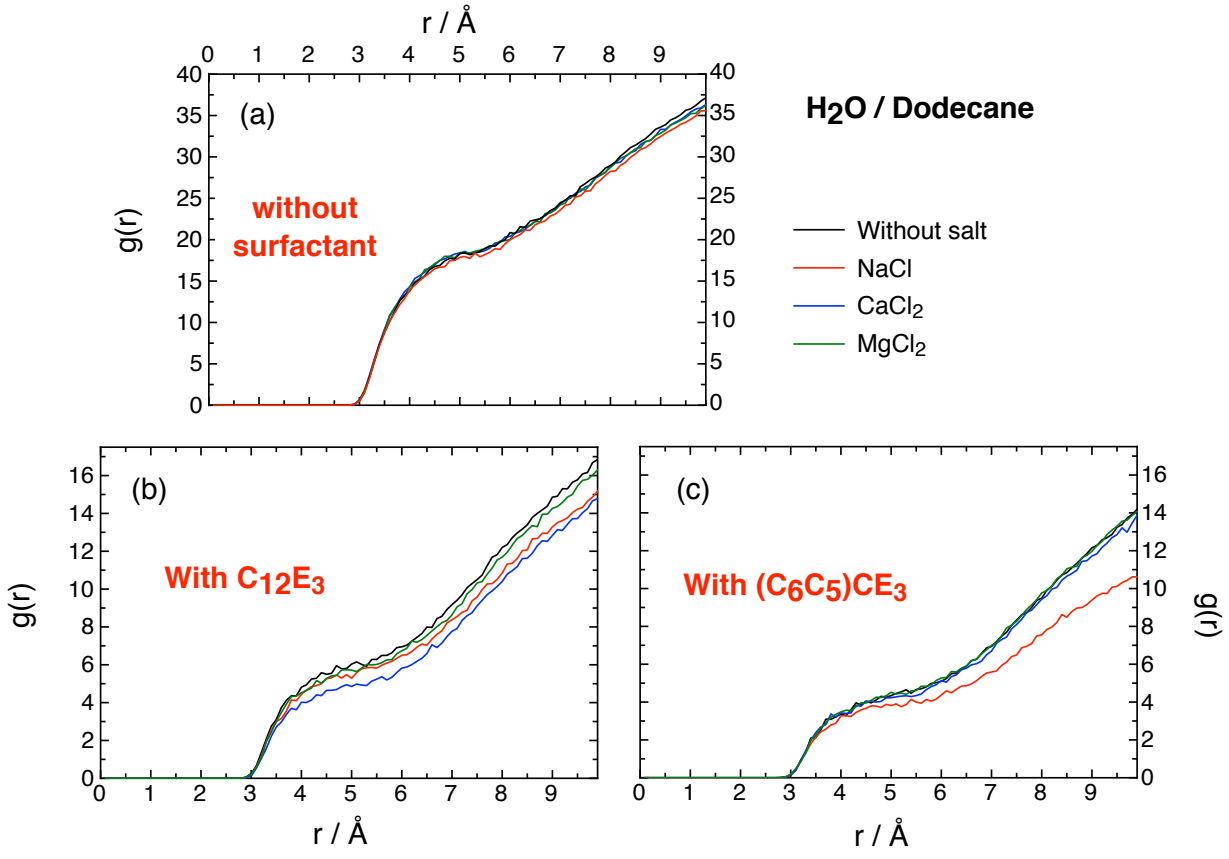

Figure 5.11. Dodecane/water RDFs at 300 K and 1 atm for species close to the interface in systems without surfactants or the two systems with surfactants.

The results compiled in Figure 5.12a-b reveal that in absence of salt, water molecules orient towards both surfactant head groups at a distance close to 2.75 Å, denoted by the large first peaks of the head/water RDF. The addition of $CaCl_2$ or $MgCl_2$ produce weak perturbations on the surfactant solvation sphere, but NaCl makes the head/water peak to almost completely disappear, which means that this salt is capable of significantly reducing the surfactant/water interactions. In fact, all of the missing water molecules close to the head groups have been substituted by Na^+ cations as suggested by the large Na^+/head peak in Figure 5.12c-d. Otherwise, the less interacting

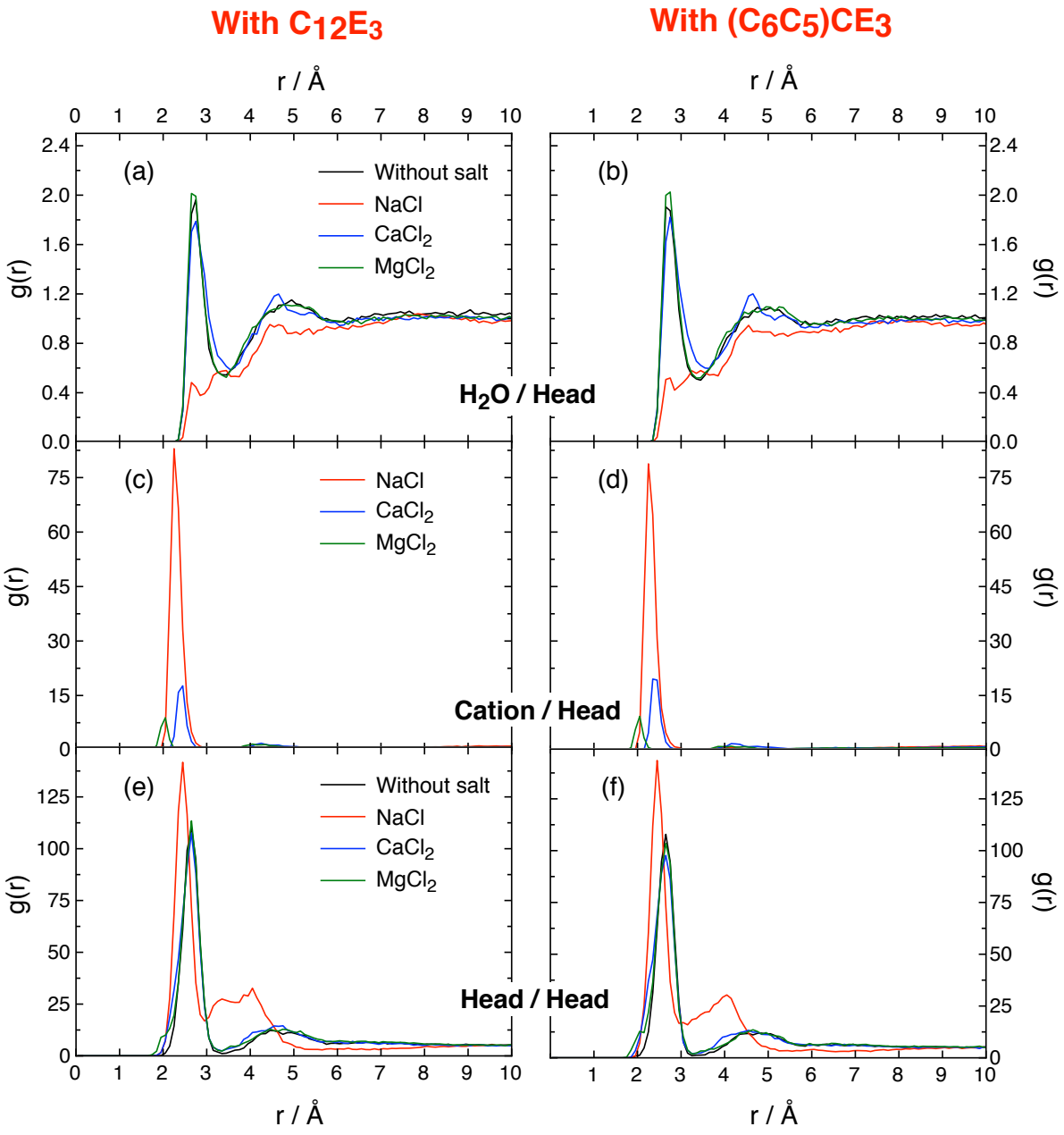

Figure 5.12. RDFs between surfactant head groups and different species present at the interface at 300 K and 1 atm, for the linear $C_{12}E_3$ and the ramified $(C_5C_6)CE_3$ surfactants, in absence and presence of salt.

species (*i.e.,* Ca^{2+} and Mg^{2+}) only exhibit low peaks at their respective cation/head equilibrium distances, which are not enough to substitute the water solvation sphere of the head groups.

Finally, salinity also affects the average distance between surfactant head groups, as proposed by the mechanisms showed in Figure 5.2.[30,31] This is evidenced in Figure 5.12e-f, where the RDF between surfactant head groups is shown (*i.e.,* the head/head RDF). The obtained results reveal that these particular surfactants arrange themselves at 2.65 Å among each other in absence of surfactant. Similarly to other properties, divalent cations do not affect this arrangement but NaCl is capable of displacing the first and the second peaks of the RDF to lower distances. This new distribution can be related to the enhanced packing that allows additional surfactant molecules to migrate to the interface in experimental setups.

The results of this section confirm that the surfactant head groups can interact with electrolytes and change their interfacial arrangement, as proposed by the experimentally derived salt/surfactant mechanisms. Specifically, this interfacial modification is promoted by the coordination of the surfactant head groups with cations, both of them after losing their solvation spheres to bind more tightly. However, aside from the tighter packing of the head groups, surfactants also tend to become, in average, more planar towards the interface. The new orientation allows the surfactants to occupy the interface more effectively and thus reducing the amount of dodecane molecules close to water and vice versa, which may also help in producing a lower IFT. Finally, the ramified surfactant is more effective than the linear surfactant in reducing the oil/water IFT, probably because its shorter ramified tail is fully located at the interface, thus occupying more interfacial area than the linear surfactant.

5.3 Summary and Conclusions

The work compiled in Chapter 5 allows to achieve two main conclusions. First, it helps to validate from a molecular point of view some of the experimentally proposed mechanisms for the salt/surfactant synergistic effects to reduce the oil/water static IFT. To that end, MD simulations were conducted adding salts (*i.e.,* NaCl, $CaCl_2$ and $MgCl_2$) and surfactants (*i.e.,* the linear $C_{12}E_3$ and the ramified $(C_5C_6)CE_3$) onto a dodecane/water system to analyse how surfactants become perturbed by salts. However, the experimental setup contains a reservoir of surfactant molecules dissolved in the oil/water bulks, while the simulations does not. For this reason, aside from validating mechanisms, alternative molecular arrangements capable of reducing the oil/water IFT were also identified. Altogether, the unveiled interactions in Chapter 5 allow to better understand all the effects with respect the cooperative interaction of salts and surfactants at interfaces.

In summary, the results obtained showed that surfactant head groups can interact with cations (*i.e.,* especially with Na^+) to partially break their hydration sphere. If the salt/surfactant interaction is strong enough, the cation can migrate to the interface and bind to the surfactant head groups by substituting almost all of their solvation waters. The new positive charges accumulated at the interface tend to attract the negatively charged anions, but as they do not interact favourably with the non-ionic head groups, they stay further away than cations. This behaviour effectively produces an electric double layer that polarizes the interface. After the migration of ions to the interface, the surfactants rearrange themselves through two different movements: (i) the surfactant head groups pack slightly tighter and (ii) they become, in average, more planar towards the interface. Overall, each surfactant molecule tends to occupy more interfacial area after the reorganization, which increase the effectivity of this species in covering the oil/water interface and reduce the IFT.

Regarding the three salts, Na^+ seems to be the electrolyte capable of interacting more strongly with the surfactant head groups because it has the weakest solvation sphere. For this reason, it can bind to the surfactants and promote the phenomena previously described. The Ca^{2+} and Mg^{2+} are also capable of interacting with the head groups but since their coulombic charge is screened by the water molecules of their solvation sphere the binding is significantly weaker and the IFT is not reduced as much as with Na^+. Finally, the ramified surfactant has two shorter tail groups whereas the $C_{12}E_3$ only has a single long tail. According to the obtained results, the tails of the ramified surfactant seem to be more capable of occupying the interface, and thus producing a stronger salt/surfactant synergistic effect than the linear surfactant.

Although this work has a significant value in unveiling the mechanisms of the salt/surfactant synergistic effect, the final IFT is only reduced by less than 5 $mN \cdot m^{-1}$. However, the strength of the salt/surfactant synergistic effect depends on the kinds of species used as well as their concentration. This means that other systems, or even the same system under different salt/surfactant concentrations might yield different IFT reductions. Even after all of the described effects in the studied system, the oil/water interface is unable to achieve the highly needed ultralow IFT to directly apply it to cEOR. However, it is expected that the knowledge obtained from this work can be used to better understand some of the mechanisms occurring at pore conditions and help to design optimal conditions to take advantage of the salt/surfactant synergistic effect.

5.4 References

1 T. F. Tadros, *An Introduction to Surfactants*, Walter de Gruyter, Berlin, 2014.

2 C. Tanford, *The Hydrophobic Effect*, John-Wiley, New York, 1980.

3 B. Jönsson, B. Lindmann, K. Holmberg and B. Kronberg, *Surfactants and Polymers in Aqueous Solution*, John Wiley & Sons, Chichester, 1998.

4 J. H. Clint, *Surfactant Aggregation*, Blackie & Son, Glasgow, 1992.

5 M. J. Rosen, *Surfactants and Interfacial Phenomena*, John Wiley & Sons, New York, 1989.

6 C. Negin, S. Ali and Q. Xie, Most Common Surfactants Employed in Chemical Enhanced Oil Recovery, *Petroleum*, 2017, **3**, 197–211.

7 B. R. Buestein and C. L. Hiliton, *Amphoteric Surfactants*, Marcel Dekker, New York, 1982.

8 W. von Rybinski, B. Guckenbiehl and H. Tesmann, Influence of Co-Surfactants on Microemulsions with Alkyl Polyglycosides, *Colloid. Surface. A*, 1998, **142**, 333–342.

9 Lu, J., PhD Dissertation, University of Texas, 2014.

10 Z. Jeirani, B. Mohamed Jan, B. Si Ali, I. M. Noor, C. H. See and W. Saphanuchart, Formulation, Optimization and Application of Triglyceride Microemulsion in Enhanced Oil Recovery, *Ind. Crops Prod.*, 2013, **43**, 6–14.

11 N. Morrow and J. Buckley, Improved Oil Recovery by Low-Salinity Waterflooding, *J. Pet. Technol.*, 2011, **63**, 106–112.

12 P. P. Jadhunandan, PhD Dissertation, New Mexico Institute of Mining & Technology, 1990.

13 A. E. Silva, G. Barratt, M. Chéron and E. S. T. Egito, Development of Oil-in-Water Microemulsions for the Oral Delivery of Amphotericin B, *Int. J. Pharm.*, 2013, **454**, 641–648.

14 H. Francke and M. Thorade, Density and Viscosity of Brine: An Overview from a Process Engineers Perspective, *Chem. Erde - Geochem.*, 2010, **70**, 23–32.

15 O. Ozdemir, S. I. Karakashev, A. V. Nguyen and J. D. Miller, Adsorption and Surface Tension Analysis of Concentrated Alkali Halide Brine Solutions, *Miner. Eng.*, 2009, **22**, 263–271.

16 A. A. Zavitsas, Properties of Water Solutions of Electrolytes and Nonelectrolytes, *J. Phys. Chem. B*, 2001, **105**, 7805–7817.

17 H. Aghdastinat, S. Javadian, A. Tehrani-Bagha and H. Gharibi, Spontaneous Formation of Nanocubic Particles and Spherical Vesicles in Catanionic Mixtures of Ester-Containing Gemini Surfactants and Sodium Dodecyl Sulfate in the Presence of Electrolyte, *J. Phys. Chem. B*, 2014, **118**, 3063–3073.

18 P. Mukerjee and C. C. Chan, Effects of High Salt Concentrations on the Micellization of Octyl Glucoside: Salting-Out of Monomers and Electrolyte Effects on the Micelle−Water Interfacial Tension, *Langmuir*, 2002, **18**, 5375–5381.

19 V. Seredyuk, E. Alami, M. Nydén, K. Holmberg, A. V. Peresypkin and F. M. Menger, Adsorption of Zwitterionic Gemini Surfactants at the Air–Water and Solid–Water Interfaces, *Colloid. Surface. A*, 2002, **203**, 245–258.

20 A. M. Howe, A. Clarke, J. Mitchell, J. Staniland, L. Hawkes and C. Whalan, Visualising Surfactant Enhanced Oil Recovery, *Colloid. Surface. A*, 2015, **480**, 449–461.

21 T. Al-Sahhaf, A. Elkamel, A. S. Ahmed and A. R. Khan, The Influence of Temperature, Pressure, Salinity, and Surfactant Concentration on the Interfacial Tension of the N-Octane-Water System, *Chem. Eng. Commun.*, 2005, **192**, 667–684.

22 A. Bera, A. Mandal and B. B. Guha, Synergistic Effect of Surfactant and Salt Mixture on Interfacial Tension Reduction between Crude Oil and Water in Enhanced Oil Recovery, *J. Chem. Eng. Data*, 2014, **59**, 89–96.

23 X. Chen, S. S. Adkins, Q. P. Nguyen, A. W. Sanders and K. P. Johnston, Interfacial Tension and the Behavior of Microemulsions and Macroemulsions of Water and Carbon Dioxide with a Branched Hydrocarbon Nonionic Surfactant, *J. Supercrit. Fluids*, 2010, **55**, 712–723.

24 V. B. Fainerman, S. V. Lylyk, E. V. Aksenenko, N. M. Kovalchuk, V. I. Kovalchuk, J. T. Petkov and R. Miller, Effect of Water Hardness on Surface Tension and Dilational Visco-Elasticity of Sodium Dodecyl Sulphate Solutions, *J. Colloid Interface Sci.*, 2012, **377**, 1–6.

25 A. Ge, Q. Peng, H. Wu, H. Liu, Y. Tong, T. Nishida, N. Yoshida, K. Suzuki, T. Sakai, M. Osawa and S. Ye, Effect of Functional Group on the Monolayer Structures of Biodegradable Quaternary Ammonium Surfactants, *Langmuir*, 2013, **29**, 14411–14420.

26 T. Jiao, X. Liu and J. Niu, Effects of Sodium Chloride on Adsorption at Different Interfaces and Aggregation Behaviors of Disulfonate Gemini Surfactants, *RSC Adv.*, 2016, **6**, 13881–13889.

27 A. M. Johannessen and K. Spildo, Enhanced Oil Recovery (EOR) by Combining Surfactant with Low Salinity Injection, *Energ. Fuel.*, 2013, **27**, 5738–5749.

28 P. Koelsch and H. Motschmann, Varying the Counterions at a Charged Interface, *Langmuir*, 2005, **21**, 3436–3442.

29 S. Kumar and A. Mandal, Studies on Interfacial Behavior and Wettability Change Phenomena by Ionic and Nonionic Surfactants in Presence of Alkalis and Salt for Enhanced Oil Recovery, *Appl. Surf. Sci.*, 2016, **372**, 42–51.

30 Z. Liu, Z. Li, X. Song, J. Zhang, L. Zhang, L. Zhang and S. Zhao, Dynamic Interfacial Tensions

of Binary Nonionic–Anionic and Nonionic Surfactant Mixtures at Water–Alkane Interfaces, *Fuel*, 2014, **135**, 91–98.

31 Z. Liu, L. Zhang, X. Cao, X. Song, Z. Jin, L. Zhang and S. Zhao, Effect of Electrolytes on Interfacial Tensions of Alkyl Ether Carboxylate Solutions, *Energ. Fuel.*, 2013, **27**, 3122–3129.

32 K. Staszak, D. Wieczorek and K. Michocka, Effect of Sodium Chloride on the Surface and Wetting Properties of Aqueous Solutions of Cocamidopropyl Betaine, *J. Surfactants Deterg.*, 2015, **18**, 321–328.

33 A. Witthayapanyanon, E. J. Acosta, J. H. Harwell and D. A. Sabatini, Formulation of Ultralow Interfacial Tension Systems Using Extended Surfactants, *J. Surfactants Deterg.*, 2006, **9**, 331–339.

34 R. Aveyard and S. M. Saleem, Interfacial Tensions at Alkane-Aqueous Electrolyte Interfaces, *J. Chem. Soc., Faraday Trans. 1*, 1976, **72**, 1609–1617.

35 D. Bhatt, J. Newman and C. J. Radke, Molecular Dynamics Simulations of Surface Tensions of Aqueous Electrolytic Solutions, *J. Phys. Chem. B*, 2004, **108**, 9077–9084.

36 E. Mayoral and E. Nahmad-Achar, Study of Interfacial Tension Between an Organic Solvent and Aqueous Electrolyte Solutions Using Electrostatic Dissipative Particle Dynamics Simulations, *J. Chem. Phys.*, 2012, **137**, 194701:1–10.

37 P. K. Weissenborn and R. J. Pugh, Surface Tension of Aqueous Solutions of Electrolytes: Relationship with Ion Hydration, Oxygen Solubility, and Bubble Coalescence, *J. Colloid Interface Sci.*, 1996, **184**, 550–563.

38 E. R. A. Lima, B. M. de Melo, L. T. Baptista and M. L. L. Paredes, Specific Ion Effects on the Interfacial Tension of Water/Hydrocarbon Systems, *Braz. J. Chem. Eng.*, 2013, **30**, 55–62.

39 H. Schott, Saturation Adsorption at Interfaces of Surfactant Solutions, *J. Pharm. Sci.*, 1980, **69**, 852–854.

40 Z. Zhao, C. Bi, Z. Li, W. Qiao and L. Cheng, Interfacial Tension Between Crude Oil and Decylmethylnaphthalene Sulfonate Surfactant Alkali-Free Flooding Systems, *Colloid. Surface. A*, 2006, **276**, 186–191.

41 J. W. Gibbs, *The Colected Works of J. W. Gibbs*, Longmans Green, New York, 1931.

42 S. Yuan, Y. Chen and G. Xu, Molecular Dynamics Studies on Octadecylammonium Chloride at the Air/Liquid Interface, *Colloid. Surface. A*, 2006, **280**, 108–115.

43 T. Zhao, G. Xu, S. Yuan, Y. Chen and H. Yan, Molecular Dynamics Study of Alkyl Benzene Sulfonate at Air/Water Interface: Effect of Inorganic Salts, *J. Phys. Chem. B*, 2010, **114**, 5025–5033.

44 C. Yang, W. Lin, Q. Wang, B. Niu and X. He, Inorganic Salts Effect on Adsorption Behavior of

Surfactant AEC at Liquid/Liquid Interface, *Res. J. Appl. Sci. Eng. Technol.*, 2013, **6**, 1424–1427.

45 Q. Xie, Y. Chen, L. You, M. M. Hossain and A. Saeedi, Drivers of Wettability Alteration for Oil/Brine/Kaolinite System: Implications for Hydraulic Fracturing Fluids Uptake in Shale Rocks, *Energies*, 2018, **11**, 1666:1–13.

46 S. Plimpton, Fast Parallel Algorithms for Short-Range Molecular Dynamics, *J. Comput. Phys.*, 1995, **117**, 1–19.

47 J. G. Kirkwood and F. P. Buff, The Statistical Mechanical Theory of Surface Tension, *J. Chem. Phys.*, 2004, **17**, 338–343.

48 J. H. Irving and J. G. Kirkwood, The Statistical Mechanical Theory of Transport Processes. IV. The Equations of Hydrodynamics, *J. Chem. Phys.*, 1950, **18**, 817–829.

49 M. G. Martin and J. I. Siepmann, Transferable Potentials for Phase Equilibria. 1. United-Atom Description of n-Alkanes, *J. Phys. Chem. B*, 1998, **102**, 2569–2577.

50 J. Wang, R. M. Wolf, J. W. Caldwell, P. A. Kollman and D. A. Case, Development and Testing of a General Amber Force Field, *J. Comput. Chem.*, 2004, **25**, 1157–1174.

51 H. J. C. Berendsen, J. R. Grigera and T. P. Straatsma, The Missing Term in Effective Pair Potentials, *J. Phys. Chem.*, 1987, **91**, 6269–6271.

52 W. L. Jorgensen, J. Chandrasekhar, J. D. Madura, R. W. Impey and M. L. Klein, Comparison of Simple Potential Functions for Simulating Liquid Water, *J. Chem. Phys.*, 1983, **79**, 926–935.

53 C. Vega and E. de Miguel, Surface Tension of the Most Popular Models of Water by Using the Test-Area Simulation Method, *J. Chem. Phys.*, 2007, **126**, 154707:1–10.

54 H. W. Horn, W. C. Swope, J. W. Pitera, J. D. Madura, T. J. Dick, G. L. Hura and T. Head-Gordon, Development of an Improved Four-Site Water Model for Biomolecular Simulations: TIP4P-Ew, *J. Chem. Phys.*, 2004, **120**, 9665–9678.

55 J. R. Lu, E. M. Lee, R. K. Thomas, J. Penfold and S. L. Flitsch, Direct Determination by Neutron Reflection of the Structure of Triethylene Glycol Monododecyl Ether Layers at the Air/Water Interface, *Langmuir*, 1993, **9**, 1352–1360.

56 S. Zeppieri, J. Rodríguez and A. L. López de Ramos, Interfacial Tension of Alkane + Water Systems, *J. Chem. Eng. Data*, 2001, **46**, 1086–1088.

57 Z. Hu, S. Ballinger, R. Pelton and E. D. Cranston, Surfactant-Enhanced Cellulose Nanocrystal Pickering Emulsions, *J. Colloid Interface Sci.*, 2015, **439**, 139–148.

58 D. E. Smith and L. X. Dang, Computer Simulations of NaCl Association in Polarizable Water, *J. Chem. Phys.*, 1998, **100**, 3757–3766.

59 J. Åqvist, Ion-Water Interaction Potentials Derived from Free Energy Perturbation Simulations, *J.*

Phys. Chem., 1990, **94**, 8021–8024.

60 D. Beglov and B. Roux, Finite Representation of an Infinite Bulk System: Solvent Boundary Potential for Computer Simulations, *J. Chem. Phys.*, 1998, **100**, 9050–9063.

61 H. A. Lorentz, Ueber die Anwendung des Satzes vom Virial in der Kinetischen Theorie der Gase, *Ann. Phys.*, 1881, **248**, 127–136.

62 H. Sun, COMPASS: An ab Initio Force-Field Optimized for Condensed-Phase Applications Overview with Details on Alkane and Benzene Compounds, *J. Phys. Chem. B*, 1998, **102**, 7338–7364.

63 P. P. Ewald, Die Berechnung Optischer und Elektrostatischer Gitterpotentiale, *Ann. Phys.*, 1921, **369**, 253–287.

64 F. Moeini, A. Hemmati-Sarapardeh, M.-H. Ghazanfari, M. Masihi and S. Ayatollahi, Toward Mechanistic Understanding of Heavy Crude Oil/Brine Interfacial Tension: The Roles of Salinity, Temperature and Pressure, *Fluid Phase Equilibr.*, 2014, **375**, 191–200.

65 D. W. Smith, Ionic Hydration Enthalpies, *J. Chem. Educ.*, 1977, **54**, 540–542.

66 D. Andrienko, Introduction to Liquid Crystals, *J. Mol. Liq.*, 2018, **267**, 520–541.

67 M. Tintaru, R. Moldovan, T. Beica and S. Frunza, Surface Tension of Some Liquid Crystals in the Cyanobiphenyl Series, *Liq. Cryst.*, 2001, **28**, 793–797.

CHAPTER 6

General Conclusions

In this thesis, different models and computational methods were employed to study two different topics of industrial interest: (i) the gas capture and separation via zeolites, MOFs and ILs, which was analyzed extensively throughout Chapter 3, and (ii) the most fundamental interactions between different model oils, water and rocks for oil recovery, which was discussed in Chapter 4. This topic was extended with the interaction of surfactants at the oil/water interface in Chapter 5. Each of the aforementioned chapters contain all the corresponding results and their own conclusions section that present the main ideas to be extracted from it. Therefore, the current chapter intends to present in an ordered and summarized manner the main conclusions extracted from Chapter 3 to Chapter 5.

On the Gas Capture and Separation for Post-Combustion Processes

- Five computational and theoretical techniques were used in this part of the thesis to evaluate the CO_2 capture and separation capacity of different promising technologies. The insights obtained by them and the good comparison with published experimental results show the quality of each approach depending on the information that wants to be obtained. First, the DFT calculations are ideal to evaluate the main gas/material interactions. Second, GCMC simulations allow to predict adsorption isotherms by explicitly modelling a microporous material in contact with an ideal gas reservoir. Third, DFT/DSL model is a good alternative when the force fields needed for GCMC are not available and there is a deep knowledge on the surface behavior. Fourth, soft-SAFT EoS shows to be a reliable technique to predict gas/IL absorption isotherms via vapor/liquid equilibria calculations. Last, COSMO-RS is a promising tool to obtain similar absorption properties, especially in the infinitely diluted region, without needing previous experimental data to fit the model.

- Na^+ cations are the most effective adsorption sites in Faujasites. So, additional extraframework cations (i.e., lower Si/Al ratio) increase the selectivity and affinity of the surface to capture CO_2. The high CO_2 affinity is driven by the electrostatic interactions of the positively charged cations (i.e., a Lewis acid) with the electron rich O atoms of the gas (i.e., a Lewis base).

- However, the presence of additional cations in a Faujasite framework also reduces the total pore volume available for gas molecules to adsorb, which implies that the loading at the saturation point is reduced. For this reason, depending on the adsorption/desorption conditions imposed, Faujasites with intermediate Al content can be more optimal than the reference NaX for CO_2 capture and separation in post-combustion flue gases

- Mg-MOF-74 is also a good material for CO_2 capture because it presents very high adsorption CO_2 capacities combined with good selectivities for this gas. The high CO_2 affinity, similarly to Faujasites, is based on the electrostatic interactions between the cations and the electron rich O of the gas. Unfortunately, some pollutants such as SO_2 interact even stronger with the Mg^{2+} cations, poisoning the surface and hampering CO_2 capture and separation. Therefore, different adsorption/desorption conditions must be used to recover the purest CO_2 possible in Mg-MOF-74 depending on the % of SO_2 present in the flue gas

- An alternative technology for gas capture and separation is the application of ILs, which can be used directly as substitutes for amines in CO_2 absorption. Specifically, the three studied phosphonium-based ILs present high absorption capacities, when compared to other widely used ILs, but they also interact strongly with SO_2.

- All the studied technologies are more selective to capture SO_2 than CO_2. Moreover, Faujasites and Mg-MOF-74 adsorb SO_2 so strongly that they cannot be easily regenerated. Otherwise, all of the studied ILs have weaker interactions with the pollutant, which allows an effective regeneration of the material by heating. This permits to apply ILs either to capture CO_2 in uncontaminated flue gases, or to strip the SO_2 from the post-combustion mixture, which can be subsequently treated with a MOF, a zeolite or a second IL to separate the CO_2.

On the Oil/Water/Rock Wettability for Enhanced Oil Recovery

- The results obtained in this part of the thesis aim to better understand the behavior of different model oils when they are in contact with water, rocks and salts via molecular simulations. Within this framework, it is intended to shed some light onto the most fundamental interactions that are involved in oil recovery processes, to open the possibility of developing new techniques that take advantage of this knowledge to improve them.

- The most polar components of oil can migrate from the bulk to the interface with water to interact with it via electrostatic interactions or hydrogen bonds. These kinds of interactions stabilize the oil/water interface, reducing its interfacial tension and increasing the interfacial width. Otherwise, the less polar compounds tend to flee from interfaces and become relegated at the oil bulk.

- The same components that are active at the oil/water interface are also attracted by the polar surfaces of minerals, attaching the oil strongly to the rock and preventing a potential oil recovery. When the surface is very hydrophilic, such as the $(10\bar{1}4)$ calcite, a thin water layer is formed between the oil and the surface. Even with the presence of this water layer, the most polar components of oil can interact with the mineral increasing the effective oil/water/rock contact angle.

- The selected asphaltene molecules modeled in the most complex oil mixtures do not have a significantly high interfacial activity. For this reason, when asphaltenes are within a non-polar naphthenic matrix they accumulate at the interfaces, while in the presence of resins their interfacial activity is significantly reduced.

- The effect of electrolytes onto the oil/water interfacial tension shows a monotonical increase with salinity concentration because the interactions of all oil components with salt are relatively weak. However, the most polar species seem to be pulled towards the oil/water interface by effect of the electrostatic interactions. This is more notable in the contact angle calculations with calcite, where it is seen that the electrolytes located in the water layer between the oil and the mineral attract the acid species of oil, so they can interact with the surface, and ultimately increase the oil/water/rock contact angle.

On the Interaction of Surfactants with Oil/Water/Salt Systems for Enhanced Oil Recovery

- The results compiled in this part of the thesis aim to give an alternative molecular point of view to the mechanisms proposed for explaining the salt/surfactant synergistic effect. With the MD simulations carried out, some of the experimentally proposed mechanisms could be observed, as well as additional molecular arrangements previously unpublished.

- The cations of brine can interact with surfactants located at the oil/water interface and act in a synergistic way to reduce the interfacial tension. The previously proposed mechanisms assumed that the salts enhanced the effect of surfactants at the interface, but the MD simulations reveal that the interfacial activity of electrolytes is also promoted by effect of surfactants.

- The tight interactions of surfactant head groups and cations substitute the hydration waters of both moieties, disrupting their solvation spheres. When this happens, the cations become attracted by the surfactant and increase their interfacial activity. However, as the attraction of the anions towards the interface is significantly weaker than the attraction of the cations, an electric double layer is formed close to the interface, strongly polarizing this region.

- The surfactants also become perturbed by the presence of electrolytes by better packing their head groups and becoming, in average, more planar towards the interface. This change in conformation makes each surfactant molecule to occupy more interfacial area, which keeps the oil and water phases more isolated among each other, affecting the final oil/water interfacial tension.

- Finally, a stronger salt/surfactant synergistic effect was seen when using a ramified surfactant instead of a linear surfactant. The reason is that the two shorter tails of the ramified surfactant are capable of better occupying the interface area in contrast to the single long tail of the linear surfactant.

CHAPTER 7

List of Publications

Publications in high quality peer-reviewed journals were written from the results compiled along Chapter 3, Chapter 4 and Chapter 5 and are listed below. Some fragments of the work were submitted during the writing of the doctoral thesis and are currently under revision, so an early publication is expected. On the other hand, additional work regarding collaborations with other research groups were not compiled in this doctoral thesis because the topics were not suitable in its framework. To conclude, this final chapter contains a list of all of the publications, as well as their current publishing status.

Publications from this Thesis

- G. Alonso, D. Bahamon, F. Keshavarz, X. Giménez, P. Gamallo and R. Sayós, Density Functional Theory-Based Adsorption Isotherms dor Pure and Flue Gas Mixtures on Mg-MOF-74. Application in CO_2 Capture Swing Adsorption Processes. *J. Phys. Chem. C,* 2018, **122,** 3945-3957.

- G. Alonso, H. Prats, D. Bahamón, F. Keshavarz, P. Gamallo, X. Giménez and R. Sayós, New Methods for CO_2 Capture and Separation Applicable to Industrial Processes. *Rev. Soc. Cat. Quím.,* 2016, **15,** 21-30.

- H. Prats, D. Bahamon, G. Alonso, X. Giménez, P. Gamallo and R. Sayós, Optimal Faujasite Structures for Post Combustion CO_2 Capture and Separation in Different Swing Adsorption Processes. *J. CO2 Util.,* 2017, **19,** 100-111.

- G. Alonso, P. Gamallo, R. Sayós and F. Llovell, Combining soft-SAFT and COSMO-RS Modeling Tools to Assess the CO_2-SO_2 Separation using Phosphonium-based Ionic Liquids. *Submitted to: J. Mol. Liq.*

- G. Alonso, P. Gamallo, A. Mejía and R.Sayós, Assessing Salt-Surfactant Synergistic Effects on Interfacial Tension from Molecular Dynamics Simulations. *Submitted to: J. Mol. Liq.*

- G. Alonso, P. Gamallo, C. Rincón and R.Sayós, Atomistic Molecular Dynamics Simulations of Interfacial Tensions for Several Oil/Water Systems. *Manuscript under preparation.*